



HAL
open science

Atmospheric aerosols at the Pierre Auger Observatory : characterization and effect on the energy estimation for ultra-high energy cosmic rays

Karim Louedec

► **To cite this version:**

Karim Louedec. Atmospheric aerosols at the Pierre Auger Observatory: characterization and effect on the energy estimation for ultra-high energy cosmic rays. Other [cond-mat.other]. Université Paris Sud - Paris XI, 2011. English. NNT : 2011PA112191 . tel-00647476

HAL Id: tel-00647476

<https://theses.hal.science/tel-00647476>

Submitted on 2 Dec 2011

HAL is a multi-disciplinary open access archive for the deposit and dissemination of scientific research documents, whether they are published or not. The documents may come from teaching and research institutions in France or abroad, or from public or private research centers.

L'archive ouverte pluridisciplinaire **HAL**, est destinée au dépôt et à la diffusion de documents scientifiques de niveau recherche, publiés ou non, émanant des établissements d'enseignement et de recherche français ou étrangers, des laboratoires publics ou privés.

UNIVERSITE PARIS-SUD 11
ECOLE DOCTORALE : PARTICULES, NOYAUX,
COSMOS – ED 517
LABORATOIRE DE L'ACCELERATEUR LINEAIRE
DISCIPLINE : ASTROPARTICULES

THESE DE DOCTORAT

Soutenue le 30/09/2011

par

Karim LOUEDEC

Atmospheric aerosols at the Pierre Auger Observatory: characterization and effect on the energy estimation for ultra-high energy cosmic rays

Directeur de thèse : Marcel URBAN

Jury :

<i>President du jury :</i>	Achille STOCCHI	-	Professeur de l'Université Paris-Sud XI
<i>Rapporteurs :</i>	Rémi LOSNO	-	Professeur de l'Université Paris-Diderot VII
	Darko VEBERIČ	-	Professeur de l'Université de Nova Gorica
<i>Examineurs :</i>	Etienne PARIZOT	-	Professeur de l'Université Paris-Diderot VII
	Sylvie ROSIER-LEES	-	Directrice de Recherche au CNRS
<i>Directeur de thèse :</i>	Marcel URBAN	-	Directeur de Recherche au CNRS

UNIVERSITE PARIS-SUD 11
ECOLE DOCTORALE : PARTICULES, NOYAUX,
COSMOS – ED 517
LABORATOIRE DE L'ACCELERATEUR LINEAIRE
DISCIPLINE : ASTROPARTICULES

THESE DE DOCTORAT

Soutenue le 30/09/2011

par

Karim LOUEDEC

Les aérosols atmosphériques à l'Observatoire Pierre Auger : caractérisation et effet sur l'estimation de l'énergie des rayons cosmiques d'ultra-haute énergie

Directeur de thèse : Marcel URBAN

Jury :

<i>President du jury :</i>	Achille STOCCHI	-	Professeur de l'Université Paris-Sud XI
<i>Rapporteurs :</i>	Rémi LOSNO	-	Professeur de l'Université Paris-Diderot VII
	Darko VEBERIČ	-	Professeur de l'Université de Nova Gorica
<i>Examineurs :</i>	Etienne PARIZOT	-	Professeur de l'Université Paris-Diderot VII
	Sylvie ROSIER-LEES	-	Directrice de Recherche au CNRS
<i>Directeur de thèse :</i>	Marcel URBAN	-	Directeur de Recherche au CNRS

Contents

Synthèse	v
Introduction	xv
1 Ultra-High Energy Cosmic Rays	1
1.1 A brief history of cosmic rays	2
1.2 Extensive air showers	4
1.2.1 Heitler model for electromagnetic cascades	5
1.2.2 Extension of the Heitler model to hadronic showers	8
1.3 Astrophysical problems presented by the highest energy cosmic rays	9
1.3.1 Origin and acceleration of cosmic rays up to 10^{20} eV	9
1.3.2 The propagation of ultra-high energy cosmic rays	13
1.4 Latest results from the Pierre Auger Observatory	20
1.4.1 Cosmic ray energy spectrum	20
1.4.2 Anisotropy and arrival directions	22
1.4.3 Mass composition	24
1.4.4 Discussion of the Auger results	27
Bibliography	29
2 The Pierre Auger Observatory	33
2.1 The surface array (SD)	35
2.1.1 Signals and tank calibration	36
2.1.2 Data acquisition and trigger system of the surface detector array	38
2.1.3 Selection and reconstruction of the SD events	40
2.2 The fluorescence detector (FD)	44
2.2.1 Description of a fluorescence telescope	45
2.2.2 Calibration	45
2.2.3 Data acquisition and triggering in a camera	47
2.2.4 Reconstruction of the FD events	48
2.2.5 Typical hybrid events	51
2.3 Observatory enhancements	54
2.3.1 HEAT – High Elevation Auger Telescopes	54
2.3.2 AMIGA – Auger Muons and Infill for the Ground Array	56
Bibliography	58

3	Muonic component and arrival directions of the highest energy events	61
3.1	Phenomenological approach to the muon component in hadronic showers	62
3.1.1	The charged pion component	63
3.1.2	Muon production in hadronic showers	68
3.1.3	Muon propagation from birth to ground	74
3.2	Muon counting using the surface detectors	82
3.2.1	The jump method	82
3.2.2	The Artificial Neural Network (ANN) method	84
3.3	Mass composition and arrival directions of the highest energy events	85
3.3.1	Centaurus A, the region with the largest arrival direction excess	86
3.3.2	Muon component as a function of arrival direction	87
3.4	Conclusion	90
	Bibliography	92
4	Atmospheric measurements at the Pierre Auger Observatory	95
4.1	Atmospheric effects on light production and its propagation in the atmosphere	97
4.1.1	Molecular transmission – Rayleigh regime	98
4.1.2	Aerosol transmission – Mie regime	100
4.1.3	Ultraviolet and visible absorption by atmospheric trace gases	102
4.1.4	Angular dependence of molecular and aerosol scattering	106
4.2	Molecular measurements at the Pierre Auger Observatory	107
4.2.1	Weather station measurements and horizontal uniformity	107
4.2.2	Radio-sonde measurements and monthly average atmospheric profiles	114
4.2.3	Towards using the Global Data Assimilation System (GDAS)	114
4.3	Aerosol measurements at the Pierre Auger Observatory	117
4.3.1	Aerosol optical depth measurements	117
4.3.2	Aerosol scattering measurements	126
4.3.3	Aerosol sampling measurements	130
4.3.4	Wavelength dependence	131
4.4	Cloud detection at the Pierre Auger Observatory	134
4.5	Impact of the atmosphere on the reconstruction accuracy of air shower parameters	137
	Bibliography	139
5	Ramsauer approach for light scattering	143
5.1	Light scattering on spherical particles	145
5.1.1	Scattering by single particles: general considerations	145
5.1.2	Scattering by small particles: Rayleigh scattering	147

5.1.3	Scattering in the intermediate size range: Mie scattering	148
5.2	Application of the Ramsauer effect for light scattering	151
5.2.1	The Ramsauer scattering phase function	151
5.2.2	The simplified Ramsauer scattering phase function	155
5.2.3	Validity of the Ramsauer solutions	156
5.2.4	Effects of averaging over sizes	158
5.3	The Ramsauer total cross section and extinction efficiency	158
5.3.1	Ramsauer total cross section via the Optical theorem	161
5.3.2	Ramsauer total cross section via the differential cross section	165
5.4	Ramsauer approach to large aerosols as a possible source of the FD halo	166
5.4.1	Description of the FD halo phenomenon, and its discovery	166
5.4.2	The Aerosol Phase Function at the Pierre Auger Observatory	168
5.4.3	On possible underestimation of phase function at small angles	169
5.4.4	Explanation of the FD halo by a component with large aerosol size	172
5.5	Conclusion	175
	Bibliography	177
6	Where do aerosols come from ? – Study done with HYSPLIT	179
6.1	HYSPLIT, an air modelling program	180
6.1.1	Trajectory computational method	181
6.1.2	Meteorological data all along the trajectory	182
6.2	Aerosol origin and their trajectory up to the Auger location	182
6.3	Seasonal profiles of the different meteorological quantities	190
6.4	Cross-checks between Aerosol optical depth data and HYSPLIT	194
6.5	HYSPLIT, a tool to better understand Rayleigh nights ?	196
6.6	Conclusion	199
	Bibliography	200
7	Extracting Aerosol properties using the Central Laser Facility	201
7.1	Laser shot characteristics for each of the FD sites	203
7.2	Extracting of the Aerosol Phase Function	205
7.2.1	Signal from the laser shots recorded by the FD eyes	206
7.2.2	Geometrical reconstruction	212
7.2.3	Parameter estimation with an example: ($\theta_{FD} = 3^\circ$, $\phi_{FD} = 6^\circ$) at Los Leones	213
7.2.4	Description of the APF reconstruction procedure	215
7.3	Test of the reconstruction validity with <u>Offline</u> simulations	216
7.3.1	Reconstruction of the phase functions by a basic fit	216

7.3.2	Estimation of the aerosol parameters using a 4-parameter fit	218
7.4	First results	218
7.5	Conclusion	221
	Bibliography	223
8	Aerosol size effect on multiple scattering and shower reconstruction	225
8.1	Aerosol size distribution and its implications for aerosol physics	228
8.1.1	Aerosol attenuation length	229
8.1.2	Aerosol phase function	230
8.2	The FD-to-SD energy ratio as a possible proof of an aerosol effect	231
8.3	Atmospheric multiple scattering of light emitted by a point source	234
8.3.1	Multiple scattering and the elevation angle	238
8.3.2	Application to the FD halo measurements	240
8.4	Effect of multiple scattering on energy and X_{\max} reconstruction	244
8.5	Conclusion	247
	Bibliography	248
	Conclusion	251
	Rayleigh night study with HYSPLIT and weather stations	257

Synthèse

Les rayons cosmiques sont des particules venant de l'Univers et bombardant la Terre perpétuellement. Leurs énergies observées sur Terre vont du MeV jusqu'à quelques 10^{20} eV. Malgré qu'ils fussent découverts il y a presque un siècle, par Victor Hess en 1912, il ne reste pas moins que leur nature et leur origine restent un mystère. Par ailleurs, notre connaissance actuelle en physique des particules fut initiée par les rayons cosmiques, avec la découverte du positron en 1932, du muon en 1937, du pion en 1947 ou bien plus tard des particules étranges comme le kaon. Néanmoins, la communauté des physiciens des particules se détourna plus tard des rayons cosmiques au profit d'expériences sur accélérateurs avec l'émergence du CERN.

Le phénomène aujourd'hui connu sous le nom de gerbe atmosphérique fut découvert par Pierre Auger en 1938. Utilisant des compteurs fonctionnant en coïncidence et séparés de plusieurs centaines de mètres, Auger démontra qu'il existe de grandes gerbes de particules arrivant au niveau du sol. Il estima que ces gerbes détectées provenaient d'un rayon cosmique primaire d'énergie pouvant atteindre une énergie de 10^6 GeV, soit un saut de cinq ordres de grandeur par rapport aux précédentes découvertes faites par Bruno Rossi.

Le spectre en énergie des rayons cosmiques, c'est-à-dire le flux de particules primaires en fonction de leur énergie, est d'une incroyable régularité (voir Figure 1.1). Son comportement en loi de puissance $E^{-\gamma}$, d'indice spectral moyen 2.7, contient cependant quelques brisures comme

- **le genou** autour de 5×10^{15} eV, communément interprété comme la fin du processus d'accélération des rayons cosmiques par les restes de supernovae galactiques,
- **le second genou** vers 10^{17} eV, représentant la fin de l'accélération des noyaux de fer par les supernovae, l'énergie atteinte par ce processus d'accélération étant proportionnelle au numéro atomique Z du noyau,
- **la cheville** à 3×10^{18} eV, interprétée comme la région de transition entre les rayons cosmiques galactiques et extragalactiques. La position de la cheville sur le spectre serait l'énergie à laquelle les deux composantes contribuent de manière équivalente au flux de rayons cosmiques,
- **la coupure** au-dessus de 3×10^{19} eV, correspondant à la fin du spectre des rayons cosmiques. Même si cette coupure semble confirmée par les derniers résultats publiés dans la communauté, son origine reste toujours inconnue.

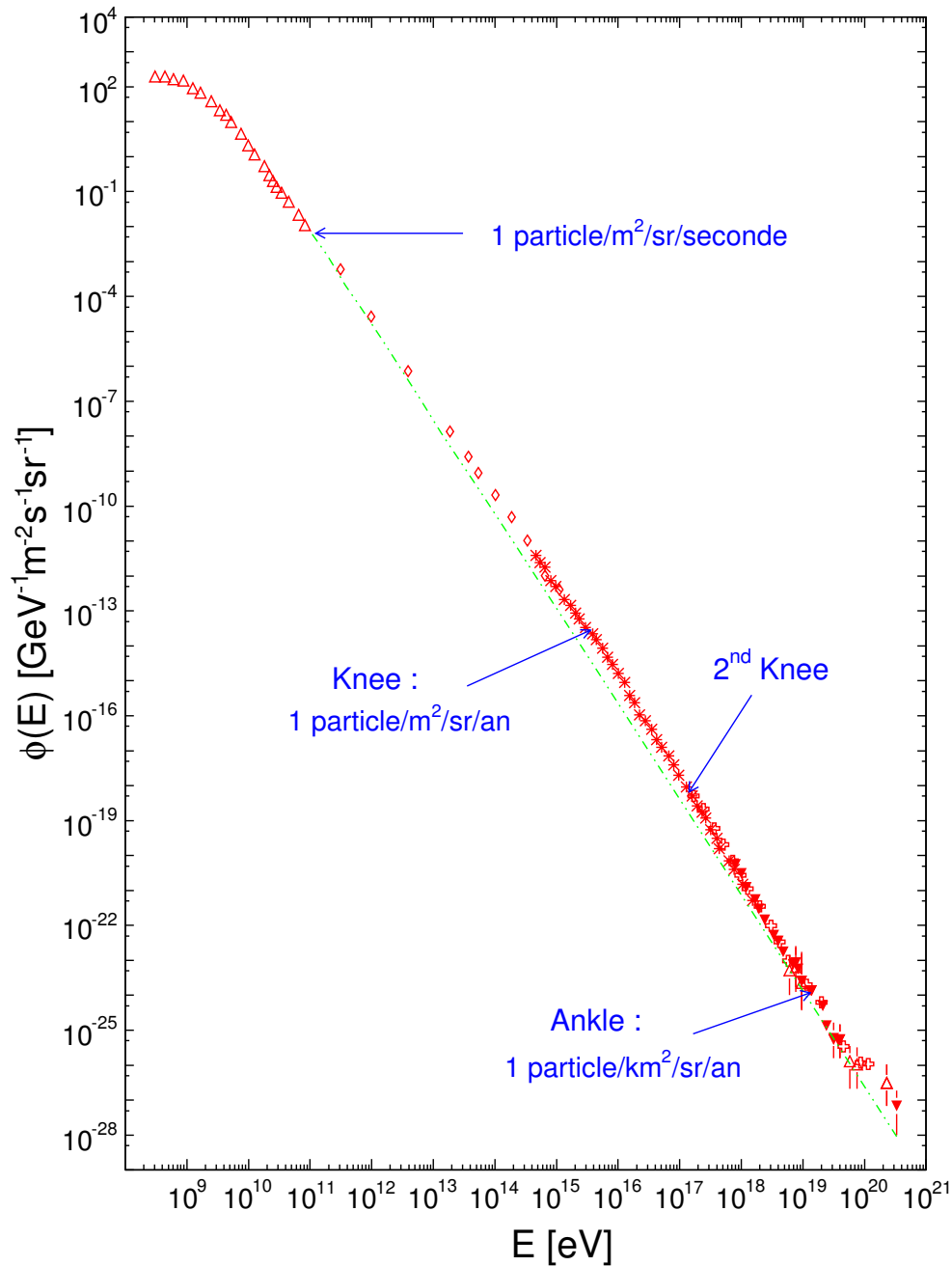


Figure 1: **Spectre en énergie des rayons cosmiques.** La ligne en trait pointillé montre une loi de puissance en E^{-3} pour comparaison. Les positions approximatives des genoux et de la cheville sont indiquées par leurs flèches respectives.

L'explication la plus répandue pour cette fin de spectre est la coupure dite *GZK*, du nom des trois physiciens Kenneth Greisen, Georgiy Zatsepin and Vadim Kuz'min. L'année qui suivit la découverte du *Fond Diffus Cosmologique* (FDC) par Penzias et Wilson, ils prédirent que l'interaction de protons d'extrême énergie avec le FDC devrait produire une coupure dans le spectre des rayons cosmiques aux énergies supérieures à quelques 50 EeV. De nos jours, cet effet est connu sous le nom d'*effet GZK*. L'interaction mise en jeu est la photo-production de pion, c'est-à-dire un proton interagit avec un photon du FDC pour créer un pion, via la résonance Δ^+ à 1232 MeV.

Dans la suite, nous allons nous intéresser exclusivement aux rayons cosmiques d'énergie supérieure à 10^{18} eV, appelés *rayons cosmiques d'ultra-haute énergie* (RCUHEs). Du fait de leur très faible flux sur Terre, environ une particule par km^2 et par siècle au-delà de 10^{19} eV, leur détection directe n'est pas réalisable. Une fois entrés dans l'atmosphère, ils produisent une gerbe de particules secondaires. Ce sont ces particules qui, après de successives interactions, arrivent au niveau du sol.

L'Observatoire Pierre Auger

L'Observatoire Pierre Auger est le plus grand détecteur de rayons cosmiques jamais construit sur Terre. Il a été conçu pour mesurer le flux, la distribution des directions d'arrivées et la composition des rayons cosmiques au-dessus de 10^{18} eV avec une grande statistique. La conception fut adaptée afin de comprendre le désaccord entre deux résultats précédemment publiés sur la fin du spectre en énergie des rayons cosmiques. En effet, deux expériences, AGASA (Akeno Giant Air Shower Array) et HiRes (High Resolution Fly's Eye), utilisant deux techniques différentes, des scintillateurs au sol et des télescopes de fluorescence, respectivement, avaient mesuré, avec un nombre d'événements limité, des spectres en énergie contradictoires. AGASA montrait l'amorce d'une augmentation du flux aux énergies supérieures à 5×10^{19} eV tandis que les données d'HiRes indiquaient une coupure autour des mêmes énergies.

L'expérience Pierre Auger est située dans la province de Mendoza, en Argentine, près de la ville de Malargüe. Sa construction fut achevée à la fin de l'année 2008 (voir Figure 2). Le détecteur est composé de 1660 stations au sol – des cuves d'eau Cherenkov et leur électronique embarqué – agencées sur un réseau triangulaire, espacées chacune de 1.5 km, et couvrant une surface totale de $3\,000 \text{ km}^2$. Durant les nuits claires sans Lune (un peu plus de 10% du temps), quatre stations optiques – Los Leones, Los Morados, Loma Amarilla, Coihueco – regardent l'atmosphère au-dessus du réseau Auger. Chaque station contient six télescopes, conçus pour récolter la lumière de fluorescence produite par les gerbes atmosphériques. Les cuves au sol détectent les particules (principalement des muons, électrons, positrons et photons) atteignant le sol, alors que les télescopes récoltent la lumière de fluorescence émise lors

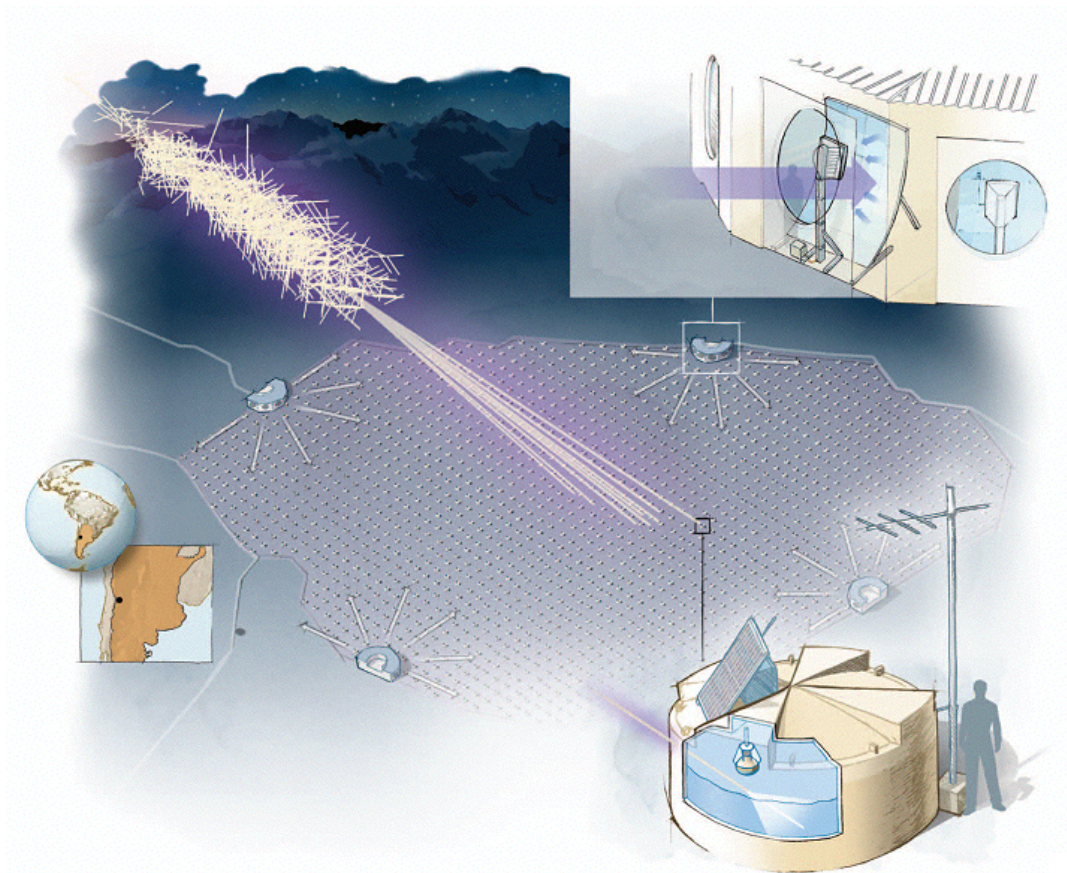


Figure 2: **Description de l'Observatoire Pierre Auger, détecteur hybride de rayons cosmiques d'UHE énergie.** Le réseau de maille triangulaire avec ses 1660 cuves est représenté au sol, entouré des 4 sites de fluorescence.

de la désexcitation du diazote.

En effet, lorsqu'une gerbe de particules se développe dans l'atmosphère, les électrons qui y sont produits excitent les molécules de diazote qui émettent ensuite une lumière de fluorescence de manière isotrope dans l'intervalle en longueur d'onde 300–430 nm. Ce nombre de photons de fluorescence émis est directement proportionnel à l'énergie déposée par la gerbe dans l'atmosphère. Dans le cas de l'expérience Auger dite *hybride*, l'estimation de l'énergie du rayon cosmique est dépendante des mesures de fluorescence. Lorsque les télescopes opèrent, c'est-à-dire environ 10% du temps, les signaux enregistrés dans les cuves au sol sont calibrés en énergie avec les mesures de fluorescence, moins dépendantes des modèles théoriques pour estimer correctement l'énergie des rayons cosmiques. Une courbe d'étalonnage est donc obtenue grâce aux événements hybrides. Puis, le reste du temps, lorsque uniquement la détection au sol n'est possible, cette calibration est utilisée pour estimer l'énergie.

Au vu de l'importance de la mesure par fluorescence dans l'estimation de l'énergie des rayons cosmiques, il est primordial de bien reconstruire les photons de fluorescence produits dans l'atmosphère. En fait, dans l'expérience Pierre Auger, l'atmosphère est utilisée comme un calorimètre géant. Contrairement aux expériences sur accélérateur, ce calorimètre est en constante évolution. Afin de réduire autant que possible les incertitudes systématiques sur les mesures de fluorescence, les propriétés de l'atmosphère doivent être suivies continuellement. Ces propriétés incluent les variables d'état comme la température, la pression ou l'humidité pour la partie moléculaire de l'atmosphère, mais également des quantités décrivant le caractère diffusant de l'atmosphère telles que la profondeur optique ou la fonction de phase¹. En effet, de leur point de production au télescope, les photons de fluorescence peuvent être diffusés et/ou absorbés par des molécules et/ou des aérosols.

Le travail de cette thèse de doctorat s'est axé sur les aérosols atmosphériques et leur effet sur l'estimation de l'énergie des rayons cosmiques. Les aérosols sont de fines particules en suspension dans l'atmosphère, avec une taille de l'ordre du micromètre. Ces particules peuvent rester dans l'atmosphère plusieurs jours, voire plusieurs semaines, tout ceci dépendant principalement de leur altitude, de leur composition chimique ou des précipitations durant la même période.

Mesure des aérosols atmosphériques à l'Observatoire Pierre Auger

Afin d'étudier et de simuler l'effet des aérosols sur la propagation des photons de fluorescence, deux quantités physiques sont nécessaires: la distance moyenne parcourue par un photon avant de rencontrer un aérosol, et l'angle de diffusion. Alors que la première grandeur est estimée par la profondeur optique des aérosols, la deuxième est extraite de la fonction de phase des aérosols.

Dans le cadre de l'expérience Pierre Auger, les aérosols sont mesurés toutes les nuits où des mesures de fluorescence sont opérées. La profondeur optique des aérosols à une altitude h et à une longueur d'onde fixée λ , notée $\tau_a(h, \lambda)$, est mesurée toutes les heures grâce au laser central installé à l'Observatoire Auger. Le principe repose sur le fait qu'un tir laser vertical voit son profil de lumière observé par les télescopes modifié en fonction de la concentration en aérosols dans l'atmosphère. La Figure 6.11(a) donne les distributions des profondeurs optiques d'aérosols à 3.5 km au-dessus du sol, pour trois sites de fluorescence. On définit comme "claires" les nuits ayant un $\tau_a \leq 0.01$ et de "sales" celles avec $\tau_a \geq 0.1$. La Figure 6.11(b) montre la distribution au cours de l'année des "nuits claires" et des "nuits sales". Il ressort clairement que les "nuits claires" ont beaucoup plus tendance à se produire durant l'hiver austral, c'est-à-dire entre juin et août.

¹Ces deux quantités peuvent être comprises comme la mesure de la concentration et de la section efficace différentielle, respectivement.

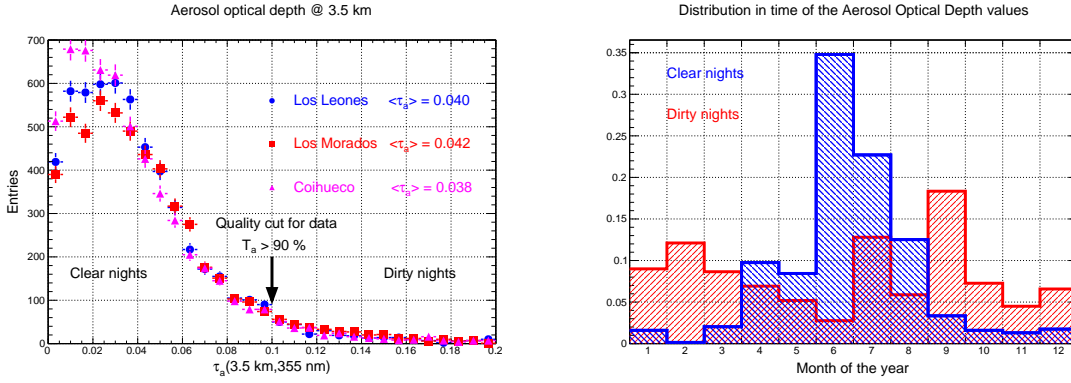


Figure 3: **Mesures de la profondeur optique d'aérosols à partir du laser central d'Auger.** (a) Profondeur optique d'aérosols à 3.5 km au-dessus du sol à Los Leones, Los Morados et Coihueco. Jeu de données entre janvier 2004 et décembre 2010. (b) Fréquence des "nuits claires" ($\tau_a \leq 0.01$) et des "nuits sales" ($\tau_a \geq 0.10$) au fil de l'année à Los Morados.

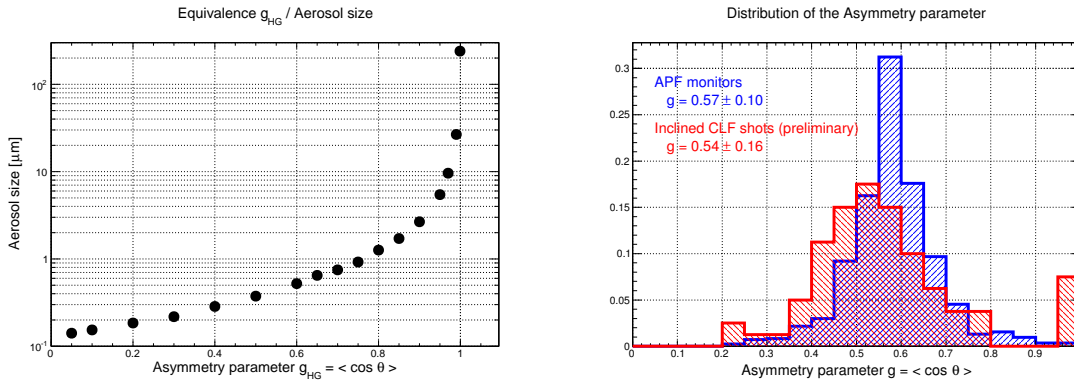


Figure 4: **Mesure de la taille des aérosols dans Auger.** (a) Relation entre le facteur d'asymétrie g de la Henyey-Greenstein et la taille moyenne des aérosols. (b) Distribution du paramètre d'asymétrie g mesurée par les moniteurs APF et par les tirs laser très inclinés.

La fonction de phase des aérosols, notée $P_a(\theta)$, représente la densité de probabilité de l'angle de diffusion θ . Dans l'expérience Auger, cette fonction de phase est paramétrée par une Henyey-Greenstein, du nom de ses deux inventeurs. Elle est définie par la relation

$$P_a(\theta|g, f) = \frac{1}{\sigma_a} \frac{d\sigma_a}{d\Omega} = \frac{1 - g^2}{4\pi} \left[\frac{1}{(1 + g^2 - 2g \cos \theta)^{3/2}} + f \frac{3 \cos^2 \theta - 1}{2(1 + g^2)^{3/2}} \right], \quad (1)$$

où $g = g_{HG} = \langle \cos \theta \rangle$ est le facteur d'asymétrie et f décrit l'importance du pic de rétrodiffusion. En utilisant une approche originale et inédite basée sur le modèle Ramsauer connu en diffusion atomique et nucléaire, nous avons établi une correspondance entre la taille moyenne des aérosols et le facteur d'asymétrie g (voir Figure 4(a)).

La Collaboration Auger détermine la fonction de phase des aérosols en mesurant le paramètre d'asymétrie g . Auparavant, la technique consistait à récolter la lumière diffusée par une lampe ayant son faisceau se propageant juste au-devant d'un site de fluorescence. Deux lampes, installées à Coihueco et Los Morados, ont pour but de mesurer la lumière diffusée pour des angles compris entre 30° et 150° . La distribution du paramètre g ainsi obtenue est donnée en Figure 4(b). Basée sur un raisonnement utilisant une nouvelle fois l'approche Ramsauer, il a été démontré que cette technique ne pouvait détecter les aérosols de grandes tailles, puisque leur pic de diffusion à l'avant est situé à des angles bien plus petits que 30° (la largeur du pic de diffusion est inversement proportionnel à la taille). Dans ces conditions, une nouvelle méthode de mesure du paramètre d'asymétrie g a été développée. Utilisant des tirs lasers très inclinés produit par le laser central d'Auger, il est possible d'accéder aux angles de diffusion plus grands qu'environ 6° . De nouvelles configurations de tirs laser ont donc été proposées, puis acceptées par la Collaboration Auger. Un résultat préliminaire de cette nouvelle méthode, basée sur des tirs laser à Los Leones, est donné en Figure 4(a). Une nouvelle population de gros aérosols est détectée via cette nouvelle technique. Les futurs données confirmeront ou non cette observation.

Origine géographique des aérosols

Les aérosols atmosphériques sont très mobiles. Ainsi, les populations d'aérosols présentes au-dessus de l'Observatoire Pierre Auger ne dépendent pas seulement des émissions locales, mais également des émissions et conditions météorologiques autour du détecteur. L'atmosphère détectée par les télescopes de fluorescence contient également des aérosols ramenés par des masses d'air voyageant au-dessus du réseau au sol.

Afin de vérifier l'influence des régions périphériques à l'Observatoire Pierre Auger, un modèle de rétrotrajectographie des masses d'air, HYSPLIT (HYbrid Single-Particle Lagrangian Integrated Trajectory), a été utilisé dans cette étude. L'idée est simple: nous avons vu précédemment que les mesures d'aérosols fait à l'Observatoire Auger pouvaient être classifiées en "nuits claires" et en "nuits sales". Partant de cette observation, voyons si ces deux catégories de nuits ont des trajectoires de masses d'air différentes. Si une telle observation était faite, cela signifierait que les aérosols présents au-dessus du détecteur Auger ne sont pas seulement affectés par le sol local, mais également par les régions avoisinantes.

La Figure 6.12 représente la distribution des rétrotrajectoires des masses d'air pour les "nuit claires" et les "nuits sales". Egalement sont données les distributions des directions des masses d'air. Lors des "nuits claires", les masses d'air proviennent directement de l'Océan Pacifique, alors que pour les "nuits sales", les masses d'air ont circulé presque exclusivement au-dessus du continent Sud-Américain. Cette observation peut être comprise par le fait que les aérosols mesurés à Auger ont pour origine majoritairement le sol. Ainsi, les masses d'air

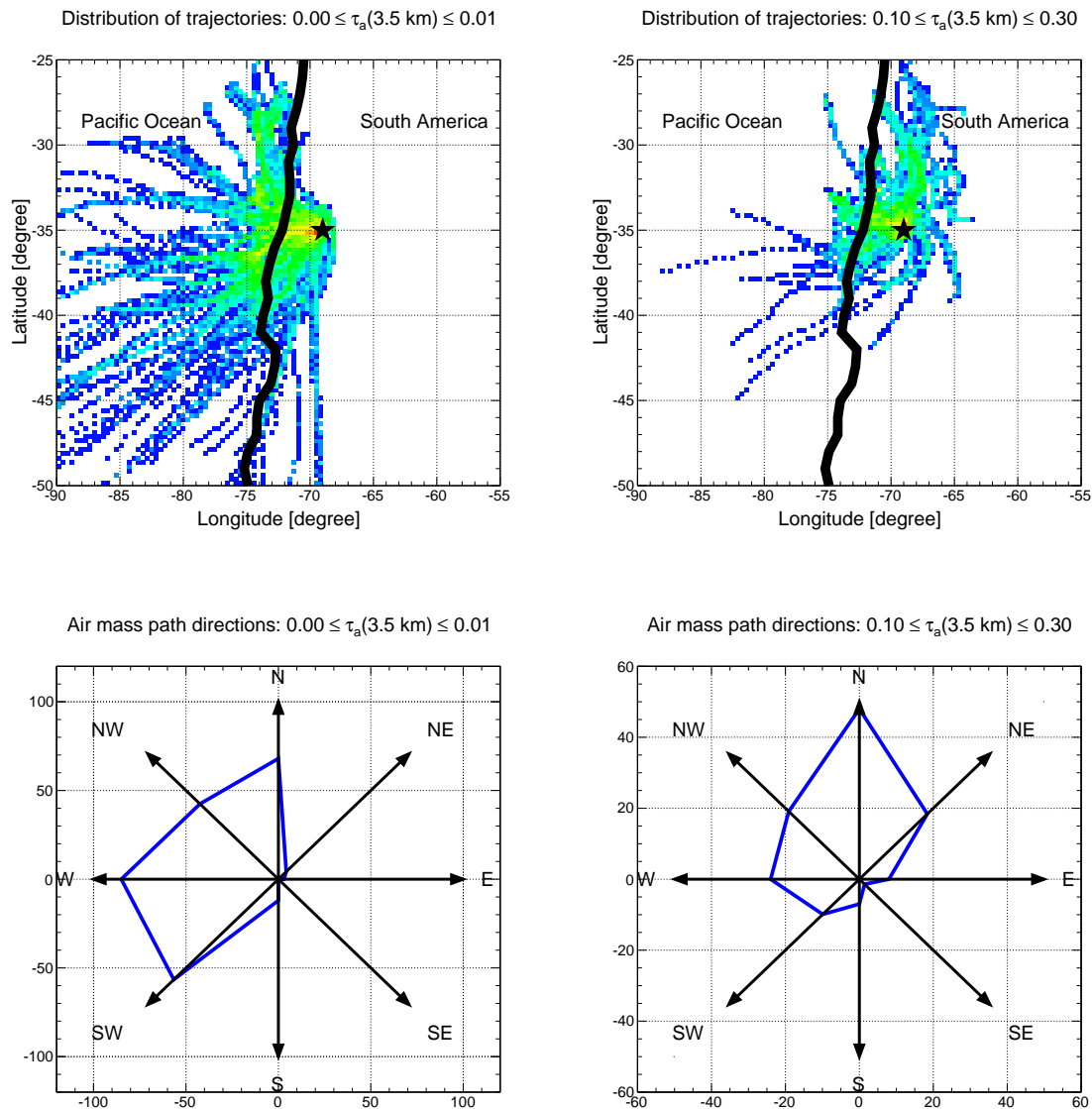


Figure 5: **Distribution des rétrotrajectoires and des directions des masses d'air pour les "nuits claires" et les "nuits sales"**. Trajectoires estimées avec HYSPLIT pour les années 2007 / 2008 / 2009, et profondeurs optiques des aérosols mesurées par le laser central. *En haut*: Distribution des rétrotrajectoires depuis la localisation de Malargüe. *En bas*: Direction des masses d'air influençant l'atmosphère d'Auger.

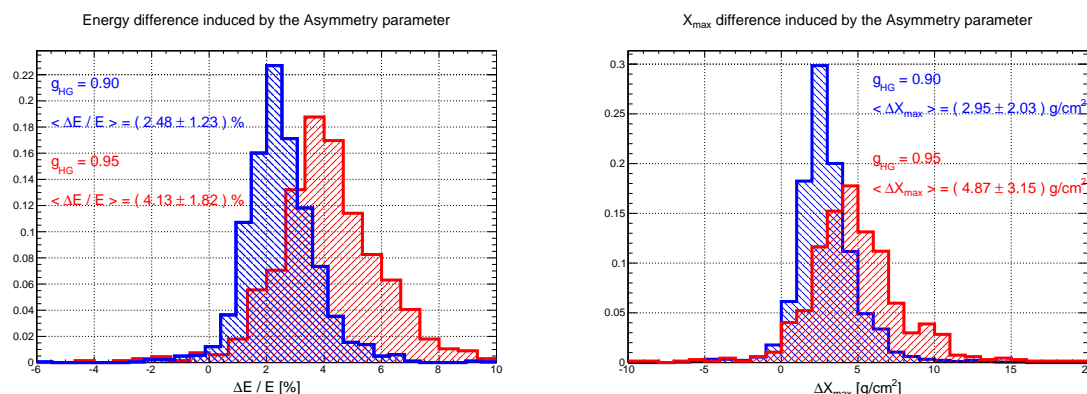


Figure 6: Erreurs sur l'énergie et le maximum de développement X_{max} induites par l'incertitude sur le facteur d'asymétrie. Les jeu de données correspond à l'année 2010, et reconstruites avec le Offline v2r6p5. Les différences sont définies par rapport à la valeur par défaut de g , soit 0.6.

traversant les zones terrestres ont le temps de se charger en aérosols.

Effet de la taille des aérosols sur la reconstruction des gerbes

L'estimation de l'énergie ou du maximum de développement de la gerbe X_{max} dépend de la diffusion multiple des photons de fluorescence dans l'atmosphère, de leur émission à leur détection. Pour la première, une étude sur l'effet de la taille des aérosols sur la diffusion des photons durant leur propagation est présentée. Jusqu'à présent, les paramétrisations reproduisant la contribution de la lumière diffusée sur la lumière directe ont toujours supposé une taille d'aérosols correspondant à un facteur d'asymétrie $g = 0.6$. La Figure 8.20 donne les erreurs sur l'énergie et le X_{max} pour $g = 0.90$ et $g = 0.95$, par rapport au cas où $g = 0.6$ (valeur par défaut choisie par la Collaboration Auger). Dans les deux cas, une surestimation de l'énergie et du X_{max} est observée. Pour les plus gros aérosols, la différence en énergie $\Delta E / E$ atteint +4% et le décalage pour le X_{max} est de +5 g/cm^2 . Sachant que les erreurs systématiques sur le X_{max} sont aux alentours de 12 g/cm^2 , l'effet des aérosols via la diffusion multiple devrait être suivie avec plus de détails.

Introduction

Cosmic rays are high-energy particles coming from the cosmos that bombard the Earth. Despite the fact that they were discovered one century ago, by Victor Hess in 1912, there remain many questions and puzzles surrounding them, not least of which are their exact nature and origin. Elementary particles such as positrons, muons or charged pions were discovered from the observation of cosmic rays and study of their induced air showers. This was the birth of elementary particle physics. However, the environment was not controlled enough for precise measurements as is the case in a laboratory. Thus, particle accelerators were built, providing higher luminosity for studying rare processes as well as known initial particle states.

The cosmic ray energy spectrum observed on Earth extends from below 1 GeV to beyond 10^{20} eV, more than 11 orders of magnitude. This energy spectrum drops rapidly with energy. Indeed, for the so-called *ultra-high energy (UHE) cosmic rays* corresponding to the right-hand limit of the spectrum, the flux is on the order of only one particle per century and per square kilometre. This makes these events only detectable indirectly through Extensive Air Showers (EAS). Nowadays, fundamental properties of these UHE cosmic rays such as their origin, their chemical composition and their acceleration mechanisms are still a mystery. These aspects are developed in Chapter 1.

The Pierre Auger Observatory was conceived to address the mystery of UHE cosmic rays. Covering more than 3 000 km², it represents a turning point in this field of research since it provides unprecedented statistics for UHE cosmic rays. It was designed as a hybrid instrument, utilizing both an array of surface detectors (SD) and nitrogen fluorescence detectors (FD). The detectors at ground record the shower's lateral profile and the telescopes detect the fluorescence light emitted during the shower development in the atmosphere. A detailed description of the Auger experiment is given in Chapter 2.

Up to now, the highest energy collision reproduced in a particle accelerator experiment is 7 TeV in the centre of mass, by the Large Hadron Collider (LHC) at CERN (Centre Européen de Recherches Nucléaires). The physics used to describe the highest energy collisions in the atmosphere is obtained by extrapolation. Hence, the characteristics of the first interactions occurring during the development of the air shower in the atmosphere are unknown. One direct effect of these extrapolations is the muonic component which seems to be different between simulation and observation. Chapter 3 presents a phenomenological approach based on average values in order to provide a better understanding of the muonic part in EAS.

One of the main challenges for the FD detection technique is the understanding of the atmosphere, used as a giant calorimeter. To minimize as much as possible the systematic uncertainties in fluorescence measurements, the Auger Collaboration has developed an extensive atmospheric monitoring program. Chapter 4 enumerates the different facilities installed at the Pierre Auger Observatory, and discusses the atmospheric data recorded over the past few years.

The purpose of this PhD thesis is to improve our knowledge of the atmospheric aerosols, and their effects on light propagation. The physics governing light attenuation by aerosols is provided by the Mie scattering theory. It is expressed as a series with many terms, obscuring the physical interpretation. Thus, Chapter 5 illustrates this scattering phenomenon by using the Ramsauer approach, a model well-known in atomic and nuclear physics. Analytical solutions are derived and applied to the Auger context.

Before studying in detail the atmospheric aerosols and their effect on air shower reconstruction, Chapter 6 focuses on their geographical origin. The aerosols probed in Auger have in general a lifetime of a few days, depending mainly on their size and on atmospheric conditions. Thus, aerosols affecting our measurements are brought by air masses travelling through the Auger Observatory. Correlations between aerosol origin and aerosol properties measured at the Auger location are to be expected.

From the Ramsauer approach and its analytical solutions, we observe that aerosols affecting the most the fluorescence light scattering are those having the largest size. Hence, a method to evaluate the aerosol size is presented in Chapter 7. This technique uses the very inclined shots fired by the Auger central laser facility to estimate the largest aerosol size ever probed by the Auger Collaboration. A first estimation of the aerosol size is given and compared with previous results obtained by the Auger Collaboration.

Finally in Chapter 8, the aerosol size dependence will be included in the parameterizations describing multiple scattering, i.e. the contribution of the scattered light to the direct light. Indeed, up to now, this dependence has not been taken into account in the light attenuation models. The purpose of this chapter is to see how the aerosol size affects the multiple scattering contribution to the direct light. A new multiple scattering parameterization dependent on the aerosol size is given. Its effect on the air shower reconstruction, i.e. the shower energy and the shower maximum development, is given.

Ultra-High Energy Cosmic Rays

Contents

1.1	A brief history of cosmic rays	2
1.2	Extensive air showers	4
1.2.1	Heitler model for electromagnetic cascades	5
1.2.2	Extension of the Heitler model to hadronic showers	8
1.3	Astrophysical problems presented by the highest energy cosmic rays	9
1.3.1	Origin and acceleration of cosmic rays up to 10^{20} eV	9
1.3.2	The propagation of ultra-high energy cosmic rays	13
1.4	Latest results from the Pierre Auger Observatory	20
1.4.1	Cosmic ray energy spectrum	20
1.4.2	Anisotropy and arrival directions	22
1.4.3	Mass composition	24
1.4.4	Discussion of the Auger results	27
	Bibliography	29

Cosmic rays are a wide topic, deeply related to many fields of physics, ranging from particle and nuclear physics to astrophysics and cosmology. Our present knowledge of elementary particles was initiated by cosmic rays, with the discovery of the positron in 1932, the muon in 1937, the pion in 1947, and later of the strange particles kaon and Λ -hyperon.

From the astrophysical point of view, however, almost one century after their discovery, fundamental questions of cosmic ray physics remain unanswered, particularly at ultra-high energy. What kind of particles are they? Where do they come from? How can they be accelerated to such high energies? What is the spatial distribution of their sources? What can they tell us about the cosmic accelerators producing such extreme energies? How strong are the magnetic fields that they traverse on their way to Earth? How do they interact with the cosmic background radiation and what secondary particles are produced from these interactions? What can we learn about particle interactions at these otherwise inaccessible energies?

Here, after a brief historical review of the subject, we will examine these different questions and recent progress towards answering some of them, including the last results from the Pierre Auger Observatory.

1.1 A brief history of cosmic rays

From balloon flights made by Victor Franz Hess as early as 1912 [1] it became clear that the ionization of the atmosphere increased very strongly with increasing altitude. Hess noted that the intensity of the ionization first decreased, but at around 1 km it started to increase markedly. This would not be expected if the origin was entirely from radioactive decay of material in the Earth's crust, as had previously been suggested. Werner Kolhörster flew balloons to altitudes exceeding 9 km in Germany and measured even higher ionization level. Hess and Kolhörster concluded that the air was being ionized by an extraterrestrial source: *cosmic rays*. The term came from Robert Millikan who was trying to prove that cosmic rays were γ -rays since they are very deeply penetrating in the atmosphere. The nature of this radiation remained unclear for many years, although it was shown by means of the "latitude" and "east-west" effects that the primary radiation included particles with energies as great as 10^{10} eV, and also that the majority were positively charged.

In 1928, a particle detector with the ability to reveal the passage of charged particles was developed. The Geiger counter, developed by Hans Geiger, was used by Walther Bothe and Werner Kohlörster to prove that cosmic rays can penetrate thick absorbers. Bruno Rossi used three Geiger counters, disposing them on a horizontal surface, so that no single particle could pass through the three detectors. He developed a coincidence circuit to select only events triggering the three detectors at the same time. This apparatus measured a great number of coincidences proving in this way the existence of secondary particle showers.

The phenomenon now known as extensive air showers (EAS) were discovered by Pierre Auger in 1938 in Paris [2], but he was also working at mountain altitudes. Using two or three counters, operated in coincidence, and separated by a variable distance of up to 300 m, Auger demonstrated that there are large particle showers arriving at ground level where particles are correlated in time and space. Pierre Auger estimated that the showers that were detected came from a primary cosmic ray of energy up to 10^6 GeV – a jump of five orders of magnitude over previous results.

The energy spectrum of cosmic rays, i.e. the primary particle flux as a function of energy, is almost featureless. Extending from 10^{10} eV (solar cosmic rays) up to 10^{20} eV, it follows a power law $E^{-\gamma}$ with an exponent γ , the so-called *spectral index*, almost constant and close to 2.7 (see Figure 1.1). This smooth power law spectrum contains three general features:

- **the cosmic ray knee** around 5×10^{15} eV, considered to be an acceleration feature. Par-

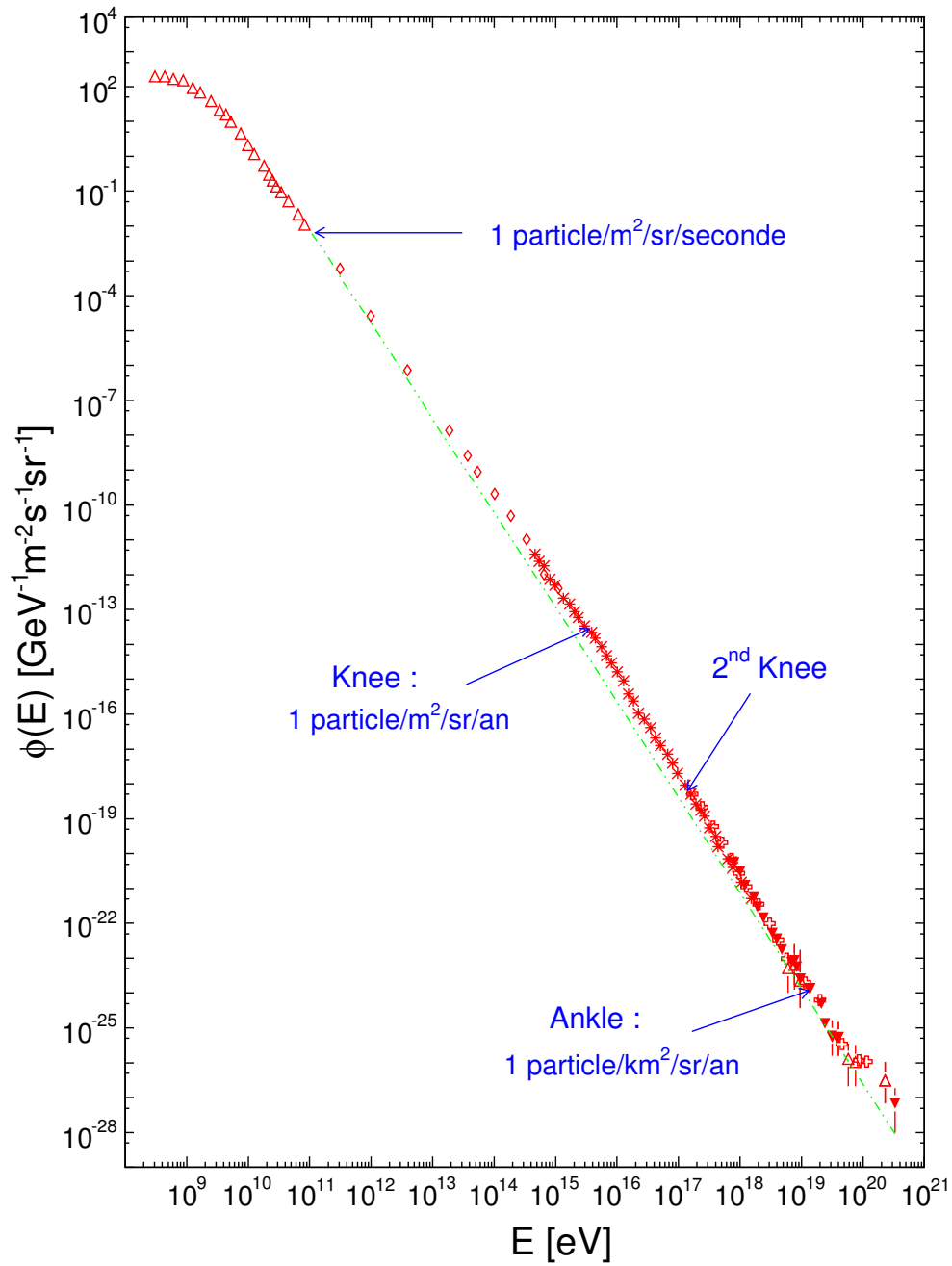


Figure 1.1: **Energy spectrum of cosmic rays.** Compilation of measurements of the differential energy spectrum. The dotted line shows an E^{-3} power law for comparison. The approximate positions of the ankle and the two knees are indicated.

ticles of energy below and around the knee are accelerated in galactic astrophysical objects such as supernova remnants. By assuming the energy of the cosmic ray to be proportional to the charge of the nucleus, the knee can be explained by successive cuts in energy of the nuclei when their charge increases, i.e. $E_{\text{knee}}(\frac{A}{Z}X) = Z \times E_{\text{knee}}(\text{proton})$. Published results from the KASCADE experiment seem to confirm this view [3]. Around 10^{17} eV, the spectrum shows a second knee, usually explained as the end-point for the acceleration of iron nuclei by supernova.

- **the cosmic ray ankle** at 3×10^{18} eV, interpreted as the transition region from cosmic rays of galactic origin to those of extragalactic origin. The extragalactic component is thought to have a pure proton composition. The position of the ankle would be the energy where the two components contribute equally to the total flux. It is not obvious how the particles above the ankle are accelerated, even if it is believed that this is done by extragalactic objects, such as active galactic nuclei (AGN) or gamma-ray bursts (GRB).
- **the cutoff** above 3×10^{19} eV, corresponding to the end of the cosmic ray energy spectrum. In standard interpretation this is explained by the interaction of the cosmic rays with the cosmic microwave background (CMB), known as the Greisen-Zatsepin-Kuz'min (GZK) cutoff. More details will be given later, in Section 1.3.

In the following, we will focus on the cosmic rays with energy above 10^{18} eV, the so-called *ultra-high energy cosmic rays*. Pioneering work by Bassi, Clark and Rossi in 1953 at MIT demonstrated that an array of ground level detectors could reconstruct the incidence direction of an EAS by a simple relative timing method [4]. This led to the Agassiz experiment which ran from 1954–1957 and was probably the first system which may be called an EAS array. As a follow up to the Agassiz facility, the first of the "giant" EAS array was constructed by Linsley and Scarsi at Volcano Ranch in New Mexico, USA (8 km^2 area), commencing operation in 1959 [5]. In 1962, a shower was recorded with a primary energy of 10^{20} eV [6] – an increase of five orders of magnitude over Auger's previous results. Discoveries continued during the next fifty years with larger and larger arrays but the total world statistics at ultra-high energy remained small.

1.2 Extensive air showers

Due to the steeply falling flux of incident particles with energy, direct observation of the primaries by using high altitude balloon and satellite experiments is only possible up to $\simeq 10^{14}$ eV. Above this limit information regarding the energy, arrival direction and nature of the particles can only be deduced by observing the cascade of secondaries.

When a cosmic ray reaches the atmosphere, it interacts with the nuclei of the air molecules, generating several secondary particles. The interaction cross section rises with energy, and also with the mass of the primary. The primary energy imparted to the particles of this second generation, which in turn interact again in the atmosphere generating new particles. The iteration of this process produces the so-called *extensive air shower*. In a 10^{19} eV proton-initiated shower, 2.4% of the primary energy goes into muons, 96% into the electromagnetic cascade, and the rest into neutrinos and hadronic particles which survive to ground level. Hence a reasonably detailed understanding of shower development processes, including hadronic interactions, is necessary.

The rapid progress of particle physics over the last fifty years has provided excellent knowledge of fundamental particle interaction properties, and the energy frontier has been pushed very high. The centre of mass energy available at the first interaction of a 10^{20} eV cosmic ray is $\simeq 400$ TeV – still two orders of magnitude above the available energy of the world’s most powerful proton-proton collider, the Large Hadron Collider (LHC) at CERN in Switzerland and France. However, it must be remembered that “standard” collider experiments are principally designed to probe rare interactions which result in products having large transverse momenta (high p_T), and in any case do not yield direct information regarding proton-nucleus collisions. Nevertheless, experimental programs specifically devoted to the study of cross sections in the forward region are ongoing. For example, at LHC, experiments like LHCf [7] or TOTEM [8] should be able to validate the EAS models at the nominal energy of the LHC.

A simple qualitative description of an ultra-high energy cascade is useful, and will be given in the following. When working with EAS it is convenient to consider position in the atmosphere in terms of g/cm^2 of overlying air mass. The relation between depth X and altitude above sea level h is approximately exponential with scale height $\simeq 8$ km, but somewhat modified by the atmospheric temperature gradient

$$X = (1000 \text{ g/cm}^2) \exp\left(\frac{h}{8 \text{ km}}\right),$$

since the sea level is at depth of 1000 g/cm^2 .

The basic properties of the development of the cascade can be extracted from a simplified model, the so-called *Heitler model* [9]. It describes the evolution of a pure electromagnetic shower.

1.2.1 Heitler model for electromagnetic cascades

The evolution of an extensive air shower is dominated by electromagnetic processes. The electromagnetic interactions can be calculated very accurately from quantum electrody-

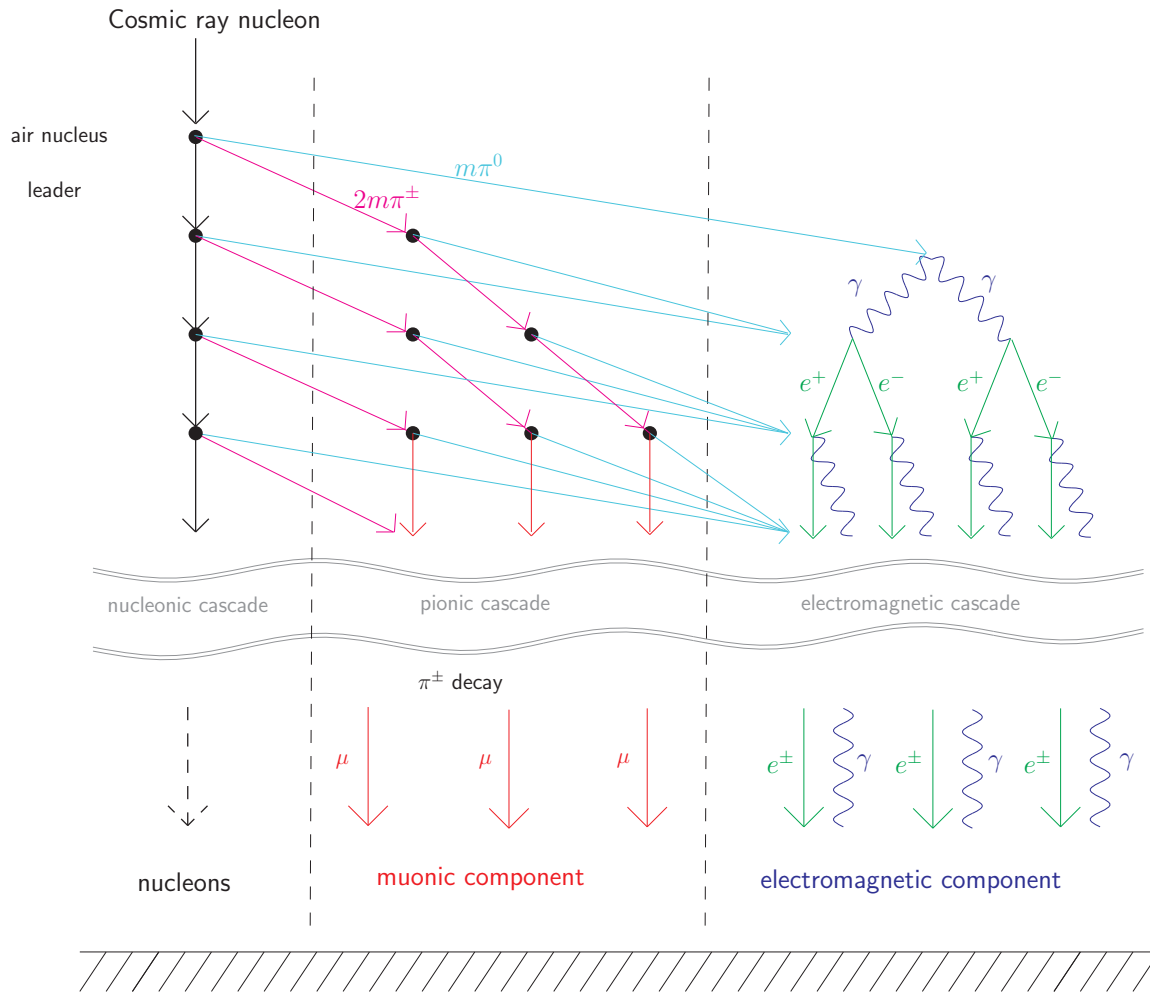


Figure 1.2: **Schematic diagram showing the principal EAS cascade processes.** An incident cosmic ray nucleon is assumed, and the resulting shower has three parts: the nucleonic cascade corresponding to the surviving primary itself (the “leading” nucleon), the pionic cascade and the electromagnetic cascade which is fed by neutral pion decay.

ics. The generation of the electromagnetic component is driven by electron bremsstrahlung and pair production. Eventually the average energy per particle drops below a critical energy, E_c^γ (80 MeV in air), at which point ionization takes over from bremsstrahlung and pair production as the dominant energy loss mechanism. The e^\pm energy loss rate due to bremsstrahlung radiation is nearly proportional to energy, whereas the ionization loss rate varies only logarithmically with the e^\pm energy. The changeover from radiation losses to ionization losses depopulates the shower. One can thus categorize the shower development in three phases:

1. **the growth phase**, in which all the particles have energy greater than E_c^γ ,

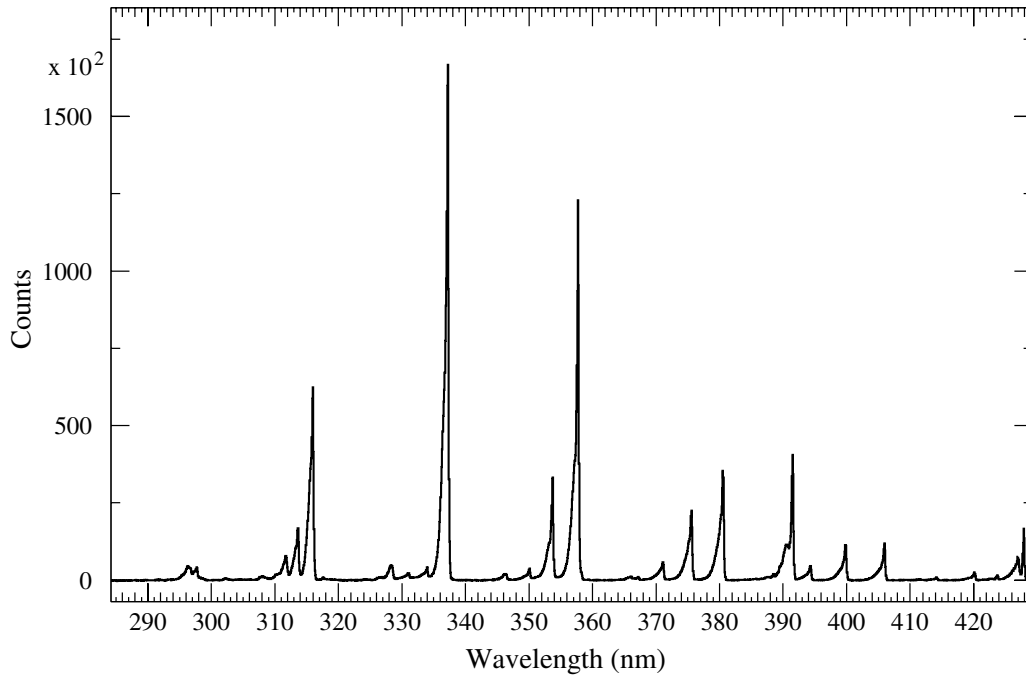


Figure 1.3: Measured fluorescence spectrum in dry air at 800 hPa and 293 K (from [10]).

2. **the shower maximum**, X_{\max} ,

3. **the shower tail**, where the particles only lose energy, get absorbed or decay.

An EAS is mainly composed of electrons and positrons with energies below 1 GeV, even if the shower is initiated by a hadronic particle. During its development through the atmosphere, the shower emits light. The principal phenomenon of interest is the production of fluorescence light, by the interaction of low-energy electrons with the N_2 molecules in the air. These molecules can radiate the acquired energy by internal transitions in the energy range of 300 to 430 nm (ultraviolet light, UV). A typical spectrum from these molecules is shown in Figure 1.3. Using this fluorescence light, longitudinal profile of the air showers can be reconstructed and subsequently the energy of the primary particle can be estimated.

The relativistic particles in an EAS also generate a large amount of Cherenkov light. Unlike the fluorescence light, this radiation is not emitted isotropically, but strongly beamed in the shower direction. If the shower is pointing directly at the fluorescence detector, the resulting Cherenkov light can easily exceed the isotropic light component of the shower. But, even if the direct beam is not pointing towards the detector, additional scattered Cherenkov light also contributes to the shower image in the telescope. Hence, air shower reconstruction methods have to take Cherenkov light into account.

1.2.2 Extension of the Heitler model to hadronic showers

Figure 1.2 is a schematic diagram showing the principal cascade processes in a shower initiated by an incident cosmic ray nucleon. Not shown are the Cherenkov (forward beamed) and fluorescence (isotropic) photons, produced principally by the electromagnetic cascade, and which reach ground level in large numbers over a wide area. At each successive generation of the nucleonic shower, approximately one half of the energy continues in nuclear particles, the great bulk being carried by a single "leading" nucleon (depending on the inelasticity). The rest of the incident energy produces pions, with roughly one sixth each going to π^- , π^+ and π^0 . The charged pions of the initial generations have such high energies that decay is effectively suppressed, and the bulk make nuclear collisions, and so give rise to a pionic cascade. However, the proper lifetime of the π^0 is so short that the majority will decay to gamma rays before interacting ($\pi^0 \rightarrow \gamma + \gamma$). Thus at each generation of the pionic cascade, one third of the available energy is lost to the electromagnetic cascade, and the remaining energy is distributed among a larger number of particles. During these successive steps, the nucleonic cascade continues to develop the pionic cascade.

The critical energy E_c^π , when decay $\pi^\pm \rightarrow \mu^\pm + \nu_\mu$ starts to dominate over nuclear interactions, determines the end of the hadronic cascade. E_c^π depends on the atmospheric density and on the pion decay length and is about 20 GeV (see Chapter 3 for more details). In this approach we neglect, from this point on, π^0 decays and their associated electromagnetic cascades and obtain a formula for the shower maximum:

$$X_{\max} = X_s(E_0|A = 1) + X_0 \ln \left(\frac{E_0}{m(E_0|A = 1) E_c^\gamma} \right), \quad (1.1)$$

where $X_s(E_0|A = 1)$ is the depth of the first interaction for a proton primary ($A = 1$), X_0 is the radiation length of the medium ($X_0 = 37 \text{ g/cm}^2$), E_0 the primary energy and $m(E_0|A = 1)$ the multiplicity of the first interaction.

The interaction of a nuclear primary is more complex with a random degree of fragmentation taking place at each step of the nucleonic cascade. However the superposition model allows us to extend the Heitler model to cover nuclei. A nucleus with atomic number A is, to a first approximation, equivalent to the superposition of A nucleons of individual energy E_0/A . Equation (3.1) can then be modified, enabling in this way the comparison between proton and iron showers

$$X_{\max} = X_s(E_0|A) + X_0 \ln \left(\frac{E_0/A}{m(E_0|A) E_c^\gamma} \right). \quad (1.2)$$

An iron initiated shower has a higher maximum than one produced by a proton with the same energy. This comes essentially from the fact that $X_s(E_0|A)$ is smaller for an iron

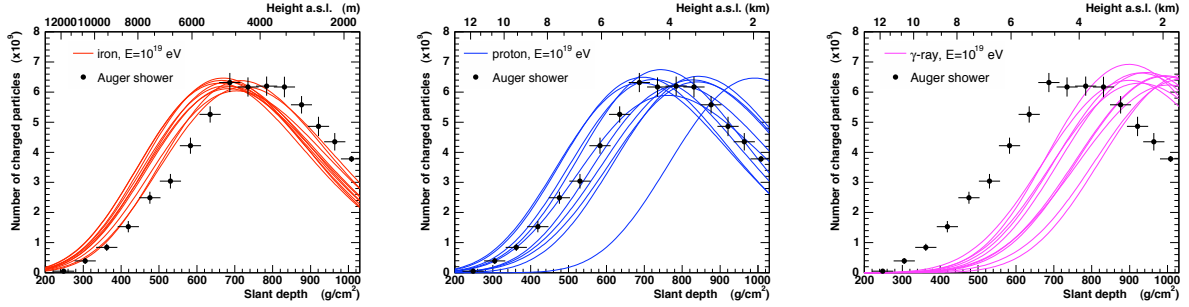


Figure 1.4: **Longitudinal profiles for three different primary cosmic rays.** (a) iron, (b) proton and (c) γ -ray. An example of a shower with an energy of 10^{19} eV recorded by the Pierre Auger Observatory is included in the three plots.

nucleus than for a proton, and also because the logarithmic term is smaller for iron ($A = 56$). Furthermore, the fluctuation of the position of X_{\max} from one shower to another is smaller for heavy nuclei than for light ones. Figure 1.4 gives the simulated longitudinal profiles for three different primaries, validating these two expectations.

From Equation (3.2) it is easy to obtain the rate of evolution of X_{\max} with energy, the so-called *elongation rate*

$$D_{10} = \frac{dX_{\max}}{d \log_{10} E_0} = \frac{dX_s(E_0|A)}{d \log_{10} E_0} + X_0 \ln 10 \times \left(1 - E_c^\gamma \frac{dm(E_0|A)}{d \log_{10} E_0} \right). \quad (1.3)$$

For nuclei and protons, the variations of the depth of the first interaction $X_s(E_0|A)$ and the multiplicity $m(E_0|A)$ are the same. Thus different nuclei will have identical elongation rates and will show up as parallel lines on a plot of X_{\max} versus primary energy E_0 .

1.3 Astrophysical problems presented by the highest energy cosmic rays

The ultra-high energy cosmic rays (UHECR) are the most energetic particles known. Understanding their origin, production and propagation can be expected to give us insight concerning basic aspects of our Universe.

1.3.1 Origin and acceleration of cosmic rays up to 10^{20} eV

It is rather difficult to identify potential sources for the highest energy cosmic rays based on current physical knowledge. The question of how to accelerate cosmic rays up to 10^{20} eV has been pending since their first observation in the 1960's. The models that can be imagined to

produce particles with sufficiently high energy are split into two categories called the top-down and bottom-up scenarios. The first involves the decay of very high mass relics from the early Universe requiring physics beyond the standard model of particles and their interactions. The second involves searching for possible acceleration sites in known astrophysical objects that can provide energies of the order of 10^{21} eV. In this section, we will briefly discuss the general characteristics of these two scenarios.

1.3.1.1 The "top-down" models

One way to overcome the many problems related to the acceleration of UHECRs is to introduce super-massive particles, having masses $m_\chi c^2$ much greater than 10^{20} eV, and originating from high-energy processes in the early Universe. These particles should typically decay to quarks and leptons. The quarks hadronize producing jets containing mainly light mesons (such as pions) with a small percentage of baryons (mainly nucleons). The pions decay to photons, (anti-)neutrinos and electrons/positrons. Hence, energetic photons, neutrinos and charged leptons, together with a small fraction of nucleons, are produced directly with energies up to $\sim m_\chi c^2$ without any acceleration mechanism, the UHECR emerging directly from this decay cascade.

In order to observe the decay products of super-massive particles as UHECRs today, three basic conditions must be satisfied: their mass must be large enough ($m_\chi c^2 \gg 10^{20}$ eV); the decay must occur in a recent cosmological epoch, i.e. at distances shorter than about 100 Mpc¹; the number density and rate of decay of the particles have to be large enough to be compatible with the observed flux of UHECRs.

The super-massive particles that could satisfy these criteria fall, basically, into two categories

1. **Topological defects**, such as magnetic monopoles or cosmic strings [11, 12]. The stability of the defect can be locally broken via radiation, interaction or collapse, producing particles that decay instantly: this happens in the false vacuum, trapped within the defect, to fall into the true vacuum, so that the gauge bosons of the field trapped in the defect acquire a mass m_χ and decay. The flux of UHECR is related to the number density of topological defects and their radiation, collapse or interaction rate.
2. **Cosmological relic particles**, with a lifetime of the order of the age of the Universe since these relics have to decay now to explain the UHECR flux presently observed [13, 14]. Super-massive relics accumulate in dark matter halos, especially in the halos of galaxies. The distribution of such relics should be linked to the galaxy distribution in

¹1 pc = 1 parsec = 3.26 light-year = 30.856×10^{12} km.

the sky. Hence the strongest signature for this model is anisotropy. The UHECR flux will depend on the ratio of the density of the relics to their lifetime.

If the “top-down” scenario dominates UHECR production above a certain energy, the photon fraction should increase. However, recent observations made by the Auger Observatory on the photon fraction and on the flux of high energy neutrinos indicate the contrary. This has considerably reduced the probability that the source of UHECRs is to find in such models.

1.3.1.2 The “bottom-up” models

It is generally assumed that the diffusive shock acceleration process is the most likely mechanism to accelerate particles to high energy.

Second-order Fermi mechanism: stochastic acceleration

The stochastic acceleration mechanism was first investigated by Enrico Fermi in 1949 [15]. The principle of Fermi acceleration is the transfer of energy from macroscopic motion to microscopic particles through their interaction with magnetic inhomogeneities. The energy transfer results from a sequence of collisionless scattering events with magnetic field turbulences. In the version elaborated by Fermi himself, magnetic scattering centres, typically interstellar clouds, had random velocities which led to an energy gain of order $\Delta E/E \propto \beta_{\text{cloud}}^2$, where β is the average velocity of the scattering centres in units of c ($\beta_{\text{cloud}} = v/c$). This process is called the *second-order Fermi mechanism* ($\beta_{\text{cloud}} \simeq 10^{-4}$).

The energy acquired depends on the time that the particle spends in the zone of magnetic turbulence and thus on the characteristics of the latter, which are poorly known for astrophysical objects. The process is also very inefficient in the non-relativistic case since $\beta_{\text{cloud}} \ll 1$, and it cannot explain the observed spectrum.

First-order Fermi mechanism: diffusive shock acceleration

An extension of the Fermi acceleration mechanism is obtained by considering multiple scattering of the particle with shock fronts. The macroscopic motion is now coherent, as for the case of a shock wave where particles can gain energy as they bounce back and forth. In this hypothesis, the average gain for an individual interaction with the shock is $\Delta E/E \propto \beta_{\text{shock}}$. This process is the so-called *first-order Fermi mechanism* ($\beta_{\text{shock}} \simeq 10^{-1}$).

Shock waves are quite frequent in the Universe, for instance where an ejecta encounters the interstellar medium. Supernova remnants (SNR) are attractive candidates for cosmic ray acceleration because they have higher magnetic fields than the average interstellar medium. Hence SNR are believed to be the sites where galactic cosmic rays are accelerated via the first-order Fermi mechanism. Popular shock regions for UHECR acceleration are gamma-ray

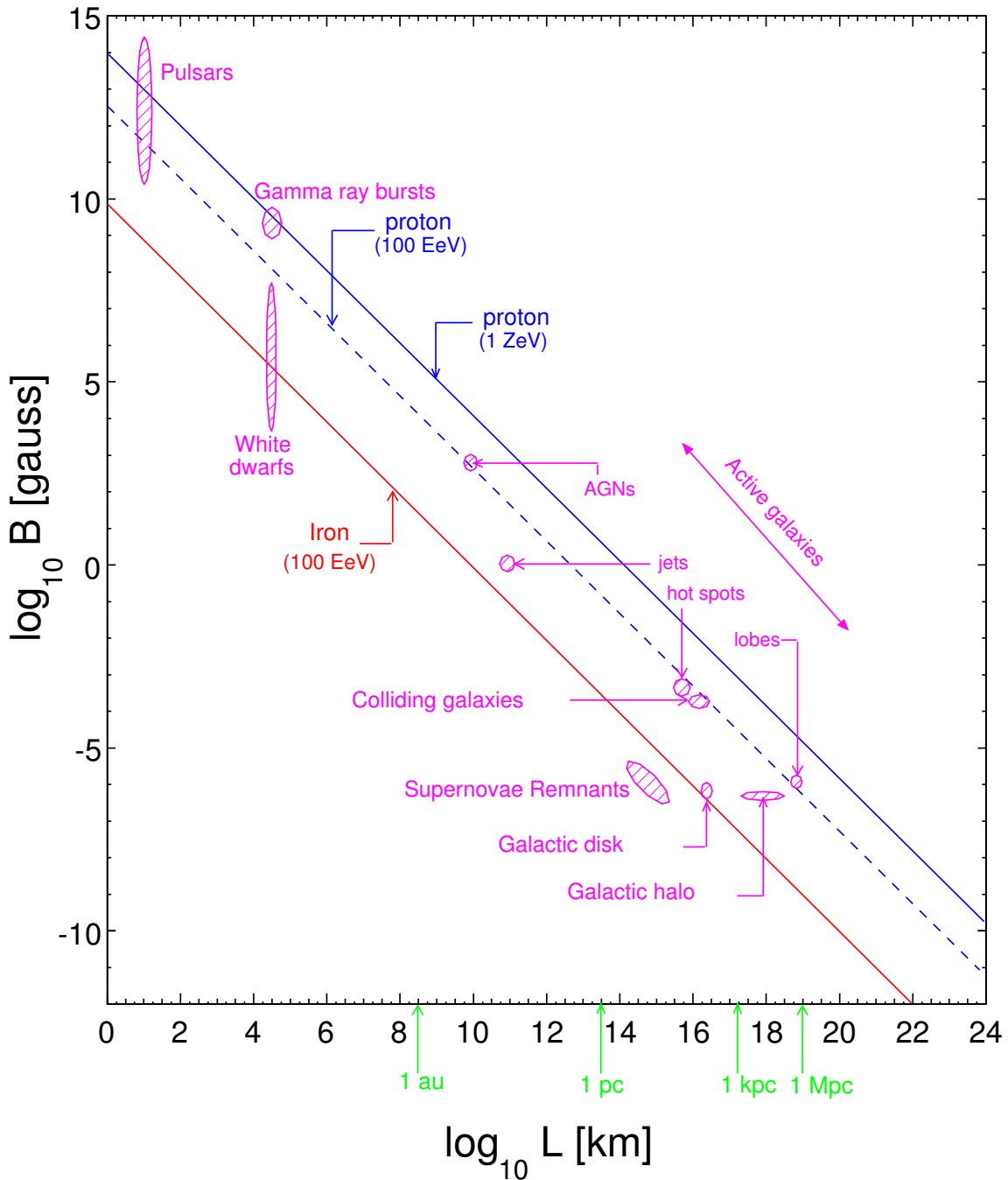


Figure 1.5: Hillas plot showing potential astrophysical sources for UHECRs. Uncertainties on the candidate source parameters are plotted. The blue line delimitates the region where protons can be confined to a maximum energy of $E_{\max} = 10^{21}$ eV. Above the dotted line, protons could be confined up to $E_{\max} = 10^{20}$ eV. Above the red line, iron nuclei could be confined up to $E_{\max} = 10^{20}$ eV.

burst (GRB) shocks, jets and hot spots of active galactic nuclei (AGN).

One of the principal advantages of the diffusive shock acceleration mechanisms is that it naturally leads to a power law spectrum whose predicted index is compatible with that measured experimentally.

Hillas criterion: possible candidate sites

At the highest energies, the Larmor radius of the accelerated particle in galactic magnetic fields is larger than the galactic halo. Thus, confinement is not maintained for UHECRs, motivating the search of extragalactic sources. Expressing the confinement criterion in the particular case of sources with magnetic field strength B and spatial extension L enables us to make a first selection of potential candidate accelerators. This is the so-called *Hillas criterion* and is defined as follows [16] ($1 \text{ EeV} = 10^{18} \text{ eV}$)

$$E_{\max} = \beta Z \left(\frac{B}{1 \mu\text{G}} \right) \left(\frac{L}{1 \text{ kpc}} \right) \text{ EeV}. \quad (1.4)$$

In the case of relativistic shock velocities with highly relativistic blast waves, Equation (5.9) corresponds to the maximum energy for the frame at rest. The maximum energy has to be multiplied by the bulk Lorentz factor Γ_{shock} for the shock, to be estimated in the galactic frame.

Figure 1.5 presents the “Hillas diagram” where candidate sources are placed in a $B - L$ phase-space. Looking at the Hillas diagram one sees that only a few astrophysical sources satisfy the acceleration requirements. Among the possible candidates are neutron stars and other similar compact objects, large-scale shocks due to merging galaxies or clusters of galaxies, the cores and jets of Active Galactic Nuclei, hot spots of radio-galaxies and processes producing Gamma Ray Bursts. In the case of iron as the primary, the situation becomes more promising for other sources, such as the galactic halo or extremely magnetic white dwarfs.

1.3.2 The propagation of ultra-high energy cosmic rays

When examining the propagation of the UHECRs from their sources to the observer, two kinds of processes have to be considered:

- interactions with the cosmic magnetic fields that affect their direction and travel time, but not their energy and composition,
- interactions with cosmic particles and radiation backgrounds that affect their energy and their composition, but not their direction.

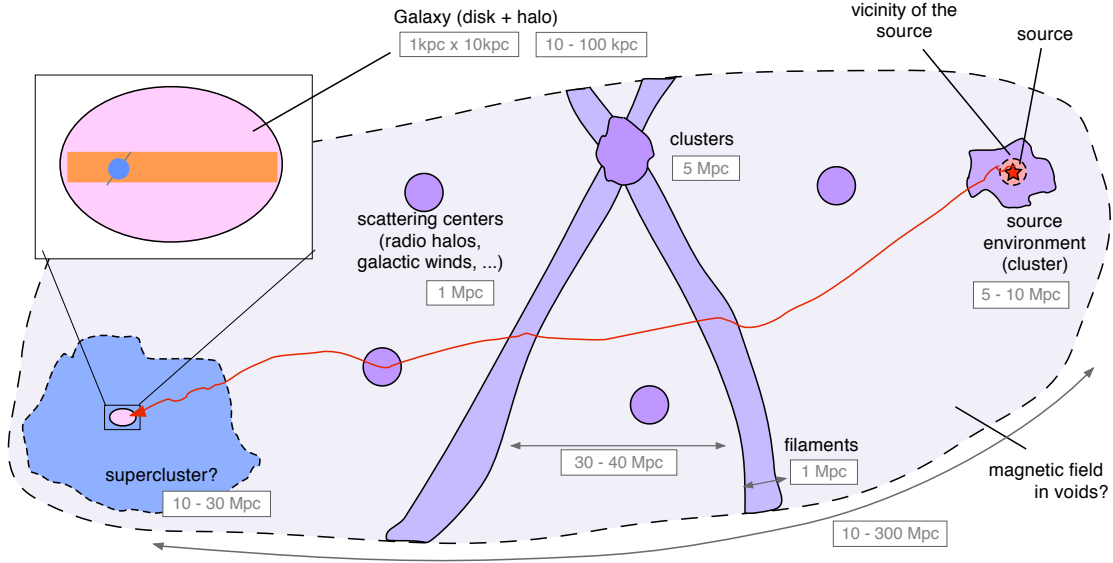


Figure 1.6: **Schematic representation of magnetised regions intervening in UHECR propagation (from [17]).** Their approximate characteristic length scales are indicated in grey.

1.3.2.1 The effects of magnetic fields

Once cosmic rays are emitted by a source, the charged ones will undergo deflections caused by the galactic magnetic field (GMF) and/or the extragalactic magnetic field (EGMF). For different energies and magnetic fields, the trajectories can be very different. Charged particles are subject to the influence of magnetic fields in the source environment, in the intergalactic medium and in the galaxy, as depicted in Figure 1.6.

The average intensity of the galactic magnetic field is expected to be around 1 to 5 μG . This means that particles of 10^{20} eV would have a Larmor radius r_L of 10 to 50 kpc, similar to the dimension of the galaxy ($r_L = E/ZeB$). Nevertheless, even though this constitutes a proof that the highest energy cosmic rays have an extragalactic origin, the GMF deflects slightly their trajectories. Large progress has been made in recent years on galactic field observations and their effect on the propagation of UHECRs [18]. These studies conclude that the deflection δ for particles of charge Ze and end energy E can be expected not to exceed

$$\delta \simeq 10^\circ Z \frac{40 \text{ EeV}}{E}. \quad (1.5)$$

The fluxes from both protons and heavier nuclei can appear dispersed around their sources, or globally translated in the sky with a small dispersion. Source image distortions are stronger for heavier nuclei [19]. Also, cosmic magnetic fields are not uniform in the sky, implying that angular deflections depend on the observed direction.

The extragalactic magnetic field is much less well known. Its structure is unknown but the average intensity is expected to be around 1 nG [20]. Neronov & Semikoz [21] have demonstrated that combining the observation of extended gamma-ray emissions around point sources with time delay measurements in gamma-ray flares should provide robust measurements on the EGMF, and help constrain the possible scenarios on their origins. Using data from the Fermi Gamma-ray Space Telescope, the existence of EGMF of order $10^{-16} - 10^{-15}$ G has been suggested based on upper limits on the secondary emission for a few blazars [22].

1.3.2.2 Interaction processes on cosmic backgrounds and GZK cutoff

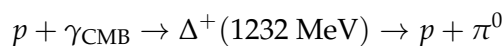
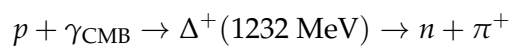
Almost fifty years ago, Penzias and Wilson reported the discovery of the cosmic 2.7 K thermal blackbody radiation, the so-called *Cosmic Microwave Background* (CMB) [23]. It was produced very early in the history of the Universe and led to the undisputed acceptance of the “Big Bang” theory of the origin of the Universe. Much more recently, the Wilkinson Microwave Anisotropy Probe (WMAP) and Planck satellites have confirmed this discovery, showing that the CMB is the most perfect thermal blackbody known to man. At the present time, it fills the entire Universe with radio to far-infrared photons with a density of 400 cm^{-3} .

Shortly after the discovery of the CMB, Kenneth Greisen [24] and Georgiy Zatsepin and Vadim Kuz'min [25] predicted that pion-producing interactions of UHECR protons with CMB photons should produce a cutoff in their spectrum at energies greater than 50 EeV. This predicted effect is nowadays known as the *GZK effect*.

Three mechanisms contribute to the energy losses of ultra-high energy protons:

1. photo-pion production, responsible for the GZK cutoff,
2. electron-positron pair production,
3. redshift from the expanding universe.

The **photoproduction interaction** between protons and background photons γ_{CMB} mainly leads to pion production



This interaction is well known thanks to particle accelerator experiments. Its highest efficiency is at the mass of the Δ^+ resonance, with a cross section of about $500 \mu\text{b}$. Other resonances are located at 1620 and 1700 MeV, but their cross sections are smaller².

²website: <http://pdg.lbl.gov>

Photo-pion production is possible when the energy in the centre of mass \sqrt{s} is higher than the sum of a proton mass m_p and pion mass m_π , where the Mandelstam variable s in the laboratory system is defined as

$$s = m_p^2 + 2 E_p E_\gamma (1 - \cos \theta), \quad (1.6)$$

where θ is the angle between the photon and the incoming proton. E_γ is the mean energy of a CMB photon. In the case of a head-on collision ($\cos \theta = -1$), the minimum proton energy is

$$E_{p,\pi} = \frac{m_\pi}{4 E_\gamma} (2 m_p + m_\pi) \simeq 6.8 \times 10^{16} \left(\frac{1 \text{ eV}}{E_\gamma} \right). \quad (1.7)$$

For a typical CMB photon with an energy of 6×10^{-4} eV, the energy threshold is about 10^{20} eV. But there are CMB photons with higher energies, leading to a GZK cutoff lower in energy, around 3×10^{19} eV. This photo-pion production creates a horizon – the GZK horizon – from which a particle with a higher energy than $E_{p,\pi}$ cannot come. Figure 1.7 shows how a degradation in energy can produce a horizon, i.e. a distance above which all the particles are seen as having the same energy, even if the source could produce more energetic particles.

There is an additional small effect at lower energies due to **electron-positron pair production**

$$p + \gamma_{\text{CMB}} \rightarrow p + e^+ + e^-$$

The addition of two electron masses to the centre of mass energy \sqrt{s} in Equation (3.15) requires a much lower proton energy

$$E_{p,ee} = \frac{m_e}{E_\gamma} (m_p + m_e) \simeq 4.8 \times 10^{14} \left(\frac{1 \text{ eV}}{E_\gamma} \right). \quad (1.8)$$

For a typical CMB photon with an energy of 6×10^{-4} eV, the energy threshold is about 8×10^{17} eV.

Interaction length and Energy loss length

Two physical quantities are usually used to characterize the energy degradation during propagation: the interaction length λ and the energy loss length x_{loss} . They are defined as follows

$$\lambda = \frac{1}{n_\gamma \sigma}, \quad \text{and} \quad x_{\text{loss}} = \left| \frac{1}{E} \frac{dE}{dt} \right|^{-1}, \quad (1.9)$$

where n_γ is the CMB photon density (400 cm^{-3}) and σ is the cross section of the physical

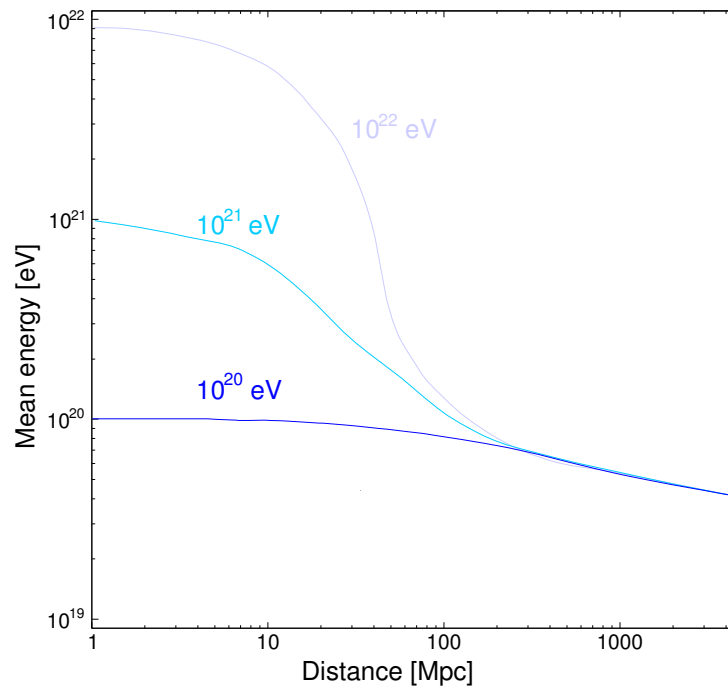


Figure 1.7: **Energy degradation of ultra-high energy protons via interactions with the cosmic microwave background radiation.** The mean proton energy is shown as a function of distance assuming initially mono-energetic beams of 10^{20} , 10^{21} and 10^{22} eV.

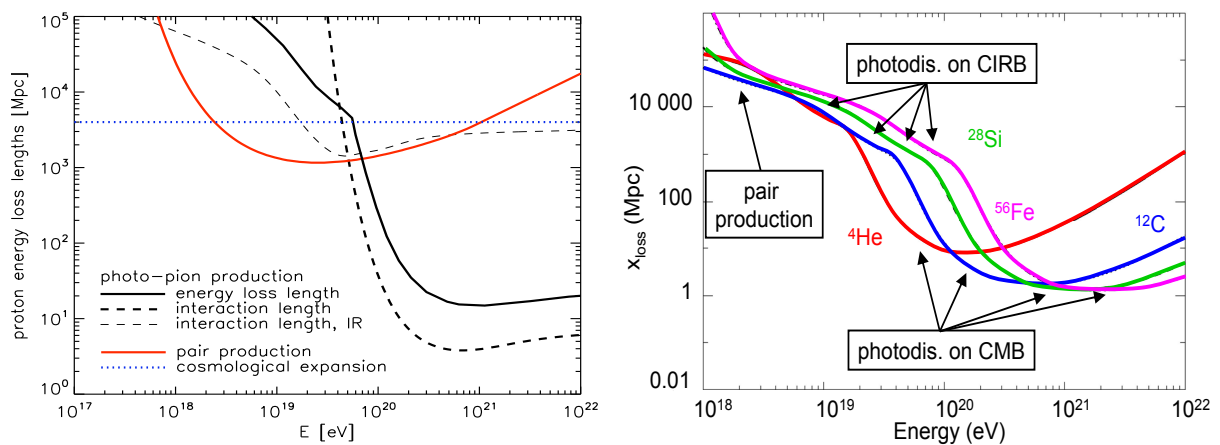


Figure 1.8: **Energy loss lengths for (left) protons and (right) nuclei for photo-pion production and for pair-production on CMB photons.** The dotted line gives the losses due to cosmological expansion (redshift). The dashed line represents the interaction length (or mean free path) for photo-pion production on the CMB.

Interaction process	E_{th} [eV]	λ	x_{loss}	ε
Photo-pion production	$\sim 6 \times 10^{19}$	~ 8 Mpc	~ 50 Mpc	$m_{\pi}/m_p \sim 0.15$
Pair production	$\sim 8 \times 10^{17}$	~ 8 Mpc	~ 8 Gpc	$2 m_e/m_p \sim 10^{-3}$
Universe expansion			~ 4 Gpc	
Photo-disintegration	$\sim 1.5 A \times 10^{19}$	~ 1 Mpc	$\sim A$ Mpc	$\sim X/A$

Table 1.1: **Properties of the different interaction processes (numerical values taken from [28]).** E_{th} corresponds to the energy threshold for each physical process. A is the number of nucleons in the incident nucleus and X is the number of nucleons produced by photodisintegration.

process. The energy loss length is linked to the interaction length via the relation

$$x_{\text{loss}} = \frac{\lambda}{\varepsilon},$$

where ε is the energy fraction lost (i.e. the inverse of the inelasticity).

The energy loss lengths x_{loss} for the three processes are shown in Figure 1.8. In the case of energy loss due to the expansion of the universe, the energy loss length can be approximated to c/H_0 , where H_0 is the Hubble constant ($H_0 = 75 \text{ km s}^{-1} \text{ Mpc}^{-1}$). Above $\sim 10^{20}$ eV, the distance that particles can travel without losing their energy shortens considerably. If cosmic rays originate from cosmological distances, their flux above this energy should be consequently suppressed.

For primary cosmic rays with mass number $A > 1$, different interaction processes come into play. At the highest energies, nuclei photo-disintegrate on CMB photons. One of the processes occurs at the Giant Dipolar Resonance (GDR), for photon energies greater than 20 MeV in the centre of mass. The cross sections involved in the GDR, even if they are not well known, are of the order of a few millibarns. The energy loss lengths for several nuclei are shown in Figure 1.8. The minimum value for x_{loss} is significantly lower for nuclei with respect to the proton case, but is reached at higher energy, typically at $A \times 10^{20}$ eV. Also, the pair production scales as Z^2/A [26].

One remarkable effect is that nuclei with mass number $A < 20$ cannot travel farther than a few tens of megaparsecs without disintegrating. Only iron has similar x_{loss} value at 10^{20} eV. Thus, it is the only element which is considered as a possible alternative to protons in the chemical composition of UHECRs at energies greater than 10^{20} eV [27].

Table 1.1 summarizes, for each interaction process, the numerical values for the different key quantities: the energy threshold E_{th} , the interaction length λ , the energy loss length x_{loss} and the energy fraction lost ε .

Secondary products of photo-pion production

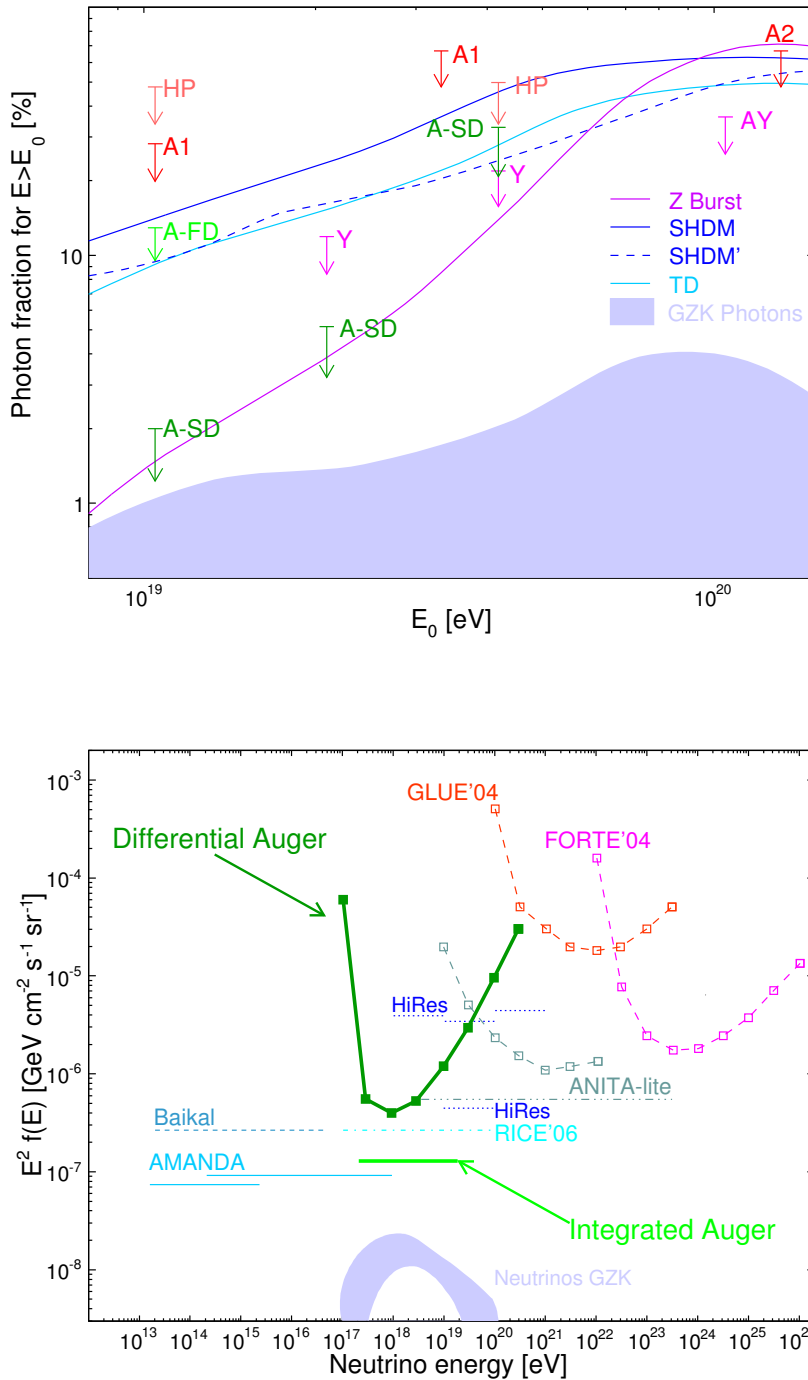


Figure 1.9: **Results of the Pierre Auger Observatory for secondary products of the pion production.** (a) Upper limits (95% confidence level) on the photon fraction in the integral cosmic ray flux for different experiments. The shaded region shows the expected GZK photon fraction. Lines indicate predictions from “top-down” models (from [29]). (b) Limits at 90% confidence level for each flavour of diffusive ultra-high energy neutrino fluxes assuming a proportion of flavours of 1:1:1 due to neutrino oscillations (from [30]). Are shown results from other experiments and theoretical predictions from “top-down” models and for cosmogenic neutrinos.

Another way to validate the GZK cutoff is by detecting the secondary products from pion production. The main particles are GZK (or cosmogenic) neutrinos and GZK photons. In the case of a proton primary, the production processes are the following

$$p + \gamma_{\text{CMB}} \rightarrow n + \pi^+$$

$$n \rightarrow p + e^- + \bar{\nu}_e$$

$$\pi^+ \rightarrow \mu^+ + \nu_\mu \rightarrow e^+ + \nu_e + \bar{\nu}_\mu + \nu_\mu$$

and

$$p + \gamma_{\text{CMB}} \rightarrow p + \pi^0$$

$$\pi^0 \rightarrow \gamma_{\text{GZK}} + \gamma_{\text{GZK}}$$

Figures 1.9(a)-1.9(b) show the upper limit on the photon fraction and on ultra-high energy neutrinos obtained by the Auger Collaboration. No evidence of GZK photons or cosmogenic neutrinos has been found yet by the Auger experiment. The different bounds produced by the Auger Collaboration already exclude many "top-down" models for the production of UHECRs through decays of super heavy particles or topological defects, since these would lead to significant photon fluxes (some predictions are shown in the figure). Hence the standard scenario of "bottom-up" acceleration in astrophysical sources is reinforced. The next years will be crucial for the different models and their corresponding predictions.

1.4 Latest results from the Pierre Auger Observatory

Before ending this chapter dedicated to UHECR physics, an overview of the current results from the Pierre Auger Observatory is presented in this section.

1.4.1 Cosmic ray energy spectrum

The energy spectrum of cosmic rays with energy above 10^{19} eV has been subject to controversy since the detection of the first particle in this energy range at Volcano Ranch [6]. Following the expectations from the GZK cutoff for protons, most of the flux above 6×10^{19} eV should come from sources closer than 100 – 200 Mpc (see Section 1.3.2.2).

Two experiments, AGASA (Akeno Giant Air Shower Array) [31] and HiRes (High Resolution Fly's Eye) [32] using different techniques, scintillators as surface detectors and fluorescence telescopes, respectively, have measured, with a limited number of events, discrepant spectra. AGASA showed a hint of a continuous flux for energies greater than 5×10^{19} eV while the HiRes data indicate a break in the flux around the same energy.

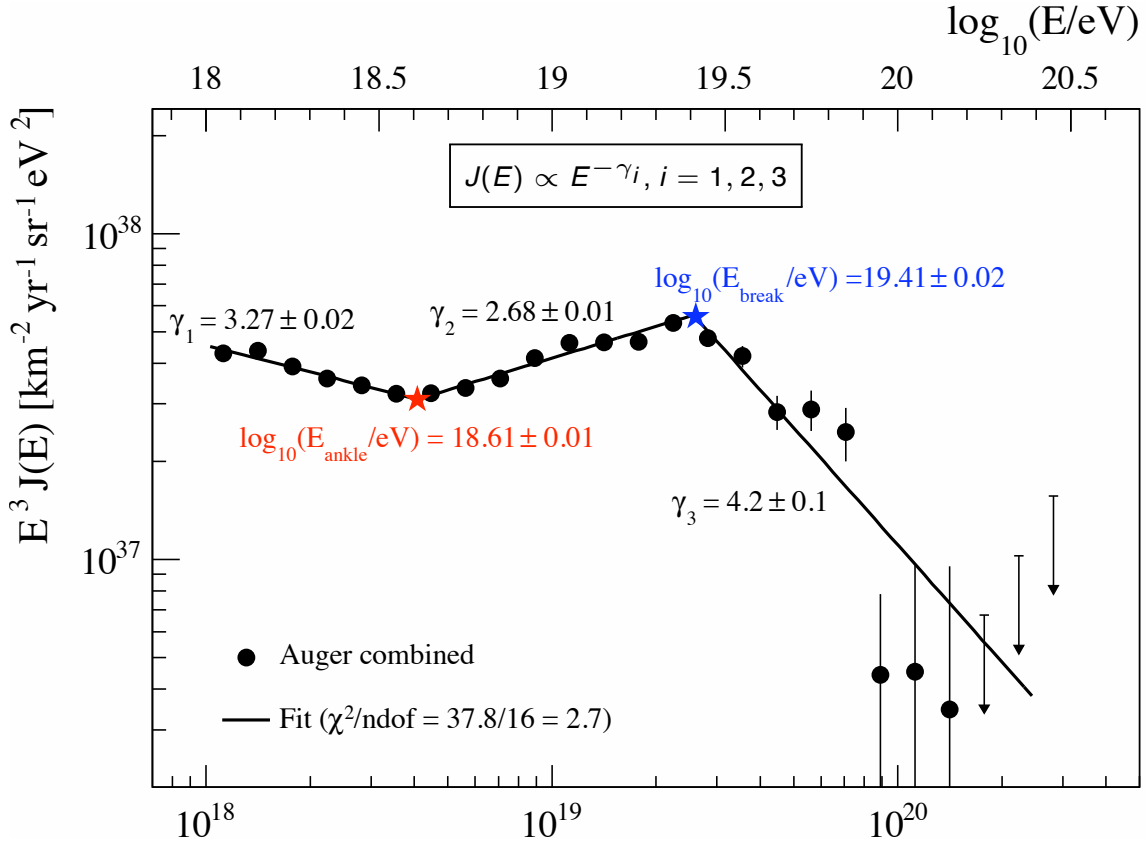


Figure 1.10: **The combined energy spectrum obtained by the Pierre Auger Collaboration.** Only statistical uncertainties are shown. The systematic uncertainty in the energy scale is 22% for the Auger data.

In 2008, the Auger Collaboration resolved this controversy by determining the energy spectrum with very good energy resolution and a well defined collection area³. A break in the spectrum was found around 4×10^{19} eV [33]. The energy spectrum at energies greater than 3×10^{18} eV has been derived using data from the surface detector array of the Pierre Auger Observatory. Up to December 2010, the exposure was 20 905 km² sr yr. It is calculated by integrating the number of active detector stations of the surface detector over time. The analysis of air showers measured with the fluorescence detector, due to its lower energy threshold and its good energy resolution, makes possible cosmic ray flux measurements down to 10^{18} eV, i.e. the region where the transition between galactic and extragalactic cosmic rays is expected. To ensure good energy reconstruction only events satisfying strict quality criteria are accepted [34]. For *hybrid events*, i.e. events reconstructed by both the surface array

³The detection techniques used by the Pierre Auger Observatory and the advantage of a hybrid detector will be discussed in the next chapter.

(at least one station) and the fluorescence telescopes, the exposure goes from $100 \text{ km}^2 \text{ sr yr}$ at 10^{18} eV , to $1000 \text{ km}^2 \text{ sr yr}$ at 10^{20} eV .

Figure 1.10 gives the most recent combined energy spectrum published by the Auger Collaboration [35]. The ankle feature seems to be somewhat more sharply defined in the Auger data. This is possibly due to the different energy resolutions of the two instruments. However, the two spectra are compatible within the systematic uncertainties. Fits have been made to the Auger spectrum. For instance, a simple power fit indicates that the ankle is located at $\log_{10}(E/\text{eV}) = 18.61 \pm 0.01$, with the spectral break at $\log_{10}(E/\text{eV}) = 19.41 \pm 0.02$. The power law indices for the energy spectrum, defined as $dN/dE \propto E^{-\gamma}$, are $\gamma = 3.27 \pm 0.02$ below the ankle, $\gamma = 2.68 \pm 0.01$ above the ankle, and $\gamma = 4.2 \pm 0.1$ at energies above the break. Using these numbers, the disagreement from a continuous spectrum along the break point can be ruled out with a five sigma significance.

Even though there is a suppression in the spectrum at the highest energies, it does not mean necessarily that this is due only to the interaction of UHECRs with the CMB radiation, i.e the GZK cutoff. Another plausible explanation would be the incapacity of the UHECR sources to accelerate to higher energies. In the case where a heavy mass composition would be confirmed, the suppression in the flux observed at $10^{19.4} \text{ eV}$ cannot be the GZK cutoff. Without knowledge of the UHECR composition or the spatial distribution of the sources, it remains difficult to obtain significant information from the energy spectrum.

1.4.2 Anisotropy and arrival directions

The arrival directions of cosmic ray particles potentially provide important information on the locations of their sources, in particular if the GZK effect takes place as expected, limiting the candidates to nearby objects. This also depends on the charge of the particle and on the magnetic fields as explained in Section 1.3.2.1.

The philosophy for point source studies has been to define a search "prescription" using an existing Auger cosmic ray data set. During the prescription's development, cuts on the data are optimized and comparison are made with several astronomical source catalogues. The final prescription is then applied to a future independent data set. Such a prescription, developed using very early Auger data up to May 2006, was set to test the correlation of arrival directions of the highest energy particles ($E > 55 \text{ EeV}$) with AGN from the Véron-Cetty & Véron catalogue. The threshold of significance set in the prescription was exceeded (9 out of the first 13 events in the subsequent data set arrived within 3.1° of an AGN closer than 75 Mpc) and the result was published in 2007 [37]. An update of this correlation has recently been published [38], and the skymap is shown in Figure 1.11. The fraction of events correlating is now $21/55$, or $(38_{-6}^{+7})\%$, well above the 21% that would be expected if the distribution was isotropic. While this degree of correlation is lower than was expected given the earlier

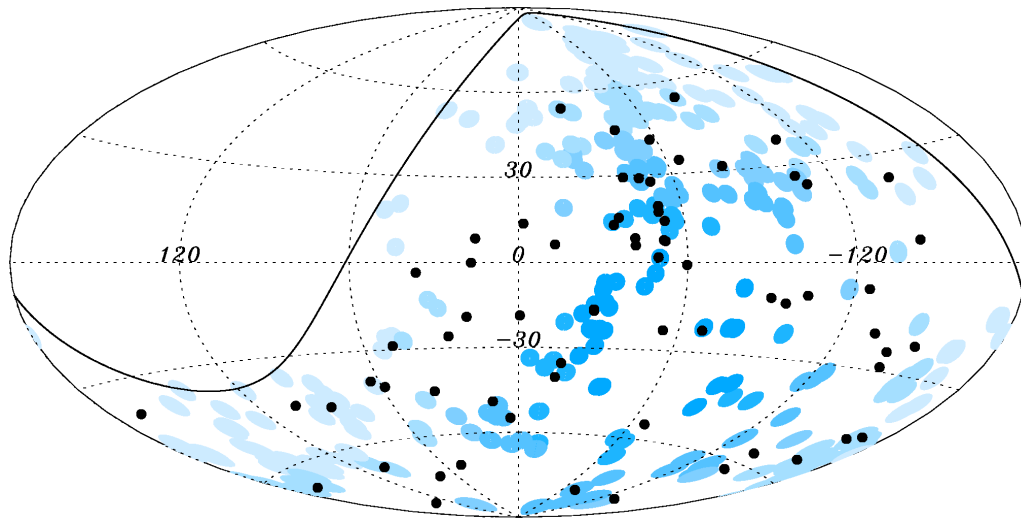


Figure 1.11: The 69 arrival directions of cosmic rays with $E > 55$ EeV detected by the Pierre Auger Observatory up to 31 December 2009. They are plotted as black dots in an Aitoff-Hammer projection of the sky in galactic coordinates. The solid line represents the border of the field of view of the Auger Observatory for zenith angles lower than 60° . Blue circles of radius 3.1° are centred on the positions of the 318 AGNs in the VCV catalogue that lie within 75 Mpc and that are within the field of view of the observatory. Darker blue indicates larger relative exposure. The exposure-weighted fraction of the sky covered by the blue circles is 21%.

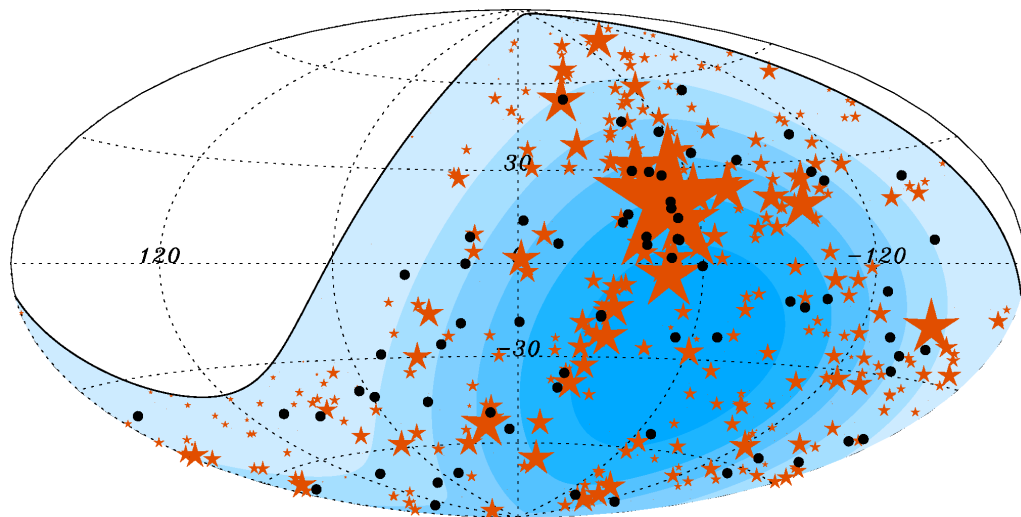


Figure 1.12: Skymap in galactic coordinates with the AGNs of the 58-month Swift-BAT catalogue plotted as red stars with area proportional to the assigned weight. Coloured bands have equal integrated exposure, and darker background colours indicate larger relative exposure. The 69 arrival directions of cosmic rays with energy $E > 55$ EeV detected by the Pierre Auger Observatory are plotted as black dots.

publication, $(69_{-13}^{+11})\%$, the arrival directions are still anisotropic at the following level: there is a 0.3% chance of finding 21 or more correlating events from an isotropic distribution of arrival directions.

Alternative studies with different catalogues have also been performed. For instance, Figure 1.12 displays the same events and the distribution of nearby (within 200 Mpc) AGN observed in X-rays by the SWIFT satellite. The size of the stars in the plot is proportional to the measured X-ray fluxes. Of course, this study has been made *a posteriori* and therefore cannot be used to estimate a confidence level for anisotropy.

A significant concentration of events is found around the location of Centaurus A, a particularly interesting AGN since it lies at only 4 Mpc from Earth. Inspecting the number of observed events as function of the angular distance from the Cen A nucleus shows a most significant departure from isotropy for 18° , for which 13 events are observed while only 3 are expected from an isotropic distribution. Whether these events come from Cen A or from other sources, such as from the Centaurus cluster lying behind (at 45 Mpc) is still unclear, but this region looks especially promising for future anisotropy searches.

1.4.3 Mass composition

The last important piece of information being used to understand the production of the highest energy particles is the mass abundance. Indeed, each acceleration mechanism produces a different fraction of elements ranging from proton to iron nuclei. The charge Ze of cosmic rays is also important to track back the origin of the particle. We have seen in Section 1.3.2.1 that particles are deviated in the galactic and extragalactic magnetic fields by amounts proportional to their charges. If the particles arriving on Earth have a low charge they may point back to their source. But if their charge is larger, their directions could be greatly deviated and the pointing information lost.

At the Pierre Auger Observatory, information on shower development can be extracted using both the surface detector and the fluorescence detector. The different observables studied are subject to independent systematic uncertainties (both experimentally and theoretically). Also, the higher statistics of showers measured with the surface detector means that higher energies can be reached than with the fluorescence detector. However, due to the large fluctuations in shower development and the uncertainties in the hadronic interaction models, primary particle identification is very difficult and not possible on an event-by-event basis.

Average depth of shower maximum $\langle X_{\max} \rangle$ and its fluctuations $\text{RMS}(X_{\max})$

The longitudinal profile, corresponding to the energy deposited in the atmosphere, is reconstructed by the fluorescence detector. In this study, hybrid events, i.e. showers observed simultaneously by the two detection techniques, are used. From the profile, the depth of

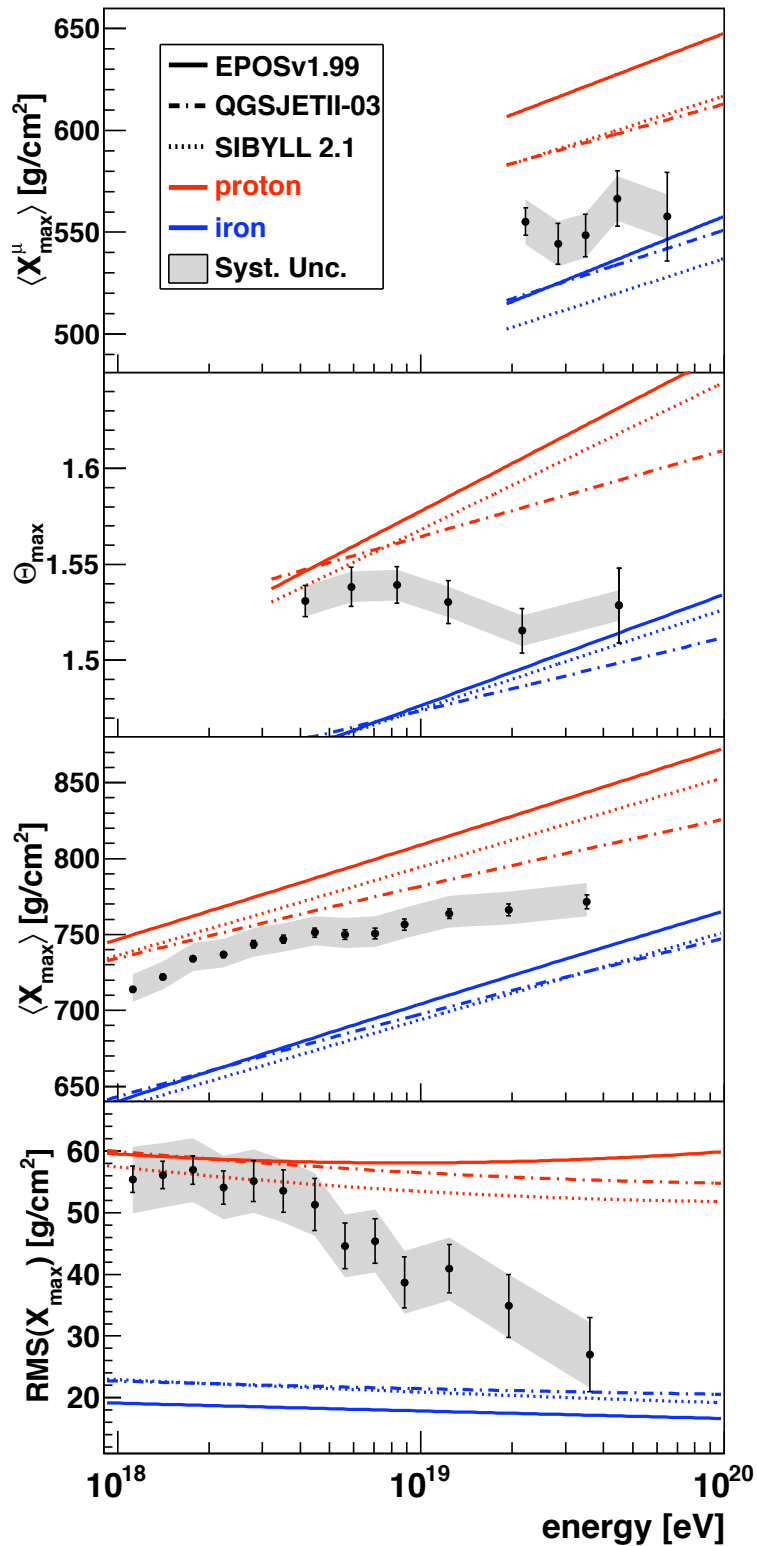


Figure 1.13: Measurements of the longitudinal development of air showers by the Pierre Auger Collaboration (from [39]). Results on observables sensitive to shower evolution are compared with model predictions. The error bars correspond to the statistical uncertainty. The systematic uncertainty is represented by the shaded bands. Three different interaction models are plotted: QGSJetII-03, SIBYLL 2.1 and EPOS 1.99.

shower maximum X_{\max} is obtained for each shower. According to the Heitler model, we have seen in Section 1.2 that this quantity is sensitive to the primary composition. Hybrid events recorded between December 2004 and September 2010 with reconstructed energy above 10^{18} eV are used for this analysis. To obtain a good resolution in the measurement of X_{\max} , several quality cuts are applied [40]. After all cuts, 6744 events are selected for the analysis. The average values of the shower maximum $\langle X_{\max} \rangle$ and its corresponding fluctuations $\text{RMS}(X_{\max})$ as a function of energy are shown in Figure 1.13. The systematic uncertainty of about 13 g/cm^2 corresponds to the uncertainties on the atmospheric conditions, calibration, event selection and reconstruction.

Asymmetry of signal risetime Θ_{\max}

The surface detector records the muonic and the electromagnetic components. Due to the absorption of the electromagnetic component, the number of these particles at ground level depends, for a given energy, on the distance to the shower maximum and therefore on the primary mass. Subsequently, the time profile of particles reaching ground is sensitive to cascade development since the higher the production height the narrower is the pulse. An observable sensitive to mass composition can be extracted from this asymmetry, known as Θ_{\max} [41]. Data collected with the surface detector from January 2004 to December 2010 are used for the Θ_{\max} analysis, with a total of 18581 events surviving the cuts. The measured values of Θ_{\max} obtained for six energy bins above 3×10^{18} eV are shown in Figure 1.13. The systematic uncertainty corresponds to the reconstruction of the core of the shower, the event selection and the risetime of the recorded signal.

Average depth of maximum muon production $\langle X_{\max}^{\mu} \rangle$

Using the time information of the signals recorded by the surface detector, it is also possible to obtain information about the longitudinal development of the hadronic component of the EAS. The muon production depth (MPD), i.e. the depth at which a given muon is produced, is reconstructed [42]. This corresponds to a conversion of the time distribution of the recorded signal, into muon production distances. The method assumes that muons travel in straight lines from production to detection. From the MPD profile, an observable can be defined, X_{\max}^{μ} , as the depth along the shower axis where the number of produced muons reaches a maximum. Up to now, the method is restricted to showers with zenith angles around 60° , since muons dominate the signal at ground level. The results of $\langle X_{\max}^{\mu} \rangle$ shown in Figure 1.13 are based on data collected between January 2004 and December 2010. The systematic uncertainty due to reconstruction bias, core position, rejection of the electromagnetic component and quality cuts amounts to 11 g/cm^2 .

The evolution of $\langle X_{\max} \rangle$, $\text{RMS}(X_{\max})$, Θ_{\max} and $\langle X_{\max}^{\mu} \rangle$ with energy is similar, despite

the fact that they come from completely independent techniques. In particular, at the highest energies, all four observables show consistently that the trend in the Auger data is to a heavier component for the mass composition as energy increases. One interesting possibility is that the composition is still dominated by protons at the highest energies, and the air shower behaviour observed is a result of changes in the interaction physics. Currently, the models are required to extrapolate significantly beyond the region where direct measurements from accelerator experiments are available.

1.4.4 Discussion of the Auger results

The Pierre Auger Observatory has set a new standard in high energy cosmic ray physics. The quality of the data, the careful analysis and the large statistics has taken this research field to a quantitative era of high energy astroparticle physics. Hints and uncertainties from the past have been definitely confirmed or refuted and the parameter space for models has been firmly restricted.

The precise measurements and large statistics of the Pierre Auger Observatory have significantly increased our knowledge of UHECRs. Looking forward, decreasing the statistical and systematic uncertainty of the three pillars of UHECR observations (spectrum, arrival direction and composition) is the key to solving the mystery of the origin of these events.

The shape of the energy spectrum observed by Auger supports the long-held notion that the sources of UHECRs are extragalactic. The steep decline in flux above 4×10^{19} eV appears as expected from the effect of interactions between extragalactic cosmic rays and the cosmic background radiation, that is the GZK cutoff. A similar cutoff could also be produced by a maximum acceleration energy at the astrophysical source. However, if a heavy mass composition would be confirmed, the suppression cannot be the GZK cutoff. Another important feature is the hardening of the spectrum at a few EeV (at the ankle energy range), which could be caused by the transition from galactic to extragalactic cosmic rays or by propagation losses if UHECRs are mostly protons.

Inhomogeneities in the spatial distribution of the candidate sources within the GZK horizon can imprint a detectable anisotropy on the UHECR arrival directions. A correlation of arrival directions with nearby matter could be expected in the case of protons, assuming that the magnetic deflections do not exceed a few degrees. However, heavy nuclei are likely to deviate more than 10° from their sources.

From 10^{18} to 10^{19} eV, measurements of the depth of shower maximum are consistent with a significant fraction of protons in the cosmic ray flux. Above 10^{19} eV, independent measurements of shower development show a trend to a heavier component for the mass composition. Knowledge of the cosmic ray composition is important to decide which of several source scenarios is the most likely. Hadronic interactions which differ significantly from

current extrapolations provide an alternative interpretation to the observed shower development behaviour.

Bibliography

- [1] V Hess, *Observations of the penetrating radiation on seven balloon flights*, *Physik. Zeitschr.* **13** (1912) 1084–1091.
- [2] P Auger *et al.*, *Extensive cosmic-ray showers*, *Review of Modern Physics* **11** (1939) 288–291.
- [3] T Antoni *et al.* [KASCADE Collaboration], *Measurements of energy spectra for elemental groups of cosmic rays: results and open problems*, *Astropart. Phys.* **24** (2005) 1–25.
- [4] P Bassi, G Clark and B Rossi, *Distribution of arrival times of air shower particles*, *Phys. Rev.* **92** (1953) 441–451.
- [5] J Linsley and L Scarsi, *Arrival times of air shower particles at large distances from the axis*, *Phys. Rev.* **128** (1962) 2384–2392.
- [6] J Linsley, *Evidence of a primary cosmic-ray particle with energy 10^{20} eV*, *Phys. Rev. Lett.* **10** (1967) 146–148.
- [7] O Adriani *et al.*, *Technical design report of the LHCf experiment: measurement of photons and neutral pions in the very forward region of LHC*, **CERN-LHCC-2006-004**.
- [8] K Eggert, *The TOTEM experiment*, LHC Days 2003, Les Diablerets, Switzerland, 2–4 Jun 2003.
- [9] J Matthews, *A Heitler model of extensive air showers*, *Astropart. Phys.* **22** (2005) 387–397.
- [10] M Ave *et al.* [AIRFLY Collaboration], *Measurement of the pressure dependence of air fluorescence emission induced by electrons*, *Astropart. Phys.* **28** (2007) 41–57.
- [11] CT Hill *et al.*, *Ultra-high-energy cosmic rays from superconducting cosmic strings*, *Phys. Rev. D* **36** (1987) 1007–1016.
- [12] V Berezhinsky *et al.*, *Signatures of topological defects*, *Phys. Rev. D* **58** (1998) 103515–103526.
- [13] V Berezhinsky *et al.*, *Ultra-high energy cosmic rays without GZK cutoff*, *Phys. Rev. Lett.* **79** (1997) 4302–4305.
- [14] V Berezhinsky, *Ultra high energy cosmic rays*, *Nuclear Physics B Proceedings Supplements* **70** (1999) 419–430.
- [15] E Fermi, *On the origin of the cosmic radiation*, *Phys. Rev.* **75** (1949) 1169–1174.
- [16] AM Hillas, *The origin of ultra-high energy cosmic rays*, *Ann. Rev. Astron. Astrophys.* **22** (1984) 425–444.

-
- [17] K Kotera and AV Olinto, *The Astrophysics of ultrahigh energy cosmic rays*, *Annu. Rev. Astron. Astrophys.* **49** (2010) 119–153.
- [18] D Harari *et al.*, *The toes of the ultra high energy cosmic ray spectrum*, *JHEP* **8** (1999) 22.
- [19] G Giacinti *et al.*, *Ultrahigh energy nuclei in the galactic magnetic field*, *JCAP* **8** (2010) 36.
- [20] PP Kronberg, *Extragalactic magnetic fields*, *Rept. Prog. Phys.* **57** (1994) 325–382.
- [21] A Neronov and D Semikoz, *Sensitivity of γ -ray telescopes for detection of magnetic fields in the intergalactic medium*, *Phys. Rev. D* **80** (2009) 123012–123027.
- [22] A Neronov and I Vovk, *Evidence for strong extragalactic magnetic fields from Fermi observations of TeV blazars*, *Science* **328** (2010) 73–75.
- [23] A A Penzias and RW Wilson, *A measurement of excess antenna temperature at 4080-mc/s*, *Astrophys. J.* **142** (1965) 419–421.
- [24] K Greisen, *End to the cosmic ray spectrum ?*, *Phys. Rev. Lett.* **16** (1966) 748–750.
- [25] GT Zatsepin and VA Kuz'min, *Upper limit of the spectrum of cosmic rays*, *JETP Lett.* **4** (1966) 78–80.
- [26] G Bertone *et al.*, *Ultrahigh energy heavy nuclei propagation in extragalactic magnetic fields*, *Phys. Rev. D* **66** (2002) 103003–103011.
- [27] D Allard *et al.*, *Implications of the cosmic ray spectrum for the mass composition at the highest energies*, *JCAP* **10** (2008) 33.
- [28] M Lemoine, *Propagation of ultra-high energy cosmic rays in the Universe*, Ecole de Gif, Montpellier (2006).
- [29] J Abraham *et al.* [Pierre Auger Collaboration], *Upper limit on the cosmic ray photon fraction at EeV energies from the Pierre Auger Observatory*, *Astropart. Phys.* **31** (2009) 399–406.
- [30] J Abraham *et al.* [Pierre Auger Collaboration], *Limit on the diffusive flux of ultra-high energy tau neutrinos with the surface detector of the Pierre Auger Observatory*, *Phys. Rev. D* **79** (2009) 102001–102015.
- [31] N Hayashida *et al.* [AGASA Collaboration], *Observation of a very energetic cosmic ray well beyond the predicted 2.7 K cutoff in the primary energy spectrum*, *Phys. Rev. Lett.* **73** (1994) 3491–3494.
- [32] RU Abbasi *et al.* [HiRes Collaboration], *Monocular measurement of the spectrum of ultra-high energy cosmic rays by the FADC detector of the HiRes experiment* *Astropart. Phys.* **23** (2005) 157–174.

-
- [33] J Abraham *et al.* [Pierre Auger Collaboration], *Observation of the suppression of the flux of cosmic rays above 4×10^{19} eV*, Phys. Rev. Lett. **101** (2008) 061101–061107.
- [34] J Abraham *et al.* [Pierre Auger Collaboration], *The exposure of the hybrid detector of the Pierre Auger Observatory*, Astropart. Phys. **34** (2011) 368–381.
- [35] F Salamida, for the Pierre Auger Collaboration, *Update on the measurement of the CR energy spectrum above 10^{18} eV made using the Pierre Auger Observatory*, Proc. 32nd ICRC, Beijing, China (2011).
- [36] RU Abbasi *et al.* [HiRes Collaboration], *Measurement of the flux of ultra high energy cosmic rays by the stereo technique*, Astropart. Phys. **32** (2009) 53–60.
- [37] J Abraham *et al.* [Pierre Auger Collaboration], *Correlation of the highest-energy cosmic rays with the position of nearby active galactic nuclei*, Astropart. Phys. **29** (2008) 188–204.
- [38] P Abreu *et al.* [Pierre Auger Collaboration], *Update on the correlation of the highest energy cosmic rays with nearby extragalactic matter*, Astropart. Phys. **34** (2010) 314–326.
- [39] D Garcia-Pinto, for the Pierre Auger Collaboration, *Measurements of the longitudinal development of air showers with the Pierre Auger Observatory*, Proc. 32nd ICRC, Beijing, China (2011).
- [40] P Facal, for the Pierre Auger Collaboration, *The distribution of shower maxima of UHECR air showers*, Proc. 32nd ICRC, Beijing, China (2011).
- [41] MT Dova, for the Pierre Auger Collaboration, *Asymmetries observed in giant air showers using water Cherenkov detectors*, Proc. 28th ICRC, Tsukuba, Japan (2003) 369–372.
- [42] D García-Gómez, for the Pierre Auger Collaboration, *Measurement of atmospheric production depths of muons with the Pierre Auger Observatory*, Proc. 32nd ICRC, Beijing, China (2011).

The Pierre Auger Observatory

Contents

2.1 The surface array (SD)	35
2.1.1 Signals and tank calibration	36
2.1.2 Data acquisition and trigger system of the surface detector array	38
2.1.3 Selection and reconstruction of the SD events	40
2.2 The fluorescence detector (FD)	44
2.2.1 Description of a fluorescence telescope	45
2.2.2 Calibration	45
2.2.3 Data acquisition and triggering in a camera	47
2.2.4 Reconstruction of the FD events	48
2.2.5 Typical hybrid events	51
2.3 Observatory enhancements	54
2.3.1 HEAT – High Elevation Auger Telescopes	54
2.3.2 AMIGA – Auger Muons and Infill for the Ground Array	56
Bibliography	58

The Pierre Auger Observatory is the largest operating cosmic ray observatory ever built. It has been conceived to measure flux, arrival direction distribution and mass composition of cosmic rays from 10^{18} eV to the very highest energies with high statistical significance. The design for the observatory was developed through a series of workshops, starting in Paris in 1992, and culminating in a 6-month study at Fermi National Accelerator Laboratory (FNAL) in 1995. The design is well suited to resolve the discrepancy at the high energy end of the cosmic ray spectrum between the results of the AGASA surface array [1] and those of the HiRes fluorescence detector [2]. The low event rate of the highest energy cosmic rays, above 10^{18} eV, requires a very large area in order to accumulate significant statistics in a reasonable time.

The Auger Observatory is located in the "Pampa Amarilla" site ($35.1^\circ - 35.5^\circ$ S, $69.0^\circ - 69.6^\circ$ W, and 1300 – 1400 m above sea level), close to Malargüe, Province of Mendoza, Argentina. Construction was completed in end of 2008 and stable data taking on a growing

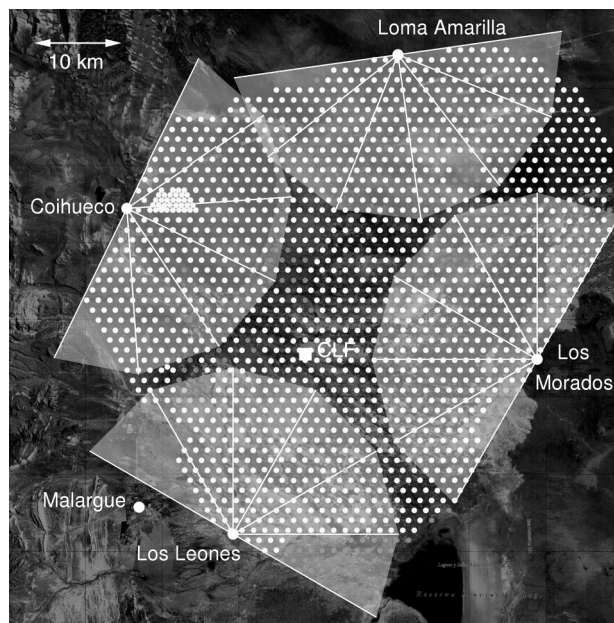


Figure 2.1: **Status of the Pierre Auger Observatory as of March 2009.** Gray dots show the positions of surface detector stations, lighter gray shades indicate deployed detectors, while dark gray defines empty positions. Light gray segments indicate the fields of view of the fluorescence telescopes which are located in four buildings on the perimeter of the surface array. A denser (infill) area is visible in the upper left. Also shown is the Central Laser Facility (CLF) used for FD calibration and atmospheric monitoring studies.

detector array started already at the beginning of 2004. The detector (see Figure 2.1) consists of 1660 surface stations – water Cherenkov tanks and their associated electronics – arranged on a triangular grid, the sides of the triangles being 1.5 km, with the grid covering an area of 3000 km². On dark nights, four optical stations view the atmosphere above the array. Each contains six telescopes, designed to detect air-fluorescence light. The water tanks respond to the particle component reaching ground level (mainly muons, electrons, positrons and photons) and the fluorescence cameras measure the emission from atmospheric nitrogen, which is excited by the charged particles of the shower as they traverse the atmosphere. Both techniques, used for many years to study extensive air showers, are for the first time brought together in a "hybrid" detector to observe showers simultaneously. The array of water tanks is known as the surface detector (SD), while the optical stations form the fluorescence detector (FD).

In this chapter, we will present in detail the two detection techniques, and we will describe the main enhancements which have come into operation in recent years.

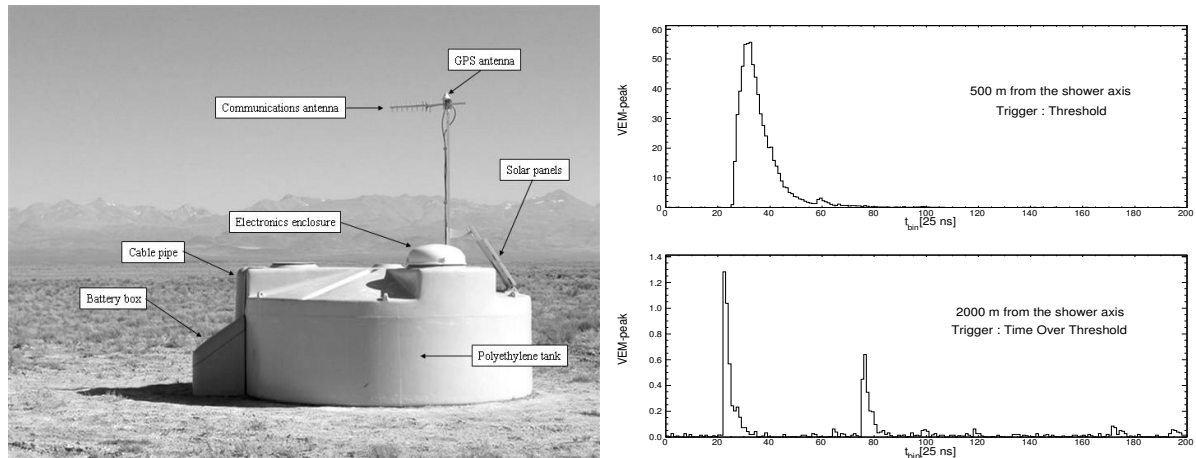


Figure 2.2: **The Pierre Auger Observatory surface detector.** *Left panel:* a detector station in the field. *Right panel:* average signals over the three PMTs recorded by two stations located at 500 m and 2000 m from the axis of a shower.

2.1 The surface array (SD)

The water-Cherenkov detector was chosen for use in the surface array because of its robustness and low cost. Each of 1660 surface detector stations includes a 3.6 m diameter cylindrical water tank containing a sealed liner with a reflective inner surface. The liner contains 12 tons of purified water. Cherenkov light produced by the passage of particles through the water is collected by three nine-inch-diameter photomultiplier tubes (PMTs) that are placed symmetrically at a distance of 1.20 m from the centre of the tank and look downwards through windows of clear polyethylene into the water. The surface detector is self-contained. A solar power system provides an average of 10 W for the PMTs and the electronics package consisting of a processor, GPS receiver, radio transceiver and power controller. The components of the surface detector are shown in Figure 2.2. A central site, located on the southwestern corner of the array (city of Malargüe), hosts the Central Data Acquisition System (CDAS), including the central trigger processors and the permanent data storage area.

The SD has an almost 100% duty cycle. The size of the array corresponds to an aperture of $7350 \text{ km}^2 \text{ sr}$ for zenith angles smaller than 60° . This is currently the largest array in the world. The SD provides good sampling of the lateral density distribution and a high quality reconstruction and reaches full trigger efficiency for energies above 3 EeV (where $1 \text{ EeV} = 10^{18} \text{ eV}$). The coverage is relatively uniform in right ascension. Modulations in the event rate due to atmospheric conditions (pressure and air density) are at the level of 2% for daily variations and about 10% for seasonal ones [3].

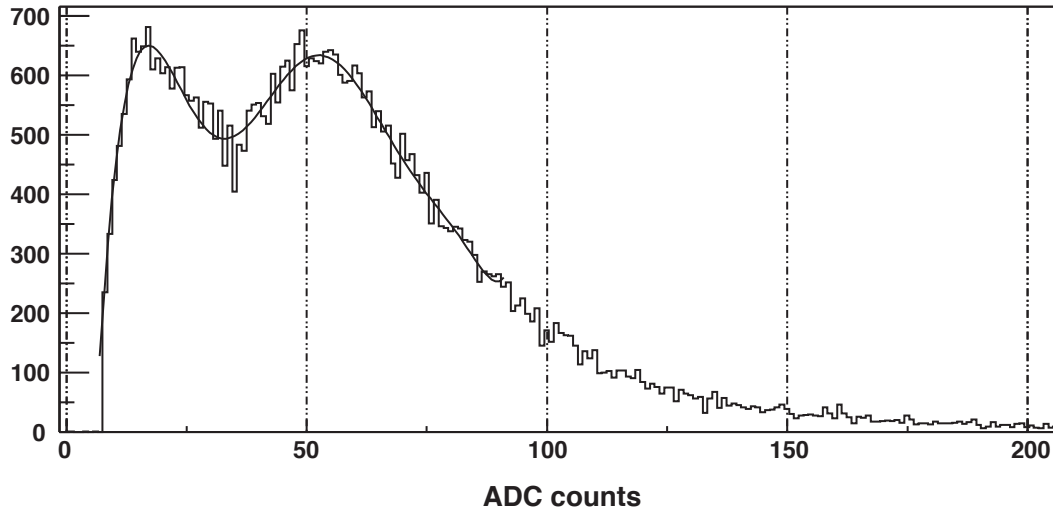


Figure 2.3: **Histogram of signals from one PMT in one of the stations of the surface array (from [4]).** The peak due to single muons is clearly visible at around 50 ADC channels. The peak at about 20 ADC channels, representing the electromagnetic part, is artificial and is due to the cut made in plotting the data.

2.1.1 Signals and tank calibration

For a given event, the signals recorded in each tank can differ a lot, depending on its distance with respect to the shower axis. The number of particles, i.e. the strength of the signal, decreases with the distance. Also, the timing structure changes: particles far from the shower axis are more affected by scattering, and are thus more dispersed (see Figure 2.2).

PMT signals are extracted from the last dynode and from the anode. An amplification of $\times 32$ is applied on the dynode signal (high gain) to match the dynamic range (low gain). The anode signal is useful for large signals, typically those seen by tanks relatively close to the core. The cross-over point corresponds roughly to the signal from a vertical event of 10^{19} eV (10 EeV) at 700 m from the core. The six signals from each tank are digitised using front-end electronics having six 10 bit Fast Analog to Digital Converters (FADC) running at 40 MHz. A signal is described by 768 bins with a time resolution of 25 ns, i.e. corresponding to a time block of 19.2 μ s. Then, the digitised signals are sent to a programmable logic device which is used to implement the various triggering decisions.

To use the data from the surface detectors, the minimum calibrations required are the dynode to anode ratio and the absolute calibration of the three dynode signals for each tank.

Muons produced in the atmosphere by low energy showers provide the basis of the calibration chain. The signal from a single muon with an energy above the Cherenkov threshold traversing a tank is proportional to the geometric path length. The calibration method

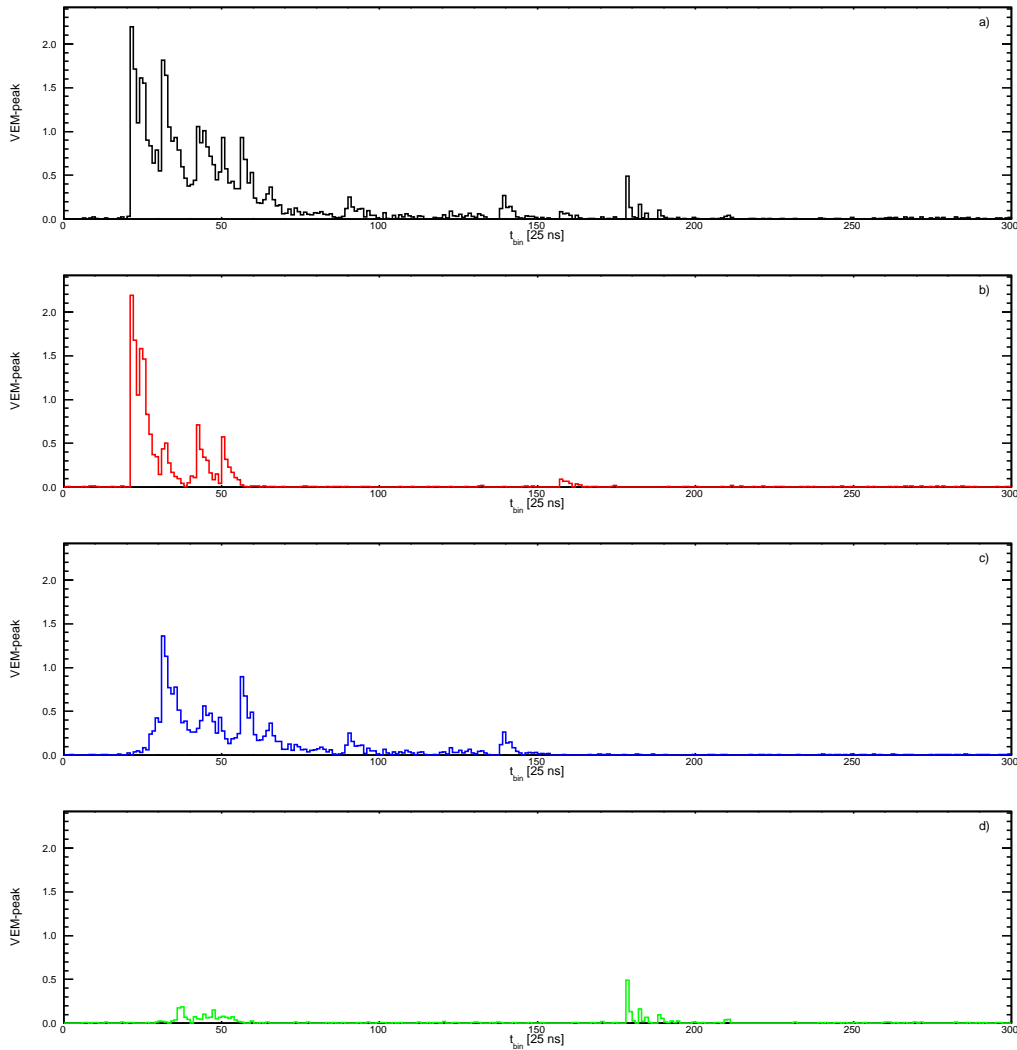


Figure 2.4: **Simulated FADC traces for a station located at 1150 m from the axis of a 10^{19} eV proton shower.** The signal for each shower component is given: (a) total signal, (b) muonic signal, (c) photon signal and (d) electron/positron signal.

developed aims to determine quantities related to the signals associated with muons. The peak due to single muons crossing the tank is clearly visible in a histogram of signals from a PMT (see Figure 2.3). The position of this peak is an important calibration parameter for the high gain channel, and can be related to the average signal produced by a high-energy down-going vertical and central muon, the so-called *Vertical Equivalent Muon* (VEM). Using the local controller, the VEM values associated with the peak and charge for each PMT are sent to the CDAS together with energy triggered event.

This calibration method has the advantage of globally taking into account the water qual-

ity, the liner quality, and the collection efficiency and gain of the dynode. All these parameters differ from one tank to another and evolve with time. However, it does not provide satisfactory calibration of the low gain channel, the signals being too low. Hence, whenever a signal is recorded above 8 VEM, but below 20 VEM, the dynode to anode ratio is computed at the station controller, both signals being integrated for 500 ns. The parameters needed for the cross-calibration of signals from any station with respect to the muon peak are then available.

The final step is to relate the peak to the physical value of reference, i.e. the signal associated with one VEM. This value has been measured using a muon telescope, with two scintillators, placed above and below a test tank situated at Malargüe.

Figure 2.4 shows a simulated FADC trace decomposed into its main components, i.e. the muonic signal, the electron/positron signal and the photon signal (via pair creation). A vertical GeV muon hitting the tank deposits an energy of about 240 MeV, to be compared to a few tens of MeV for an average electron. The electromagnetic (photon and electron/positron) component and the muonic component have signals of different shape; muonic signals are less dispersed in time, and stronger in intensity.

2.1.2 Data acquisition and trigger system of the surface detector array

The trigger for the surface detector array is hierarchical [5]. Two levels of trigger (called T1 and T2) are formed at each station. T2 triggers are produced with those from other detectors and examined for spatial and temporal correlations, leading to an array trigger (T3). The T3 trigger initiates data acquisition and storage. The logic of this trigger system is summarised in Figure 2.5.

2.1.2.1 Single detector triggers / T1 and T2

Several triggers are available for selecting the data for recording. The triggers of the first level are local to the station, the so-called **T1** triggers. The data are stored in a local memory during a short period of time so that, in case of a higher level trigger request, they can be sent later to the CDAS. Two kinds of first level triggers are defined:

- **ToT (Time-over-Threshold):** is a 2-fold coincidence (i.e. two PMTs) of at least 13 bins above 0.2 VEM in a sliding window of 3 μ s, i.e. 120 bins. It is optimized to detect low signals with large arrival-time spread, typical of those produced far from the shower core. The *ToT* background rate is about 2 Hz for each station.
- **ThT (Threshold):** is a 3-fold coincidence of signals above 1.75 VEM. It is designed to detect large signals with small time spread. It is particularly effective for very inclined showers that have crossed a large amount of atmosphere and are consequently dominated by muons. The *ThT* background rate is about 100 Hz.

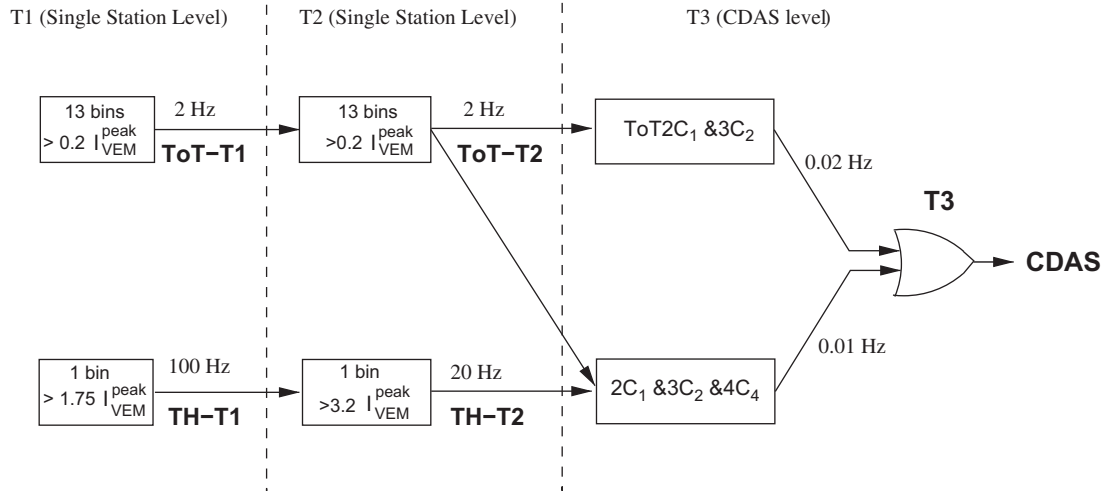


Figure 2.5: **Trigger system hierarchy of the Auger surface detector (from [5]).** C_1, C_2, C_3, C_4 indicate the first, second, third, and fourth ring of neighbours, respectively, 1.5, 3, 4.5 and 6 km from a given station.

The second level of trigger, the so-called **T2** trigger, is applied to reduce the amount of data sent to the CDAS. A T2 is either a *ToT* trigger or a *ThT* trigger with three coincident signals above 3.2 VEM. The T2 background rate is about 20 Hz per station.

2.1.2.2 The surface array trigger / T3

Once at the CDAS, an algorithm begins by searching for clustering of groups of stations in time and space. This is the so-called third level **T3** trigger. It is based on the spatial and temporal combination of the T2 signals. Once a T3 is formed, all FADC signals from the stations having sent a T2 are collected by the CDAS, as well as those from detectors displaying a T1 (but not T2 level) provided that they are within $30 \mu\text{s}$ of the T3 time. The global array trigger has two modes operating simultaneously:

- **3-fold T3 mode:** selecting predominantly physics events. The rate of this T3 with the full array in operation is around 1600 events per day, meaning that each station participates in an event about three times per day. This trigger is extremely pure since 90% of the events are real showers having zenith angles below 60° .
- **4-fold T3 mode:** efficient for the detection of horizontal showers. The latter, rich in muons, generate in the stations signals that have narrow time spread, whereas the shower footprint on the ground is wide-spread, involving many stations. With the full array configuration, this trigger selects about 1200 events per day.

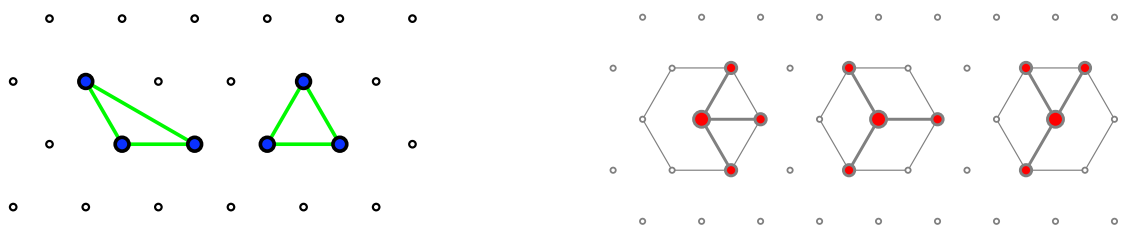


Figure 2.6: **Description of the physics trigger T4 (from [6]).** (a) The two possible 3ToT compact configurations. (b) The three (minimal) $4C_1$ configurations. (All the possible symmetry transformations on the triangular grid are taken into account.)

2.1.3 Selection and reconstruction of the SD events

In this section, we describe the event selection process and the event reconstruction technique. The results provide an estimation of the shower energy and values for its geometrical parameters.

2.1.3.1 Event selection for the SD array for showers with zenith angle below 60°

A selection of physics events is made after data acquisition, i.e. *off-line*. Indeed, a large number of chance coincidence events is expected due to the large number of possible combinations among the single stations. Thus, there is a fourth level trigger, **T4**, used to select the interesting physical events and to reject random coincidences. Two different criteria are defined:

- **the 3ToT**, requiring three nearby stations passing the T2-ToT in an equilateral triangular pattern or one with an extended base (see Figure 2.6(a)). This selects mainly physics events with zenith angles below 60° .
- **the 4C1**, requiring four adjacent stations having signaled a T2 trigger of either kind where the "central" station is 1.5 km from each of the others. Thus the three surrounding stations are placed on the so-called first *crow*n C_1 (see Figure 2.6(b)). With this criterion, a significant fraction of the nearly horizontal showers are detected.

Finally, a fifth level trigger **T5** was designed exclusively for events falling close to the limits of the surface array – a fiducial trigger. Such events are subject to large errors in the core position. Also, the acceptance for events not fully contained by the array can be difficult to compute. Thus, this trigger is based on the shower core position: the station with the largest signal must have at least five working stations (not necessarily triggered) in its closest neighbour ring C_1 .

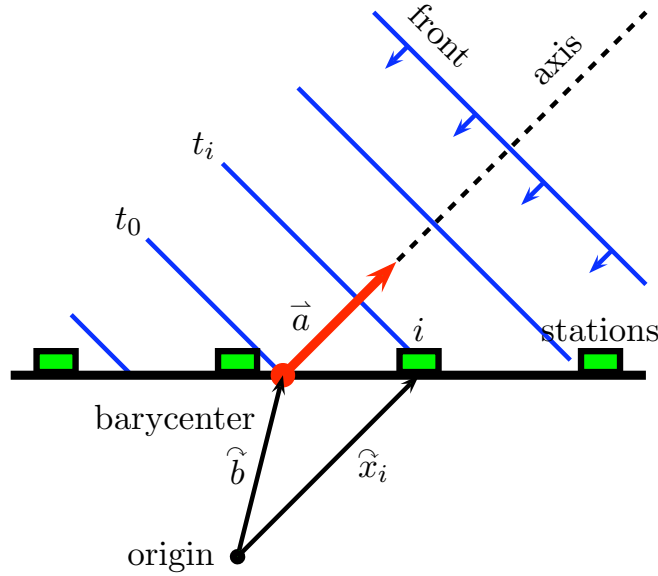


Figure 2.7: **Shower front reaching the stations at ground (from [7]).** In this approximation, all the particles are considered to travel in a plane.

2.1.3.2 Geometrical reconstruction

Once the involved stations have been selected for geometrical reconstruction, an SD event is defined as a series of trigger timings t_i corresponding to the tank coordinates $\vec{x}_i = (x_i, y_i, z_i)$ (and their associated FADC traces). To find the arrival direction of the air shower, we assume as a first approximation that the shower front is a plane perpendicular to the shower axis as shown in Figure 2.7. The time origin is defined as t_0 .

We define the shower axis as $\vec{a} = (u, v, w)$. Assuming that the shower plane moves with the speed of light c , the time at which the shower front reaches the station i is given by

$$ct_i(\vec{x}_i) = ct_0 - (\vec{x}(t) - \vec{b})\vec{a} \quad (2.1)$$

where \vec{b} is the signal-weighted barycentre of the stations involved in the event. In the case where the station positions are known with infinite accuracy, the only error comes from the uncertainty σ_{t_i} on the arrival times, and the function to minimize is thus the squares of the time differences between the measured signal and the time value expected from Equation (2.1)

$$\chi^2 = \sum_i \frac{(ct_i - ct_0 + x_i u + y_i v + z_i w)^2}{\sigma_{t_i}^2} \quad (2.2)$$

However, the problem is obviously not linear, due to the constraint $u^2 + v^2 + w^2 = 1$. An approximate linear solution are obtained when the relative altitudes z_i of the stations is

negligible with respect to x_i, y_i . A more realistic model taking into account the curvature of the shower front is used. The value of this curvature is linked to the altitude of the particle production in the shower. A "parabolic" term $\rho \ll R_c$ is added to Equation (2.1) which becomes

$$ct_i(x_i) = ct_0 - a x + \frac{\rho(x)^2}{2R_c} \quad (2.3)$$

where $\rho(\vec{x})^2 = (\vec{a} \times \vec{x})^2 = x^2 - (\vec{a}\vec{x})^2$ is the perpendicular distance to the shower axis and R_c is the radius of curvature. This is the so-called *parallel-parabola curvature model*.

If the number of triggered stations is greater than four, a tri-dimensional minimization ($z_i \neq 0$) of the function

$$\chi^2 = \sum_i \frac{[c(t_i - t_0) - |R_c \vec{a} - \vec{x}_i|]^2}{\sigma_{t_i}^2} \quad (2.4)$$

is computed as explained in [6]. This is the so-called *concentric-spherical front model*.

The errors on the arrival times σ_{t_i} (around several 10 ns) play a key role in the determination of the arrival direction. The angular resolution of the surface array increases with the number of triggered stations, i.e. when the shower energy and/or the zenith angle increase. The time resolution permits an angular resolution of better than 1° above 10^{19} eV.

2.1.3.3 Lateral density function and energy estimation

The estimation of the energy of the primary particle with the surface array is done using the lateral profile of charged particles of the air shower. The lateral distribution of the signal at ground as a function of the distance to the shower axis, $S(r)$, and measured in VEM units, is parameterized by the *Lateral Distribution Function* (LDF) as

$$S(r) = S(1000 \text{ m}) f_{\text{LDF}}(r) \quad (2.5)$$

where $f_{\text{LDF}}(r)$ is function of the distance to the shower axis r and normalized by $f_{\text{LDF}}(1000 \text{ m}) = 1$. $S(1000 \text{ m})$ is the signal, in VEM, at 1000 m from the shower axis. The tank signal accuracy can be modelled using a Poissonian distribution, with a normalization constant related to the zenith angle of the air shower.

The lateral distribution of the Auger tank signals is fitted to an NKG function, developed by Nishimura, Kamata and Greisen [8, 9]

$$f_{\text{LDF}}(r) = \left(\frac{r}{r_{1000}} \right)^\beta \left(\frac{r + r_{700}}{r_{1000} + r_{700}} \right)^{\beta+\gamma}, \quad (2.6)$$

where $r_{700} = 700 \text{ m}$ and $r_{1000} = 1000 \text{ m}$. β is the LDF slope and adjusted on the data using a second order polynomial in $\sec \theta$. The constant γ is zero in small showers and a free

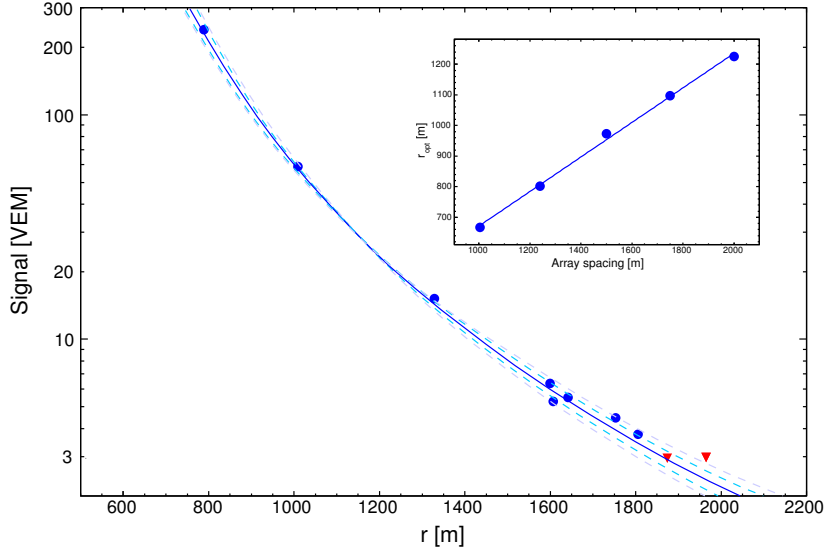


Figure 2.8: **Lateral distribution functions of an SD event, fitted with different slope parameters.** Red points indicate stations with zero signal (only upper limit is shown). The inset shows how the optimum ground parameter r_{opt} varies with the array spacing. The optimum distance r_{opt} corresponds to the distance where the signal fluctuations are minimised.

parameter in events with a high station multiplicity.

The $S(1000\text{ m})$ parameter is the energy estimator for the SD events. An energy estimator should be as insensitive as possible to shower fluctuations (caused by statistics or by systematics related to the first interaction point of the shower). For the configuration of the Auger array and the shower energy range probed (about 10^{19} eV), the optimum point, i.e. the region where the impact of fluctuations is minimal, is around 1 km away from the shower core (see Figure 2.8) [10, 11].

For a given energy, the value of $S(1000\text{ m})$ decreases with the zenith angle θ due to the attenuation of the shower particles and geometrical effects. Assuming an isotropic flux of primary cosmic rays, the shape of the attenuation curve $\text{CIC}(\theta)$ is extracted from the data using the *Constant Intensity Cut* method [12]. The attenuation curve is fitted with a second degree polynomial in $x = \cos^2 \theta - \cos^2 \langle \theta \rangle$: $\text{CIC}(\theta) = 1 + ax + bx^2$. The average angle, $\langle \theta \rangle \simeq 38^\circ$, is taken as a reference to reduce the bias introduced by the CIC procedure. For each SD event, the S_{38} parameter is calculated

$$S_{38} \equiv S_{38}(1000\text{ m}) = \frac{S(1000\text{ m})}{\text{CIC}(\theta)}, \quad (2.7)$$

and may be regarded as the signal $S(1000\text{ m})$ the shower would have produced if it had

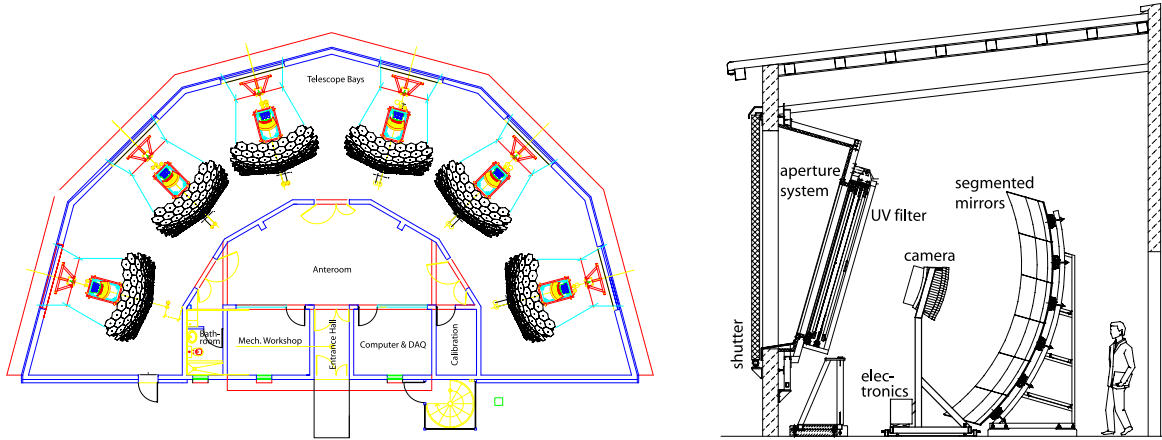


Figure 2.9: **The fluorescence detector at the Pierre Auger Observatory.** (a) A fluorescence building with its six telescopes. (b) An individual telescope.

arrived at $\theta = 38^\circ$.

The relation between S_{38} and the energy of the event E_{SD} is well described by a single power-law function

$$E_{SD} = A (S_{38})^B, \quad (2.8)$$

where $A = (1.68 \pm 0.05) \times 10^{17}$ eV and $B = 1.035 \pm 0.009$ [14]. This relation has been established by the fluorescence detector.

The resolution in the SD energy E_{SD} , with its statistical uncertainty, is $(15.8 \pm 0.9)\%$ for $3 \text{ EeV} \leq E_{SD} \leq 6 \text{ EeV}$, $(13.0 \pm 1.0)\%$ for $6 \text{ EeV} \leq E_{SD} \leq 10 \text{ EeV}$ and $(12.0 \pm 1.0)\%$ for $E_{SD} > 10 \text{ EeV}$.

2.2 The fluorescence detector (FD)

The detection of ultra-high energy cosmic rays using nitrogen fluorescence emission induced by extensive air showers is a well established technique, used previously by the Fly's Eye [13] and HiRes [2] experiments. Charged particles generated during the development of extensive air showers excite atmospheric nitrogen molecules, and these molecules then emit fluorescence light in the 300 – 430 nm range. The number of fluorescence photons emitted is proportional to the energy deposited in the atmosphere due to the electromagnetic energy losses undergone by the charged particles.

The fluorescence detector (FD) comprises four observation sites – Los Leones/LL, Los Morados/LM, Loma Amarilla/LA and Coihueco/CO – located atop small hills on the perimeter of the surface array [15]. Six independent telescopes, each with a field of view of $30^\circ \times 28.1^\circ$ in azimuth and elevation with lower edge 2° above the ground, are located at

each FD site. A set of six telescopes covers 180° in azimuth, observing the atmosphere above the ground array. Figure 2.9(a) shows the arrangement of the telescopes inside an observation site and Figure 2.9(b) shows an individual telescope. The four FD sites ensure full detection efficiency for air showers in excess of 10^{19} eV over the entire surface of the array.

2.2.1 Description of a fluorescence telescope

The basic elements of the optical system of each FD telescope are a filter at the entrance window, a circular aperture with a radius of 1.1 m, a corrector ring, a spherical mirror and a camera composed of photomultipliers.

The window is an optical filter made of Schott MUG-6 glass [16], absorbing visible light and transmitting UV photons from 290 nm to 410 nm. It includes almost the entire nitrogen fluorescence spectrum. The transmission maximum is 85% at 360 nm and decreases to 20% at 300 nm and 400 nm. Despite this attenuation of the visible wavelengths, the FD telescopes can only operate during clear nights with low moonfraction, i.e. corresponding to a duty cycle of 11% to 14%.

The aperture, the corrector ring, the mirror with a surface of around 13 m^2 , and the PMT camera constitute a modified Schmidt camera design that partially corrects for spherical aberration. The remaining angular spread is 0.5° . A complete simulation of the optical system was developed using Geant4 [17], a Monte Carlo toolkit for particle interactions and light propagation. Figure 2.10(a) shows rays traced by Geant4. There is also a faster implementation of photon tracking without using Geant4.

The camera is composed of a matrix of 440 pixels (22 rows by 20 columns) located on the focal surface of the telescope (see Figure 2.10(b)). A cosmic ray shower is imaged on the camera as a line of activated pixels having a track-like geometrical pattern and also a clear time sequence. Each pixel has a Winston cone to collect the light that otherwise would fall between the photocathodes: the collection efficiency is in this way increased from 70% to 94%.

2.2.2 Calibration

The reconstruction of air shower profiles and the ability to estimate the total energy of a reconstructed shower require conversion of ADC counts to a light flux at the telescope aperture. It is necessary to have methods for evaluating the response of each pixel to a given flux of incident photons. This procedure has to include the effects of optical filter transmittance, reflection at optical surfaces, mirror reflectivity, pixel light collection efficiency, cathode quantum efficiency and PMT gain, etc.: this is the so-called *end-to-end calibration*.

The absolute calibration of the fluorescence detectors uses a 2.5 m diameter light source (called a “drum”) placed at the telescope aperture, providing the same flux of light at each

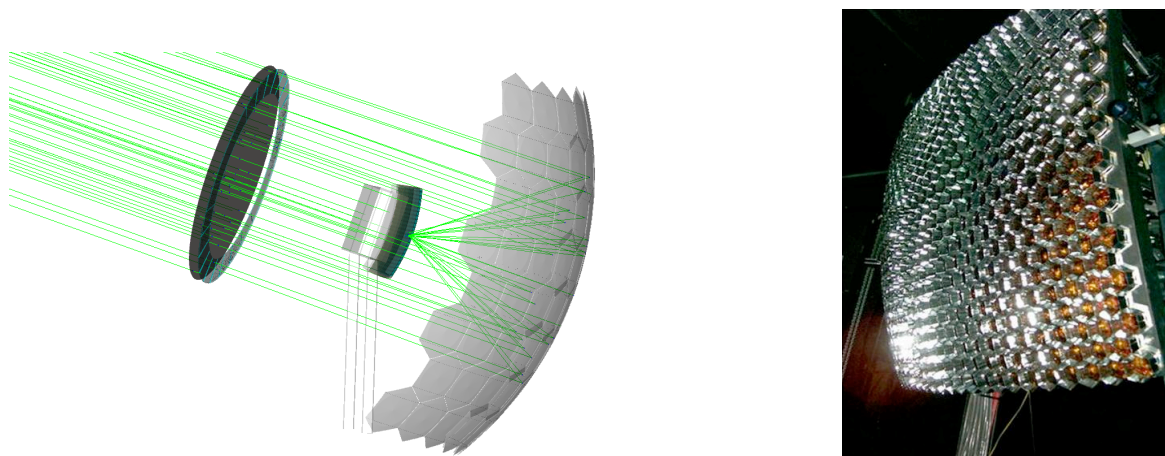


Figure 2.10: **The FD telescope.** (a) Ray tracing simulation of the optical system of the telescope made using Geant4 [17]. (b) The camera body. Each hole is equipped with a photomultiplier, corresponding to one pixel.

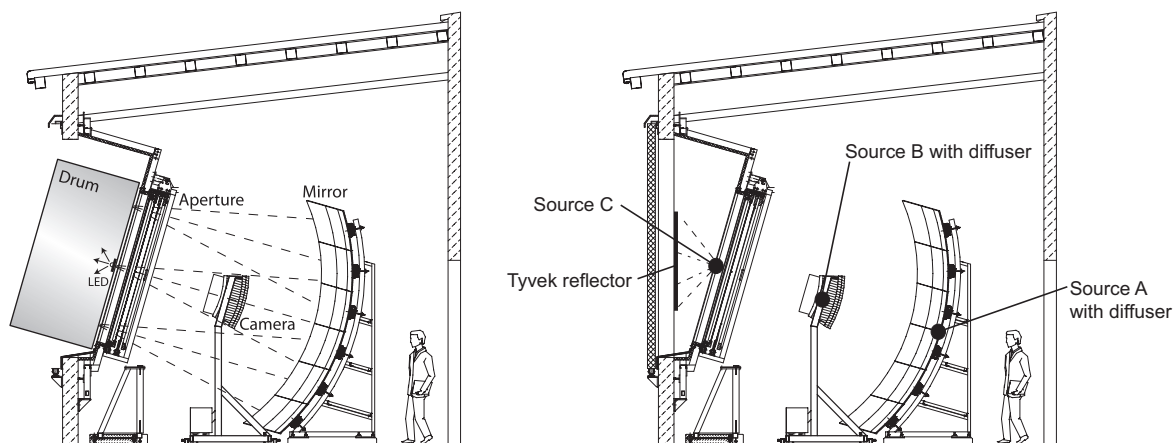


Figure 2.11: **FD telescope calibration.** (a) The calibration drum mounted in front of a telescope aperture. (b) Light source positions for three different relative calibration methods.

pixel (see Figure 2.11(a)). The source provides a pulsed photon flux intensity and uniformity across the aperture. By combination of two diffusively reflective surfaces inside the drum, the light emitted per unit solid angle from any small area A of the drum surface depends only on the angle α with respect to the normal direction according to the Lambert law $I(\alpha) = I_0 A \cos \alpha$. The known flux from the light source and the response of the acquisition system give the required calibration for each pixel. The drum measurement is performed yearly.

Three relative calibration techniques are used for rapid detection of modifications with time of the system's performance. Before and after each night of FD data-taking, three posi-

tions are illuminated for each camera, monitoring different groups of detector components (see Figure 2.11(b)). They are

- **Cal A**, illuminating the photomultipliers directly through a diffuser placed at the centre of the mirror. This monitors the stability and linearity of the PMTs.
- **Cal B**, a source located at the side of the camera and sending light to the mirrors through a Teflon diffuser. This checks the PMT response and monitors the mirror reflectivity.
- **Cal C**, sending a signal to ports on the sides of the entrance aperture where the light is directed at reflective Tyvek targets mounted on the telescope doors from which it is reflected back into the telescopes. Five interference filters are used to monitor the stability of the telescope at wavelengths between 330 and 410 nm.

2.2.3 Data acquisition and triggering in a camera

Each camera has its own data acquisition system and operates independently. The recorded signals are digitized at 10 MHz with a 12-bit ADC. Before an event is read out, the criteria of four types of trigger must be met. The duration of the signal from a pixel depends of the shower geometry. For instance, a vertical shower 30 km away from the detector crosses the field of view of the camera in 50 μs . The time limit chosen for the buffer is 100 μs , corresponding to a horizontal shower crossing 30 km in the field of view.

The FD telescopes are used to record fluorescence signals of widely varying intensity on top of large, and continuously changing, light background. This presents a significant challenge for the design of the electronics and the data acquisition system, which must provide a large dynamic range and strong background rejection, while accepting any physically plausible air shower.

- The **First Level Trigger (FLT)** module is the heart of the digital front-end electronics. The FADC values are integrated over 10 time bins improving the signal to noise ratio by a factor $\sqrt{10}$. The threshold is adjusted continuously to achieve a trigger rate of 100 Hz per pixel.
- The **Second Level Trigger (SLT)** consists of a purely geometric pattern recognition, also done using hardware. It searches for 4 or 5 adjacent pixels giving FLT triggers in a time window of 1 to 32 μs . Counting all different four-fold patterns originating from the five-pixel track segments in Figure 2.12, one finds 108 different pattern classes. The SLT rate is 0.1 Hz per telescope.
- The **Third Level Trigger (TLT)** is a software algorithm designed to eliminate from the air shower data stream noise events that satisfy the LT and SLT conditions. It is optimized for fast rejection of random coincidence triggers as well as those caused by

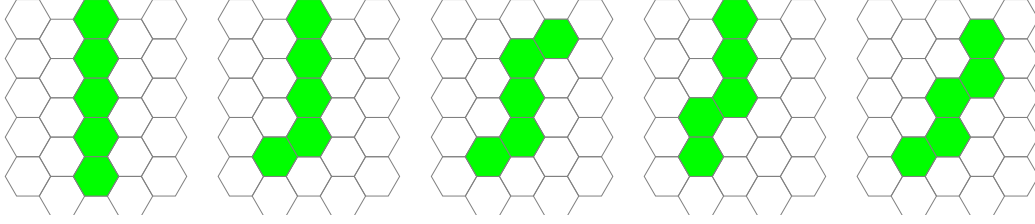


Figure 2.12: Fundamental types of patterns regarded as straight track segments.

lightning, and muon impacts on the camera. A correlation between the spatial arrangement and peak signal times of triggered pixels is required to discard noisy channels far off the light track. This decreases the rate to 0.02 Hz per FD building.

- The **Hybrid Trigger (T3)** is an algorithm calculating a preliminary shower direction and a ground impact time using a simple online reconstruction method. Once these data arrive at the CDAS, a request is sent to the SD for signals recorded close to the calculated impact point and time. For each T3 trigger, the closest stations to the reconstructed impact position are read out. The FD and SD data are merged off-line for possible hybrid analysis.

2.2.4 Reconstruction of the FD events

One of the main goals of the hybrid reconstruction is the energy calibration of the surface detector. The reconstruction is called *hybrid* since the procedure uses information from the surface detector station(s).

2.2.4.1 Geometrical reconstruction

Cosmic rays are detected as a sequence of triggered pixels in the camera as explained in Section 2.2.3. The first step in the analysis is the determination of the Shower Detector Plane (SDP), the plane including the location of the eye and the line of the shower axis as shown in Figure 2.13. Then, the timing information from the pixels is used to reconstruct the shower axis within the SDP. The latter is defined by two parameters: the perpendicular distance R_p from the camera to the track, and the angle χ_0 that the track makes with a horizontal line in the SDP. Each pixel observing the track has a pointing direction which makes an angle χ_i with the horizontal line. Let t_0 be the time at which the shower core reaches the point of closest approach. The expected arrival time t_i of the signal in a pixel is defined as follows

$$t_i = t_0 + \frac{R_p}{c} \tan \left(\frac{\chi_0 - \chi_i}{2} \right). \quad (2.9)$$

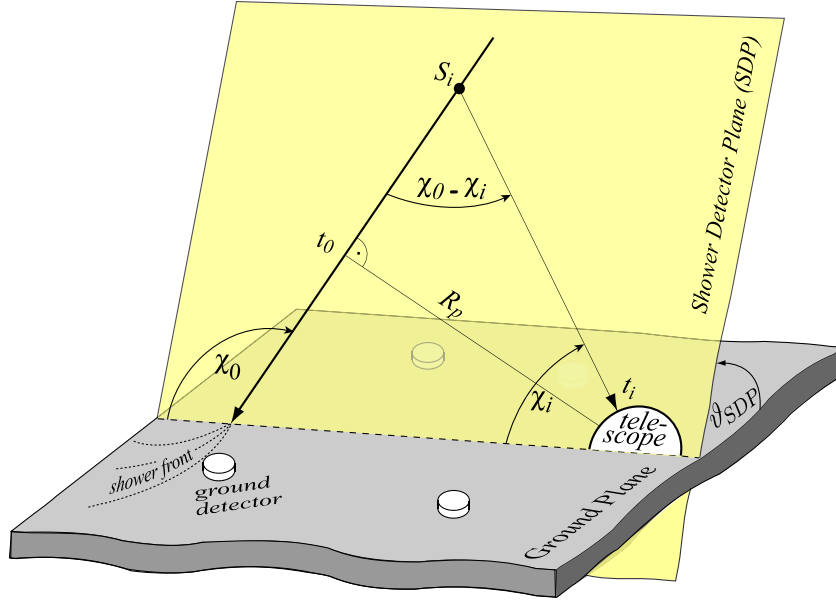


Figure 2.13: Geometrical shower reconstruction variables for the fluorescence detector.

The correlation between the variables is large, a slight deviation in the elevation angle χ_0 inducing a large change of the other two parameters. This degeneracy can be broken by including the timing information from a single SD station. The reconstruction accuracy of hybrid events is much better than what can be achieved using SD or FD data independently. For instance, the angular resolution of hybrid measurements is better than 0.5° above 10^{18} eV compared with about 3° for the surface detector data (for the same energy range, this angular resolution improving with the number of triggered stations).

2.2.4.2 Longitudinal profile and energy estimation

Once the geometry of the shower is known, the light collected at the aperture as a function of time can be converted to energy deposit by the shower as a function of slant depth. The two major contributions to the light at the FD aperture are the fluorescence light from nitrogen molecules (emitted isotropically) and Cherenkov radiation photons (strongly beamed in the shower direction). Both contributions are affected by scattering and absorption in the atmosphere.

The amount of fluorescence light is directly proportional to the energy deposited by the air shower along its path in the atmosphere. Given the fluorescence yield Y_i^f at a point in the atmosphere, the number of photons produced by the shower is

$$N_\gamma^f(X_i) = Y_i^f dE/dX_i, \quad (2.10)$$

where dE/dX_i denotes the energy deposited at slant depth X_i . For instance, using the absolute fluorescence yield in air in the most efficient band (337 nm), around 5 photons are emitted per MeV of energy deposited.

After subtracting the Cherenkov photons, the total energy deposit is just the sum of the energy loss of electrons in the atmosphere, dE/dX_i , which is related to the number of electrons $N_e(X_i)$ by

$$dE/dX_i = N_e(X_i) \int_0^\infty f_e(E, X_i) dE/dX_e(E, X_i) dE, \quad (2.11)$$

where $dE/dX_e(E, X_i)$ is the energy loss of a single electron with energy E and $f_e(E, X_i)$ denotes the normalized electron energy distribution. The electron energy spectrum $f_e(E, X_i)$ has a universal dependence on shower age [18–20], i.e. it does not depend on the primary mass or energy. Also, since the electron energy loss depends only slightly on the local density, Equation (2.11) can be reduced to

$$dE/dX_i = N_e(X_i) \alpha_i, \quad (2.12)$$

where α_i is the average energy deposit per electron at shower age $s_i = 3/(1 + 2X_{\max}/X_i)$ [20].

The electromagnetic energy is given by the integral over the energy deposit profile

$$E_{\text{em}} = \int_0^\infty f_{\text{GH}}(X) dX, \quad (2.13)$$

where $f_{\text{GH}}(X)$ corresponds to the Gaisser-Hillas function defined as follows [21]

$$f_{\text{GH}}(X) = dE/dX_{\max} \cdot \left(\frac{X - X_0}{X_{\max} - X_0} \right)^{(X_{\max} - X_0)/\lambda} \exp\left(\frac{X_{\max} - X}{\lambda} \right), \quad (2.14)$$

where X_0 depends on the first interaction point and λ is an attenuation length.

Not all of the energy of a primary cosmic ray goes into the electromagnetic component of the air shower. Neutrinos escape undetected and muons need long path lengths to release their energy. This is usually accounted for by multiplying the electromagnetic energy with a correction factor f_{inv} determined from shower simulations to obtain the total primary energy

$$E_{\text{tot}} = (1 + f_{\text{inv}}) E_{\text{em}}. \quad (2.15)$$

The invisible energy correction f_{inv} is based on the average for proton and iron showers simulated with the QGSJetII-03 model and amounts to about 9% at 10 EeV for a mixed primary composition [22]. The neutrino and muon production probabilities have energy dependencies due to the meson decay probabilities in the atmosphere so that f_{inv} falls from $\sim 10.5\%$ at 10^{18} eV to $\sim 8.5\%$ at 10^{20} eV.

The FD energy resolution is determined by propagating the statistical uncertainty on the

light flux, the invisible energy uncertainty due to shower fluctuations and the uncertainties on air shower geometry and aerosol conditions. The overall energy resolution is 7.6% and it is almost constant with energy [14].

The systematic uncertainty on the FD energy scale is about 22%. It includes contributions from the absolute fluorescence yield (14%) [23], calibration of the fluorescence telescopes (9.5%), the invisible energy correction (4%), systematics in the reconstruction method used to calculate the shower longitudinal profile (10%), and atmospheric effects (7%) (see Chapter 4).

2.2.5 Typical hybrid events

Figure 2.14 shows an event detected in May 2008 which is independently reconstructible by the surface detector and the fluorescence detector methods: this kind of events are called *Golden hybrid events*¹. The air shower was recorded by three FD eyes: Los Morados (LM), Loma Amarilla (LA) and Coihueco (CO). We note that 66.0% of the FD events are recorded by only one eye, 28.8% by two eyes, 4.6% by three eyes and 0.6% by the whole FD detector (four eyes). The energy estimations from the three FD eyes and the SD detector are plotted in Figure 2.16. A clear under-estimation of the energy can be observed for the surface detector. In the following, we will present only the reconstruction done with the Los Morados eye.

For this event, thirteen surface detectors were triggered (see Figure 2.14(e)) and its LDF has been reconstructed (see Figure 2.14(g)). Figure 2.14(b) shows the optical image on the camera where the colour code corresponds to the arrival time of the signals. The number of pixels is much greater than the number of stations. Also, the time is longer for the FD signal. Therefore the geometry of the shower, reconstructed from the timing information (see Figure 2.14(D)) is more reliable than the one from the surface detector (see Figure 2.14(e)). The shower geometry reconstructed by the surface detector and the fluorescence detector are in agreement for this event:

$$[\theta, \phi] = [(65.55 \pm 0.14)^\circ, (178.24 \pm 0.17)^\circ]_{\text{SD}} \text{ vs. } [(66.2 \pm 0.6)^\circ, (178.5 \pm 0.9)^\circ]_{\text{LM}}.$$

After separating the different contributions to the light falling on the aperture, shown in Figure 2.14(c), the profile reconstruction is performed. For this event the scattered Cherenkov photons dominate over the direct Cherenkov light because the air shower direction is pointing away from the telescope. The energy deposit as a function of the slant depth is illustrated in Figure 2.14(f). The energy of the extensive air shower is computed as the integral over the whole slant depth of the Gaisser-Hillas function which describes the profile with a reduced χ^2 of 0.73. The shower maximum is at $X_{\text{max}} = 783 \pm 36 \text{ g/cm}^2$.

¹The figures come from the ADST program, *Advanced Data Summary Tree*, which provides storage and visualization for the Auger events. The official program for the event reconstruction in the Auger Collaboration is the so-called *Offline*.

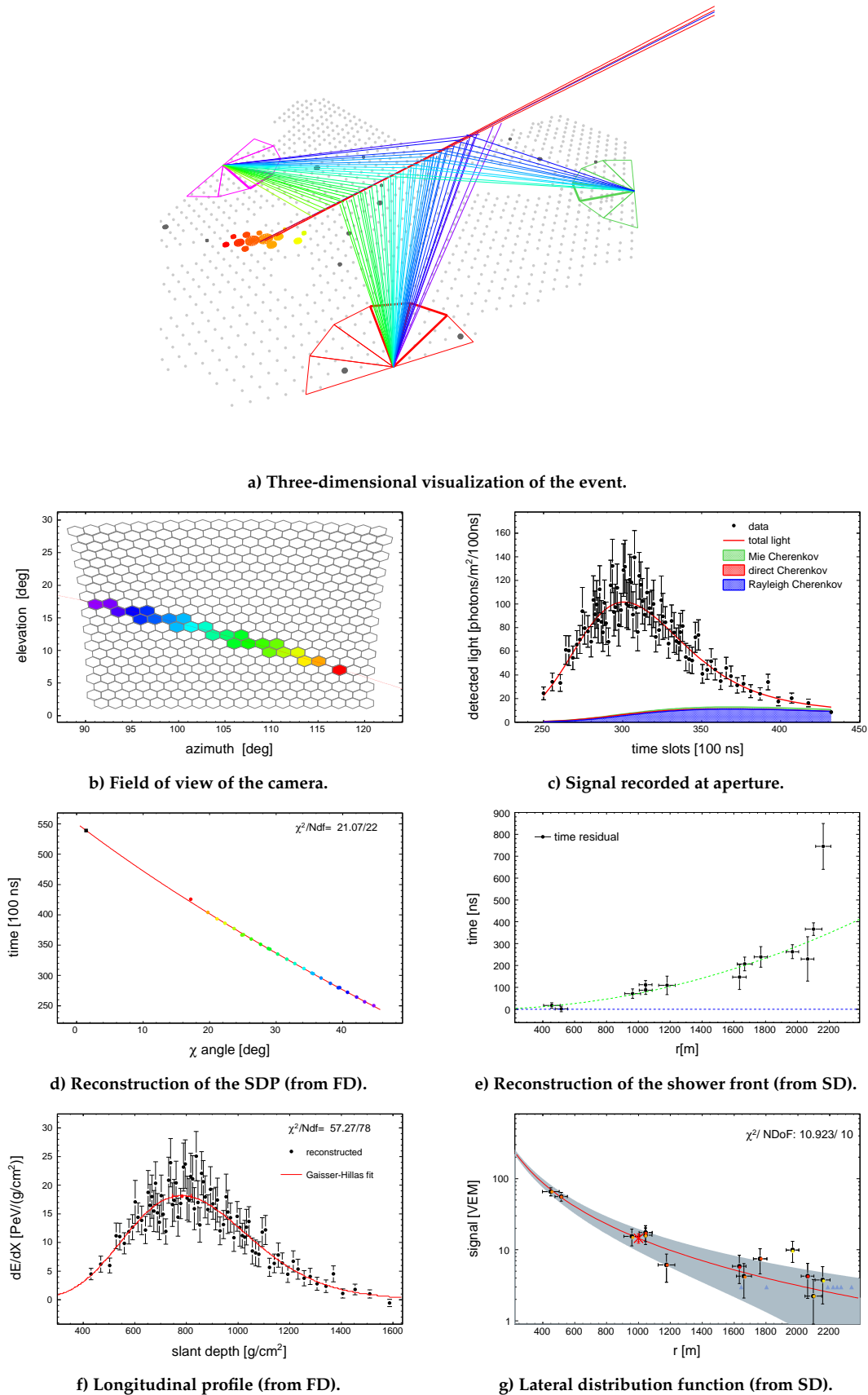


Figure 2.14: Reconstruction in Offline of a golden hybrid event (ID 4880772). The FD data come from the reconstruction at the Los Morados site.

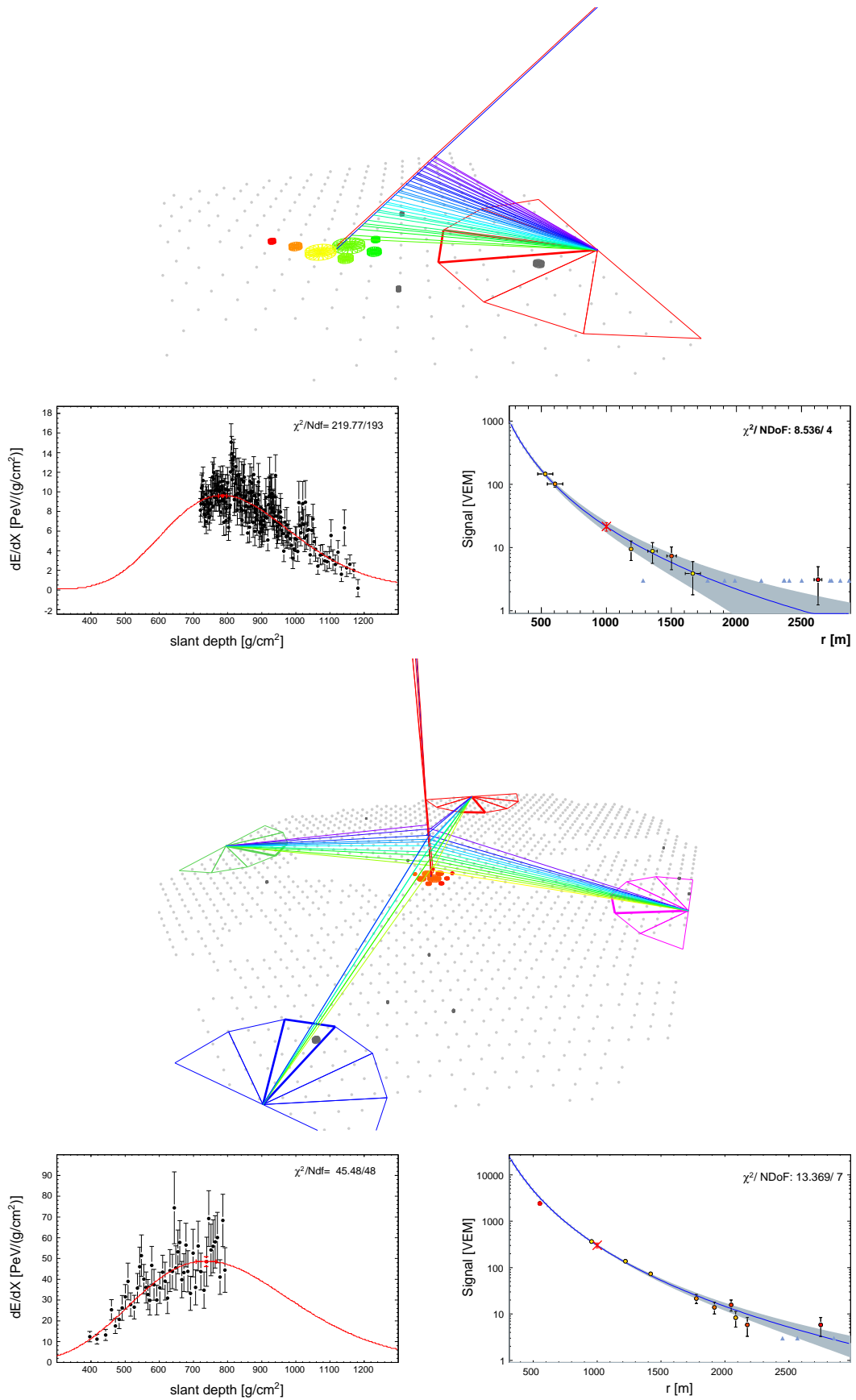


Figure 2.15: Reconstruction in Offline of two golden hybrid events. Top panel: ID 4886352. Bottom panel: ID 4665675.

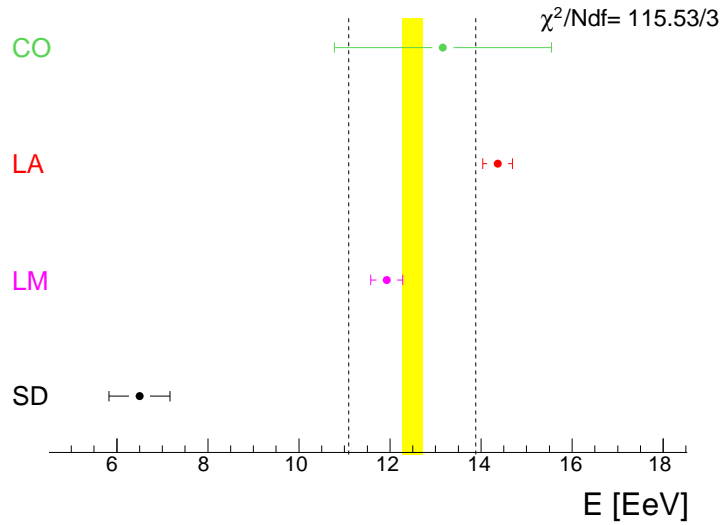


Figure 2.16: Energy estimations furnished by the different Auger detectors. CO: Coihueco, LA: Loma Amarilla, LM: Los Morados, SD: Surface Detector.

Figure 2.15 shows two other examples of golden hybrid events, with energies estimated at $(4.76 \pm 0.28) \times 10^{18}$ eV (top panel) and $(6.23 \pm 0.23) \times 10^{19}$ eV (bottom panel).

2.3 Observatory enhancements

The Pierre Auger Observatory is now collecting around 7000 km² sr of exposure per year. New detector systems are mainly intended to extend the energy range and to provide a better measurement of the muonic component. HEAT (High Elevation Auger Telescopes) has three telescopes which are now constructed, and located 180 m north-east of the Coihueco FD site. During the same period, the collaboration deployed additional surface detector stations paired with underground muon counters as an infill array of 24 km² close to and in the field of view of HEAT. This extension is called AMIGA, i.e. Auger Muon and Infill for the Ground Array. The layout of HEAT and the infill array is shown in Figure 2.17(a).

2.3.1 HEAT – High Elevation Auger Telescopes

The design of HEAT is very similar to the original FD system, except for the ability to tilt the telescopes upward by 29° since, at lower energy, the shower development is shallower in the atmosphere [24]. In both cases, a large field of view of about 30° × 30° is obtained using Schmidt optics. Differences between the conventional FD telescopes and HEAT are introduced by the tilting mechanism. While the original 24 FD telescopes are housed in four solid concrete buildings, the three HEAT telescopes are installed in individual, pivot-mounted en-

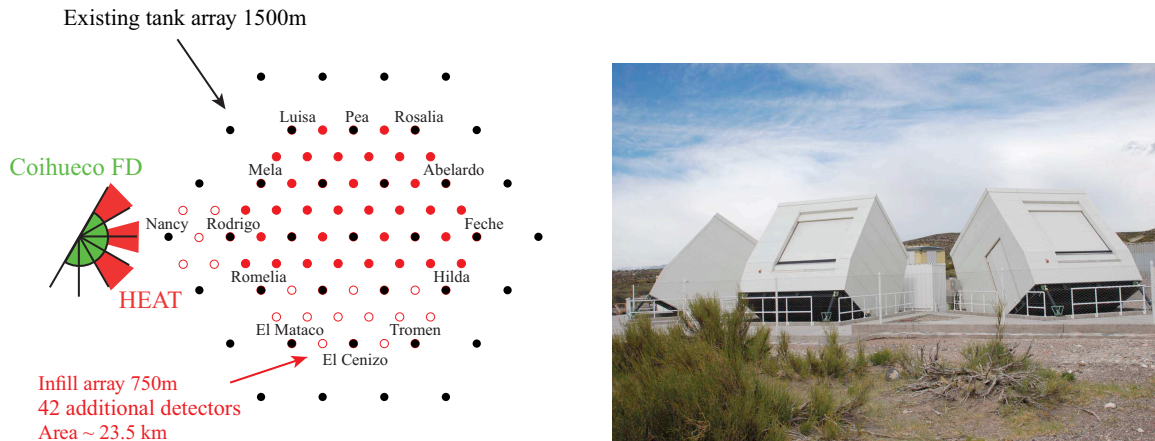


Figure 2.17: **Enhancements at the Pierre Auger Observatory.** (a) Layout of the infill array and the Coihueco and HEAT fluorescence telescopes. The additional infill stations are shown in red. (b) HEAT in its tilted mode upwards with closed shutters.

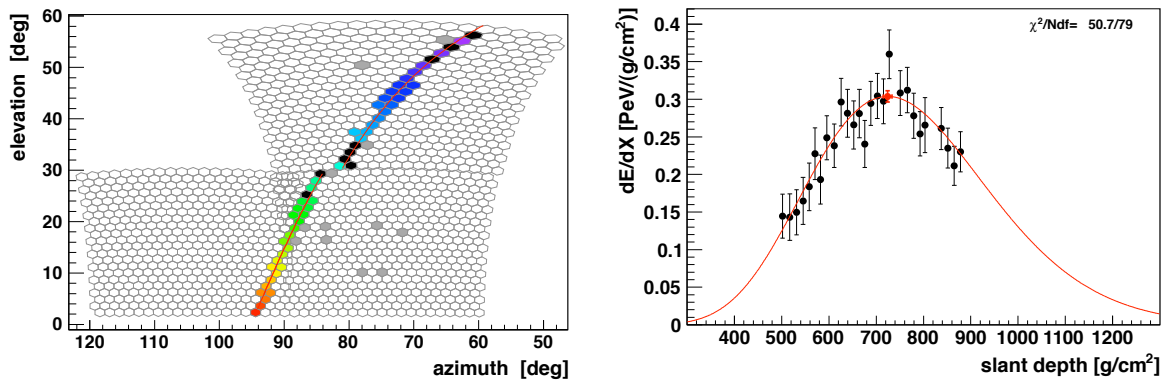


Figure 2.18: **Example of a low-energy event recorded in coincidence by HEAT and two Coihueco telescopes.** (a) Camera image of the recorded signal. The arrival time of the light is colour-coded (blue early, late red) (b) Reconstructed energy deposit profile. This almost vertical event has a reconstructed energy of about 1.7×10^{17} eV.

closures (see Figure 2.17(b)).

Data taking with the new HEAT telescopes is possible in horizontal (“down”) position as well as in the tilted (“up”) position. The horizontal position is used for the absolute calibration of the telescopes. Indeed, in this position the field of view of the HEAT telescopes overlaps with those of the Coihueco telescopes. This offers the possibility of doing special analyses of events recorded simultaneously at both sites.

With the “up” configuration, the combined HEAT-Coihueco telescopes cover an elevation range from 2° above the horizon to 58° . This extended field of view enables the reconstruction of low-energy showers (galactic to extragalactic transition in the energy spectrum) and

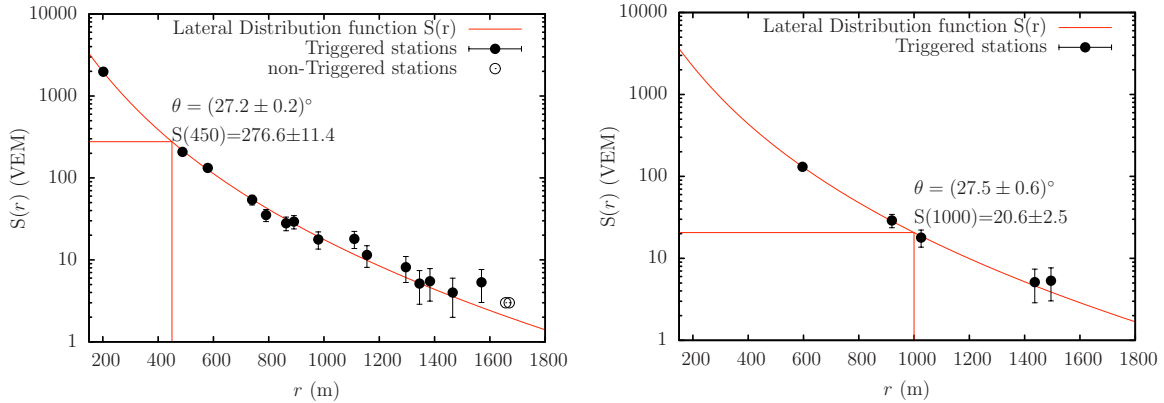


Figure 2.19: The same event reconstructed with the infill (a) and the regular SD array (b). Solid and open circles are triggered and non-triggered stations, respectively.

resolves ambiguities in the X_{\max} determination. An example of one of the first low energy showers recorded with HEAT and the regular Coihueco station is shown in Figures 2.18(a) and 2.18(b).

2.3.2 AMIGA – Auger Muons and Infill for the Ground Array

AMIGA consists of an array of water-Cherenkov detectors deployed on a hexagonal grid with sides of 750 m and 433 m, and an associated set of muon detectors each of 30 m² area, buried at a depth of 2.3 m [25, 26]. The infill spacings allow cosmic rays to be detected with full efficiency down to an energy of 3×10^{17} eV and 10^{17} eV, respectively. As of April 2011, 53 out of 61 surface stations planned for the 750 m infill have been deployed. For the closer-spaced array, 24 new detectors will be installed after the completion of the 750 m array.

The angular resolution of the 750 m array was found to be 1.3° for events with at least 4 stations. To reconstruct the events, the distribution of the SD signals on the ground as a function of their distance to the shower axis is fitted with a LDF, $S(r)$. The optimum distance r_{opt} where the signal fluctuations are minimized was found to be 450 m. An advantage of having the infill within the regular surface array is that it is possible to make cross-checks of results in the overlap region. As an example, the LDF of a well-contained infill event of 2.7×10^{18} eV arriving with a zenith angle of 27° is shown in Figure 2.19(a) using the infill array, and in Figure 2.19(b) using the regular array. The two reconstructions are compatible. As is the case for the main surface array, the energy of an event is estimated from the ground parameter independently of the zenith angle of the air shower by means of the CIC method. A value is obtained for $S(450)$ with a reference angle of 35° (S_{35}).

The muon detector is still in its prototype phase. It consists of seven buried detectors composed of 30 m² area scintillator counters that will be installed hexagonally around a central

point. At present, four scintillator modules have already been deployed.

Bibliography

- [1] M Takeda *et al.*, *Energy determination in the Akeno Giant Air Shower Array experiment*, *Astropart. Phys.* **19** (2003) 447–462.
- [2] T Abu-Zayyad *et al.*, *Monocular Measurement of the Spectrum of UHE Cosmic Rays by the FADC Detector of the HiRes Experiment*, *Astropart. Phys.* **23** (2005) 157–174.
- [3] J Abraham *et al.* [Pierre Auger Collaboration], *Atmospheric effects on extensive air showers observed with the surface detector of the Pierre Auger observatory*, *Astropart. Phys.* **32** (2009) 89–99.
- [4] J Abraham *et al.* [Pierre Auger Collaboration], *Properties and performance of the prototype instrument for the Pierre Auger Observatory*, *NIM A* **523** (2004) 50–95.
- [5] J Abraham *et al.* [Pierre Auger Collaboration], *Trigger and aperture of the surface detector of the Pierre Auger Observatory*, *NIM A* **613** (2010) 29–39.
- [6] D Veberič and M Roth, *SD reconstruction; Offline reference manual*, **GAP-2005-035**.
- [7] I C Maris, *Measurement of the ultra high nergy cosmic ray flux using data of the Pierre Auger Observatory*, **GAP-2008-026**.
- [8] K Kamata and J Nishimura, *The lateral and the angular structure functions of electron showers* *Progress of Theoretical Physics Supplement*, **6** (1958) 93–155.
- [9] K Greisen, *Progress in Comic Ray Physics*, (1956).
- [10] D Newton *et al.*, *The Optimum Distance at which to Determine the Size of a Giant Air Shower*, **GAP-2006-045**.
- [11] D Barnhill *et al.*, for the Pierre Auger Collaboration, *Measurement of the lateral distribution function of UHECR air showers with the Pierre Auger Observatory*, *Proc. 29th ICRC, Pune, India* (2005).
- [12] J Hersil *et al.*, *Observations of Extensive Air Showers near the Maximum of Their Longitudinal Development*, *Phys. Rev. Lett.* **6** (1961) 22–23.
- [13] RM Baltrusaitis *et al.*, *The Utah Fly’s Eye detector*, *NIM A* **240** (1985) 410–428.
- [14] R Pesce, for the Pierre Auger Collaboration *Energy calibration of data recorded with the surface detectors of the Pierre Auger Observatory*, *Proc. 32nd ICRC, Beijing, China* (2011).
- [15] J Abraham *et al.* [Pierre Auger Collaboration], *The fluorescence detector of the Pierre Auger Observatory*, *NIM A* **620** (2010) 227–251.

-
- [16] Schott Glaswerke, Mainz, Germany; <http://www.schott.com>.
- [17] S Agostinelli *et al.* [Geant 4 Collaboration], *Geant 4 - A simulation toolkit*, NIM A **506** (2003) 250–303.
- [18] AM Hillas, *Angular and energy distributions of charged particles in electron-photon cascades in air*, J. Phys. G **8** (1982) 1461–1473.
- [19] M Giller *et al.*, *Energy spectra of electrons in the extensive air showers of ultra-high energy*, J. Phys. G **30** (2004) 97–105.
- [20] F Nerling *et al.*, *Description of Cherenkov light production in high-energy air showers*, Astropart. Phys. **24** (2006) 421–437.
- [21] TK Gaisser and AM Hillas, Proc. 15th ICRC, Plovdiv, Bulgaria **8** (1977) 353.
- [22] AG Mariazzi, for the Pierre Auger Collaboration, *A new method for determining the primary energy from the calorimetric energy of showers observed in hybrid mode on a shower-by-shower basis*, Proc. 32nd ICRC, Beijing, China (2011).
- [23] M Nagano *et al.*, *New measurement on photon yields from air and the application to the energy estimation of primary cosmic rays*, Astropart. Phys. **22** (2004) 235–248.
- [24] T H Mathes, for the Pierre Auger Collaboration, *The HEAT telescopes of the Pierre Auger Observatory: status and first data*, Proc. 32nd ICRC, Beijing, China (2011).
- [25] F Sánchez, for the Pierre Auger Collaboration, *The AMIGA detector of the Pierre Auger Observatory: an overview*, Proc. 32nd ICRC, Beijing, China (2011).
- [26] I C Maris, for the Pierre Auger Collaboration, *The AMIGA infill detector of the Pierre Auger Observatory: performance and first data*, Proc. 32nd ICRC, Beijing, China (2011).

Muonic component and arrival directions of the highest energy events

Contents

3.1 Phenomenological approach to the muon component in hadronic showers . . .	62
3.1.1 The charged pion component	63
3.1.2 Muon production in hadronic showers	68
3.1.3 Muon propagation from birth to ground	74
3.2 Muon counting using the surface detectors	82
3.2.1 The jump method	82
3.2.2 The Artificial Neural Network (ANN) method	84
3.3 Mass composition and arrival directions of the highest energy events	85
3.3.1 Centaurus A, the region with the largest arrival direction excess	86
3.3.2 Muon component as a function of arrival direction	87
3.4 Conclusion	90
Bibliography	92

Introduction: This chapter analyses phenomenologically the muon component in hadronic showers. It develops an original “toy” model based on simple arguments and average values. Then, after having presented the two muon counting methods developed by the Auger-LAL group, the highest energy events are analyzed using this technique. The case of Centaurus A is presented and treated taking into consideration the muonic properties of the events.

This work is inspired from two internal notes¹² published during my PhD thesis. Also, I took part in the development of the new muon counting method at the Auger-LAL group³. My task was to furnish the observables extracted from the FADC traces, for the simulations and the SD data. For this work, several large simulation libraries have been produced and made accessible to the rest of the Auger Collaboration.

¹PN Diep and K Louedec, *Jumps in the sky* **GAP-2010-071**

²K Louedec and PN Diep, *Mass composition and arrival directions of the highest energy hybrid events* **GAP-2010-072**

³B Kégl *et al.*, *Reconstructing $N_{\mu 19}(1000)$* **GAP-2011-054**

3.1 Phenomenological approach to the muon component in hadronic showers

When a cosmic ray enters the atmosphere, it strikes a nucleus in an air molecule and produces, among other fragments, pions and kaons. While neutral pions π^0 decay almost immediately into two photons and consequently contribute to the electromagnetic component, charged pions remain part of the hadronic cascade producing new hadronic interactions. Even if the situation is a bit more complicated for kaons since they have multiple decay channels, the idea is the same. In the end, up to 10% of all the muons are produced via the kaon channels.

Hadronic interactions occurring during shower development can be approximated with the Heitler model as in the case of electromagnetic showers [1]. In this study, the primary is a proton of energy E_0 which interacts with the atmosphere creating n_{tot} new particles with energy E_0/n_{tot} . In a first approximation, we consider that one third of the primary energy

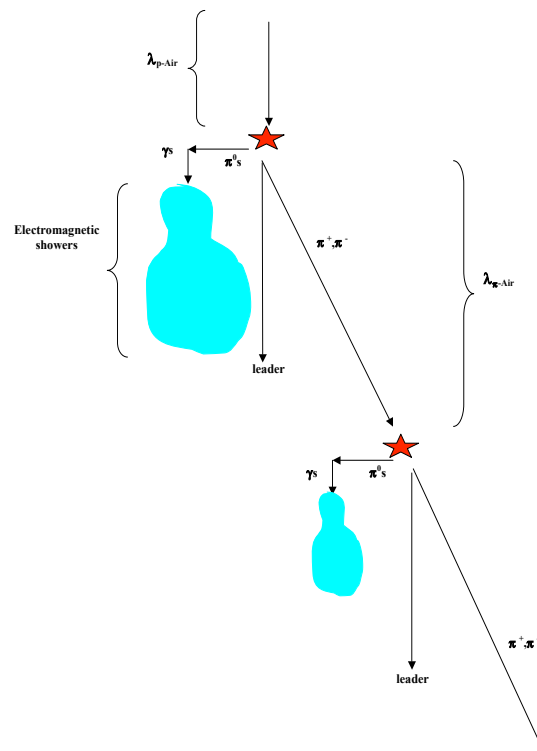


Figure 3.1: Schematic view of hadronic cascades in a shower.

goes to neutral pions π^0 and two thirds to the charged pions π^\pm (see Figure 3.1). Thus, after n generations, there are $N_{\pi^\pm} = (N_{\text{ch}})^n$ total charged pions and they carry a total energy given by

$$E_{\text{had}} \simeq E_{\pi^\pm}^{\text{tot}} = \left(\frac{2}{3}\right)^n E_0. \quad (3.1)$$

where N_{ch} represents the multiplicity of charged particles in the collision.

This basic approach does not take into account the distribution of the incoming energy between the produced particles and the leading particle. Indeed, when two hadrons interact, a significant fraction of the total energy is carried away by a single leading particle. This energy is unavailable for immediate new particle production. The fraction of the total energy going into pion production is given by the parameter k , the so-called *inelasticity*. During an interaction initiated by a particle of energy E , the energy is shared as follows: $(1 - k)E$ is taken by a single leading particle, $(2/3)kE$ is used to produce N_{ch} charged pions and $(1/3)kE$ is carried by $(1/2)N_{\text{ch}}$ neutral pions. Thus, after n interactions, the total energy carried by the hadronic component becomes

$$E_{\text{had}} = \left[(1 - k) + \frac{2}{3}k \right]^n E_0 = \left[1 - \frac{1}{3}k \right]^n E_0. \quad (3.2)$$

It corresponds to the energy of all the particles except the neutral pions π^0 .

In the following, the inelasticity k and the charged particle multiplicity N_{ch} are assumed to be the same for p -air and π^\pm -air collisions.

3.1.1 The charged pion component

In hadronic showers, muons come mainly from the decay of charged pions ($\simeq 90\%$) and charged kaons ($\simeq 10\%$). Thus the number of muons is approximately equal to N_{π^\pm} . Consequently, charged pions are a good tracker for studying the evolution of the muon component.

$$\pi^\pm \longrightarrow \mu^\pm + \nu_\mu (\sim 100\%)$$

$$K^\pm \longrightarrow \mu^\pm + \nu_\mu (\sim 63.5\%)$$

3.1.1.1 Physics governing the charged pion component

Charged pions have a mean free path for decay greater than the mean free path for interaction at high energies. Thus charged pions interact several times and then decay when their energy drops below a mean critical energy $\langle E_{\pi^\pm} \rangle_-$. The number of generations n depends on the primary energy, on the primary type, on the multiplicity and on inelasticity. At each interaction with the atmosphere, the charged pions create a new generation of pions with multiplicity N_{ch} .

The height of maximum of the muon production is considered to be the point where the mean free path for decay is equal to that for interaction with atmosphere.

Decay

The mean free path for decay, L_{D,π^\pm} , is given by

$$L_{D,\pi^\pm} = \beta_{\pi^\pm} \gamma_{\pi^\pm} c \tau_{\pi^\pm} = \sqrt{\gamma_{\pi^\pm}^2 - 1} c \tau_{\pi^\pm} \quad (3.3)$$

where τ_{π^\pm} is the pion lifetime at rest. For charged pions, $c\tau_{\pi^\pm}$ is equal to 7.8 m and $\gamma_{\pi^\pm} = E_{\pi^\pm}/m_{\pi^\pm}$. But, at the energies involved here, the ultra-relativistic approximation can be used. Thus L_{D,π^\pm} becomes

$$L_{D,\pi^\pm} [\text{m}] = 56 E_{\pi^\pm} [\text{GeV}]. \quad (3.4)$$

Interaction with the atmosphere

The collision described by the hadronic Heitler model is $\pi^\pm + \text{air} \rightarrow \sum \pi^\pm + \sum \pi^0$. The collision length $\lambda_{\pi^\pm-\text{air}}$ (in g/cm^2) is defined as

$$\lambda_{\pi^\pm-\text{air}} = \int_{h_i}^{h_f} \rho_{\text{air}}(h) \frac{dh}{\cos \theta}, \quad (3.5)$$

where $\rho_{\text{air}}(h) = \rho_0 e^{-h/8000 \text{ m}} = 1.2 \times 10^{-3} e^{-h/8000} \text{ m g cm}^{-3}$ is the atmospheric density as a function of the altitude h (following closely the US standard model) and θ the zenith angle. Then we integrate between $h_i = h$ and $h_f = h_i + L_{I,\pi^\pm} \cos \theta$, where L_{I,π^\pm} represents the mean free path for interaction, i.e. the mean length between two collisions with the atmosphere. Equation (3.5) becomes

$$\begin{aligned} \lambda_{\pi^\pm-\text{air}} &= \frac{\rho_0}{\cos \theta} 8000 \left[\exp\left(-\frac{h}{8000 \text{ m}}\right) - \exp\left(-\frac{h + L_{I,\pi^\pm} \cos \theta}{8000 \text{ m}}\right) \right] \\ &= \frac{\rho_0}{\cos \theta} 8000 \exp\left(-\frac{h}{8000 \text{ m}}\right) \left[1 - \exp\left(-\frac{L_{I,\pi^\pm} \cos \theta}{8000 \text{ m}}\right) \right] \\ &= \rho_{\text{air}}(h) \frac{8000}{\cos \theta} \left[1 - \exp\left(-\frac{L_{I,\pi^\pm} \cos \theta}{8000 \text{ m}}\right) \right]. \end{aligned} \quad (3.6)$$

Using the hypothesis that the distance between two collisions is negligible compared to 8000 m, Equation (3.6) becomes

$$L_{I,\pi^\pm} = \frac{\lambda_{\pi^\pm-\text{air}}}{\rho_{\text{air}}(h)} \quad (3.7)$$

A basic link is established between the mean free path for interaction L_{I,π^\pm} and the hadronic interaction length $\lambda_{\pi^\pm-\text{air}}$. Thus it will be very easy to use inelastic cross sections $\sigma_{\pi^\pm-\text{air}}$ from high energy hadronic models since there exists a relation linking the two physi-

cal quantities

$$\lambda_{\pi^\pm\text{-air}}[\text{g}/\text{cm}^2] = \frac{14.54[\text{g}/\text{mol}]}{\sigma_{\pi^\pm\text{-air}}[\text{cm}^2/\text{mol}]} = \frac{14.54}{\sigma_{\pi^\pm\text{-air}}[\text{mb}] \times 10^{-27} N_A}. \quad (3.8)$$

with N_A the Avogadro number.

In Figure 3.2, the cross section, the multiplicity and the inelasticity are shown for proton-air and π^\pm -air interactions for three hadronic models QGSJetII-03 [3], SIBYLL 2.1 [4] and EPOS 1.6 [2].

To describe the charged pion propagation process from initial production to decay, the total distance travelled in the atmosphere has to be determined. This quantity can be easily linked to the mean free paths $\lambda_{\text{p-air}}$ and $\lambda_{\pi^\pm\text{-air}}$. Thus, for a proton shower with a zenith angle θ and a primary energy E_0 , one obtains (in the approximation where the pion-air cross section is constant with energy)

$$\begin{aligned} \lambda_{\text{p-air}}(E_0) + (n-1) \times \lambda_{\pi^\pm\text{-air}}(E_{\pi^\pm}) &= \int_{h(\theta)}^{\infty} \rho_{\text{air}}(h) \frac{dh}{\cos \theta} \\ \lambda_{\text{p-air}}(E_0) + (n-1) \times \lambda_{\pi^\pm\text{-air}}(E_{\pi^\pm}) &\simeq \frac{10^3}{\cos \theta} \times \exp\left(-\frac{h}{8000 \text{ m}}\right) [\text{g}/\text{cm}^2]. \end{aligned} \quad (3.9)$$

3.1.1.2 Evolution of charged pion energy with altitude

The charged pion decay and their collision in the atmosphere are presently understood. Thus it is possible to predict when the length of Equation (3.4) is equal to that of Equation (3.7) and so evaluate the number of hadronic generations, the energy or the altitude of charged pions when they decay. From Equations (3.4)–(3.7), one can calculate the average charged pion energy when decay and interaction with the atmosphere occur with the same frequency

$$\langle E_{\pi^\pm}[\text{GeV}] \rangle_{=} = \frac{\lambda_{\pi^\pm\text{-air}}[\text{g}/\text{cm}^2]}{7} \exp\left(\frac{h_{=}}{8000 \text{ m}}\right). \quad (3.10)$$

The average charged pion energy $\langle E_{\pi^\pm} \rangle$ can be plotted as a function of the altitude h . In fact, this representation is a simple way to follow the evolution of the charged pion component in a hadronic shower. The case of a vertical proton shower at 10 EeV using QGSJetII-03 is shown in Figure 3.3. It can be noted that proton cross sections and multiplicities are used only for the first interaction (upper right). Afterwards, only hadronic data for the π^\pm -air interaction are used. The black line corresponding to $L_I = L_D$ is the boundary between the situation where charged pion decay is, *on average*, more probable (under the line) and the one where a collision with the atmosphere is, *on average*, expected (above the line). Here, it is shown that, *on average*, pions decay after a number of hadronic generations n between five and six with an energy $\langle E_{\pi^\pm}[\text{GeV}] \rangle_{=}$ around 50 GeV.

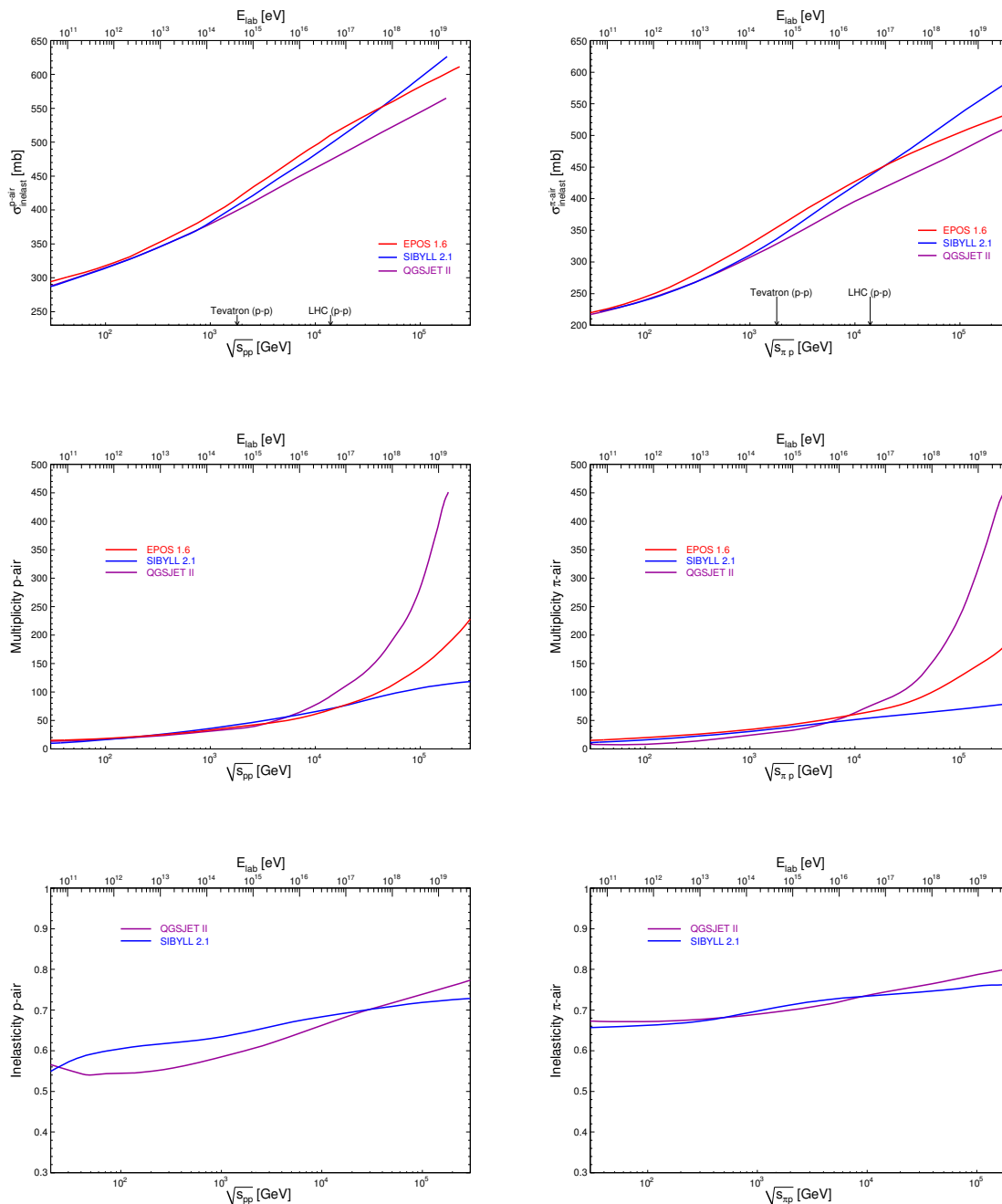


Figure 3.2: Evolution of the cross sections proton-air (*left panel*) and pion-air (*right panel*) with energy for different hadronic models. QGSJetII-03 [3], SIBYLL 2.1 [4] and EPOS 1.6 [2].

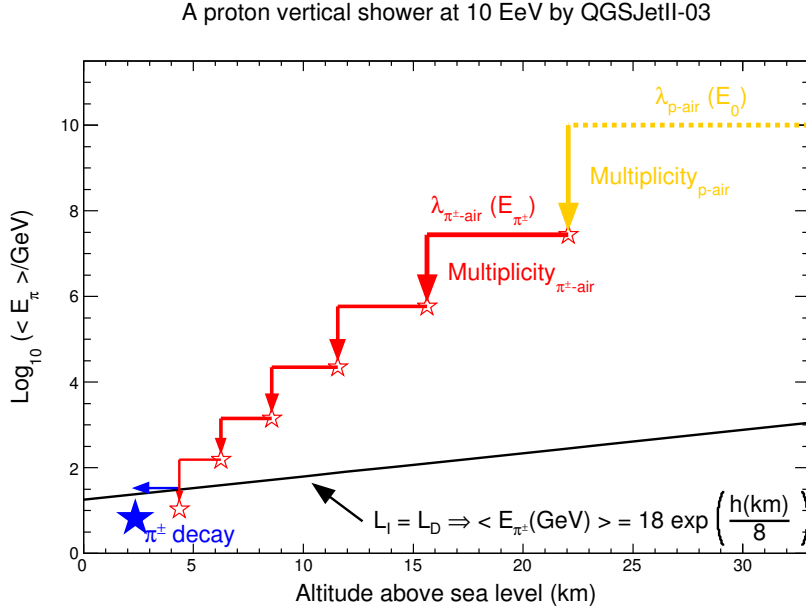


Figure 3.3: Evolution of the average charged pion energy as a function of altitude above sea level for a vertical proton shower at 10 EeV using QGSJetII-03. Each red star represents an interaction with the atmosphere. The blue star indicates the point of maximum muon production.

This number of interactions has been checked with the QGSJetII-03 predictions using the program CORSIKA [5]. Even if the mean value n_{\pm} found with this toy model is in agreement with the CORSIKA values, the CORSIKA program provides distributions that have a large spread. Based on a preliminary study, we conclude that the wide inelasticity distribution is the cause of these large fluctuations around the n_{\pm} value.

3.1.1.3 Determination of the pion energy and the pion number at $L_I = L_D$

The goal of this section is to obtain the energy $\langle E_{\pi^{\pm}} \rangle_{\pm}$ and the number of charged pions produced $\langle N_{\pi^{\pm}} \rangle_{\pm}$ at $L_I = L_D$, as a function of the primary energy E_0 and the inelasticity k (assumed constant with the energy here).

Number of charged pions produced $\langle N_{\pi^{\pm}} \rangle_{\pm}$

During the development of hadronic showers, the number of charged pions produced is just the product of the charged multiplicities at each interaction level. In this study, we express multiplicity as a function of energy (as in the QGSJetII-03 model)

$$N_{\text{ch}}(E) = \left(\frac{E}{\Delta} \right)^{\delta}, \quad (3.11)$$

where Δ is a normalisation constant and δ is the exponent representing the energy dependence.

Here we have a geometric series and the number of pions produced at $L_I = L_D$ is given by

$$\langle N_{\pi^\pm} \rangle = N_{\text{ch}}(E_0) \times N_{\text{ch}}(E_1) \times \dots \times N_{\text{ch}}(E_{n=}) = \left(\frac{E_0}{\Delta} \right)^{1-(1-\delta)^{n=}}. \quad (3.12)$$

Charged pion energy $\langle E_{\pi^\pm} \rangle =$

The mean energy of the charged pions can be calculated using Equations (3.2) and (3.12). Indeed, the energy is just the ratio of the total hadronic energy E_{had} to the number of charged pions produced $\langle N_{\pi^\pm} \rangle =$

$$\begin{aligned} \langle E_{\pi^\pm} \rangle &= \frac{E_{\text{had}}}{\langle N_{\pi^\pm} \rangle} \simeq \frac{E_{\pi^\pm}^{\text{tot}}}{\langle N_{\pi^\pm} \rangle} \simeq \left(1 - \frac{1}{3}k \right)^{n=} \frac{E_0}{\left(\frac{E_0}{\Delta} \right)^{1-(1-\delta)^{n=}}} \\ \langle E_{\pi^\pm} \rangle &= \Delta \left(1 - \frac{1}{3}k \right)^{n=} \left(\frac{E_0}{\Delta} \right)^{(1-\delta)^{n=}}. \end{aligned} \quad (3.13)$$

3.1.2 Muon production in hadronic showers

Muons are produced when the charged mesons decay. The kinematic problem studied here is just a two-body decay since we have $\pi^\pm \rightarrow \mu^\pm + \nu_\mu$ or $K^\pm \rightarrow \mu^\pm + \nu_\mu$ ⁴. In the centre of mass of the charged mesons π^\pm , the decay is isotropic because they have spin zero. Thus, a uniform distribution is used for the cosine of the emission angle in the centre of mass. The decay can be represented in the centre of mass and in the laboratory frame as shown in Figure 3.4.

From conservation of energy, we easily find the muon energy and the muon momentum in the centre of mass

$$\begin{aligned} E_\mu^{\text{cm}} &= \frac{m_{\pi/K}^2 + m_\mu^2}{2m_{\pi/K}} \simeq \begin{cases} 110 \text{ MeV} & \text{for } \pi \text{ meson,} \\ 258 \text{ MeV} & \text{for K meson;} \end{cases} \\ p_\mu^{\text{cm}} &= \frac{m_{\pi/K}^2 - m_\mu^2}{2m_{\pi/K}} \simeq \begin{cases} 30 \text{ MeV/c} & \text{for } \pi \text{ meson,} \\ 235 \text{ MeV/c} & \text{for K meson.} \end{cases} \end{aligned} \quad (3.14)$$

The corresponding values in the laboratory frame are obtained after applying the Lorentz

⁴However, for the kaon case, it can be noticed that this channel has a branching ratio of only 64%. Then, 21% of charged kaons decay via $K^\pm \rightarrow \pi^\pm + \pi_0$.

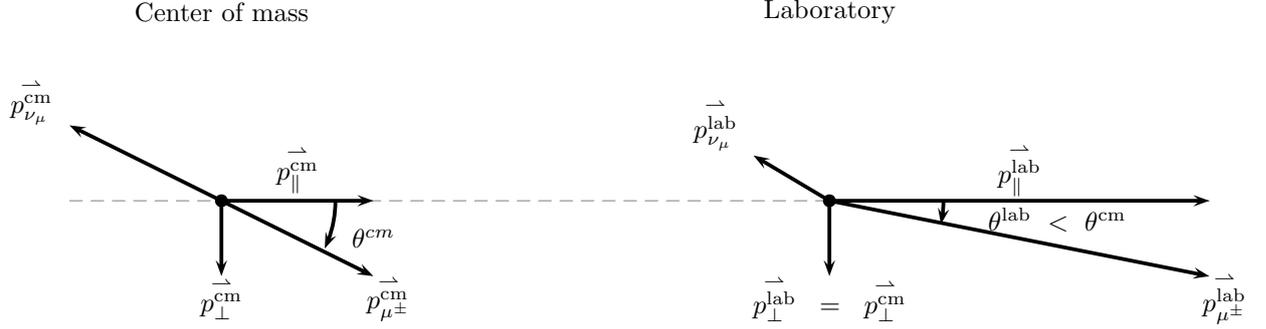


Figure 3.4: Kinematics for pion decay $\pi^\pm \rightarrow \mu^\pm + \nu_\mu$ and kaon decay $K^\pm \rightarrow \mu^\pm + \nu_\mu$.

boost $\beta = v/c$

$$E_\mu^{\text{lab}} = \gamma(E_\mu^{\text{cm}} + \beta p_\mu^{\text{cm}} \cos \theta^{\text{cm}}) \simeq p_{\mu,\parallel}^{\text{lab}} c \simeq \begin{cases} E_\pi \frac{110+30 \cos \theta^{\text{cm}}}{139} & \text{for } \pi \text{ meson,} \\ E_K \frac{258+235 \cos \theta^{\text{cm}}}{493} & \text{for K meson;} \end{cases} \quad (3.15)$$

$$p_{\mu,\perp}^{\text{lab}} = p_{\mu,\perp}^{\text{cm}} = p_\mu^{\text{cm}} \sin \theta^{\text{cm}} = \begin{cases} 30 \sin \theta^{\text{cm}} & \text{for } \pi \text{ meson,} \\ 235 \sin \theta^{\text{cm}} & \text{for K meson.} \end{cases}$$

where $\beta \simeq 1$ and $\gamma = 1/\sqrt{1-\beta^2} = E/m$ in the ultra-relativistic case. The muon energy E_μ^{lab} is equal to its longitudinal momentum $p_{\mu,\parallel}^{\text{lab}}$ in the laboratory system. Moreover, with a Lorentz transformation, the transversal momenta in the centre of mass and in the laboratory are equal.

The maximum and minimum values for the muon energy are given by $\cos \theta^{\text{cm}} = \pm 1$. Thus, one obtains

$$\begin{cases} 0.57 \leq E_\mu^{\text{lab}}/E_\pi \leq 1.00 \iff \langle E_\mu^{\text{lab}} \rangle = 0.79 E_\pi, \\ 0.04 \leq E_\mu^{\text{lab}}/E_K \leq 1.00 \iff \langle E_\mu^{\text{lab}} \rangle = 0.52 E_K. \end{cases} \quad (3.16)$$

Using the fact that $\cos \theta^{\text{cm}}$ has a uniform distribution, one can conclude that the average muon energy is around $0.79 E_\pi$ in pion decay and $0.52 E_K$ in kaon decay. Figure 3.5 shows the distribution of the muon energy for pion and kaon decay. Hence, following a pion (kaon) decay, the muons carry around three quarter (one half) of the pion (kaon) energy. Since

$$E_\mu^{\text{lab}} \simeq p_{\mu,\parallel}^{\text{lab}} c \quad \text{and} \quad p_{\mu,\perp}^{\text{lab}}/p_{\mu,\parallel}^{\text{lab}} \ll 1,$$

this rule also applies to the momenta, i.e.

$$p_\mu^{\text{lab}} \simeq \frac{3}{4} \times p_{\pi^\pm}^{\text{lab}} \quad \text{and} \quad p_\mu^{\text{lab}} \simeq \frac{1}{2} \times p_{K^\pm}^{\text{lab}}.$$

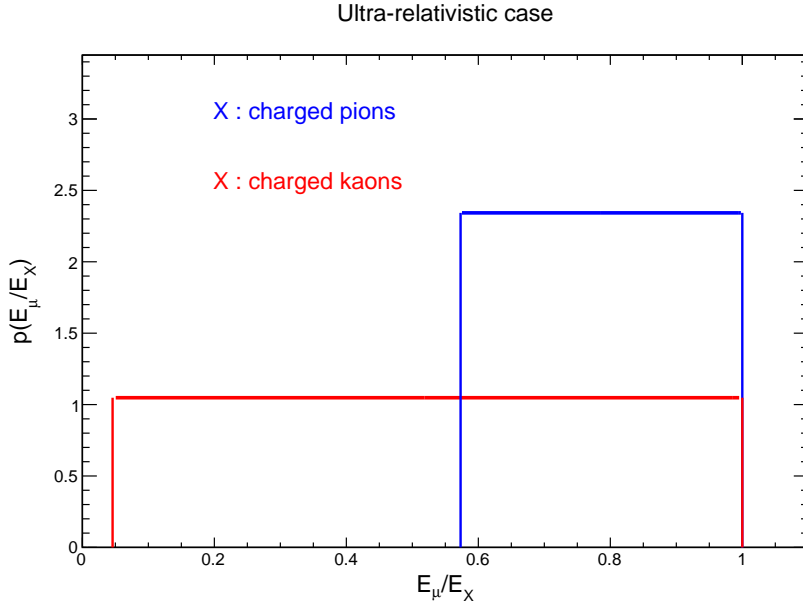


Figure 3.5: **Distribution of the ratio of the muon energy to the total initial energy, for pion and kaon decay.** The curves correspond to the probability density function for the two ratios E_μ/E_π and E_μ/E_K .

3.1.2.1 Description of the muon component at birth

Muons have a mean free path for interaction much larger than for decay. Thus, it is usually assumed that muons do not interact with the atmosphere during shower development. Using the properties of the pion component we can predict those of the muons. In Section 3.1.1, the altitude $\langle h_\pm \rangle$ where $L_I = L_D$ and the corresponding energy $\langle E_{\pi^\pm} \rangle_\pm$ were obtained. From them we can calculate various quantities pertaining to the muons.

1. **The altitude of maximum muon production $\langle h_\mu \rangle$.** Once the charged pion component has crossed the line $L_I = L_D$, pions can on average travel only a distance equal to L_{D,π^\pm} . Thus one can conclude that

$$\langle h_\mu \rangle = \langle h_\pm \rangle - L_{D,\pi^\pm}.$$

2. **The average muon energy at birth $\langle E_{\mu,\text{birth}} \rangle$.** Our model gives the charged pion energy $\langle E_{\pi^\pm} \rangle_\pm$. We have just shown that, on average, 79% of the pion energy goes to muons

$$\langle E_{\mu,\text{birth}} \rangle = 0.79 \langle E_{\pi^\pm} \rangle_\pm.$$

3. **The average number of muons produced $\langle N_{\mu,\text{birth}} \rangle$.** Each muon is produced via charged meson decay. Thus, the muon number is given by the number of charged

pions produced in an extensive air shower

$$\langle N_{\mu,\text{birth}} \rangle = \langle N_{\pi^\pm} \rangle = \frac{E_{\text{had}}}{\langle E_{\pi^\pm} \rangle} = \left(1 - \frac{1}{3}k\right)^{n=} \frac{E_0}{\langle E_{\pi^\pm} \rangle}.$$

Unlike the electrons, muons are relatively unaffected by multiple Coulomb scattering, and so their lateral distribution function (LDF) contains information about the parent pion trajectories. We consider a shower of zenith angle θ . At ground level, we will determine the muon density in the plane perpendicular to the shower axis, the so-called *transverse plane*. We assume that the muon's trajectory will be determined by the $p_{\mu,\perp}$ inherited from its parent pion (kaon), causing it to arrive at a distance r from the shower axis in the transverse plane. Thus multiple scattering for muons is neglected. In this case r is simply given by

$$r = h_\mu \frac{p_{\pi,\perp}}{p_{\pi,\parallel}} = h_\mu \frac{p_{\pi,\perp}}{\sqrt{E_\pi^2 - p_{\pi,\perp}^2 - m_\pi^2}}, \quad (3.17)$$

where h_μ is the height of muon production. The virtue of this model is that it shows easily the dependence of the distance r on the pion energy E_π and its transverse momentum $p_{\pi,\perp}$. The muonic density, $\rho_\mu(r)$, is given by

$$\rho_\mu(r) = \frac{1}{2\pi r} \frac{dN}{dr} = \frac{1}{2\pi r} \frac{dE_\pi}{dr} \frac{dN}{dE_\pi}. \quad (3.18)$$

Then, the deflections due to the Earth's magnetic field should be also considered.

A key parameter in the previous formulas is the transverse momentum of the charged pions $p_{\pi,\perp}$. Associated with $p_{\pi,\parallel}$, it defines the emission angle of the muons since this latter is usually assumed collinear to their initial direction. Figure 3.6 gives the distribution of the transverse momentum of charged pions produced in a proton–air interactions at 10 EeV. Transverse momenta in hadronic collisions are usually described by

$$\frac{dN}{d\vec{p}_T} = \frac{1}{2\pi p_T} \frac{dN}{dp_T} \propto \exp\left(-\frac{p_T}{p_{T,0}}\right), \quad (3.19)$$

where $p_{T,0}$ is a constant characteristic of the hadronic model.

3.1.2.2 Evolution of the muon component with respect to zenith angle

The zenith angle affects the three physical quantities enumerated previously. In Figure 3.7 the average charged pion energy is shown for two showers with different zenith angles θ_1 and θ_2 .

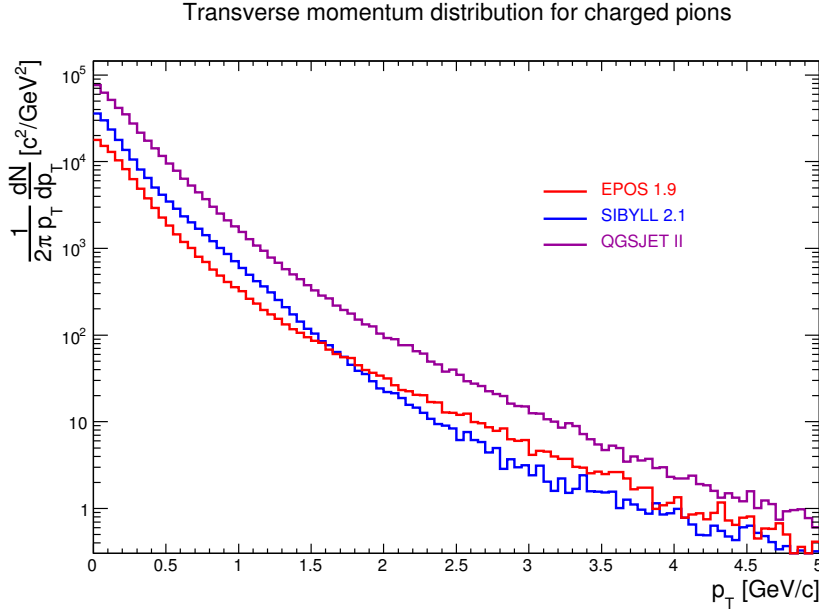


Figure 3.6: **Distribution of the transverse momenta of charged pions produced in a proton–air collision at 10 EeV.** The distributions for the three main hadronic models are plotted. The curves are obtained using the CONEX simulation program.

Altitude of maximum muon production

Combining the result shown in Figure 3.7 where the two showers are different uniquely by their zenith angle with the relations from Equation (3.9), one can write

$$\lambda_{p\text{-air}}(E_0) + (n - 1) \times \lambda_{\pi^\pm\text{-air}}(\langle E_{\pi^\pm} \rangle(\theta_1)) = \lambda_{p\text{-air}}(E_0) + (n - 1) \times \lambda_{\pi^\pm\text{-air}}(\langle E_{\pi^\pm} \rangle(\theta_2))$$

$$\frac{\lambda_{\pi^\pm\text{-air}}(\langle E_{\pi^\pm} \rangle(\theta_1))}{\lambda_{\pi^\pm\text{-air}}(\langle E_{\pi^\pm} \rangle(\theta_2))} = \frac{\cos \theta_1}{\cos \theta_2} \times \exp\left(-\frac{h(\theta_1) - h(\theta_2)}{8000 \text{ m}}\right) = 1$$

$$h(\theta_2) - h(\theta_1)[\text{m}] = 8000 \times \ln\left(\frac{\cos \theta_1}{\cos \theta_2}\right)$$

$$h(\theta)[\text{m}] \propto -8000 \times \ln(\cos \theta).$$

(3.20)

This last relation shows that the altitude of charged pion decay, as is the case for the altitude of maximum muon production, increases with zenith angle. This is illustrated in Figure 3.8 where predictions from this toy model are compared with results provided by the Monte Carlo programs CORSIKA and CONEX [6]-[7]. It can be concluded that with our intuitive approach we obtain values in agreement with the usual Monte Carlo simulations.

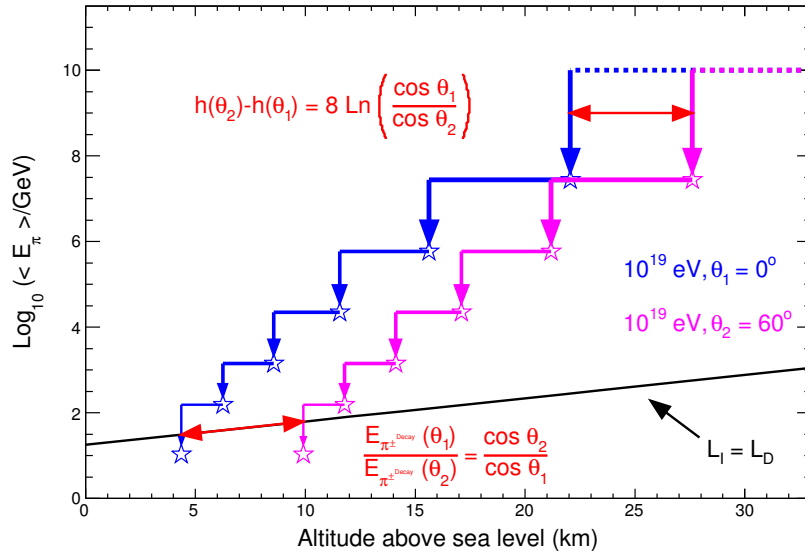


Figure 3.7: Evolution of the average charged pion energy as a function of the altitude above sea level for proton showers at 10 EeV with QGSJetII-03. The development of the charged pion component is shown for two zenith angles: $\theta = 0^\circ$ and $\theta = 60^\circ$.

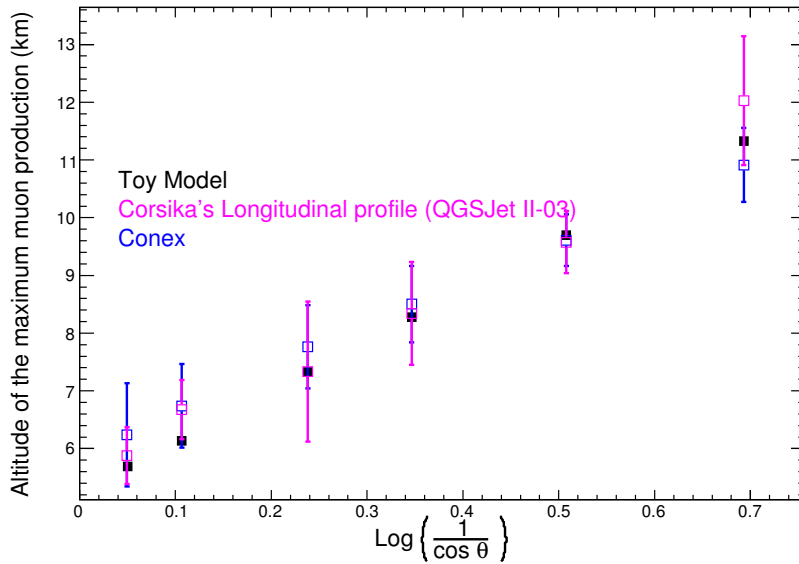


Figure 3.8: Evolution of the altitude for maximum muon production for a proton shower at 10 EeV for different zenith angles. Results are shown for our model, from CORSIKA with five showers per bin and from CONEX [6]-[7] with one hundred showers per bin. The hadronic models used are FLUKA at low energy and QGSJetII-03 at high energy.

Muon energy and number of muons produced

The altitudes corresponding to two zenith angles θ_1 and θ_2 can be supplied to Equation (3.10).

The ratio of the values obtained is

$$\begin{aligned} \frac{\langle E_{\pi^\pm} \rangle(\theta_1)_=}{\langle E_{\pi^\pm} \rangle(\theta_2)_=} &= \exp\left(\frac{h(\theta_1) - h(\theta_2)}{8000 \text{ m}}\right) \\ \frac{\langle E_{\pi^\pm} \rangle(\theta_1)_=}{\langle E_{\pi^\pm} \rangle(\theta_2)_=} &= \exp\left[-\ln\left(\frac{\cos \theta_1}{\cos \theta_2}\right)\right] = \frac{\cos \theta_2}{\cos \theta_1} \\ \langle E_{\pi^\pm} \rangle(\theta)_= &\propto \frac{1}{\cos \theta}. \end{aligned} \quad (3.21)$$

But it has been shown in Equation (3.16) that the distribution of muon energies for charged pion decay is uniform between $0.57 E_{\pi^\pm}$ and $1.00 E_{\pi^\pm}$. Thus, on the average, muon energies also have the same behaviour with respect to zenith angle θ : $\langle E_{\mu,\text{birth}} \rangle \propto 1/\cos \theta$.

Since the number of muons produced is just the ratio between primary energy and $\langle E_{\pi^\pm} \rangle$, $\langle N_{\mu,\text{birth}} \rangle$ behaves as

$$\langle N_{\mu,\text{birth}} \rangle(\theta) \propto \cos \theta. \quad (3.22)$$

From this toy model a trend emerges for the evolution of the number of muons produced with zenith angle. In Figure 3.3, lines representing inclined showers would cross the black line at a pion energy higher than that for the vertical shower. Consequently, the number of muons produced decreases with zenith angle.

3.1.2.3 Dependence of the muon component on hadronic models

The last interaction of charged pions with the atmosphere occurs at an energy around a few hundred GeV, i.e. in a domain treated by high energy hadronic models. The main hadronic models are QGSJetII-03, SIBYLL 2.1 and EPOS 1.6. Among the critical hadronic parameters, one can cite the cross section, the multiplicity and the inelasticity. In Figure 3.2 we have given the muon predictions using the three models. Discrepancies between models come mainly from the treatment of QCD in the low transverse momentum area. Currently, different theories are proposed and the data are not sufficient to choose between them. Figure 3.9 gives the location of maximum muon production using these three hadronic models.

3.1.3 Muon propagation from birth to ground

The muon energy spectrum is modified between the altitude where muons are produced and the altitude where muons are detected at ground. The lifetime of muons ($2.2 \mu\text{s}$) and their mean energies are such that muon decay has to be taken into account during their propagation in the atmosphere (the losses by bremsstrahlung are negligible for muons with energies

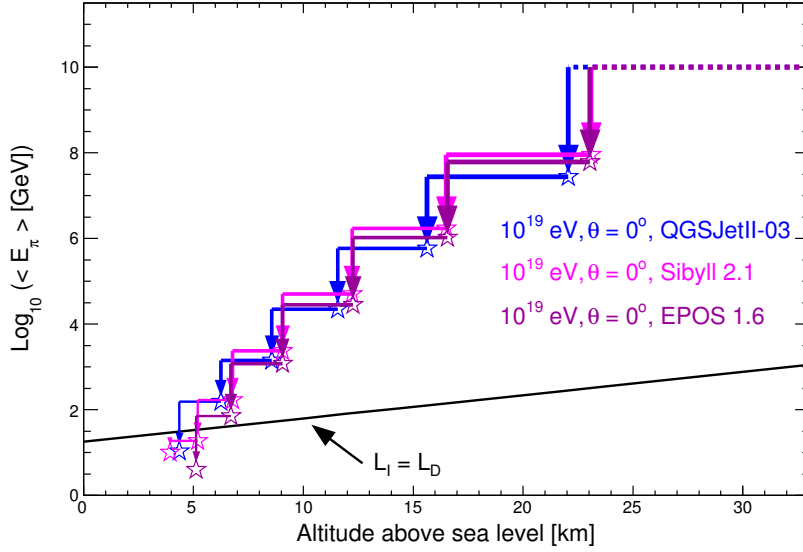


Figure 3.9: Evolution of the average charged pion energy as a function of the altitude above sea level for a vertical proton shower at 10 EeV for three hadronic models. The charged pion component is calculated using QGSJetII-03, SIBYLL 2.1 and EPOS 1.6.

lower than 1 TeV). Showers with a zenith angle θ produce the majority of their muons at an altitude $H(z_0, \cos \theta) = h_{\text{Auger}} + z_0 \cos \theta$ (see Figure 3.10). The purpose of this section is to see how the spectrum changes during muon propagation and to examine its dependence on the zenith angle θ and the distance travelled z_0 .

The mean free path for decay, written $L_{D,\mu}$, is given by

$$L_{D,\mu} = \beta_\mu \gamma_\mu c \tau_\mu = \sqrt{\gamma_\mu^2 - 1} c \tau_\mu \quad (3.23)$$

where τ_μ is the muon lifetime at rest. For muons, $c \tau_\mu$ is equal to 658 meters and $\gamma_\mu = E_\mu / m_\mu$. Thus $L_{D,\mu}$ can be written as a function of the muon kinetic energy in the laboratory frame T_μ

$$L_{D,\mu}[\text{m}] = 658 \sqrt{\left(\frac{T_\mu}{m_\mu c^2} + 1\right)^2 - 1}. \quad (3.24)$$

Along the z -axis of Figure 3.10, the number of muons after an infinitesimal length dz is $N(z + dz) = N(z) + N(z) \times dz / L_{D,\mu}$, i.e. $dN/dz = N / L_{D,\mu}$. Thus the probability $P_{D,\mu}$ that a muon produced at an altitude $H(z_0, \cos \theta)$ is still present after a length $(z_0 - z)$ is

$$P_{D,\mu} = \frac{1}{L_{D,\mu}} e^{-(z_0 - z) / L_{D,\mu}}. \quad (3.25)$$

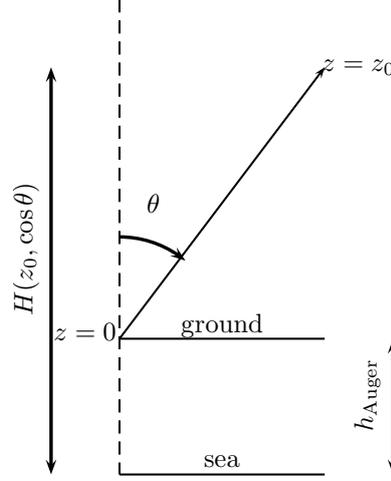


Figure 3.10: **Representation of the shower geometry.** The zenith angle is the angle between the vertical and the z -axis. The altitude $H(z_0, \cos \theta)$ reference is the sea level.

Up to now, it has been supposed that the muon energy is constant along its path. But particles lose energy during their passage through matter. The muon kinetic energy range is between a few MeV and several hundreds of GeV for a typical hadronic shower detected by the Pierre Auger Observatory. At these energies, the main cause of energy loss is ionization (radiative processes are negligible). The energy loss rate $\langle dT_\mu/dz \rangle$ is nearly constant for relativistic particles and it depends somewhat on the medium. Compared to the critical energy $T_{\mu,c}$, the energy range we need to consider is lower ($T_{\mu,c} \simeq 1000$ GeV). Thus the average rate of muon energy loss in the atmosphere is

$$\left\langle -\frac{dT_\mu}{dz} \right\rangle = a \simeq 2 \text{ MeV g}^{-1} \text{ cm}^2 \simeq 0.24 \exp\left(-\frac{H(z, \cos \theta)[\text{m}]}{8000}\right) \text{ MeV m}^{-1} \quad (3.26)$$

when using $\rho_{\text{air}}(H) = 1.2 \times 10^{-3} e^{-H/8000} \text{ m g cm}^{-3}$ as the atmospheric density (close to that of the US standard model).

Ionization losses can now be taken into account in the decay Equation (3.24): the kinetic energy has to be replaced by $T_\mu(z) = T_\mu(z_0) - a(z_0 - z)$ where $(z_0 - z)$ corresponds to the distance travelled and $T_\mu(z_0)$ the muon energy at birth. The muon kinetic energy is given by

$$\begin{aligned} T_\mu(z) &= T_\mu(z_0) - \int_{z_0}^z 0.24 \exp\left(-\frac{H(z, \cos \theta)}{8000}\right) dz \\ T_\mu(z) &= T_\mu(z_0) - \frac{1920}{\cos \theta} \exp\left(-\frac{h_{\text{Auger}}}{8000}\right) \left[\exp\left(-\frac{z \cos \theta}{8000}\right) - \exp\left(-\frac{z_0 \cos \theta}{8000}\right) \right], \end{aligned} \quad (3.27)$$

where the lengths are in meters and the energies in MeV.

Before studying the muon propagation in the atmosphere, it is necessary to have a muon

energy spectrum at birth. Usually, the pion energy spectrum, i.e. the energy spectrum of the mother particles, is expressed as a power law with an index equal to -2 . In Section 3.1.2, it has been demonstrated that muons produced by pion decay have their total energies uniformly distributed between $0.57 E_\pi$ and E_π . Thus the distribution law for muon energy at birth is

$$N(E_\mu) \propto \int_{E_\mu}^{E_\mu} \frac{dE_\pi}{E_\pi^2} = - \left[\frac{1}{1.75E_\mu} - \frac{1}{E_\mu} \right] \propto \frac{1}{E_\mu} \Rightarrow \frac{dN(E_\mu)}{dE_\mu} \propto \frac{1}{E_\mu^2} \quad (3.28)$$

This result obtained for total energy E_μ is of course the same for kinetic energy T_μ , since $E_\mu \simeq T_\mu$.

In the following, these different formulae will be applied to this spectrum to describe muon propagation in the atmosphere down to the ground. Two methods are used: the first involves a toy Monte Carlo (toy MC) and the second analytical formulae.

3.1.3.1 Muon energy spectrum at ground using a toy Monte Carlo

An efficient way to check the validity of our formulae is to make a toy Monte Carlo. The principle is simple and given in Figure 3.11: we choose randomly a muon energy at birth according to the inverse of the energy squared then a loop *while* is executed to simulate ionization losses and decay in the atmosphere during propagation. At each step, it is determined if the muon decays or not. In the second case, the loop is finished and the final spectrum is not incremented. If at ground ($z = 0$) the loop *while* is still in execution, the final muon energy spectrum is incremented by one at the corresponding kinetic energy bin $T_\mu(z = 0)$.

In Figure 3.12 is given the histogram output from the toy MC for vertical muons distributed according to the inverse of their energy squared and produced at an altitude of 5000 meters. One sees that decay concerns mainly muons with low kinetic energy. This result was expected by considering Equation (3.25): when the muon energy decreases, the mean free path for decay $L_{D,\mu}$ also decreases and therefore the probability of decay is greater. Of course this effect is amplified when ionization losses are taken into account because they decrease the original muon energy. In the case of this shower, it is around 635 MeV which is lost only taking into account the ionization losses. Moreover, even if the effect is not clearly visible on this plot because of the *log-scale*, there is a shift in energy between the red and blue curves since ionization losses imply a decrease of energy from $T_\mu(z_0)$ to $T_\mu(z = 0)$. This explains the fact that the red and blue curves intersect at low energy in the plot.

Figure 3.13 gives the energy spectrum at ground with and without the ionization losses, for two different shower geometries. A shower having its altitude of maximum for muon production higher has a higher mean energy for muons at ground level. This conclusion was expected by the toy model presented in Section 3.1.2. It comes from the fact that muons have

Algorithm Toy Monte Carlo

1. **for** $i \leftarrow 1$ **to** n
2. **do** $T_\mu(z_0) \leftarrow \{\text{muon energy spectrum at birth}\}$
3. **while** $z \geq 0$
4. **do** $T_\mu(z) \rightarrow T_\mu(z - d, z_0)$, with d the step in distance
5. $L_{D,\mu}(z - d, z_0)$
6. **if** $\frac{d}{L_{D,\mu}(z-d, z_0)} \geq \text{RND}$, with RND a float from a uniform distribution $]0, 1]$
7. **then** break the while loop : the muon decays $\rightarrow \text{Decay} = +1$
8. **else** next iteration in the while loop
9. **if** $\text{Decay} \neq +1$
10. **then** add one event at the kinetic energy $T_\mu(z = 0)$ in the histogram
11. **return** final muon energy spectrum

Figure 3.11: **Toy Monte Carlo runs for n muons.** For each muon i , the loop *while* is executed to determine if the muon i will decay during its propagation down to the ground. The final spectrum is given in a histogram.

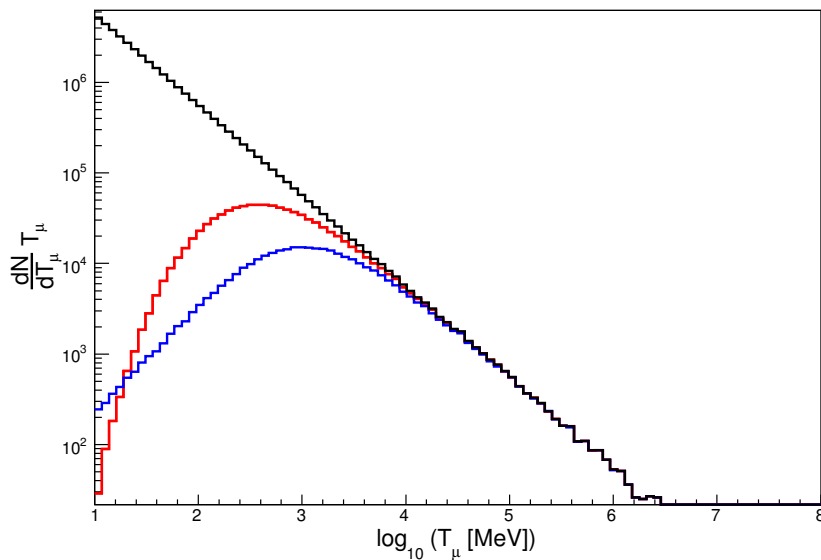


Figure 3.12: **Results from the toy Monte Carlo for $H(z_0, \cos \theta = 1) = 5000$ meters.** The original muon spectrum, i.e. the energy distribution at muon birth, following an inverse square law, is given in black. The red curve illustrates the case where only decay is taken into account whereas the blue curve also includes ionization losses.

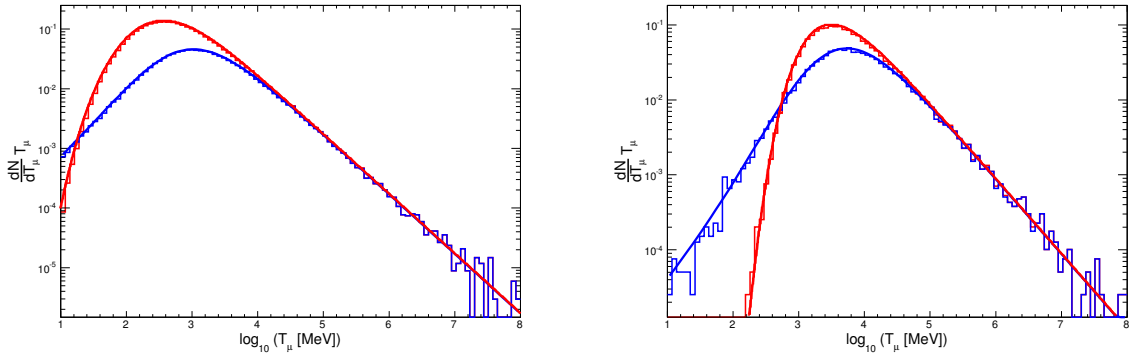


Figure 3.13: **Muon energy distribution from a power spectrum with index -2 at ground.** *Left panel:* $H(z_0, \cos \theta = 1) = 5000$ m. *Right panel:* $H(z_0, \cos \theta = 0.5) = 12000$ m. For the red curves only decay is taken into account while the blue curves include ionization losses. The solid lines correspond to the analytical formula and the histograms represent the toy Monte Carlo calculations.

to travel longer distances in the case $\theta = 60^\circ$. Even though it cannot be seen in this figure since we plot the probability density functions, more muons decay when the zenith angle increases.

3.1.3.2 Muon energy spectrum at ground using an analytical solution

A much more convenient way to represent the energy spectrum is to obtain an analytical formula. The analysis presented here is done without approximations, in the relativistic case. For an infinitesimal length dz , we have $dN/dz = N/L_{D,\mu}$ where $L_{D,\mu}$ is given by Equation (3.24). As a consequence, when ionization losses are taken into account, the probability decay $P_{D,\mu}$ cannot be obtained directly. In what follows, the units for physical quantities are *meters* for lengths and *MeV* for energies.

The goal is to integrate the following relation

$$\frac{dN}{N} = \frac{dz}{658 \sqrt{\left(\frac{T_\mu(z_0)}{m_\mu c^2} + 1\right)^2 - 1}} = \frac{1}{658} \frac{dz}{\sqrt{(A + Be^{-z/C})^2 - 1}} \quad (3.29)$$

with

$$\begin{aligned} A &= \frac{T_\mu(z_0) + m_\mu c^2}{m_\mu c^2} + \frac{1920}{\cos \theta} \frac{1}{m_\mu c^2} \exp\left(-\frac{H(z_0, \cos \theta)}{8000}\right), \\ B &= -\frac{1920}{\cos \theta} \frac{1}{m_\mu c^2} \exp\left(-\frac{h_{\text{Auger}}}{8000}\right), \\ C &= \frac{8000}{\cos \theta}. \end{aligned}$$

Setting $\cosh u = A + Be^{-z/C}$ ($u \geq 0$), Equation (3.29) becomes

$$\begin{aligned} \frac{dN}{N} &= \frac{1}{658} \frac{\frac{\sinh u}{(A/C) - (\cosh u/u)} du}{\sqrt{\cosh^2 u - 1}} = \frac{C}{658} \frac{du}{A - \cosh u} \\ &= \frac{C}{658} \frac{du}{A - (e^u + e^{-u})/2} = -\frac{2C}{658} \frac{e^u du}{(e^u)^2 - 2Ae^u + 1}. \end{aligned} \quad (3.30)$$

After operating a second variable change, $X = e^u$, Equation (3.30) simplifies to

$$\frac{dN}{N} = -\frac{2C}{658} \frac{dX}{P(X)} = -\frac{2C}{658} \frac{1}{X_1 - X_2} \left(\frac{dX}{X - X_1} - \frac{dX}{X - X_2} \right) \quad (3.31)$$

where $P(X) = X^2 - 2AX + 1$ is a polynomial which admits two different roots, X_1 and X_2 , equal to

$$\{X_1 \simeq 0; X_2 \simeq 2A\}$$

in the case $A \gg 1$.

Let's integrate Equation (3.31) between $X(z_0)$ and $X(z)$ where, because of the two variable changes, $X(z) = \exp\left[\cosh^{-1}(A + Be^{-z/C})\right]$

$$\begin{aligned} [\ln N]_{z_0}^z &= \frac{C}{658A} \left[\ln \left(\frac{X}{X - 2A} \right) \right]_{X(z_0)}^{X(z)} \\ \ln \left(\frac{N(z)}{N(z_0)} \right) &= \frac{C}{658A} \ln \left(\frac{X(z)}{X(z) - 2A} \frac{X(z_0) - 2A}{X(z_0)} \right) \\ N(z) &= N(z_0) \left(\frac{X(z)}{X(z) - 2A} \frac{X(z_0) - 2A}{X(z_0)} \right)^{C/(658A)} \end{aligned} \quad (3.32)$$

In the case of the Pierre Auger experiment, muons are detected at ground: the number of muons measured is $N(z = 0)$. The integration limits are

$$\begin{aligned} X(0) &= e^s = \exp\left(\cosh^{-1}(A + Be^0)\right) = \gamma_\mu(0) + \sqrt{\gamma_\mu(0)^2 - 1}, \\ X(z_0) &= e^t = \exp\left(\cosh^{-1}(A + Be^{-z_0/C})\right) = \gamma_\mu(z_0) + \sqrt{\gamma_\mu(z_0)^2 - 1} \end{aligned}$$

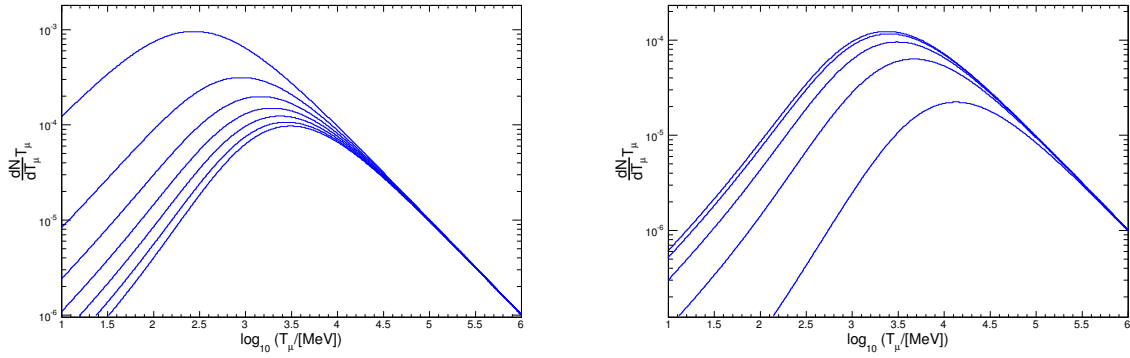


Figure 3.14: **Ground level muon energy distribution from a power spectrum with index -2 .** *Left panel:* From left to right, $H(z_0, \cos \theta = 1) = 2$ km, 4 km, 6 km, 8 km, 10 km, 12 km and 14 km. *Right panel:* $H(z_0, \cos \theta) = 10$ km, and from left to right $\theta = 0^\circ, 20^\circ, 40^\circ, 60^\circ$ and 80° .

since

$$\cosh^{-1} y = \ln(y \pm \sqrt{y^2 - 1}).$$

By integrating using these limits, Equation (3.32) can be written

$$\begin{aligned} N(z=0) &= N(z_0) \left(\frac{e^s}{e^s - 2A} \frac{e^t - 2A}{e^s} \right)^{C/(658A)} \\ N(z=0) &= N(z_0) \left(\frac{1 - 2Ae^{-t}}{1 - 2Ae^{-s}} \right)^{C/(658A)}. \end{aligned} \quad (3.33)$$

Finally, the number of muons at ground $N(z=0)$ is given by

$$N_{\text{ground}} = N(z=0) = N(z_0) \left(\frac{1 - \frac{2A}{\gamma_\mu(z_0) + \sqrt{\gamma_\mu(z_0)^2 - 1}}}{1 - \frac{2A}{\gamma_\mu(0) + \sqrt{\gamma_\mu(0)^2 - 1}}} \right)^{\frac{8000}{658A(z_0, \cos \theta) \cos \theta}} \quad (3.34)$$

with

$$A(z_0, \cos \theta) = \frac{T_\mu(z_0) + m_\mu c^2}{m_\mu c^2} + \frac{1920}{\cos \theta} \frac{1}{m_\mu c^2} \exp\left(-\frac{H(z_0, \cos \theta)}{8000}\right).$$

Using this analytical solution, it is presently easy to predict how the muon energy spectrum observed at ground changes with the altitude $H(z_0, \cos \theta)$. Figure 3.14 gives the muon energy spectra obtained for various values of z_0 (left panel) and zenith angle θ (right panel).

3.2 Muon counting using the surface detectors

Counting muons in the FADC traces is a notoriously difficult problem. Indeed, in showers with zenith angle $\theta < 60^\circ$, the electromagnetic “contamination” is non-negligible, so the main difficulty is to decouple the muonic and electromagnetic components. There are two distinct approaches that tackle the problem based on the average signal characteristics of the muonic and the electromagnetic components. Both approaches use the observation that, in general, muonic signals are characterized by distinct peaks or jumps, whereas the electromagnetic component constitutes a smooth “background” signal for the muonic peaks. The first approach is based on *counting* high peaks or jumps [8, 9], whereas the second approach attempts to *remove* jumps using a smoothing approach [10], and infer the muonic signal by the difference between the total signal and the smoothed signal. Of course, both approaches are intrinsically limited by electromagnetic peaks caused by high-energy photons, and small amplitude peaks from low-tracklength or low-energy muons.

This section briefly presents the two methods developed by the Auger-LAL group during recent years: the *jump method* [8, 9] and the *Artificial Neural Network (ANN) method* [11].

3.2.1 The jump method

The main idea was to evaluate the sum of the jumps above a threshold, where jumps are defined as the difference of two consecutive FADC values. The jump method correlates the sum of the thresholded discrete derivatives (*jumps*)

$$J_\delta = \sum_{\text{FADC bin } i} \underbrace{(x_{i+1} - x_i)}_{\text{jump}} \|x_{i+1} - x_i > \delta\|^5$$

to the number of muons N_μ in the FADC trace (Figure 3.15(a)). The threshold δ was set to 0.5 VEM, the best compromise between muon selection efficiency and electromagnetic contamination [8, 9].

The main problem with J_δ is, in fact, not overall bias or variance but its dependence on various shower parameters (mainly distance from the core r , energy of the shower E , or the zenith angle θ) that may generate energy – and zenith angle – trends in the bias. To decrease

⁵The indicator function $\|A\|$ is 1 if its argument A is true and 0 otherwise, and x_i is the FADC signal measured in the i th bin in VEMpeak units.

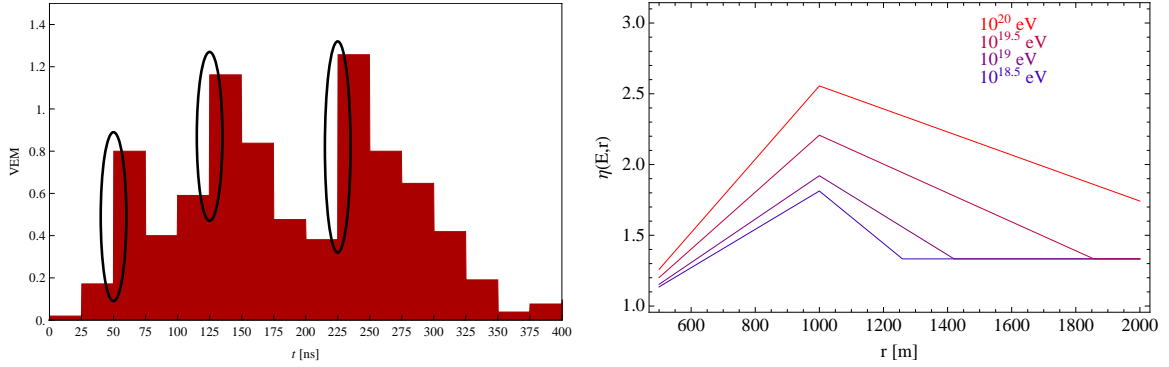


Figure 3.15: **The Jump method.** (a) Jumps with $\delta = 0.5$ VEM. The FADC trace of three vertical through going muons arriving at 45, 120, and 225 ns. (b) The $\eta(E, r)$ factor, used in the Jump method [9].

the bias and its variability, Garrido *et al.* introduced a correction factor [9]

$$\eta(E, r) = \begin{cases} 1 + (\eta_{\max}(E) - 1) \frac{r - 400 \text{ m}}{600 \text{ m}} & \text{if } 400 \text{ m} \leq r < 1000 \text{ m}, \\ \eta_{\max}(E) - (\eta_{\max}(E) - 4/3) \frac{r - 1000 \text{ m}}{r_{\text{trigger}}(E) - 1000 \text{ m}} & \text{if } r < r_{\text{trigger}}(E), \\ 4/3 & \text{otherwise,} \end{cases} \quad (3.35)$$

where the maximum correction factor is

$$\eta_{\max}(E) = 1.76 + 0.017 \log(E/\text{eV}) - 0.00009043 \log^2(E/\text{eV}),$$

and the threshold for trigger bias is

$$r_{\text{trigger}}(E)/\text{m} = 1181 + 25.11 \log(E/\text{eV}) - 0.119 \log^2(E/\text{eV}).$$

Figure 3.15(b) plots $\eta(E, r)$ for four different energies as a function of the distance from the shower core r . The general shape of $\eta(E, r)$ was designed based on intuition on what makes the raw estimator $J_{0.5}$ biased. The actual numbers in the formulas were tuned using a set of proton and iron showers simulated with the hadronic model SIBYLL 2.1. Note also that the correction factor is designed for energies below 10^{20} eV. Using $\eta(E, r)$, the jump estimator for the number of muons in a tank is

$$\hat{N}_{\mu\text{jump}} = \eta(E, r) J_{0.5}.$$

Simulations show that the RMS variance of the jump method is about 40%. The original jump method has two main shortcomings. First, the correction factor $\eta(E, r)$ was tuned using

a single set of simulations which is known to produce a very low number of muons compared to those using other hadronic models, so $\eta(E, r)$ (and especially the parameter $\eta_{\max}(E)$) may have a significant model-dependent systematic bias. Second, the correction factor $\eta(E, r)$ depends explicitly on the energy, and its form is basically related to the muon density in the FADC signal, so if N_μ is undersimulated, the bias of the correction factor $\eta(E, r)$ could appear as a horizontal shift rather than a simple rescaling of J_δ . This means that an implicit systematic trend could be generated through the slopes $\partial N_\mu / \partial E$ and $\partial \eta(E, r) / \partial E$.

3.2.2 The Artificial Neural Network (ANN) method

The goal of the ANN method was to overcome these two problems. In this method, the correction factor depends only on intrinsic features of the FADC signal. This choice eliminates any explicit bias related to the energy or other "global" parameters of the shower. The design of this correction factor is based on a large set of simulated individual FADC signals. Although only proton and iron showers simulated by QGSJetII-03 are used, the tankwise muon estimator does not have access to any shower parameters, so it cannot bias its estimate explicitly. The procedure does not eliminate the bias completely, but the bias is smaller than that of the jump method.

The FADC signal has several high-level characteristics that are known to be correlated to the number of muons crossing the tank. The integrated thresholded discrete derivative, the so-called *jump*, is only one of them. The main idea of this technique is to extract as much information from the FADC signal as possible through variables that are plausibly correlated to muon content, and let a non-parametric predictor to construct a correction-factor estimator based on a large set of simulations of various kinds. Among them, we can cite the number of jumps, the signal length and the rise-time. Each of them are extracted for different threshold δ values, from 0.1 VEM to 3.0 VEM. In the end, 172 observables being plausibly correlated to muon content are obtained.

Of course, most of the extracted variables are correlated even if the number of muons is given, so the first step of the analysis is to perform a Principal Component Analysis (PCA) to reduce the dimensionality of the data. PCA is a mathematical procedure using an orthogonal transformation to convert a set of observations of possibly correlated variables into a set of values of uncorrelated variables called *principal components*. This transformation is defined in such a way that the first component has the largest variance, or information content, of the sample. The second component has the second largest dispersion and so on. One advantage of the PCA method is that, involving only rotations, the principal components are only linear combinations of the original observables. After this step, each FADC signal is represented by 19 linear combinations of the original variables extracted from the FADC signal. Even if they no longer have any "physical" meaning, these 19 first principal components account for 99%

of the total variance. Indeed, they capture the variance of the FADC signal and they “inherit” all the information from the original observables.

The next step is the actual training of the nonparametric predictor. This method uses the NETLAB implementation [12] of the neural network technique described in [13]. The particular ANN implementation of [12] has a useful property: beside value estimates, it also provides reliable uncertainty estimates on individual values which we can easily convert into uncertainties on the tankwise muon number estimate. Since the global goal of the analysis is to obtain a single observable for each *shower*, these uncertainties greatly improve the lateral distribution function (LDF) fit and, in turn, the final estimator of muon content at 1000 m from the shower axis.

Finally, the output of the ANN is compiled into a probability table

$$P_{\text{ANN}} = P(N_{\mu} = N | \text{FADCsignal}).$$

The RMS variance of this estimator is about 25%.

3.3 Mass composition and arrival directions of the highest energy events

There exist several models that describe the flux of ultra-high energy cosmic rays detected on Earth by the Pierre Auger Observatory [14]. Although most of them account for the general features that have been observed, they differ in their predictions concerning the dependence on mass composition and an important aim of the Auger Observatory is therefore to measure this parameter. This can only be done indirectly using physical observables that are sensitive to it. Among these are the elongation rate (depth of X_{max}) [15] measured by the fluorescence detector, the ground density of the muon component [8, 9], the azimuthal asymmetry parameters [16] and quantities derived from the rise time [17, 18], all measured by the surface detector. However, lack of sufficient statistics makes it usually impossible to draw significant conclusions concerning the mass composition.

Since the publication in November 2007 of evidence for a correlation with nearby extragalactic objects [19], several studies have focused on the mass composition of the highest energy cosmic rays coming from Active Galactic Nuclei (AGN), Centaurus A (Cen A) or from the whole sky. Motivated by the remark that a significant fraction of UHECRs detected by the surface array originate from the neighbourhood of Centaurus A and that a shower pointing to a source is more likely to have a proton primary, heavy nuclei undergoing more magnetic deflection in the Milky Way, this section looks for a possible difference in muon content between the showers pointing to Cen A and those of the whole sky.

This work is also aimed at providing additional information of relevance to a recent anal-

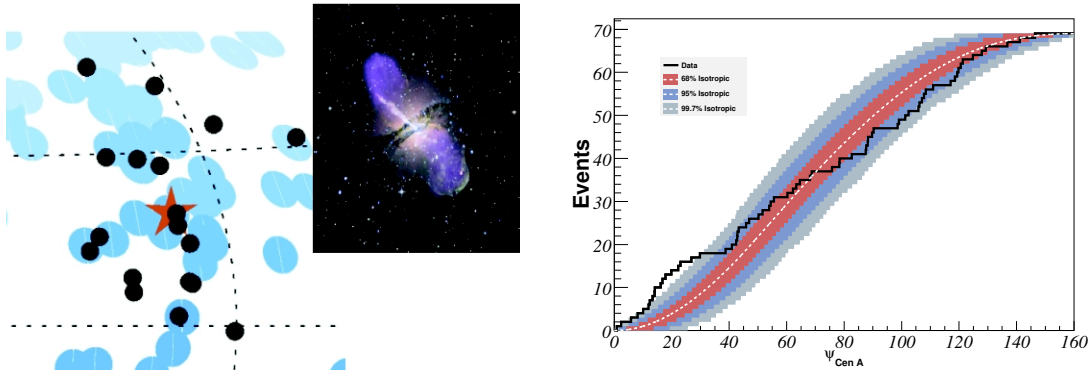


Figure 3.16: Number of experimental events with $E \geq 55 \text{ EeV}$ as a function of the angular distance to Centaurus A (from [21]). The bands correspond to the 68%, 95% and 99.7% dispersion expected for an isotropic flux.

ysis from Nosek et al., using hybrid data. They claimed that Cen A showers detected in the energy range between $10^{18.6} \text{ eV}$ and $10^{19.2} \text{ eV}$ develop on average at higher altitudes than showers from the whole sky [20], and suggested that Cen A showers might be initiated by heavier primaries. Using hybrid data implies a strong reduction of the available event sample compared to using SD data, making a critical evaluation of the statistical significance of the result essential. Moreover, at lower energies and/or heavier masses, the angular deflection due to the galactic magnetic field is larger, making it necessary to enlarge the angle within which one can observe cosmic rays coming from a specific source such as Cen A. Indeed, a proton of $10^{18.6} \text{ eV}$ is expected to be deflected by some 13° . These points seem not to have been taken into due consideration by the authors of [20].

3.3.1 Centaurus A, the region with the largest arrival direction excess

After having analysed the correlation of the Auger events with nearby extragalactic objects, the main question for the Auger Collaboration was why there are so many events coming from directions close to Centaurus A. This object, 3.8 Mpc away from us, is the closest AGN. The proximity of Cen A makes it one of the brightest and largest extragalactic sources in the sky: its giant lobes extend over nearly 10° .

The region with the largest arrival direction excess for the 69 highest energy events published in [21], as estimated by the excess above isotropic expectations in circular windows, is centred at galactic coordinates $(l, b) = (-46.4^\circ, 17.7^\circ)$. There are 12 arrival directions inside a window with radius 13° centred in that location, whereas 1.7 is the isotropic expectation. The centre of this region is only 4° away from the location of the radiogalaxy Cen A $(-50.5^\circ, 19.4^\circ)$ and it is not so far from the direction of the Centaurus cluster $(-57.6^\circ, 21.6^\circ)$.

Figure 3.16 shows the number of events with energy $E \geq 55 \text{ EeV}$ coming within a variable

angular radius from Cen A. The excess with largest significance is produced by 13 arrival directions within 18° , in which 3.2 arrival directions are expected if the flux were isotropic. In contrast to the region around Cen A and the Centaurus cluster, there is a paucity of events from the region around the radiogalaxy M87 and the Virgo cluster. None of the 69 events with $E \geq 55$ EeV is within 18° of M87. Due to its northern declination, however, M87 gets only one-third of the exposure of Cen A. Also, M87 is around five times farther away than Cen A, so the flux would be 25 times less if the sources had equal cosmic ray luminosities. However, one would expect 13/75 events to come from M87 if it has the same luminosity as Cen A.

3.3.2 Muon component as a function of arrival direction

The idea of this analysis is to compare the muon densities at 1000 m from the shower axis, $\rho_\mu(1000 \text{ m})$, for Cen A events with those coming from the whole sky, in the same spirit as that of Nosek et al. using X_{max} from Auger hybrid data. As for the case of the X_{max} or the $\text{RMS}(X_{\text{max}})$ parameters, the muon composition depends on the primary composition. Thus, a larger muon number indicates that the mass composition is heavier. In this work, the muon density at 1000 meters from the shower axis is obtained using both the Jump method and the ANN method. After getting the muonic lateral distribution function (LDF), the muon number at 1000 meters is calculated using a fit to the function

$$N_\mu(r_i, \beta) = N_\mu(1000 \text{ m}) \left(\frac{r_i}{1000 \text{ m}} \right)^\beta \quad (3.36)$$

where r_i is the distance from the tank i to the shower axis and β the slope of the muonic LDF. Figure 3.17 gives an example of a muonic LDF. The grey dashed area corresponds to the distance range where the muon number estimation is affected by the trigger bias. These tanks are not taken into account in the fit procedure. Then, the muonic density at 1000 meters $\rho_\mu(1000 \text{ m})$ is obtained by dividing $N_\mu(1000 \text{ m})$ by the collection surface

$$\rho_\mu(1000 \text{ m}) = \frac{N_\mu(1000 \text{ m})}{\pi R_{\text{tank}}^2 \cos \theta + 2R_{\text{tank}} H_{\text{tank}} \sin \theta'} \quad (3.37)$$

where R_{tank} is the tank radius and H_{tank} the tank height.

We applied the two muon counting methods to the Observer SD data reconstructed with the Offline version v2r7p4⁶. Data retained in this study are T5 triggers having energy $E \geq 4$ EeV, zenith angle $\theta \geq 60^\circ$, recorded from January 2004 to September 2010. Showers pointing to Cen A within 18° are called Cen A events.

The increase of the muonic density $\rho_\mu(1000 \text{ m})$ with energy results from the associated

⁶<http://augerobserver.fzk.de/doku.php?id=v2r7p4:home>

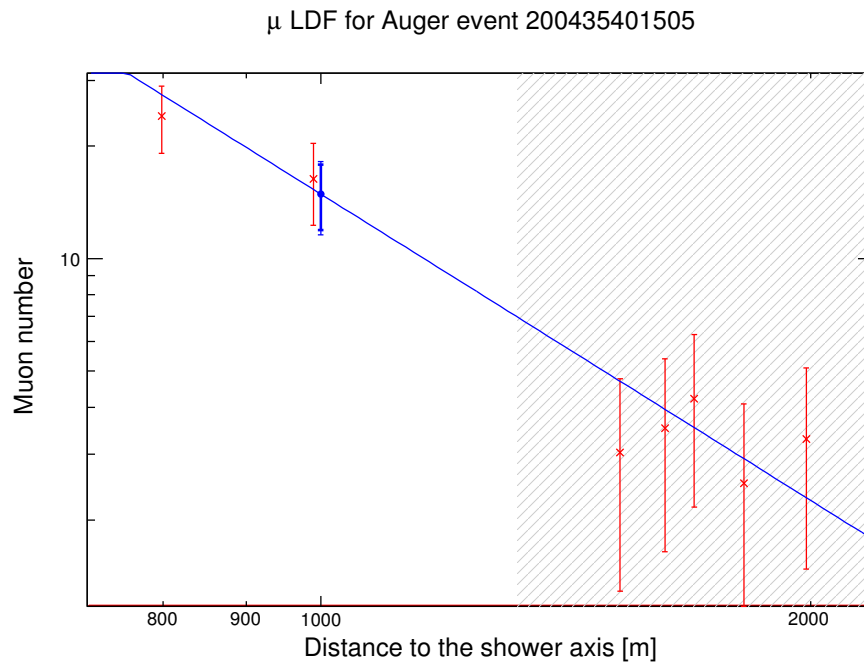


Figure 3.17: **Muonic Lateral Distribution Function for one event.** The muon number in each tank is given by the red crosses. Then the muon number at one thousand meters (blue dot) is obtained from the muonic LDF fit procedure, without taking into account tanks in the grey dashed area.

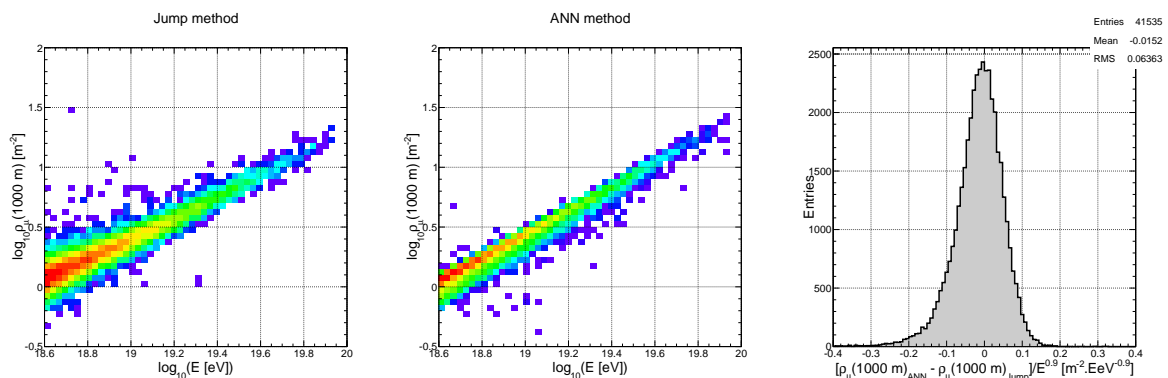


Figure 3.18: **Energy dependence of the muon density at 1000 m, for the Jump method and the ANN method.** The distribution of the difference between the two methods is also given on the right.

increase of the particle density on ground. Figure 3.18 shows the energy dependence of $\rho_\mu(1000 \text{ m})$, in log-log plots, for the Jump method and the ANN method. For the ANN calculations, the dispersion of $\log_{10} \rho_\mu(1000 \text{ m})$ is remarkably small.

Figure 3.19 shows, for the two muon counting methods, the muonic density normalized

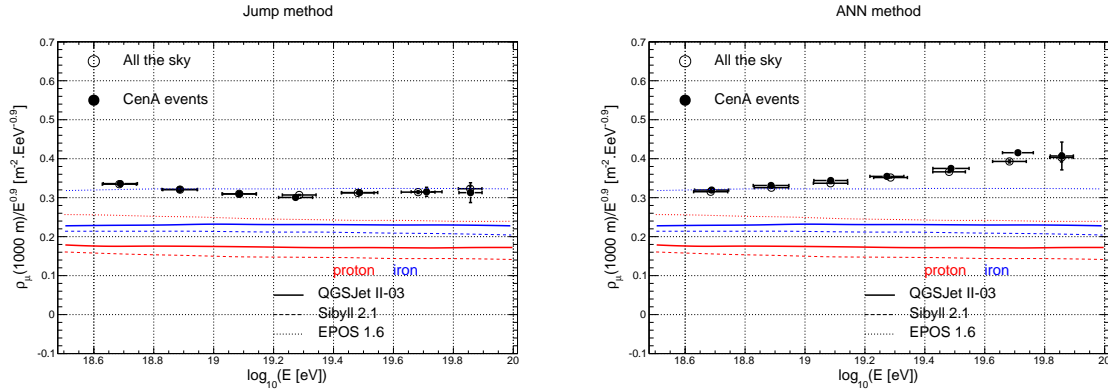


Figure 3.19: Evolution of the muonic density at 1000 meters normalized to its energy dependence, with respect to the primary energy. The data set used here correspond to the SD data measured by the Pierre Auger Observatory from January 2004 to September 2010 and to a subset from the Cen A region. For each figure, predictions from three hadronic models, QGSJetII-03, SIBYLL 2.1 and EPOS 1.6, are plotted.

$\langle \log_{10}(E[\text{eV}]) \rangle$	18.7	18.9	19.1	19.3	19.5	19.7	≥ 19.8
Whole sky	14491	6558	3055	1308	479	121	30
CenA	660	301	135	72	28	13	5

Table 3.1: Number of events for each energy bin of the whole sky and Cen A events.

to the energy at one thousand meters with respect to the shower energy, and Table 3.1 gives the number of events for each energy bin. The 0.9 power is the dependence to the energy expected by the hadronic models for the muonic density at one thousand meters. Low energy events containing data from only three tanks are hard to use; consequently, the study is done only for the energies greater than $10^{18.6}$ eV. In the two analyses, the muon density observed is much greater than that predicted by models. Only the EPOS 1.6 model, in the case of the jump method, can reproduce the data assuming an iron composition for the cosmic ray primary. In the case of the ANN method, and contrary to the jump method, the mass composition passes from a light component at $10^{18.6}$ eV to a heavy composition at greater energies. In addition, no evidence is found for a difference in the mass compositions between Centaurus A events and the whole sky sample. Indeed, it is obvious from the figure that there is no significant difference in the $\rho_{\mu}(1000 \text{ m})/E^{0.9}$ values of the two samples. The implication of this statement on a possible difference in primary mass depends on the value of the sensitivity of $\rho_{\mu}(1000 \text{ m})/E^{0.9}$ to the muon content and of the muon content to the primary mass.

Having evaluated the muon densities of the highest energy events makes it possible to look at their distribution in the sky. Does one see clusters of muon rich (or poor) events ? (it

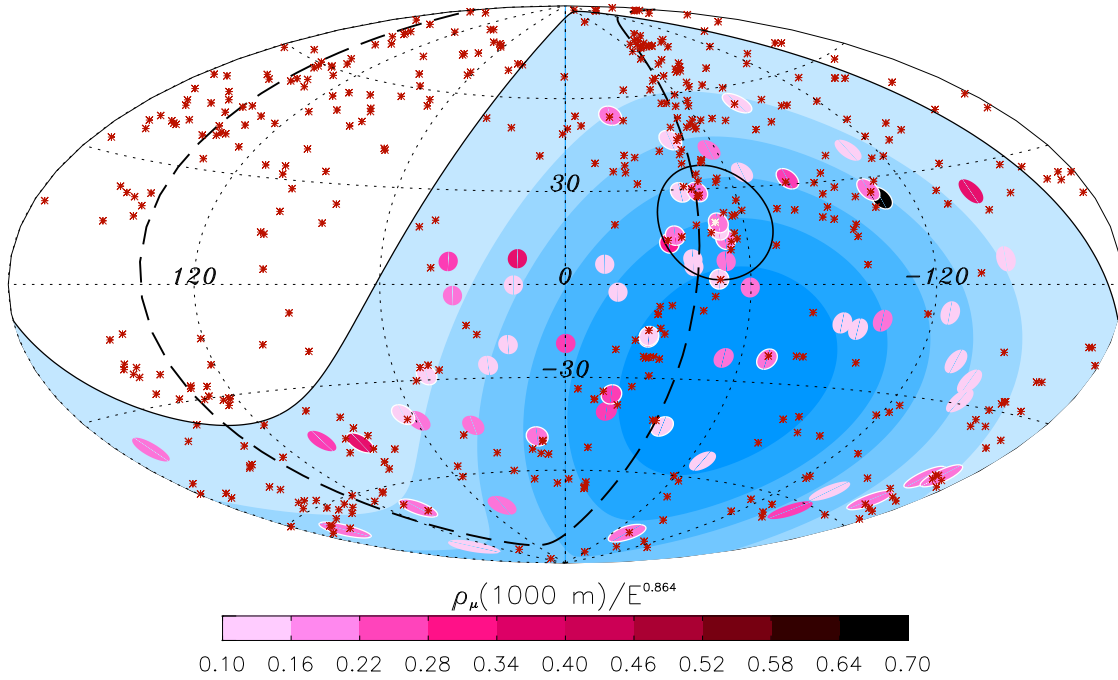


Figure 3.20: **Muonic density at one thousand meters from the jump method for energy events greater than 55 EeV.** The 3.1° circles represent the event arrival directions, the colour index being proportional to their $\rho_\mu(1000 \text{ m})/E^{0.9}$ value. The 472 AGNs with a redshift lower than 0.018 (~ 75 Mpc) from the 12th edition of the Veron-Cetty catalogue [22] are indicated by red crosses. The solid line represents the border of the field of view (zenith angles greater than 60°). Darker colour indicates larger relative exposure. Each coloured band has equal integrated exposure. The dashed line is the supergalactic plane. Centaurus A is marked with a white cross, the black curve around it corresponding to an 18° circle.

must be clear, however, that it is not possible to assign a primary mass value reliably at the level of a single event). Figure 3.20 shows a sky map for the SD events having $E \geq 55$ EeV analyzed using the jump method. The sky map shows no evidence for clusters of muon rich events. It is interesting to note the presence of events not correlated with AGNs but coming from voids, quite far from the closest AGN; several of them are relatively muon poor (therefore on the proton side, having in principle a reliable arrival direction). What are the sources of such events? The question remains open.

3.4 Conclusion

Throughout this chapter we have presented briefly the muon component in a hadronic shower. Using a model based on averaged values, the charged pion component can be understood intuitively. The altitude of maximum muon production has been determined, and

other physical quantities related to the muon component have been derived.

After having presented briefly the two muon counting methods developed by the Auger-LAL group in previous years, they have been used to study events. The muon content of showers detected by the Auger surface array has been investigated. Those coming from the Centaurus A direction have been studied separately to look for a possible difference in mass composition. Using both muon counting methods, no significant difference between the Cen A and the whole sky samples has been found.

Bibliography

- [1] J Matthews, *A Heitler model of extensive air showers*, *Astropart. Phys.* **22** (2005) 387–397.
- [2] K Werner, F Liu and T Pierog, *Parton ladder splitting and the rapidity dependence of transverse momentum spectra in deuteron-gold collisions at the BNL relativistic heavy ion collider*, *Phys. Rev. C* **74** (2006) 044902–044912.
- [3] SS Ostapchenko, *Nonlinear screening effects in high energy hadronic interactions*, *Phys. Rev. D* **74** (2006) 014026–014042.
- [4] R Engel, TK Gaisser, P Lipari and T Stanev, *Proc. 26th Int. Cosmic Ray Conf., Salt Lake City (USA)*, **1** (1999).
- [5] D Heck, J Knapp, JN Capdevielle, G Schatz and T Thouw, *Report FZKA 6019*, Forschungszentrum Karlsruhe (1998).
- [6] T Bergmann *et al.*, *One-dimensional hybrid approach to extensive air shower simulation*, *Astropart. Phys.* **26** (2007) 420–432.
- [7] T Pierog *et al.*, *First results of fast one-dimensional hybrid simulation of EAS using CONEX*, *Nucl. Phys. B (Proc. Suppl.)* **151** (2006) 159–162.
- [8] X Garrido *et al.*, *Measurement of the number of muons in Auger tanks by the FADC jump counting method*, **GAP-2007-060**.
- [9] X Garrido *et al.*, *Update and new results from the FADC jump counting method*, **GAP-2009-023**.
- [10] A Castellina and G Navarra, *Separating the electromagnetic and muonic components in the FADC traces of the Auger Surface Detectors*, **GAP-2006-065**.
- [11] B Kégl *et al.*, *Reconstructing $N_{\mu 19}(1000)$* , **GAP-2011-054**.
- [12] I Nabney, *Netlab: Algorithms for pattern recognition*, Springer (2002).
- [13] CM Bishop, *Neural networks for pattern recognition*, Oxford University Press (1995).
- [14] T Wibig and AW Wolfendale, *Heavy cosmic ray nuclei from extragalactic sources above the ankle*, **arXiv:0712.3403** (2007).
- [15] J Abraham *et al.* [Pierre Auger Collaboration], *Measurement of the depth of maximum of extensive air showers above 10^{18} eV*, *Phys. Rev. Lett.* **104** (2010) 091101–091107.
- [16] MT Dova *et al.*, *Primary composition from asymmetries in EAS – new approach*, **GAP-2005-014**.

-
- [17] K Mora *et al.*, *Composition studies of ultra high energy cosmic rays using data of the Pierre Auger Observatory*, **GAP-2010-037**.
- [18] R Bruijn *et al.*, *An exploration of the development of showers that correlate and do not correlate with AGNs*, **GAP-2009-084**.
- [19] J Abraham *et al.* [Pierre Auger Collaboration], *Correlation of the highest-energy cosmic rays with the position of nearby active galactic nuclei*, *Astropart. Phys.* **29** (2008) 188–204.
- [20] D Nosek *et al.*, *Heavy cosmic ray primaries from the region around Centaurus A*, **GAP-2010-007**.
- [21] P Abreu *et al.* [Pierre Auger Collaboration], *Update on the correlation of the highest energy cosmic rays with nearby extragalactic matter*, *Astropart. Phys.* **34** (2010) 314–326.
- [22] M-P Véron-Cetty and P Véron, *A catalogue of quasars and active nuclei: 12th edition*, *Astron. Astrophys.* **455** (2006) 773–777.

Atmospheric measurements at the Pierre Auger Observatory

Contents

4.1 Atmospheric effects on light production and its propagation in the atmosphere	97
4.1.1 Molecular transmission – Rayleigh regime	98
4.1.2 Aerosol transmission – Mie regime	100
4.1.3 Ultraviolet and visible absorption by atmospheric trace gases	102
4.1.4 Angular dependence of molecular and aerosol scattering	106
4.2 Molecular measurements at the Pierre Auger Observatory	107
4.2.1 Weather station measurements and horizontal uniformity	107
4.2.2 Radio-sonde measurements and monthly average atmospheric profiles	114
4.2.3 Towards using the Global Data Assimilation System (GDAS)	114
4.3 Aerosol measurements at the Pierre Auger Observatory	117
4.3.1 Aerosol optical depth measurements	117
4.3.2 Aerosol scattering measurements	126
4.3.3 Aerosol sampling measurements	130
4.3.4 Wavelength dependence	131
4.4 Cloud detection at the Pierre Auger Observatory	134
4.5 Impact of the atmosphere on the reconstruction accuracy of air shower parameters	137
Bibliography	139

Introduction: Thanks to a collection of atmospheric monitoring data, the Auger Collaboration has accumulated a large database of atmospheric measurements. This effort significantly reduced the systematic uncertainties in the air shower reconstruction. During my PhD thesis in the Auger Collaboration, I took part mainly in the aerosol analysis. This chapter is inspired from the proceeding published at the International Cosmic Ray Conference (ICRC) which took place at Beijing (China) during August 2011¹.

¹K Louedec, for the Pierre Auger Collaboration *Atmospheric monitoring at the Pierre Auger Observatory – Status and Update* Proc. 32nd ICRC, Beijing, China (2011).

Due to the extremely low flux of cosmic rays on Earth, their direct detection is not feasible. Once they enter into the atmosphere, they induce extensive air showers composed of secondary particles. In the Auger facility, the atmosphere is used as a giant calorimeter, representing a detector volume larger than $30\,000\text{ km}^3$. To minimize as much as possible the systematics on the fluorescence measurements, the atmosphere properties have to be continuously monitored. These properties include atmospheric state variables such as temperature, pressure or humidity for the molecular part of the atmosphere, but also physical quantities such as optical depth or phase function² describing the scattering behaviour of the atmosphere, due to the presence of aerosols.

The role of hybrid energy calibration played by the FD depends strongly on a detailed knowledge of the atmospheric conditions. During the development of an extensive air shower, the production rate of fluorescence photons depends on the temperature, pressure and humidity of the air. Then, from their production point to the telescope, photons can be scattered and/or absorbed by molecules and/or aerosols. Thus, in order to track atmospheric parameters, an extensive, and unique in the world, atmospheric monitoring system has been developed covering the whole SD array.

Figure 4.1 lists the different experimental facilities and their locations. Atmospheric properties at ground level are provided by a network of five weather stations located at each FD site and at the Central Laser Facility (CLF). They furnish atmospheric state variable measurements every five minutes. Also, meteorological radio-sonde flights with balloons have been operated, during daytime and at night, to get altitude profiles of the main atmospheric quantities. The balloon flight program ended in December 2010 after having been operated 331 times. This complete database, representing several years of measurements, has been used to produce monthly atmospheric profiles.

For the aerosol component, and only during FD data-taking, the Central Laser Facility fires 50 vertical shots every 15 minutes. FD telescopes, recording the UV laser tracks, are able to deduce the aerosol concentration at different altitudes. Since November 2008, a new laser facility called the eXtreme Laser Facility, or XLF, has been deployed. These concentration measurements are completed with four elastic backscattering lidars located at each eye. A Raman lidar currently under test in Colorado (USA) is scheduled to be moved to the Auger Observatory for the Super-Test-Beam project [1]. To improve our knowledge of photon scattering on aerosols, two Aerosol Phase Function monitors (APF) have been installed at Coihueco and Los Morados: they consist of a collimated horizontal light beam produced by a Xenon flasher which passes in front of one FD eye. The aerosol attenuation depends on the incident wavelength: its measurement is the main goal of two optical telescopes in Auger, the Horizontal Attenuation Monitor, or HAM, and the (F/ph)otometric Robotic Telescope for

²These two quantities will be described in detail later in the manuscript, but basically, they can be seen as the measurement of concentration and the differential cross section, respectively.

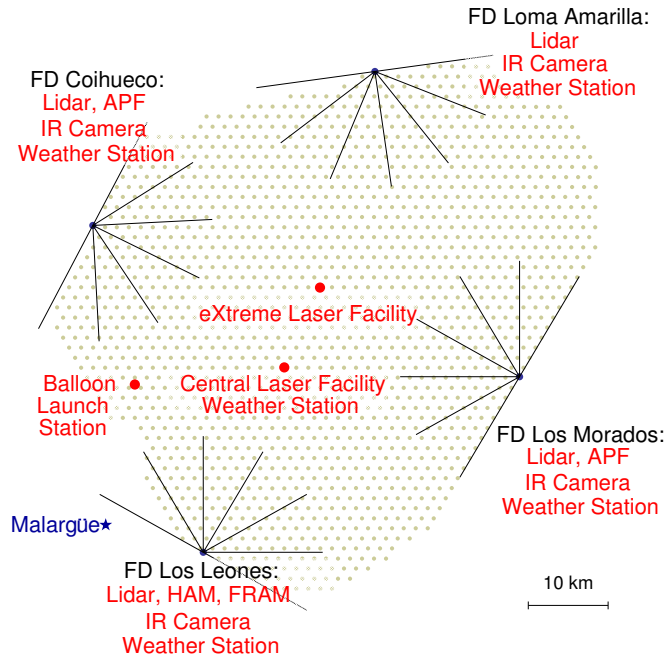


Figure 4.1: **Atmospheric monitoring map of the Pierre Auger Observatory.** Each FD site hosts several atmospheric monitoring facilities.

Atmospheric Monitoring, or FRAM. Finally, to exclude absorption effects from clouds, four infrared camera are installed on the roof of each FD building continuously scanning the sky and producing one full-sky image every five minutes.

4.1 Atmospheric effects on light production and its propagation in the atmosphere

Atmospheric conditions affect both the production and the propagation of UV light coming from air showers. Even if the fluorescence yield remains the largest source of uncertainty for FD measurements, weather effects also contribute significantly to systematic uncertainties.

Cherenkov and fluorescence light production at a given wavelength λ depends on the atmospheric variables pressure P , temperature T and vapour pressure e . Whereas the Cherenkov light yield can be directly calculated from the refractive index of the atmosphere $n(\lambda, P, T)$, the weather dependence of the fluorescence production is much more difficult to determine. Among the effects which are hard to measure experimentally, we can cite the collisional quenching of fluorescence emission. In this phenomenon, the radiative transitions of excited nitrogen molecules are suppressed by molecular collisions [2]. Also, water vapour contributes to collisional quenching: thus, the fluorescence yield has an additional depen-

dence on the atmosphere humidity.

It is not enough to understand and take into account in shower reconstruction weather effects on UV light production; atmospheric effects all along the photon's trajectory have to be studied too. In this case the photons have a wavelength in the UV domain, the absorption mechanism in the air is negligible. Thus, in the following, attenuation will represent only the scattering phenomena, which are the most significant here. The main atmospheric attenuation processes are Rayleigh scattering, for the molecular component, and Mie scattering, for the aerosol component, both being elastic. It can be noted that inelastic Raman scattering, much less efficient, will not be considered in the following.

Attenuation of light from an air shower to the FD telescope can be expressed as a transmission coefficient Γ , or optical transmittance, which gives the fraction of incident light at a specified wavelength λ that passes through an atmosphere of thickness x . If τ is the optical depth, then Γ is estimated using the Beer-Lambert law

$$\Gamma(x, \lambda) = \Gamma_m(x, \lambda) \Gamma_a(x, \lambda) = \exp [-\tau(x, \lambda)],$$

where τ can be decomposed in $\tau = \tau_m + \tau_a$, the molecular component and the aerosol component, respectively.

Usually, atmosphere can be described as a superposition of several horizontally uniform layers, so spatial dependence of the optical depth can be reduced to an altitude dependence. Hence, the transmittance from an altitude h to the ground through a slanted path of zenith angle θ is

$$\Gamma(h, \theta, \lambda) = (1 + H.O.) \exp \left[-\frac{\tau(h, \lambda)}{\cos \theta} \right],$$

where *H.O.* represents a higher-order correction that accounts for the single and multiple scattering of Cherenkov and fluorescence photons into the field of view of the telescope.

The goal of atmospheric monitoring in Auger is to estimate the attenuation factors and the scattering properties needed to obtain the higher-order corrections. Also, their dependence in altitude and wavelength has to be constrained. For these quantities, the contributions due to molecules and aerosols are considered separately in the following.

4.1.1 Molecular transmission – Rayleigh regime

The air is a medium with a mass composed of 78% dinitrogen N_2 and 21% dioxygen O_2 (then, traces of argon Ar, neon Ne, helium He, dihydrogen H_2 and xenon Xe). They correspond to the "permanent" gases composing the atmosphere. The resulting molecular mass for an "air molecule" is $M_0 = 28.97$ g/mol for standard temperature and pressure at sea level. To take into account humidity effects to this, air must be added a factor corresponding to the vapour pressure. The final molecular mass is the sum of the two components, weighted by their

volume fractions

$$M_{\text{air}} = \alpha_{\text{dry}} M_0 + \alpha_{\text{w}} M_{\text{w}},$$

where the molecular masses for dry air and vapour pressure are 28.97 g/mol and 44.01 g/mol, respectively. The fraction of water α_{w} is directly the vapour pressure divided by the pressure [3].

Molecular attenuation in the near UV can be approximated using uniquely the elastic Rayleigh scattering process, since it dominates inelastic Raman scattering (by around three orders of magnitude) or absorption [4]. Hence, the molecular transmission can be reduced to the scattering phenomenon only. The total Rayleigh scattering cross section per air molecule is given analytically by the following formula [5]

$$\sigma_{\text{R}}(\lambda) = \frac{24\pi^3}{\lambda^4 N_{\text{s}}^2} \left(\frac{n_{\text{s}}^2(\lambda, N_{\text{s}}) - 1}{n_{\text{s}}^2(\lambda, N_{\text{s}}) + 1} \right)^2 \frac{6 + 3\rho_{\text{n}}(\lambda)}{6 - 7\rho_{\text{n}}(\lambda)}, \quad (4.1)$$

where $n_{\text{s}}(\lambda, N_{\text{s}})$ is the refractive index for standard air, N_{s} the molecular number density and $\rho_{\text{n}}(\lambda)$ the depolarization factor taking into account the anisotropy of the air molecules. $\rho_{\text{n}}(\lambda)$ is determined by the asymmetry of N_2 and O_2 molecules, and equal to zero for point-like scattering centres [6]. The depolarization factor varies by approximately 60% from the near IR ($\rho_{\text{n}} \simeq 0.045$) to the UV domain ($\rho_{\text{n}} \simeq 0.028$), introducing a corresponding variation with wavelength of around 3% for the Rayleigh cross section. The value used for Auger in the near UV is fixed at 0.03, shifting the wavelength dependence of the molecular scattering from the well known $\lambda^{-4.0}$ behaviour to an effective value of $\lambda^{-4.2}$.

For wavelengths greater than 230 nm and an atmosphere in the standard temperature and pressure conditions at the sea level ($T_{\text{s}} = 288.15$ K, $P_{\text{s}} = 1013.25 \times 10^2$ Pa), Peck and Reeder [7] proposed the following formula to obtain the refractive index

$$n_{\text{s}}(\lambda, N_{\text{s}}) = 1 + \frac{0.05791817}{238.0185 - (1 \mu\text{m}/\lambda)^2} + \frac{0.00167909}{57.362 - (1 \mu\text{m}/\lambda)^2}. \quad (4.2)$$

Molecular scattering coefficient: $\beta_{\text{m}}(h, \lambda)$

The probability per unit length that a photon is Rayleigh scattered at a fixed wavelength λ at an altitude h is the so-called *scattering coefficient*, β , given by the following equation

$$\beta_{\text{m}}(h, \lambda) = N(h) \sigma_{\text{R}}(\lambda), \quad (4.3)$$

where $N(h)$ is the molecular number density at a given pressure and temperature (i.e. altitude).

The coefficient $\beta_{\text{m}}(h, \lambda)$ scales with the molecular number density N_{s} . Thus, it is straightforward to correct it for any pressure P and temperature T . We use the fact that air is close to

being an ideal gas to obtain

$$\beta_m(h, \lambda) = \beta_{m,s} \frac{N}{N_s} = \beta_{m,s} \frac{P}{P_s} \frac{T_s}{T}, \quad (4.4)$$

where $\{N_s, P_s, T_s\}$ are the reference parameters and $\{N, P, T\}$ are those for any conditions (i.e. at any altitude).

Molecular attenuation length: $\Lambda_m(h, \lambda)$

The mean free path, representing the mean length travelled by a photon before Rayleigh scattering, called also the molecular attenuation length, is given by

$$\Lambda_m(h, \lambda) = \frac{1}{N(h) \sigma_R(\lambda)} = \frac{1}{\beta_m(h, \lambda)}. \quad (4.5)$$

In the case where the attenuation length is to be expressed in atmospheric mass depth, the following relation can be useful since it is linked directly to the Rayleigh cross section

$$X_m(\lambda) = \frac{M_{\text{air}}}{\sigma_R(\lambda) N_A}, \quad (4.6)$$

where N_A is the Avogadro constant ($N_A = 6.02 \times 10^{23} \text{ mol}^{-1}$).

Molecular optical depth: $\tau_m(h, \lambda)$

The molecular optical depth between a telescope at ground level h_{ground} and a point at altitude h is expressed as the integral of the molecular scattering coefficient over the altitude

$$\tau_m(h, \lambda) = \int_{h_{\text{ground}}}^h \beta_m(h', \lambda) dh'. \quad (4.7)$$

After this brief summary of molecular scattering, the main objective of the Auger collaboration concerning the molecular part of the atmosphere will be to obtain the profiles $P(h)$ and $T(h)$. Later in the manuscript, two different methods will be presented: measurements from balloon-borne radio-sonde flights or data from a global climate model such as the Global Data Assimilation System (GDAS) provided by the National Oceanic and Atmospheric Administration (NOAA).

4.1.2 Aerosol transmission – Mie regime

Although atmosphere is mainly composed of molecules, a small fraction of larger particles such as dust or droplets are in suspension. These particles are called *aerosols* and their typical size is around a micron. Since the size of these particles is no longer small with respect to

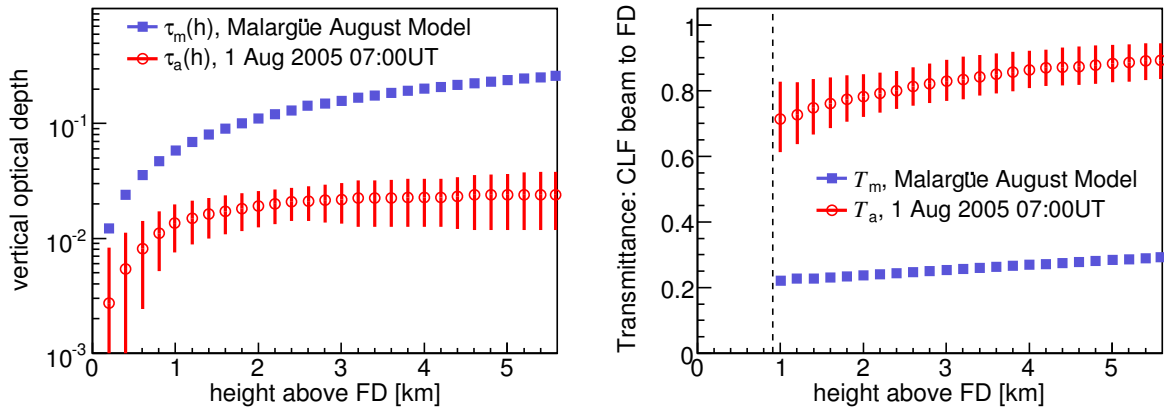


Figure 4.2: **Light transmission in the atmosphere (from [9]).** *Left panel:* example of a vertical aerosol optical depth profile measured at Los Leones with vertical laser shots from the CLF (25 km). Systematic effects dominate the uncertainties. Also shown is the monthly average molecular optical depth for August. *Right panel:* molecular and aerosol light transmission factors for the atmosphere between the vertical CLF laser beam and Los Leones. The vertical dashed line represents the lower edge of the FD field-of-view at this distance.

the incident wavelength, the analytical Rayleigh formulae cannot be applied in this case. The Mie scattering that they produce is much more complex: for instance, it depends on particle composition and shape and on the size distribution. Also, aerosol populations, unlike the molecular component, change quite rapidly in time, depending on the wind and weather conditions.

Therefore, knowledge of the aerosol transmission parameters in Auger will be acquired through measurements of the aerosol optical depth $\tau_a(h, \lambda)$ at different location in the SD array, throughout the night. Usually, the aerosol concentration decreases rapidly with the altitude. Most of the aerosols are present in the planetary boundary layer, i.e. in the first few kilometres above ground level. Consequently, as shown in Figure 4.2, a characteristic behaviour can be seen in the altitude profile of $\tau_a(h, \lambda)$: a more or less linear increase at the beginning, then a flattening since the aerosol concentration decreases quickly with the altitude.

The aerosol optical depths are measured in the field at a fixed wavelength $\lambda_0 = 355$ nm, approximately in the centre of the nitrogen fluorescence spectrum. To evaluate the aerosol extinction for a given incident wavelength, a common parameterization used is a power law due to Ångström,

$$\tau_a(h, \lambda) = \tau_a(h, \lambda_0) \left(\frac{\lambda_0}{\lambda} \right)^\gamma, \quad (4.8)$$

where γ is known as the Ångström coefficient. This exponent depends on the size distribu-

tion of the aerosols. When the aerosol particle size approaches the size of air molecules, γ should tend to 4 (mainly dominated by *accumulation-mode* aerosols), and for very large particles, typically larger than 1 μm , it should approach zero (dominated by *coarse-mode* aerosols). Usually, a $\gamma \simeq 0$ is characteristic of a desert environment and the aerosol optical depth is more or less independent of the wavelength. In Auger, measurements gave γ values between 0.2 and 1.2 (see Section 4.3.4).

4.1.3 Ultraviolet and visible absorption by atmospheric trace gases

The atmosphere is not only composed of the "permanent gases", corresponding to the molecular part, and of the aerosols. As already mentioned in Section 4.1.1, water vapour H_2O has to be considered and may account for up to 4% of the atmospheric gases in some temperature conditions. Then, several "variable gases" are present in a very small quantity in the atmosphere. Among them, the main gases are carbon oxides CO and CO_2 , methane CH_4 , ozone O_3 , nitrogen oxides NO and NO_2 , or sulfur dioxides SO_2 . To these components, we have to add also the Volatile Organic Compounds (VOCs) which are a class of organic compounds, most of them being hydrocarbons.

These atmospheric trace gases come from both *natural sources* and *human activities*. Examples of natural sources include wind picking up dust and soot from the Earth's surface and carrying it aloft, volcanoes belching tons of ash and dust into our atmosphere, or forest fires producing vast quantities of drifting smoke. As human-induced sources, one cites usually transportation, fuel combustion or industrial processes. These different gases had previously constant concentration in the atmosphere, since their origin was exclusively natural. But, nowadays, human activities increase the concentrations of these gases called as air pollutants.

After a brief listing of the main gases, an estimation of their effect on the light propagation in the atmosphere will be done. Then, it will be concluded if they should be taken into account in studies of light attenuation.

4.1.3.1 Principal gases in the atmosphere

Absorption of UV-Vis(ible) light in the atmosphere is mainly dominated by two atmospheric gases: dioxygen and ozone, corresponding to the largest photoabsorption cross sections. The other minor atmospheric species are optically thin to UV-Vis radiations [10]. The principal absorption features of molecular oxygen are absorption bands of the Schumann-Runge system between 175 nm and 200 nm, and the weak Herzberg dissociation continuum extending from 175 nm to 260 nm (see Figure 4.3). Concerning ozone, it shows absorption in almost the entire UV-Vis region, from the very strong Hartley band in the UV, to the much weaker Huggins and Chappuis bands in the near-UV and visible.

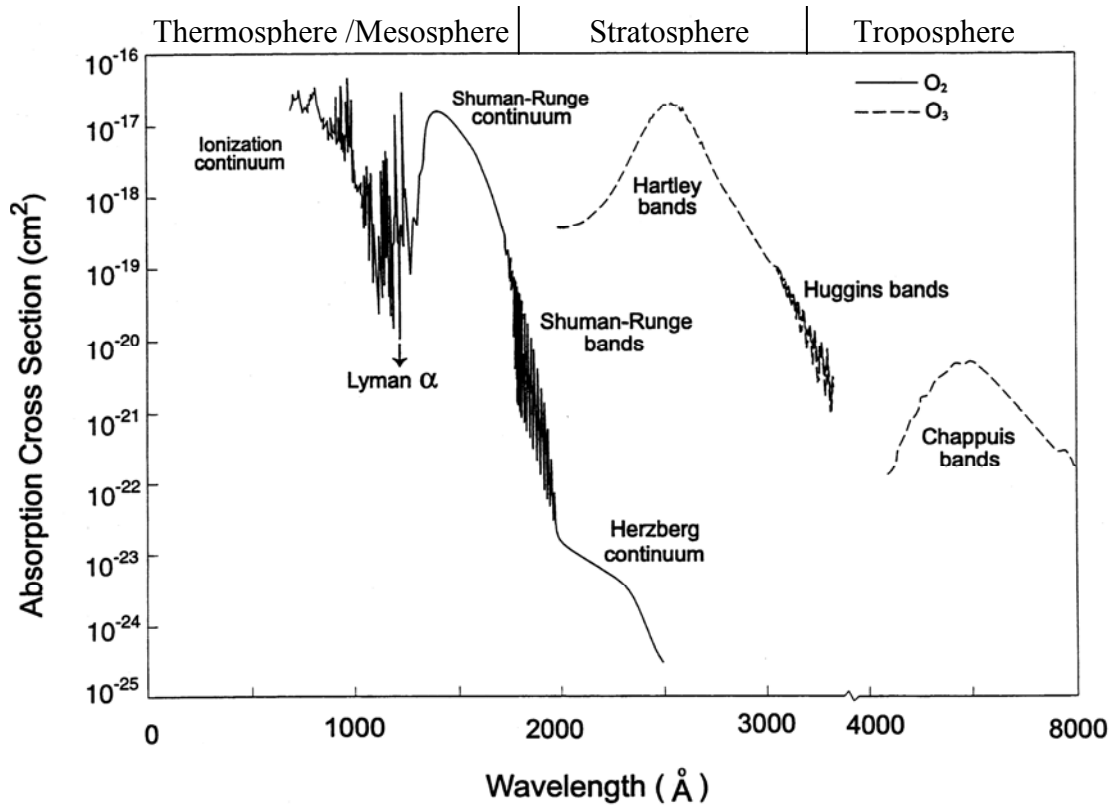


Figure 4.3: Spectral absorption cross section for dioxygen O_2 and ozone O_3 , in the UV-Vis range. The corresponding altitudes where the phenomena take place in the atmosphere are indicated in the top of the plot.

Atmospheric gas	Absorption wavelengths [nm]
Dinitrogen N_2	$\lambda \leq 100$
Dioxygen O_2	$\lambda \leq 240$
Ozone O_3	$170 \leq \lambda \leq 350$ and $450 \leq \lambda \leq 750$
Water vapour H_2O	$\lambda \leq 210$ and $600 \leq \lambda \leq 720$
Carbon monoxide CO	$2320 \leq \lambda \leq 2335$
Carbon dioxide CO_2	$\lambda \leq 205$
Methane CH_4	$1630 \leq \lambda \leq 1670$
Nitrogen dioxide NO_2	$\lambda \leq 600$
Nitrogen trioxide NO_3	$410 \leq \lambda \leq 670$
Sulfur dioxide SO_2	$250 \leq \lambda \leq 350$
Nitric acid HNO_3	$\lambda \leq 330$

Table 4.1: Wavelengths of absorption in the UV-Vis range for several atmospheric gases (from [11]). NO_2 absorbs at $\lambda \leq 600$ nm, but dissociates at $\lambda \leq 400$ nm.

Presently, theoretical models are not generally available to provide absorption cross sections for each species at different temperature and pressures. Thus, the cross section of the absorbers are measured in laboratories at fixed temperature and pressure, then empirical models are used to interpolate them to intermediate values of temperature and pressure [12].

An overview of the different species present in the atmosphere with their corresponding spectral range where they are the most absorbing is given in Table 4.1. These values are given for temperature and pressure corresponding to the low part of the atmosphere. At this ambient temperature, for instance, the carbon dioxide CO_2 is transparent in the ultraviolet (UV) at wavelengths longer than 205 nm. Nevertheless, it is interesting to stress that at higher temperatures, typically above 1000°K , the CO_2 absorption cross section becomes significant in the region between 200 and 320 nm.

In the case of the Pierre Auger experiment, the spectral range probed is centred around 350 nm. Thus, according to Table 4.1, the photoabsorption is mainly caused by ozone O_3 , followed then by nitrogen dioxide NO_2 , sulfur dioxide SO_2 and nitric acid HNO_3 . The next section will be focused on the light attenuation due to these trace gases.

4.1.3.2 Light attenuation due to trace gases in Ultraviolet

At the surface, **ozone** O_3 is the primary ingredient of the *photochemical smog*³ Even if the majority of atmospheric ozone (about 97%) is found in the upper atmosphere – in the stratosphere – where it is produced naturally, approximately 0.04 ppm (parts per million) is present in the low part of the atmosphere.

The **sulfur dioxide** SO_2 is a colourless gas coming primarily from the burning of sulfur-containing fossil fuels (such as coal or oil). However, it can enter the atmosphere naturally during volcanic eruptions and as sulfate particles from ocean spray. As it is known, the region where the Pierre Auger Observatory is installed is affected by air masses coming from the Pacific Ocean, and is a active volcanic region.

The **nitrogen dioxide** NO_2 is a gas that forms when some of the nitrogen in the air reacts with oxygen during the high-temperature combustion of fuel. Although it is produced naturally, its concentration in urban environments is 10 to 100 times greater than in nonurban regions. In moist air, nitrogen dioxide reacts with water vapour to form corrosive **nitric acid** HNO_3 , a substance that adds to the problem of acid rain. Moreover, nitrogen dioxide is highly reactive and plays a key role in producing ozone and other ingredients of photochemical smog.

Table 4.2 gives the photoabsorption cross section and the concentration at ground for the four species just enumerated previously. The cross sections are given for ambient tempera-

³The word *smog*, originally meant the combining of smoke and fog. Nowadays, it mainly refers to the type of smog that forms in large cities where, with the presence of sunlight, occur chemical reactions.

Atmospheric gas	Cross section at 350 nm [cm ²]	Concentration [μg/m ³]	Λ _{abs} [km]
Ozone O ₃	2 × 10 ⁻²² [13]	80 μg/m ³ [16]	50 000
Nitrogen dioxide NO ₂	4 × 10 ⁻¹⁹ [12]	30 μg/m ³ [17]	64
Sulfur dioxide SO ₂	8 × 10 ⁻²³ [14]	8 μg/m ³ [18]	2 × 10 ⁶
Nitric acid HNO ₃	1 × 10 ⁻²⁴ [15]	2 μg/m ³ [19]	5 × 10 ⁸

Table 4.2: List of the most efficient absorbers around 350 nm. Their concentration in the low part of the atmosphere, and their corresponding photoabsorption cross section are given for each atmospheric gas. Λ_{abs} is the attenuation length.

ture, at a pressure of one atmosphere. Then, for each gas, the equivalent attenuation lengths are calculated. Thus, whereas ozone, sulfur dioxide and nitric acid have attenuation lengths very large compared to the Rayleigh or Mie scattering processes, nitrogen dioxide, due to a large cross section, gets an attenuation length around 60 km. Such a value cannot be neglected in light attenuation studies at the Pierre Auger Observatory. Indeed, considering an average distance ℓ for the air shower of about 20 km, the resulting transmission factor is given by

$$\Gamma_{\text{NO}_2} = \exp\left(-\frac{\ell}{\Lambda_{\text{NO}_2}}\right) \simeq 0.70.$$

Hence, in this case, almost one third of the total light produced by the air shower is absorbed by nitrogen dioxide. After such observations, it could be interesting to consider a monitoring of the NO₂ concentrations above the Auger array. Indeed, the NO₂ concentrations should be affected by the air masses travelling through the Pierre Auger Observatory, as it is already the case for the aerosol population (see Chapter 6 for more details). Since the Auger observatory is located in a nonurban region, the NO₂ concentrations are probably relatively low. But some nights would be affected by the NO₂ absorption when, for instance, the air masses have previously travelled cities. If such a monitoring can be undertaken by the Auger Collaboration, it could be useful to measure other species concentrations as ozone O₃, oxygen dimer O₄, bromine monoxide BrO or chlorine dioxide OClO, since their photoabsorption cross sections are of the same order of the nitrogen dioxide one [20].

In the following of this manuscript, the absorption due to nitrogen dioxide will not be treated. Indeed, since the NO₂ concentration evolves through the year, take into account this effect requires to collect data from satellites or laser shots measuring the NO₂ concentrations. Anyway, when this study will be done, it will consist only to apply a correction factor to the equations of light propagation to take into account the NO₂ absorption.

4.1.4 Angular dependence of molecular and aerosol scattering

Due to the limited field of view of the FD telescopes and the typical geometry of an air shower, only a small fraction of the photons produced in the air shower are detected without scattering. Thus, the scattering properties of the atmosphere need to be well estimated. As in the transmission study, two primary forms of angular dependence are considered: the molecular one, mainly due to nitrogen and oxygen, and the aerosol one, due to airborne particles.

The angular dependence for both types of scattering may be described by a phase function $P(\zeta)$, defined as the probability per unit solid angle for scattering out of the beam path through an angle ζ . Following the convention for the atmospheric domain, $\sigma_m^{-1} d\sigma_m/d\Omega$ and $\sigma_a^{-1} d\sigma_a/d\Omega$ are the normalized differential molecular and aerosol scattering cross sections, respectively, which are identical to the phase functions $P_m(\zeta)$ and $P_a(\zeta)$. The integrals of $P_m(\zeta)$ and $P_a(\zeta)$ over all solid angles have to be equal to unity.

Rayleigh scattering provides an analytical form. The molecular phase function, symmetric in the forward-backward direction, is proportional to the $(1 + \cos^2 \zeta)$ factor. Due to the anisotropy of the N_2 and O_2 molecules, a small correction factor δ is included and is equal to around one percent in the case of air,

$$P_m(\zeta|\delta) = \frac{3}{16\pi(1+2\delta)} [(1+3\delta) + (1-\delta)\cos^2\zeta], \quad (4.9)$$

where the depolarization factor ρ_n is part of the new parameter δ

$$\delta = \frac{\rho_n}{2 - \rho_n}.$$

For Mie scattering, there is no analytical function to describe the photon scattering by aerosols. This is due to the fact that the cross section depends on the size distribution and shape of the scattering centres. Typically, forward scattering dominates in the Mie regime and the forward-backward ratio can vary strongly with aerosol type (see Figure 4.4). More details on the Mie phase function can be found in Chapter ?? where a phenomenological approach is developed.

The aerosol phase function is usually parameterized by the Henyey-Greenstein function [8]

$$P_a(\zeta|g, f) = \frac{1-g^2}{4\pi} \left[\frac{1}{(1+g^2-2g\cos\zeta)^{3/2}} + f \frac{3\cos^2\zeta-1}{2(1+g^2)^{3/2}} \right], \quad (4.10)$$

where $g = \langle \cos \zeta \rangle$ is the asymmetry parameter and f the relative strength of the forward to backward scattering peaks ($f = 0$ meaning no backward peak). The asymmetry parameter provides the scattered light intensity in the forward direction: a larger g means more forward-

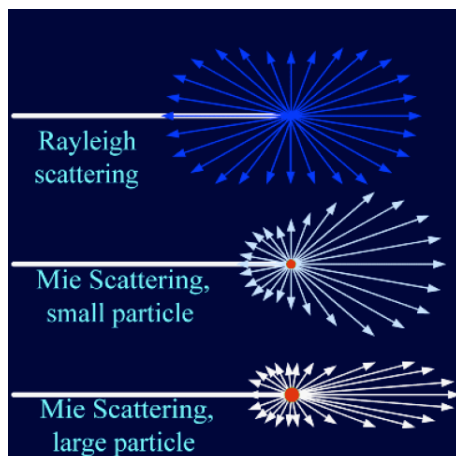


Figure 4.4: **Polar scattering plots in the Rayleigh regime and in the Mie regime.** Whereas Rayleigh scattering exhibits symmetry in the scattering angles, with a minimum reached at 90° , Mie scattering displays a large forward peak.

scattered light. Values go from $g = 1$ (pure forward scattering) to $g = -1$ (pure backward scattering), with $g = 0$ meaning isotropic scattering. The second term in the expression – a second-order Legendre polynomial, chosen not to affect the normalization of the phase function – is introduced to describe the extra backscattering component.

In Auger, the goal in monitoring the aerosol phase function will be to estimate the $\{g, f\}$ parameters, two observable quantities which depend on local aerosol properties.

4.2 Molecular measurements at the Pierre Auger Observatory

4.2.1 Weather station measurements and horizontal uniformity

Two main measurements of the molecular component are performed at the Pierre Auger Observatory. Firstly, close to each of the FD buildings and the CLF, ground-based weather stations were installed to record the temperature, pressure, relative humidity and wind speed every five minutes, even when FD data-taking is not operating. The first weather station was installed at Los Leones (LL) in January 2002, then the following one at the CLF in June 2004, at Los Morados (LM) in May 2007, at Loma Amarilla (LA) in November 2007 and at Coihueco (CO) in October 2009. Figure 4.5 shows the data accumulated in time for each weather station: to date, it is the CLF station which has recorded the largest amount of atmospheric data. The measurement errors are estimated to be $0.2 - 0.5^\circ\text{C}$ in temperature, $0.2 - 0.5$ hPa in pressure and 2% in relative humidity.

Figures 4.6–4.10 show the evolution in time of the monthly values for different physical quantities measured or calculated from the ground-based weather station data: temperature,

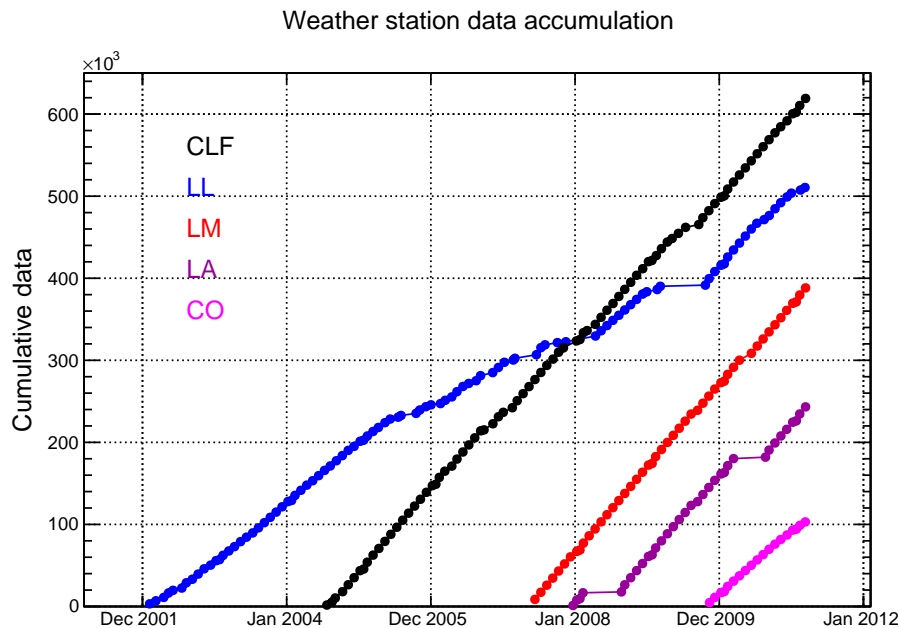


Figure 4.5: **Atmospheric data accumulation for each ground-based weather station.** Under typical data acquisition conditions, a station records monthly up to around 9000 measurements. A plateau in time means that the station could not store data because of problems due to lightning or power cuts, for example.

air density, vapour pressure and wind speed at the five locations. A clear seasonal cycle is observed for temperature, air density and vapour pressure. On the other hand, the wind speed does not display such a behaviour and an average speed around 3 m/s is measured throughout the year. In Figure 4.7, the measurements done at Los Leones depict high discontinuities since 2008. In fact, this weather stations had trouble in cold and wet conditions. Also, due to a faulty pressure sensor, data for 2007, 2008 and most of 2009 have been removed from weather analysis.

In Section 4.1, all the results were derived for the case where the atmospheric layers are horizontally uniform. Thus, it is important to check in the weather station data if such an assumption is verified since otherwise systematic errors could be introduced into the transmission calculation. Figure 4.11 plots the differences in temperature, air density, vapour pressure and wind speed between the CLF and one of the FD eyes. Despite the large horizontal separation of the different locations, the measurements are generally in good agreement. Table 4.3 gives the mean values and RMS values of the different quantities, for each FD eye. The dispersion for the vapour pressure is due to the lower accuracy for the relative humidity measurements. Based on these plots and observations, we can conclude that the molecular component of the atmosphere may be treated as uniform which is what will be done from

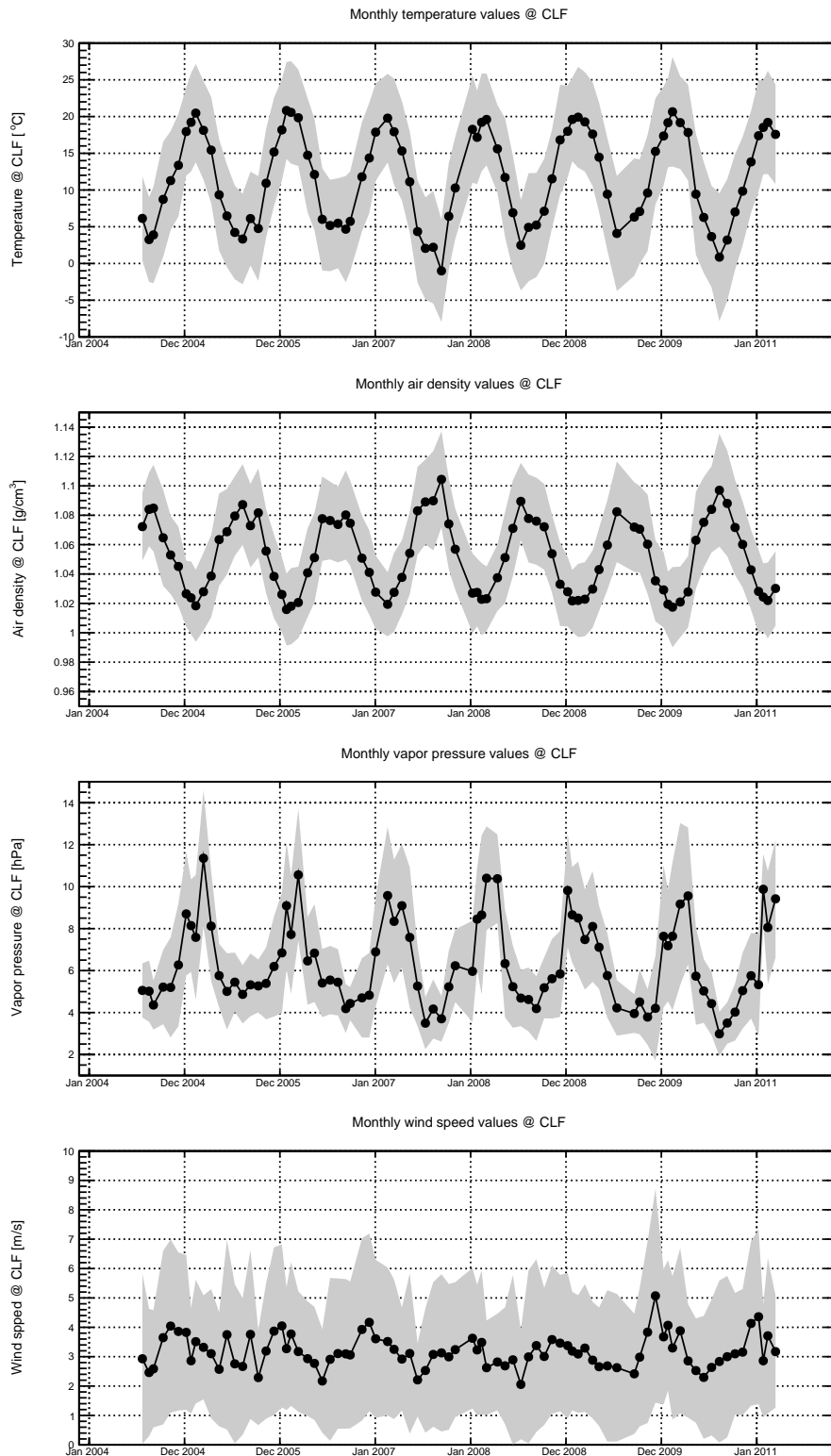


Figure 4.6: Monthly median ground temperature, pressure, and water vapour pressure observed at the CLF weather station (1.4 km above sea level). The gray contour contains 68% of the measurements. The vapour pressure has been calculated using measurements of the temperature and relative humidity.

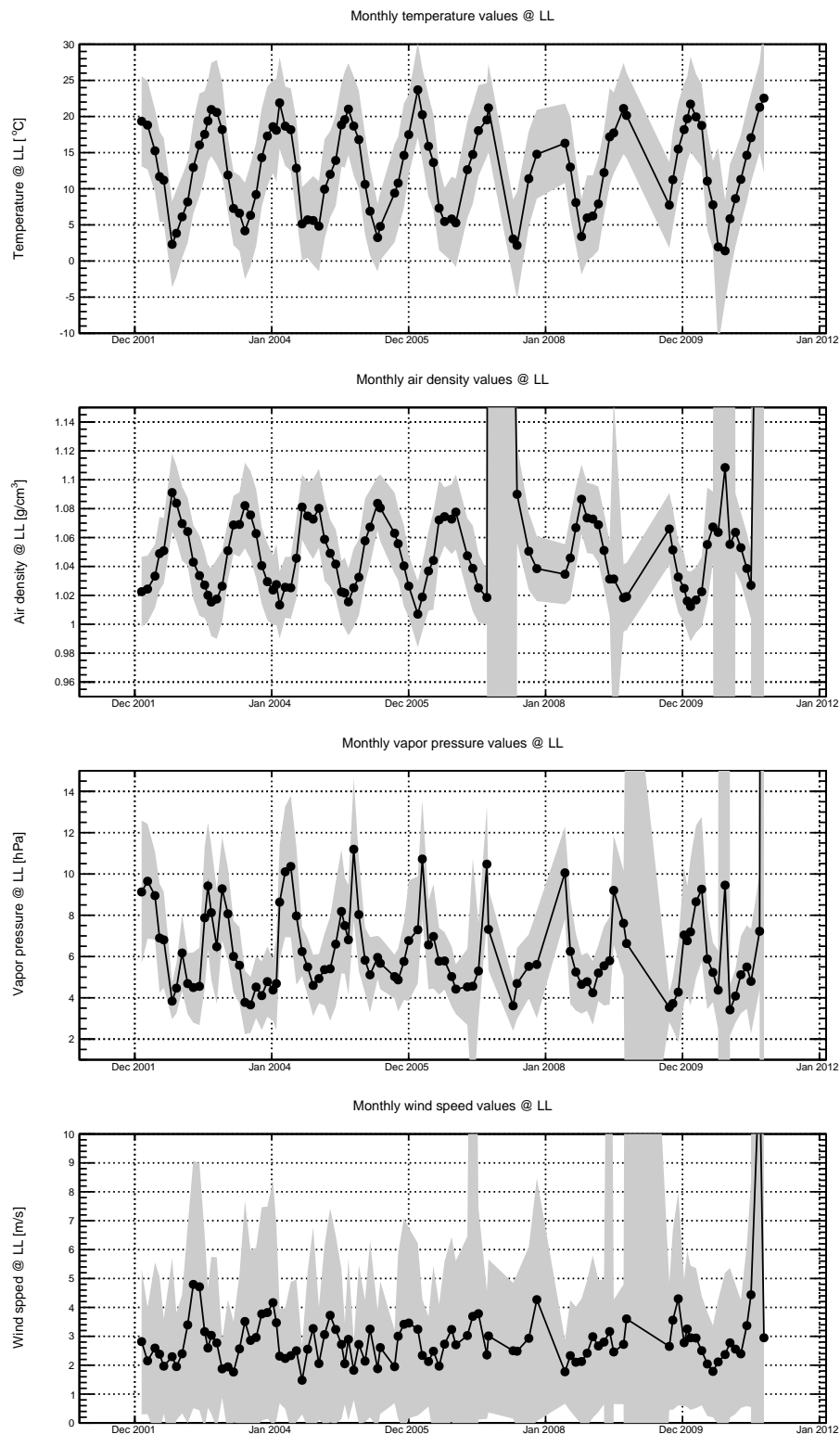


Figure 4.7: Monthly median ground temperature, pressure, and water vapour pressure observed at the Los Leones weather station (1.4 km above sea level). The gray contour contains 68% of the measurements. The vapour pressure has been calculated using measurements of the temperature and relative humidity.

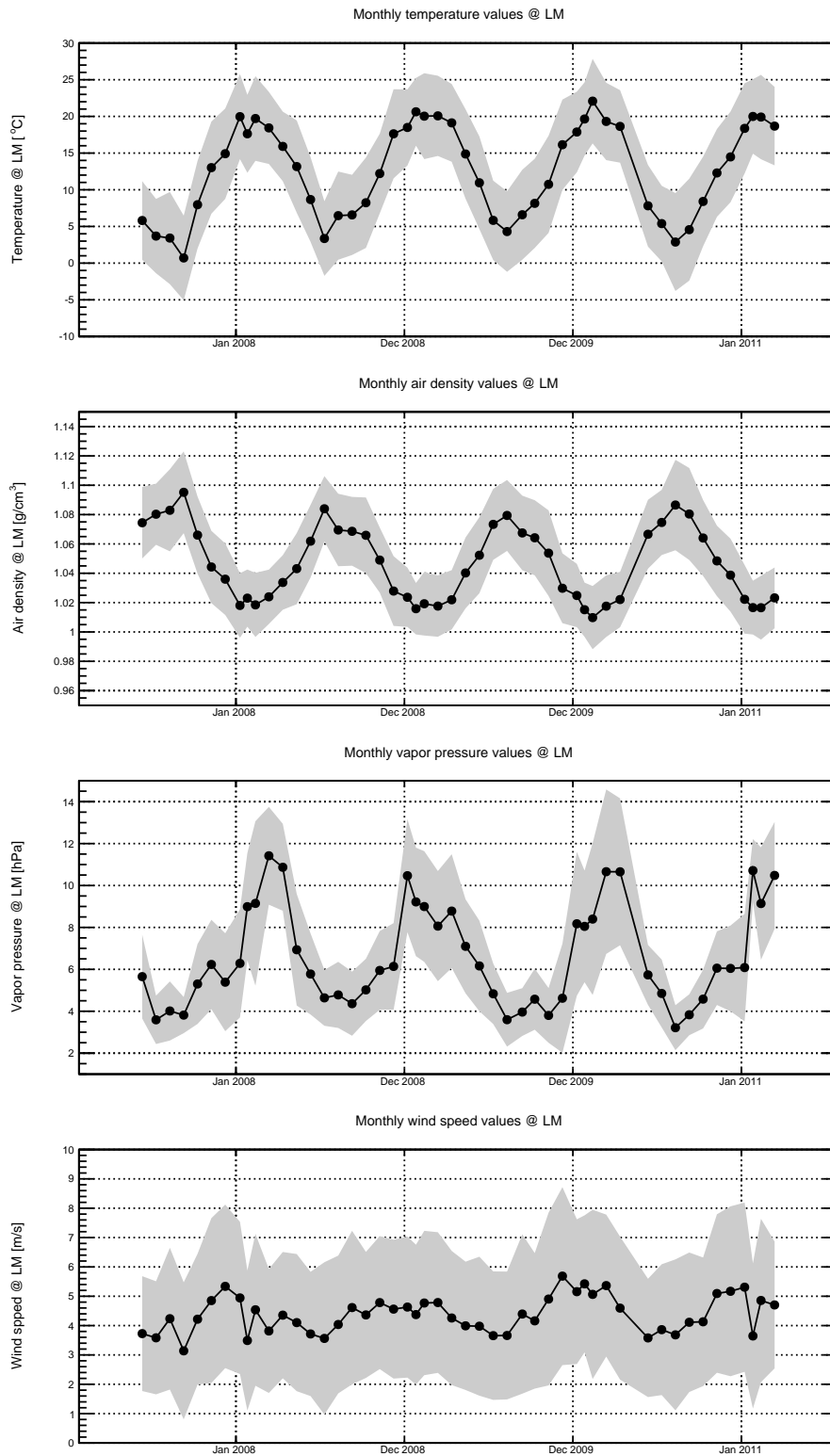


Figure 4.8: Monthly median ground temperature, pressure, and water vapour pressure observed at the Los Morados weather station (1.4 km above sea level). The gray contour contains 68% of the measurements. The vapour pressure has been calculated using measurements of the temperature and relative humidity.

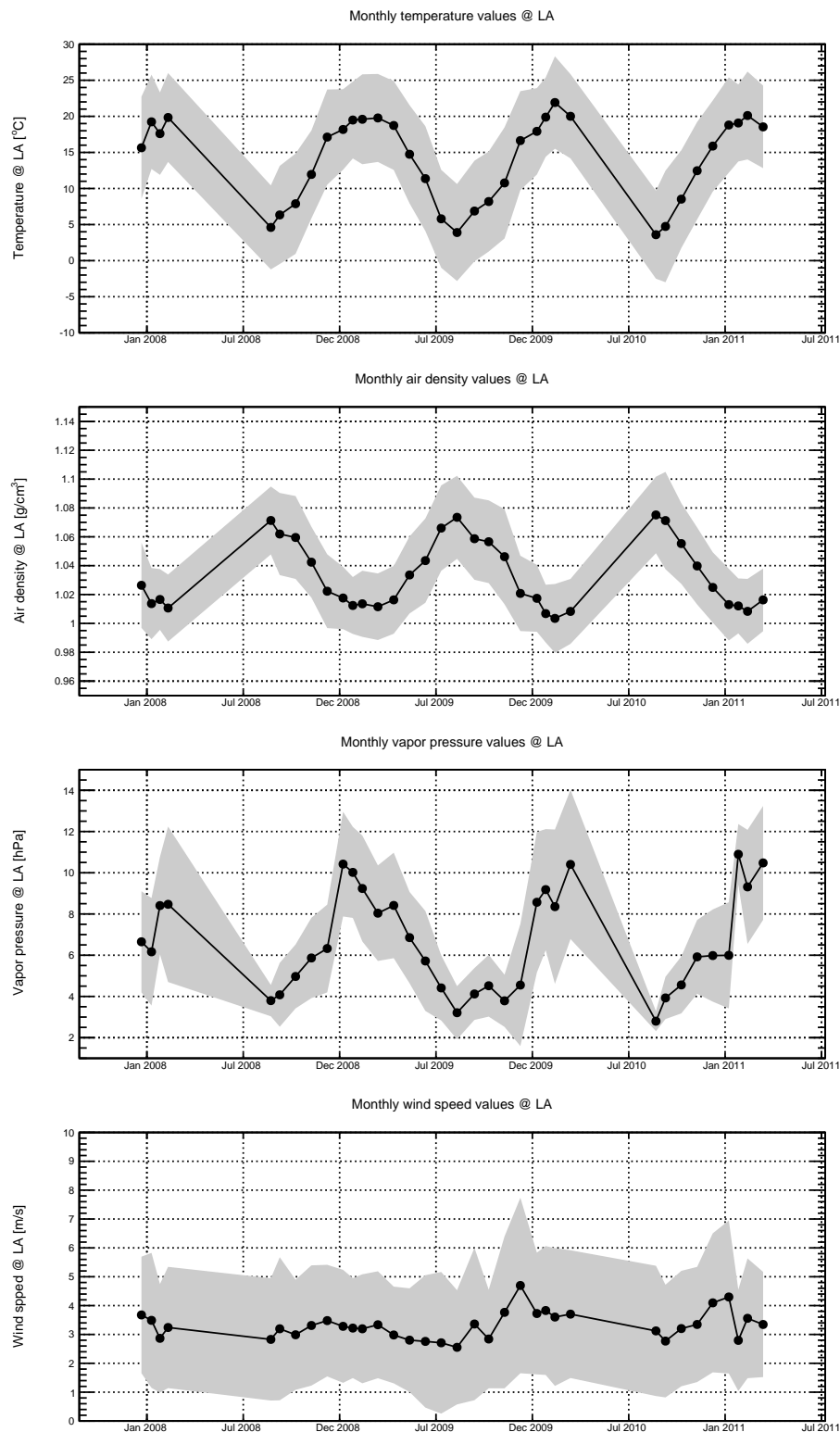


Figure 4.9: Monthly median ground temperature, pressure, and water vapour pressure observed at the Loma Amarilla weather station (1.5 km above sea level). The gray contour contains 68% of the measurements. The vapour pressure has been calculated using measurements of the temperature and relative humidity.

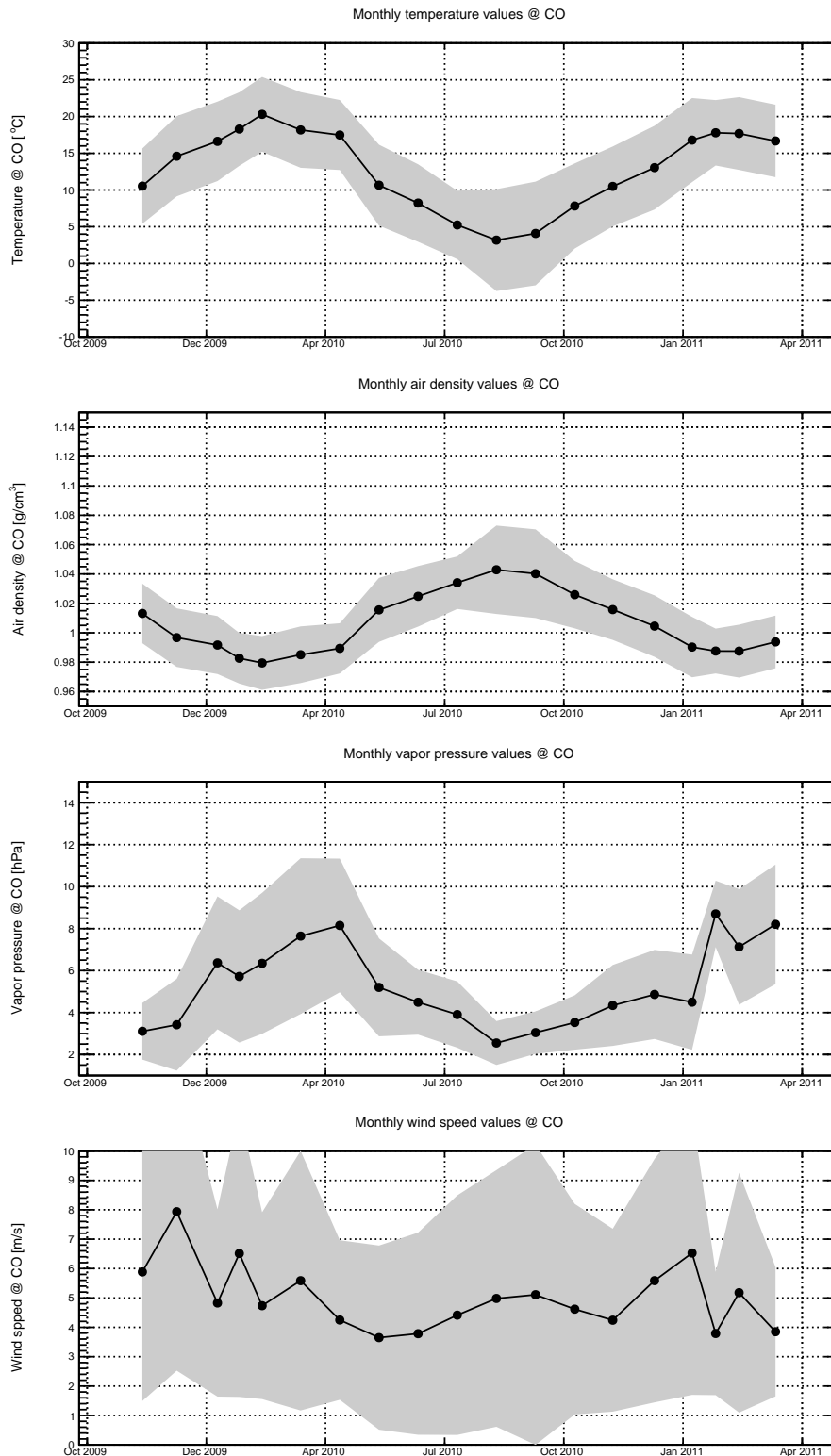


Figure 4.10: Monthly median ground temperature, pressure, and water vapour pressure observed at the Caihueco weather station (1.7 km above sea level). The gray contour contains 68% of the measurements. The vapour pressure has been calculated using measurements of the temperature and relative humidity.

here on in this manuscript.

FD	$\langle X_{\text{FD}} - X_{\text{CLF}} \rangle$				RMS($\langle X_{\text{FD}} - X_{\text{CLF}} \rangle$)			
	T [K]	n [g/cm ³]	e [hPa]	v_w [m/s]	T [K]	n [g/cm ³]	e [hPa]	v_w [m/s]
<i>LL</i>	+1.86	-0.003	-0.39	-0.78	0.51	0.006	1.44	2.28
<i>LM</i>	+2.78	-0.006	+1.07	+1.33	0.89	0.010	1.50	1.90
<i>LA</i>	+2.19	-0.014	+1.15	+0.01	0.92	0.008	1.63	1.69
<i>CO</i>	+3.05	-0.039	-1.04	+1.25	0.30	0.011	1.52	2.77

Table 4.3: **Horizontal uniformity of weather station data and dispersion.** Mean values and RMS values are given for the different histograms plotted in Figure 4.11. T : temperature, n : air density, e : vapour pressure, v_w : wind speed.

4.2.2 Radio-sonde measurements and monthly average atmospheric profiles

In addition to the weather stations on the ground, measurements on the latitude dependence of the state variables are needed to estimate the vertical molecular optical depth. Therefore, local atmospheric soundings have been performed over the SD array since 2003. At the beginning, several week-long campaigns of launches were performed. Then, the launches were repeated during the FD shifts and finally, with the Balloon-the-Shower (BtS) program, soundings are triggered by the detection of particularly high-energy events. The radio-sonde records data every 20 m, approximately, up to an average altitude of 25 km, well above the fiducial volume of the fluorescence detector. The measurement accuracies are around 0.2°C in temperature, 0.5 – 1.0 hPa in pressure and 5% in relative humidity.

The balloon measurements have shown that there are large daily variations in the temperature and pressure profiles. Figure 4.12 shows the atmospheric depth profile $X(h)$ with respect to the altitude above sea level. The largest daily fluctuations are around 5 g/cm² at ground level, increasing to 10 – 15 g/cm² between 6 and 12 km in altitude. The fluctuations during the Austral summer are lower than during the Austral winter.

In order to provide a set of atmospheric data for every event triggering the fluorescence detector, the soundings have been averaged to produce monthly models. Even if the models on average describe the atmosphere well, their use introduces systematic errors into measurements of shower energies and shower maxima.

4.2.3 Towards using the Global Data Assimilation System (GDAS)

Considerable effort is needed to estimate these monthly atmospheric profiles. Also, there is always a significant time delay between air shower detection and atmospheric measurements. Thus, recently, the Pierre Auger Collaboration began investigating the possibility of

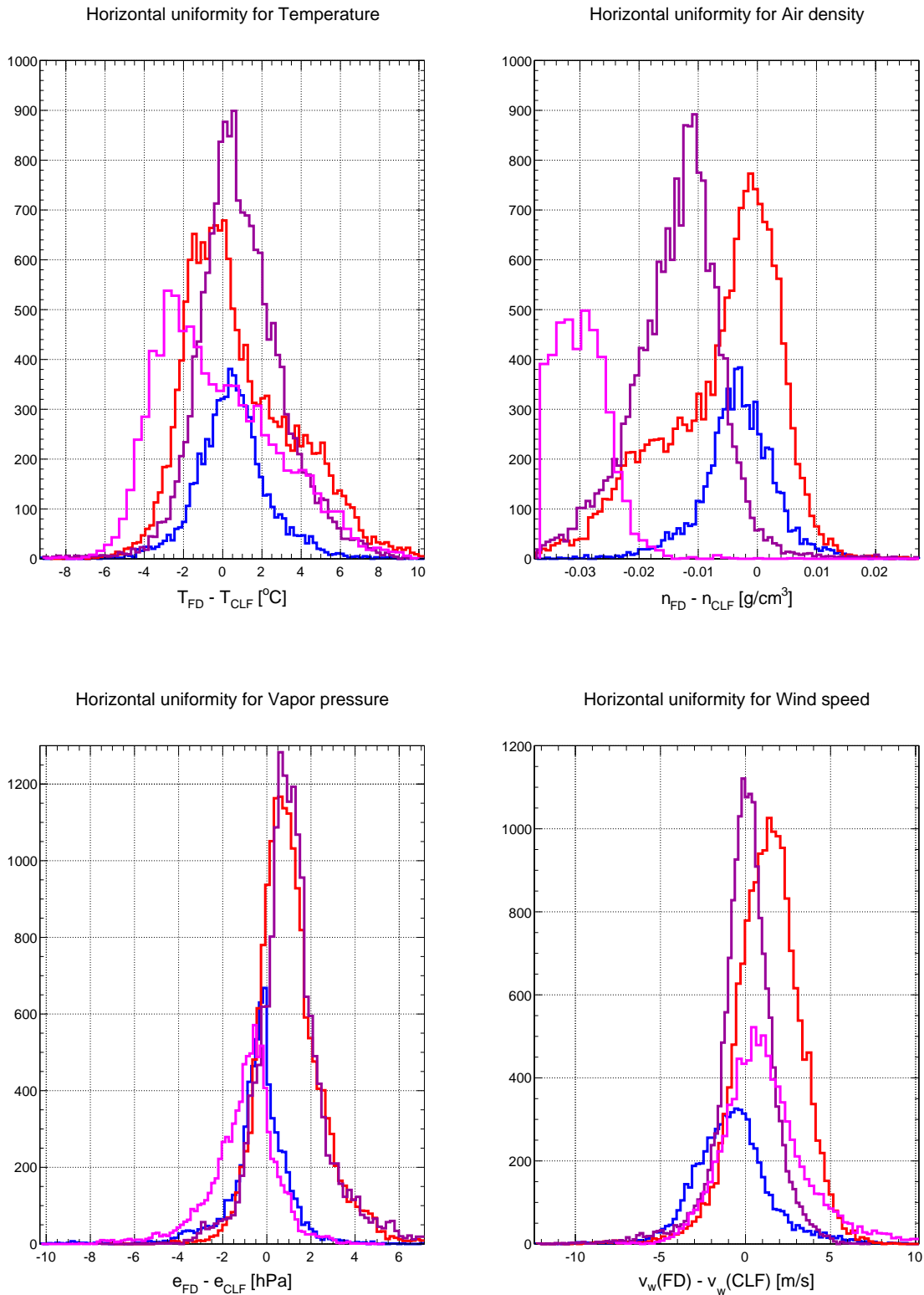


Figure 4.11: **Horizontal uniformity of weather station data and dispersion.** Difference between data measured at the CLF and one of the FD eyes: *Los Leones* in blue, *Los Morados* in red, *Loma Amarilla* in magenta and *Coihueco* in pink. The data set used is for the measurements done in 2011 only, epoch [where all the ground-based weather stations were working].

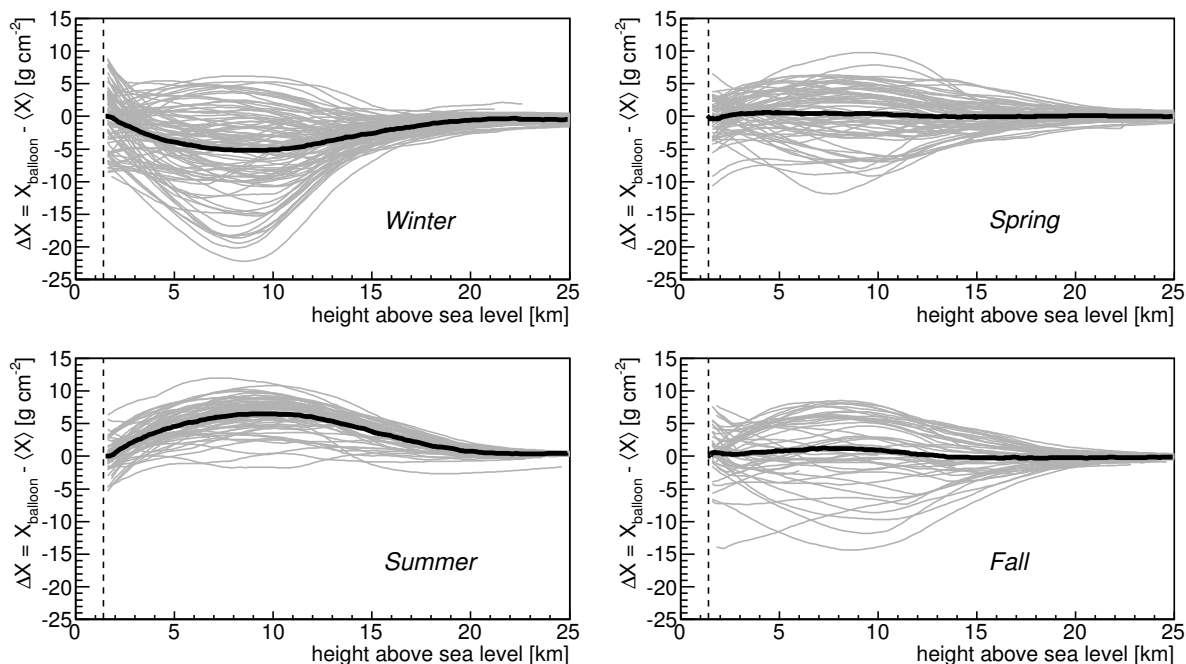


Figure 4.12: **Radio-sonde measurements of the depth profile recorded during balloon flights between 2002 and 2009.** The data are plotted as deviations from the average profile from all the data sets, and are grouped by season. The dark lines represent the mean seasonal profiles.

applying data coming from a global atmospheric model.

An atmospheric model is a mathematical model describing the atmospheric state at a given time and location. Most atmospheric models use a method called *data assimilation*: it combines several observations with expectations from a numerical weather prediction model. Usually, data come from observational networks of meteorological instruments placed all around the world. Mainly, these instruments are weather stations for the ground level and weather satellites to get vertical profiles of temperature, pressure or humidity. These observations are used to initialize the models.

In Auger, the model used is the Global Data Assimilation System (GDAS)⁴, an atmospheric model developed by the National Oceanic and Atmospheric Administration (NOAA). GDAS data became available starting in January 2005. They are updated every three hours over a one degree latitude/longitude grid ($360^\circ \times 180^\circ$). GDAS provides 23 pressure levels, i.e. 23 different altitudes. The GDAS grid point closest to the SD array is (35° S, 69° W), which is at the east of Loma Amarilla.

Before applying the GDAS model to the air shower reconstruction procedure, its data

⁴<http://ready.arl.noaa.gov/gdas1.php>

were compared with the weather station measurements and the monthly atmospheric profiles coming from the radio-sonde flights [3, 21]. Beyond 5 km, the GDAS data show only slight differences with respect to the radio-sonde data. At lower altitude, differences become larger. This disagreement can be investigated at ground level thanks to the Auger weather stations. While radio-sondes may suffer from uncertainties close to the ground, the weather stations are designed to continuously measure the ground values. Table 4.4 reports the differences for the atmospheric variables between the GDAS data and the ground-based weather station data.

	$\langle X_{\text{FD}} - X_{\text{GDAS}} \rangle$			$\text{RMS}(\langle X_{\text{FD}} - X_{\text{GDAS}} \rangle)$		
FD	T [K]	P [hPa]	e [hPa]	T [K]	P [hPa]	e [hPa]
CLF	+1.28	+0.35	-0.17	3.91	1.21	2.09
LA	-0.03	+0.15	-0.65	3.90	1.12	2.28

Table 4.4: **Comparison of the atmospheric quantities between the GDAS data and the weather station data.** Comparison done for CLF and LA sites, with the data recorded during 2009 [3]. T : temperature, n : air density and e : vapour pressure.

Despite the differences observed between radio-sonde data and GDAS at ground level, the comparison of GDAS data to the weather station data shows good agreement. It seems that the GDAS data can reproduce very well the measured data at ground level too. Thus it was shown that it is possible to use the GDAS data for the air shower reconstruction. Currently, a GDAS molecular database is implemented in the Offline software.

4.3 Aerosol measurements at the Pierre Auger Observatory

Several instruments are deployed at the Pierre Auger Observatory to observe aerosol scattering properties. The aerosol optical depth is estimated using UV laser measurements from the central lasers and scanning lidars; the aerosol phase function is determined with APF monitors and the wavelength dependence of the aerosol optical depth is measured with the optical telescopes HAM and FRAM.

4.3.1 Aerosol optical depth measurements

In the Pierre Auger experiment, the aerosol optical depth is measured through the night using two kinds of instruments, central laser facilities and lidars.

4.3.1.1 The Central Laser Facility (CLF)

The Central Laser Facility (CLF) is located on-site towards the centre of the Auger surface detector (see Table 4.5). Figure 4.13 holds a photograph of the facility as it can be seen in the Argentinean Pampa. It is powered by a battery, self-charged by thirteen solar panels, generating a maximum power of 885 Watts [22]. It is operated remotely via a wireless microwave internet link to the Coihueco FD site. Outside the container in which all the components are stored, a propane heater maintains a temperature above 10°C to prevent freezing of the instrument liquids. The main component is a laser producing a linearly polarized beam which becomes randomly polarized after a depolarizer (see Figure 4.14). The wavelength is 355 nm, in the middle of the nitrogen fluorescence spectrum produced by air showers. The pulse width of the beam is 7 ns and a maximum energy per pulse is around 7 mJ. This is of the order of fluorescence light produced by a shower with an energy of 10^{20} eV. To estimate the relative energy of each laser pulse, a portion of the beam is diverted into a photo-diode detector. The beam is generally directed vertically. Nevertheless, a mirror can send the light to a steering head mounted on the roof of the container. This consists of two rotatable mirrors making it possible to direct the beam towards any direction above the horizon. A filter can be used to make low-energy laser pulses which is especially useful for the laser shots directed almost horizontally towards the FD telescopes.

CLF location	
UTM Easting [zone 19H]	0469378
UTM Northing [zone 19H]	6095769
Altitude a.s.l. [meter]	1 412
Latitude [degree]	35 S
Longitude [degree]	69 W
Average vertical depth [g/cm ²]	880 ± 4.4
Distance to FD eyes [meter]	
Los Leones	25 987
Los Morados	29 566
Loma Amarilla	39 956
Coihueco	30 271

Table 4.5: **Absolute and relative positions of the CLF.** The geographical position and distances to each FD building are given here.

The main role of the CLF is to produce calibrated laser "test beams"⁵. When a laser shot

⁵In November 2008, the eXtreme Laser Facility (XLF) was deployed close to the CLF. After firing only vertical beams for the first two years, a steerable system was added in February 2011 allowing shots to be fired in any direction.



Figure 4.13: The Central Laser Facility, including the container, the solar panels and the propane heater, and the nearest SD tank, called Celeste. The tank, linked to the CLF by a fibre, receives laser light when a shutter, mounted on the optical table, is opened. The procedure allows synchronizing the SD array and the FD telescopes.

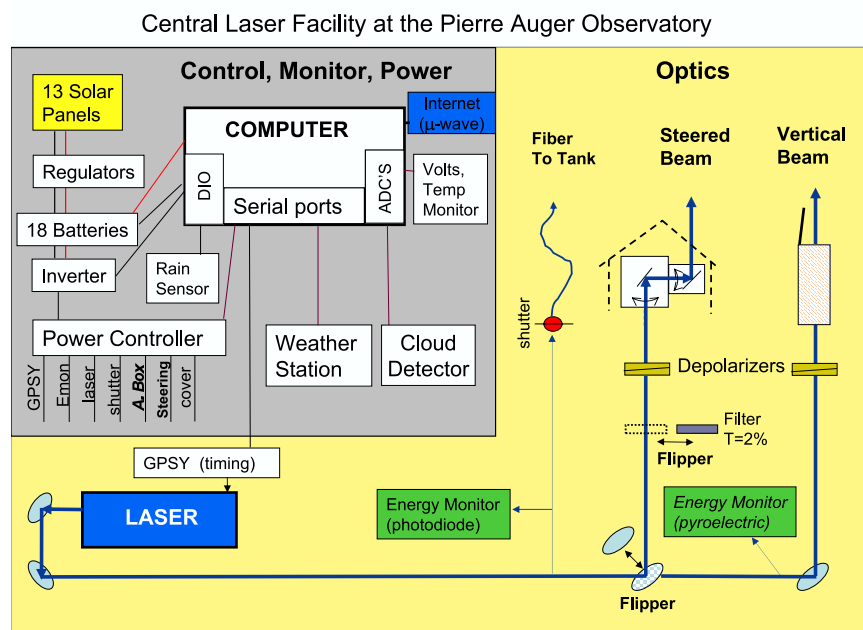


Figure 4.14: Schematic diagram of the CLF hardware (from [22]). The whole of the infrastructure is described in the grey box. The optics, producing the vertical and steered beams, is represented in the yellow region.

CLF laser system parameters		
	Vertical beam	Steered beam
<i>Energy calibration</i>	10%	12%
<i>Direction</i>	0.04°	0.2°
<i>Polarization</i>	< 4%	< 5%

Table 4.6: **Parameters of the CLF laser system.** Usually twice a year, the energy, direction and polarization are calibrated and if necessary readjusted to maintain them within the tolerances listed here.

is fired, the FD eyes collect a small fraction of the light scattered out of the laser beam. The recorded signal is not constant but depends on the atmosphere properties. Thus, a method has been developed in the Auger Collaboration to estimate the vertical aerosol optical depth $\tau_a(h, \lambda_0)$ with the CLF, where λ_0 is the CLF wavelength.

The method to determine $\tau_a(h, \lambda_0)$ normalizes the measurement of the laser beam to the signal that would be recorded under aerosol-free atmospheric conditions. The molecular references are average CLF laser profiles measured during very clear nights, the so-called "Rayleigh nights". Once a light profile, averaged over one hour, is normalized using a clear-night reference, the attenuation of the remaining light is due to aerosol scattering along the path from the laser beam to the FD telescope.

Estimation of the Aerosol optical depth by the CLF

The method assumes a horizontal uniformity for the molecular and aerosol components. The amount of light from the laser beam that reaches the detector at the elevation angle α is written as [23]

$$N_{\text{obs}}(\alpha) = N_0 (\Gamma_m \Gamma_a)_1 \left[P_m \left(\frac{\pi}{2} + \alpha \right) + P_a \left(\frac{\pi}{2} + \alpha \right) \right] (\Gamma_m \Gamma_a)_2, \quad (4.11)$$

where N_0 is the number of photons produced per laser pulse, $\{\Gamma_m, \Gamma_a\}$ are the molecular and aerosol transmission factors, and $\{P_m, P_a\}$ are the molecular and aerosol phase functions (see Section 4.1.4). The indices 1 and 2 correspond to the way from the CLF to the scattering location, and this from the scattering location to the detector, respectively.

In the case of a clear night, the aerosol transmission factor Γ_a is equal to one and the scattering over aerosols is negligible. Equation (4.11) is reduced to molecular part only

$$N_{\text{mol}}(\alpha) = N_0 (\Gamma_m)_1 \left[P_m \left(\frac{\pi}{2} + \alpha \right) \right] (\Gamma_m)_2.$$

Applying the aerosol horizontal uniformity condition, $\Gamma_a(h, \alpha, \lambda_0) =$

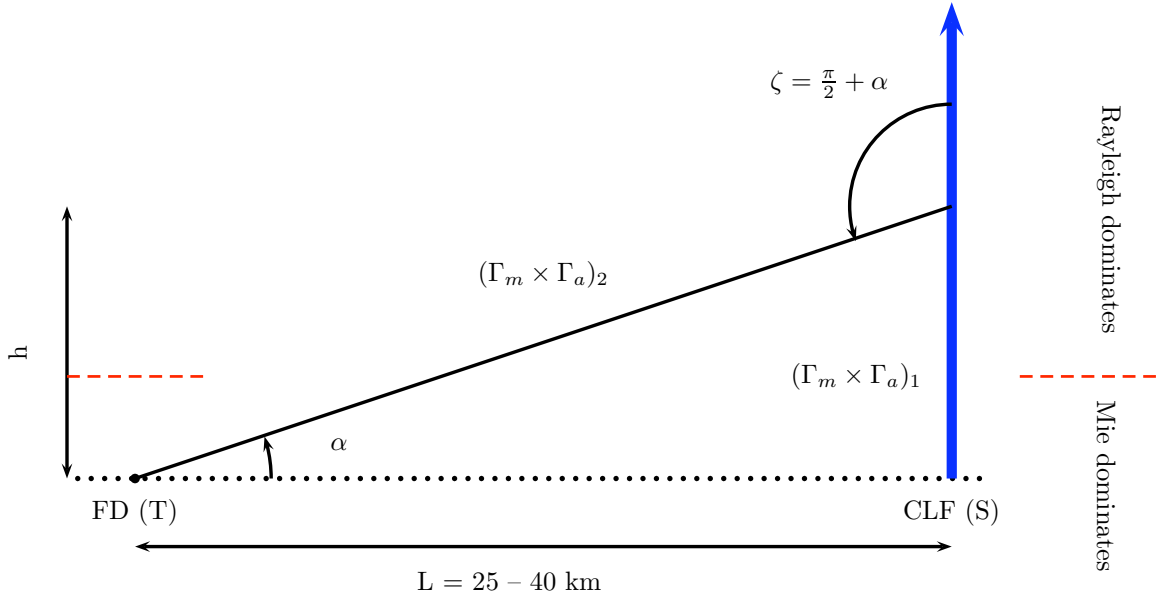


Figure 4.15: **Geometrical arrangement, viewed from the side, of the central laser CLF and the FD telescope.** The light is scattered out of the laser beam at a height h corresponding to an elevation angle α and a scattering angle $\zeta = \pi/2 + \alpha$. $(\Gamma_m \Gamma_a)_1$ and $(\Gamma_m \Gamma_a)_2$ are the total attenuations from the CLF to the scattering location and from the scattering location to the FD, respectively. The transition between the Mie domination and the Rayleigh domination is located just few kilometres above ground level, depending on the aerosol conditions.

$\exp[-\tau_a(h, \lambda_0)/\sin \alpha]$, and combining N_{obs} and N_{mol} , Equation (4.11) becomes

$$\tau_a(h, \lambda_0) = -\frac{\sin \alpha}{1 + \sin \alpha} \left[\ln \left(\frac{N_{\text{obs}}(\alpha)}{N_{\text{mol}}(\alpha)} \right) - \ln \left(1 + \frac{P_a(\frac{\pi}{2} + \alpha)}{P_m(\frac{\pi}{2} + \alpha)} \right) \right]. \quad (4.12)$$

In the scattering angle range seen by the FD eye (between 90° and 120° here) the aerosol scattering contribution is much lower than the molecular contribution. Equation (4.12) simplifies to

$$\tau_a(h, \lambda_0) = \frac{\sin \alpha}{1 + \sin \alpha} \ln \left(\frac{N_{\text{mol}}(\alpha)}{N_{\text{obs}}(\alpha)} \right). \quad (4.13)$$

With these approximations, the aerosol optical depth formula depends only on the elevation angle α of each laser track segment, linked to the altitude by $h = L \tan \alpha + h_{\text{Auger}}$, where L is the horizontal distance between the FD eye and the CLF, and h_{Auger} the altitude of the SD array above sea level.

Two different ways have been developed in the Collaboration to use this result. In fact, $N_{\text{mol}}(\alpha)$ can be determined either by Monte Carlo simulation [24], or from data collected under aerosol-free conditions [25]. The latter method does not require absolute calibration of

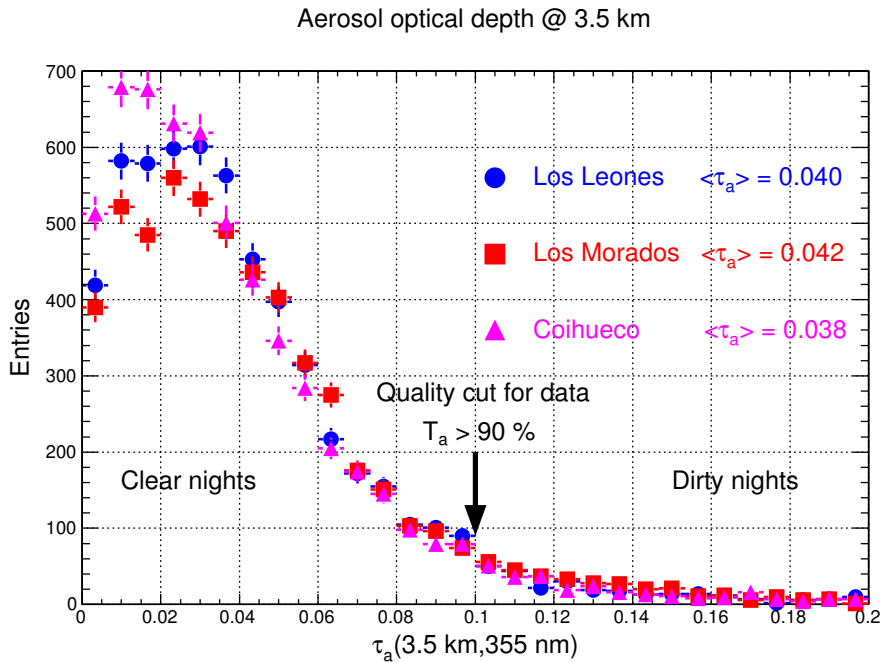


Figure 4.16: **Aerosol optical depth at 3.5 km above the fluorescence telescopes at Los Leones, Los Morados and Coihueco.** The wavelength, that of the CLF laser, is 355 nm. Data was acquired between January 2004 and December 2010.

the laser or the FD eye, all the factors being included in the recorded signals. On the other hand, normalizing to simulated events requires absolute calibrations and simulation of light propagation through a molecular atmosphere.

Figure 4.16 depicts the aerosol optical depth distribution recorded at Los Leones, Los Morados and Coihueco between 2004 and 2010. Measurements from Loma Amarilla are not available due to its large distance from the CLF site. The XLF, closer to Loma Amarilla, could provide optical depth information for this eye soon. Typically, at 3.5 km above the FD level, the mean value for $\tau_a(h, \lambda_0)$ is around 0.04. Note that a cut at 0.1 is used in the air shower reconstruction as a quality cut: all the events occurring in a night with a $\tau_a(h, \lambda_0) \geq 0.1$ are rejected.

Typical signals recorded during an aerosol-free night

The goal in this part is to calculate the signal recorded by the fluorescence telescope as a function of the elevation angle α . Indeed, in the case of "molecular" nights, typical profiles are expected for the collected light.

The atmosphere profile is approximated by an exponential. Thus, the molecular attenua-

tion length simplifies to

$$\Lambda_m(h) = \Lambda_0 \exp\left(\frac{h}{h_0}\right),$$

where $\Lambda_0 = 14.2$ km is the molecular attenuation length at sea level in the standard atmospheric conditions for a wavelength fixed at 355 nm; $h_0 = 8$ km is the molecular vertical scale.

During a "molecular night", the FD telescopes observe only photons scattered by the Rayleigh phenomenon. $N(h)$ is defined as the number of non-scattered photons after a length equal to $(h + h/\sin\alpha)$, corresponding to the sum of the travels from the CLF to the scattering location and from the scattering location to the fluorescence detector. For an infinitesimal altitude dh , we have

$$\begin{aligned} N(h + dh) &= N(h) - N(h) \left(1 + \frac{1}{\sin\alpha}\right) \frac{dh}{\Lambda_m(h)}, \\ \frac{dN}{N} &= - \left(1 + \frac{1}{\sin\alpha}\right) \frac{dh}{\Lambda_0} \exp\left(-\frac{h}{h_0}\right), \end{aligned} \quad (4.14)$$

where $h_{\text{Auger}} = 1452$ m is the ground altitude above sea level for the Pierre Auger Observatory.

By integrating Equation (4.14) between $h = h_{\text{Auger}}$ and h , we obtain

$$\begin{aligned} [\ln N]_{h_{\text{Auger}}}^h &= \left(1 + \frac{1}{\sin\alpha}\right) \frac{h_0}{\Lambda_0} \left[\exp\left(-\frac{h}{h_0}\right) \right]_{h_{\text{Auger}}}^h, \\ N(h) &= N(h_{\text{Auger}}) \exp \left[\frac{h_0}{\Lambda_0} \left(1 + \frac{1}{\sin\alpha}\right) \left(e^{-h/h_0} - e^{-h_{\text{Auger}}/h_0} \right) \right]. \end{aligned} \quad (4.15)$$

In order to take into account geometrical effects and scattering phenomena, we have to apply various multiplicative factors to the equation obtained:

1. The telescope collects only a part of the scattered signal. This part is given by the solid angle

$$\Delta\Omega = \frac{S_{\text{tel}} / \cos\alpha}{(L / \cos\alpha)^2},$$

where S_{tel} is the area of collection of one telescope.

2. In order to be detected by the FD telescope at a view angle α , photons emitted by the CLF have to be scattered by an angle equal to $(\pi/2 + \alpha)$. This probability is given by the Rayleigh phase function, i.e. the differential cross section normalized to the total scattering cross section

$$\frac{1 + \cos^2(\pi/2 + \alpha)}{2} = \frac{1 + \sin^2\alpha}{2}.$$

3. Moreover, this scattering is possible along the length Δh following an exponential law linked to the attenuation length. Thus the number of photons collected from a point at an altitude h has to be multiplied by the ratio between the length viewed by the telescope Δh and the attenuation length value at this corresponding altitude $\Lambda_m(h)$

$$\frac{\Delta h}{\Lambda_m(h)} = \frac{L \frac{d \tan \alpha}{d \alpha} \Delta \alpha}{\Lambda_0 \exp\left(\frac{h}{h_0}\right)} = \frac{L}{\Lambda_0} \frac{\Delta \alpha}{\cos^2 \alpha} \exp\left(-\frac{h}{h_0}\right),$$

where $\Delta \alpha$ is the angular diameter of a pixel ($\Delta \alpha = 1.5^\circ = 2.6 \cdot 10^{-2}$ rad). Indeed, $\Delta \alpha$ is the angular resolution of the detector: projected to the laser shot, it corresponds to the length Δh .

We know that $h = L \tan \alpha + h_{\text{Auger}}$. The number of photons collected as a function of the view angle α becomes

$$\begin{aligned} N(h) &= N_0 \exp\left[\frac{h_0}{\Lambda_0} \left(1 + \frac{1}{\sin \alpha}\right) \left(e^{-h/h_0} - e^{-h_{\text{Auger}}/h_0}\right)\right] \times \\ &\quad \frac{\Delta h}{\Lambda_m(h)} \Delta \Omega \frac{1 + \sin^2 \alpha}{2}, \\ N(\alpha) &= N_0 \exp\left[\frac{h_0}{\Lambda_0} \left(1 + \frac{1}{\sin \alpha}\right) \left(e^{-(L \tan \alpha + h_{\text{Auger}})/h_0} - e^{-h_{\text{Auger}}/h_0}\right)\right] \times \\ &\quad \frac{L}{\Lambda_0} \frac{\Delta \alpha}{\cos^2 \alpha} \exp\left(-\frac{L \tan \alpha + h_{\text{Auger}}}{h_0}\right) \frac{S_{\text{tel}} / \cos \alpha}{(L / \cos \alpha)^2} \frac{(1 + \sin^2 \alpha)}{2}, \\ N(\alpha) &= N_0 \frac{L}{\Lambda_0} \frac{\Delta \alpha}{\cos^2 \alpha} \frac{S_{\text{tel}} \cos \alpha}{L^2} \frac{(1 + \sin^2 \alpha)}{2} \times \\ &\quad \exp\left[\frac{h_0}{\Lambda_0} \left(1 + \frac{1}{\sin \alpha}\right) e^{-h_{\text{Auger}}/h_0} \left(e^{-(L \tan \alpha)/h_0} - 1\right) - \frac{L \tan \alpha + h_{\text{Auger}}}{h_0}\right]. \end{aligned} \tag{4.16}$$

4.3.1.2 Lidar observations

In addition to the CLF, a system of four elastic⁶ backscatter lidar stations is operated one at each fluorescence site. At each station, a UV laser emits short light pulses in the direction to be probed (see Figure 4.17). The backscattered light is detected as a function of time by photomultiplier tubes at the foci of parabolic mirrors. Both the laser and the mirrors are mounted on a steering frame that allows the lidar to cover the full range of azimuthal and elevation angles.

Once per hour, during FD data acquisition, the lidars perform a routine scan of the sky over each FD. By assuming a horizontal distribution of aerosols close to each lidar station, the

⁶the term *elastic* refers to the light scattering process: the return signal is measured at the same wavelength as the incident signal coming from the laser.

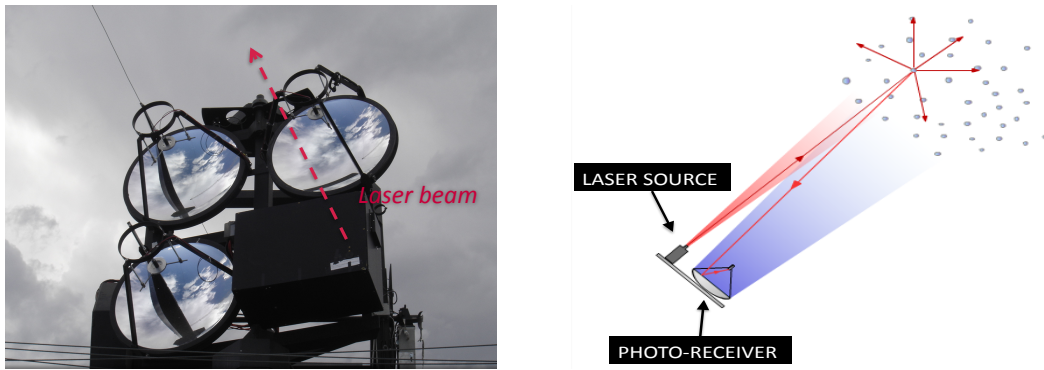


Figure 4.17: **Elastic backscatter LIDAR (Light Detection And Ranging)**. *Left panel:* One of the four lidars installed at the Pierre Auger Observatory. The three parabolic mirrors can be well seen. *Right panel:* Scheme of the lidar technique. The light, emitted by a laser and then backscattered in the atmosphere, is detected by the photo-receiver (photomultiplier).

vertical aerosol optical depth $\tau_a(h, \lambda_0)$ can be estimated from the differences in the backscattered light recorded at different angles. Also, clouds can be easily detected thanks to such a setup. Most of the time the lidar sweeps occur outside the FD field of view to avoid triggering the detector. Figure 4.18 gives a $\tau_a(h, \lambda_0)$ profile measured by lidar with vertical shots, and the corresponding CLF aerosol profile during a period of low atmospheric clarity. Up to 5 km above the FD level, the two measurements are in agreement within their systematic uncertainties. Two explanations are usually given for the disagreement between the two curves at greater altitudes. It could be due to an artifact of the reconstruction algorithm or perhaps something linked to the calibration, but this is not really understood at this stage. The challenge is that our sensitivity to aerosols decreases with height because the slant depth becomes smaller.

In addition to this automatic sweep program, the lidars are used for *Rapid Monitoring* [26]: if a high energy hybrid event is observed ($E > 20$ EeV), the routine scan is stopped and, within a few minutes of the event detection, the lidar scans the atmosphere in the region of the air shower recorded by the FD eye. This procedure, called "shoot-the-shower" (StS), makes it possible to reject events whose light profiles are distorted by clouds or aerosol non-uniformities.

4.3.1.3 Horizontal uniformity of aerosol optical depth

The horizontal uniformity has been emphasized previously for the molecular component, in Section 4.2.1. The purpose here is to see if the same assumption is valid for the aerosol part. Figure 4.19 shows the scatter plots of the aerosol optical depth $\tau_a(h, \lambda_0)$ measured at Los Morados and Coihueco with respect to the ones measured at Los Leones. The histograms of the differences between the optical depths are also given. The altitude is fixed at 3.5 km above

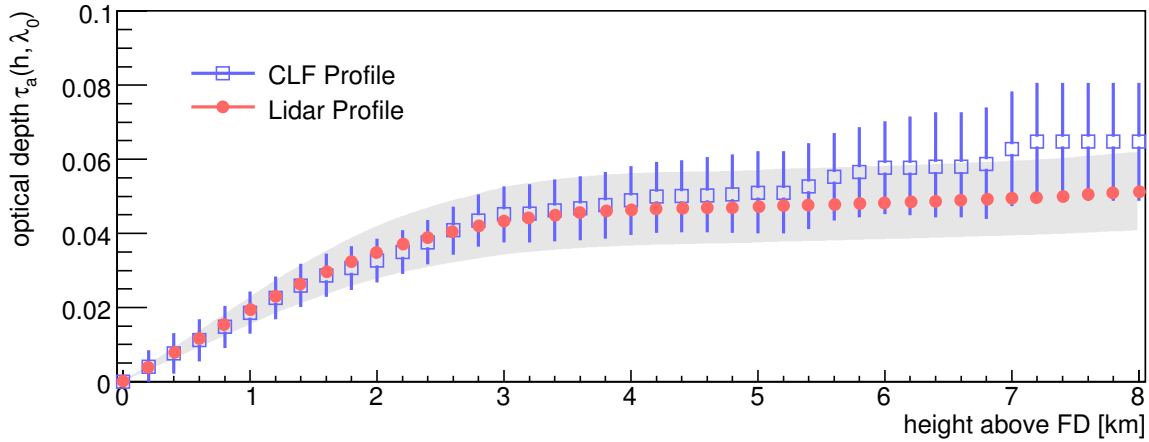


Figure 4.18: **Hourly aerosol optical depth observed by the CLF and the lidar at Coihueco (from [9]).** The grey band depicts the systematic uncertainty in the lidar aerosol profile.

the FD level and the wavelength at 355 nm (CLF wavelength). This means that different altitudes are probed at Los Leones and Coihueco, the latter being almost 300 m higher.

The optical depth data for the different sites suggest that aerosol conditions differ with location. The agreement is better between Los Leones and Los Morados, two sites which differ only slightly in altitude. The difference could be also explained by a different composition of the soil between the Coihueco site and the other ones, aerosols coming mainly from the ground. To take into account this non-uniformity, the implementation of the aerosol parameters into the Auger Offline software divides the SD array into five zones centred on the midpoints between the FD buildings and the CLF. Horizontal uniformity of the aerosol component is assumed in each slice. Then, each region is divided vertically into layers, each layer having a thickness equal to 200 meters.

4.3.2 Aerosol scattering measurements

The FD reconstruction of the cosmic ray energy has to take into account not only the light attenuated during propagation, but also has to remove the multiple scattering component which adds to the fluorescence light contamination. Aerosol scattering is described by the aerosol phase function $P_a(\zeta)$ which can be parameterized by a Henyey-Greenstein function as in Equation (4.10). To monitor this phase function through the night, values of the parameters $\{g, f\}$ are extracted.

At the Pierre Auger Observatory, two Aerosol Phase Function monitors (APF), in conjunction with the FD telescopes, are used to measure the parameters $\{g, f\}$ on an hourly basis during FD data acquisition (see Figure 4.20). The APF light sources emit a near-horizontal pulsed light beam in the field of view of their nearby FD eye at Coihueco and Los Mora-

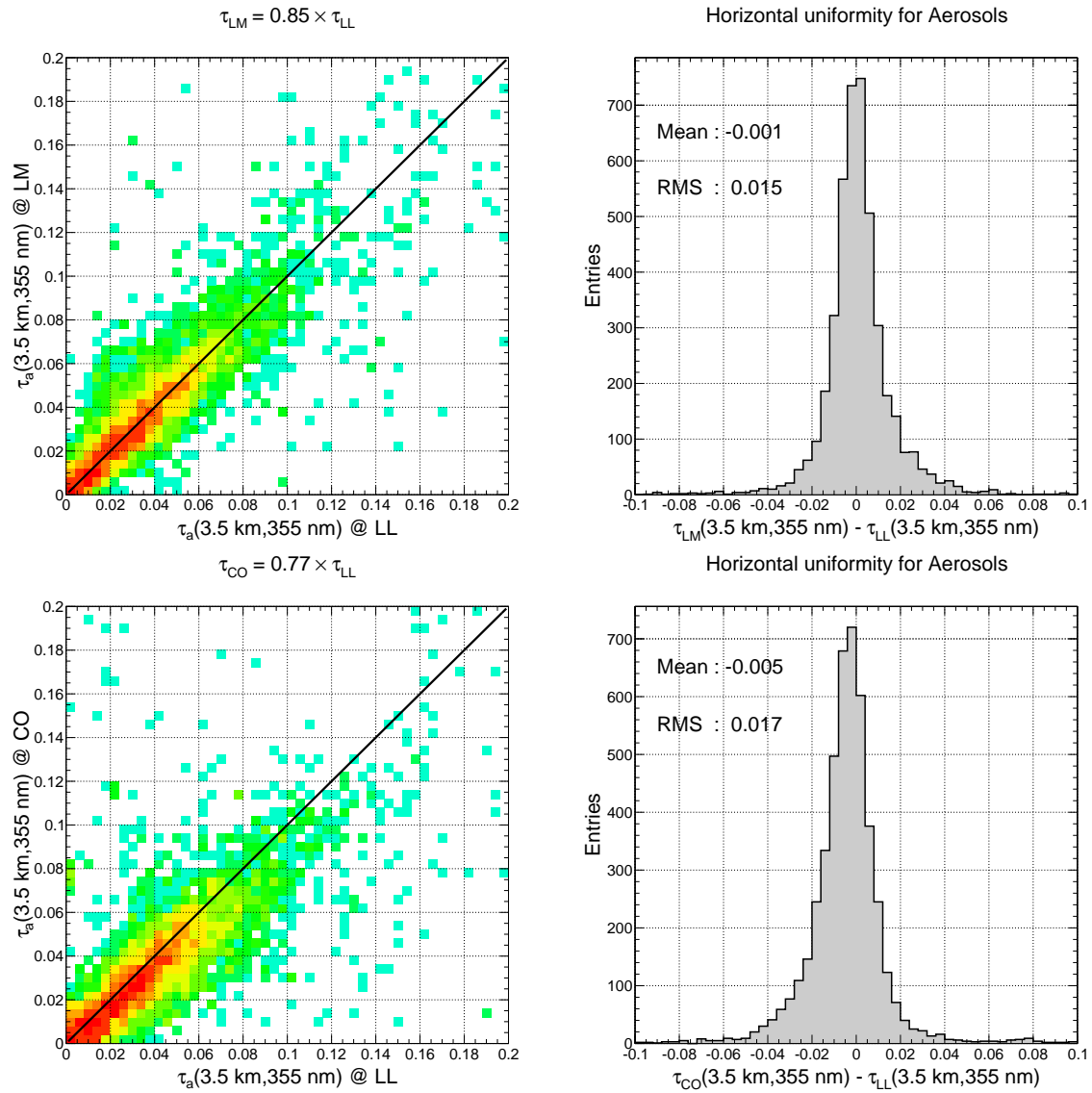


Figure 4.19: **Horizontal uniformity of the aerosol optical depths measured with CLF shots at Los Leones, Los Morados and Coihueco.** *On the left*, scatter plots show the correlation between two FD eyes, the solid line representing full agreement between two data points. *On the right*, histograms of the differences between the optical depths are plotted.

dos. Each APF building contains Xenon flash lamp sources which fire an hourly sequence of 350 nm and 390 nm shots. The aerosol phase function is then reconstructed from the intensity of the light observed by the FD cameras as a function of scattering angle ζ , for angles between 30° and 150° . After corrections to geometry, attenuation and collection efficiency for each pixel, the binned APF signal $S(\zeta)$ observed is subjected to a 4-parameter fit

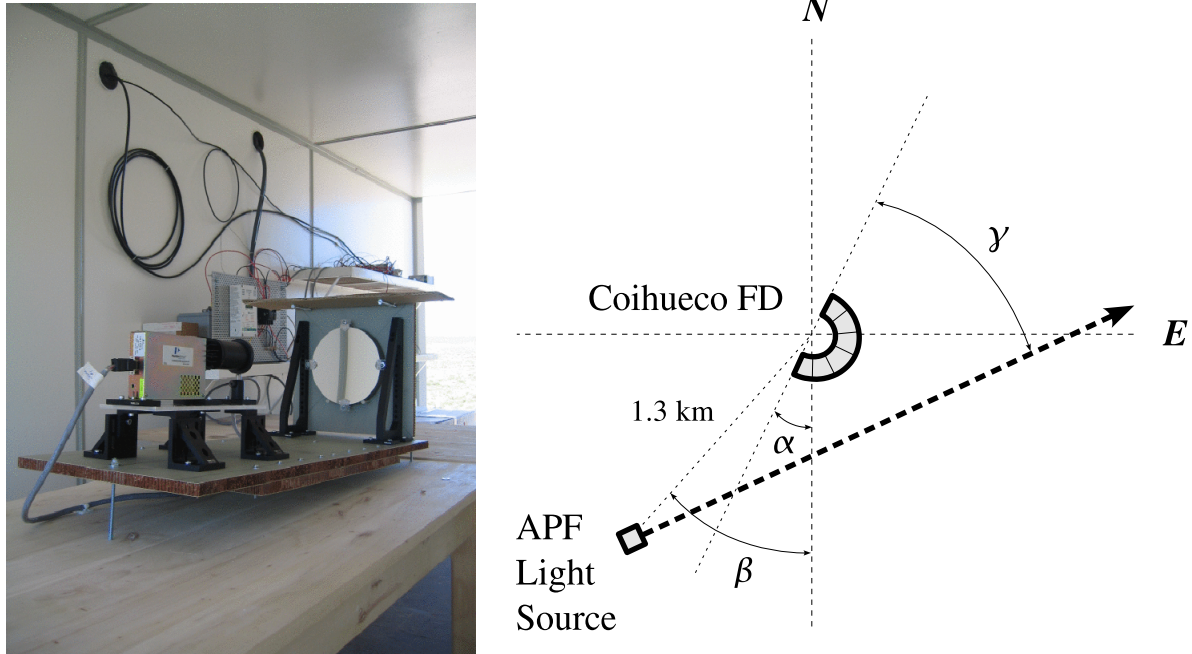


Figure 4.20: **Aerosol Phase function monitors at the Pierre Auger Observatory.** *Left panel:* Photograph of the light source of the APF monitor. *Right panel:* Scheme of the location of the Coihueco APF monitor relative to the Coihueco FD building.

$$S(\zeta) = C \left[\frac{1}{\Lambda_m(h_{\text{Auger}})} P_m(\zeta) + \frac{1}{\Lambda_a(h_{\text{Auger}})} P_a(\zeta|g, f) \right], \quad (4.17)$$

where $\{C/\Lambda_m(h_{\text{Auger}}), C/\Lambda_a(h_{\text{Auger}}), g, f\}$ are the fit parameters. The first two fit parameters can be used to estimate the molecular attenuation length and the aerosol attenuation length, respectively; while g and f are used to estimate the aerosol size distribution.

Figure 4.21 shows the distributions for the fit parameters measured at Coihueco between June 2006 and July 2008. It also gives the reduced- χ^2 distribution corresponding to the fit, indicating that the Henyey-Greenstein function describes reasonably well the aerosol phase function in this scattering angle range. The average g value is $\langle g \rangle = 0.56 \pm 0.10$, when one excludes the $g = 0$ nights corresponding to aerosol-free nights. Such a value for the asymmetry parameter corresponds to values usually measured in desert locations with significant levels of sand and soil dust [27]. The second parameter of the Henyey-Greenstein function, the backscatter coefficient, is estimated as $\langle f \rangle = 0.40 \pm 0.10$. It means that it exits a backward peak for the aerosol phase function. Hence, at the Pierre Auger Observatory, the typical aerosol phase function is described by $P_a(\zeta|g = 0.6, f = 0.4)$.

The measurements done by the APF monitors can also be compared to other atmospheric data to check the consistency between the different monitor setups installed at Malargüe. For

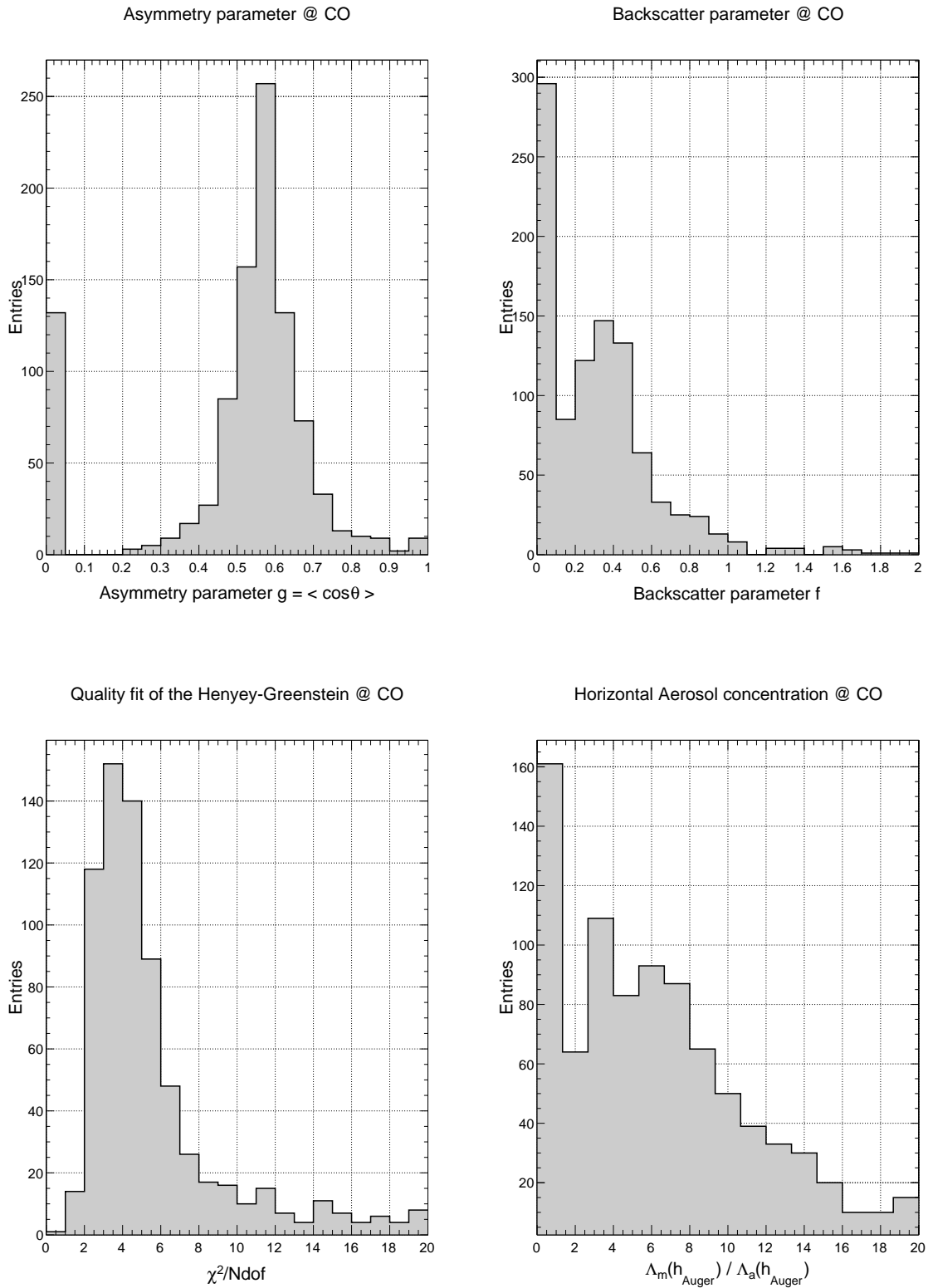


Figure 4.21: **Parameter distributions deduced from the Henyey-Greenstein fit to the APF data recorded at Coihueco between June 2006 and July 2008.** Only measurements at 350 nm are used here. The peaks in the low edge of the histograms for the asymmetry parameter g , the backscatter parameter f and the molecular concentration tracker Λ_m/Λ_a correspond to the aerosol-free night.

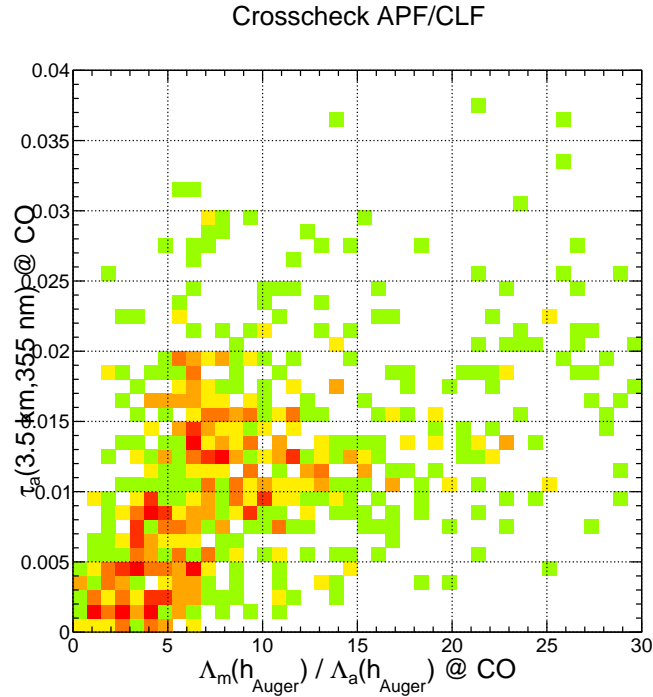


Figure 4.22: Crosscheck for the aerosol concentration measured by the CLF and the APF monitor, at Coihueco.

instance, Figure 4.22 checks the agreement between measurements done by the APF monitors and the CLF at Coihueco. From the APF data, it is possible to extract, for each recorded signal, the ratio Λ_m/Λ_a at the FD level, this quantity being a tracker for the aerosol concentration. It is shown that for the same period, a good correlation with aerosol optical depth data coming from the CLF is verified. To take into account the fact that APF monitors operate at ground level, the optical depths are measured at an altitude of 600 m above ground level.

4.3.3 Aerosol sampling measurements

So far, all the techniques mentioned before provide information on aerosols as attenuators or scattering centres but do not characterize the aerosols themselves. Such a characterization could help in the understanding of aerosol behaviour in the attenuation process. For instance, the atmospheric aerosols at the Pierre Auger Observatory are assumed to be desert-type particles. Also, in the air shower reconstruction done in the Offline software, the aerosols are pure scatterers: absorption is not taken into account, since it is assumed to be very small. But this assumption depends on the chemical composition of the aerosols. The results from aerosol sampling add new information about the aerosols at the site and can be compared with measurements obtained by the instruments using optical techniques such as the CLF or

the lidars. They can give a clearer idea about the origin of the aerosols present at the Auger Observatory, their sources and trajectories (see Chapter 6), and the connection between their composition and the meteorological variables in the region.

An Andersen-Graseby 240 dichotomous sampler (see Figure 4.23(a)) provided with polycarbonate membrane filters was used to separate fine size particles $PM_{2.5}$ (i.e. with an aerodynamic⁷ diameter $d \leq 2.5 \mu\text{m}$) and coarse particles PM_{10} ($d \leq 10 \mu\text{m}$) [28]. The sampling period was one day, beginning at 12 : 00 AM and ending at 11 : 59 AM of the following day. The samples were collected from June to November 2008, at the Coihueco location, on the roof of the FD building.

For gravimetric analysis and concentration measurements, a total of 34 filters containing fine particles ($PM_{2.5}$) and 37 filters containing coarse particles ($PM_{2.5-10}$) were considered. The concentrations, expressed as $\mu\text{g}/\text{cm}^3$, were calculated as the ratio between the collected mass and the volume of air passed through the sampler during a full sampling period. Figure 4.23(b) gives the evolution in time of the measured aerosol mass concentrations, from June to November 2008. An increase of the aerosol concentration is observed from winter to spring, which could be related to decreasing snowfall and increasing temperature. Although snowfalls are rare during winter, the low temperatures keep the snow from melting for long periods, reducing atmospheric particulates near the ground.

Particle morphology and elemental composition were studied using a Scanning Electron Microscope (SEM) equipped with an Energy Dispersive X-ray system (EDX). Table 4.7 gives average compositions determined by SEM/EDX on at least 30 individual particles. It shows that Si, Al, Ca, Mg, Fe and K, the typical mineral soil elements, are the major components. This indicates that aerosols are mainly dust suspended in the atmosphere. $PM_{2.5}$ fractions show more undetected particles due to the fact that beam focusing precision is insufficient to get a proper X-ray signal on particles smaller than one micron; thus many of them cannot be detected. Also, some particles in both fractions giving no detectable X-ray signal may be composed of light elements ($Z < 11$), presumably organic matter. SEM micrographs of two representative $PM_{2.5}$ and $PM_{2.5-10}$ samples are shown in Figure 4.24.

4.3.4 Wavelength dependence

Up to now, the measurements to estimate the aerosol optical depth have been done at a fixed wavelength, that of the laser of the CLF or the lidar. The empirical parameterization defined in Equation (4.8) gives a basic way to get the aerosol effect for any wavelength if the Ångström exponent is known. At the Auger Observatory, two different facilities were

⁷*Aerodynamic diameter* is a physical property of a particle in a viscous fluid such as air. In general, particles have irregular shapes with actual geometric diameters that are difficult to measure. Aerodynamic diameter is an expression of a particle aerodynamic behaviour as if it were a perfect sphere with unit-density and diameter equal to the aerodynamic diameter.

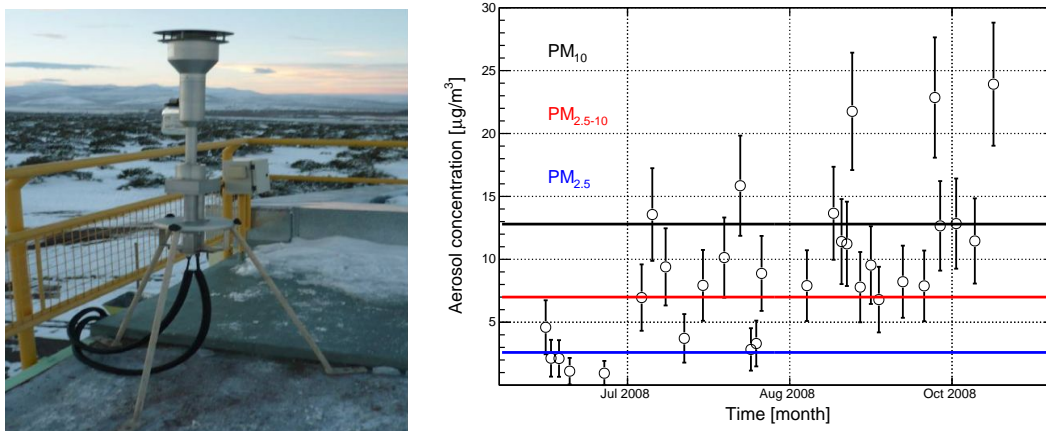


Figure 4.23: **Aerosol sampling at the Coihueco site.** (a) Andersen-Graseby 240 dichotomous sampler located at Coihueco, on the roof of the FD building. (b) Aerosol mass concentration for PM_{10} measurements at the Coihueco sampling site (the circles). The mean values for the three aerosol samplings are also given by the horizontal lines.

Concentration fractions for each element									
	Mg	Al	Si	P	S	K	Ca	Fe	Sum
$PM_{2.5}$ [%]	3.5	11.1	60.0		1.2		6.3		82
$PM_{2.5-10}$ [%]	4.4	16.3	69.4	0.7	0.3	0.5	4.6	3.7	100

Table 4.7: **Element concentrations of $PM_{2.5}$ and $PM_{2.5-10}$ fractions, obtained by SEM/EDX.**

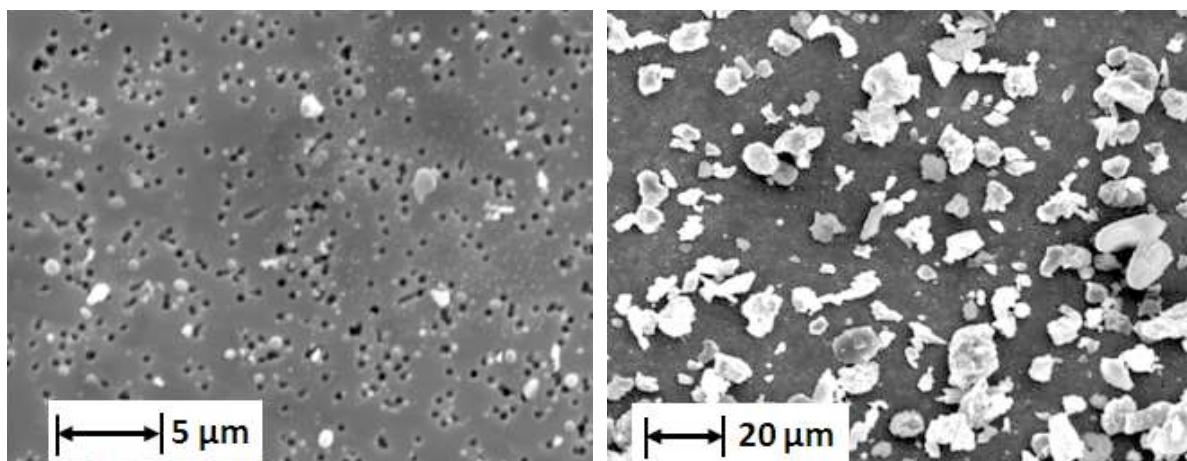


Figure 4.24: **Micrograph using Scanning Electron Microscopy (from [28]).** Left panel: Sampling of $PM_{2.5}$, collected on 7th July 2008. Right panel: Sampling of $PM_{2.5-10}$, collected on 27th October 2008.

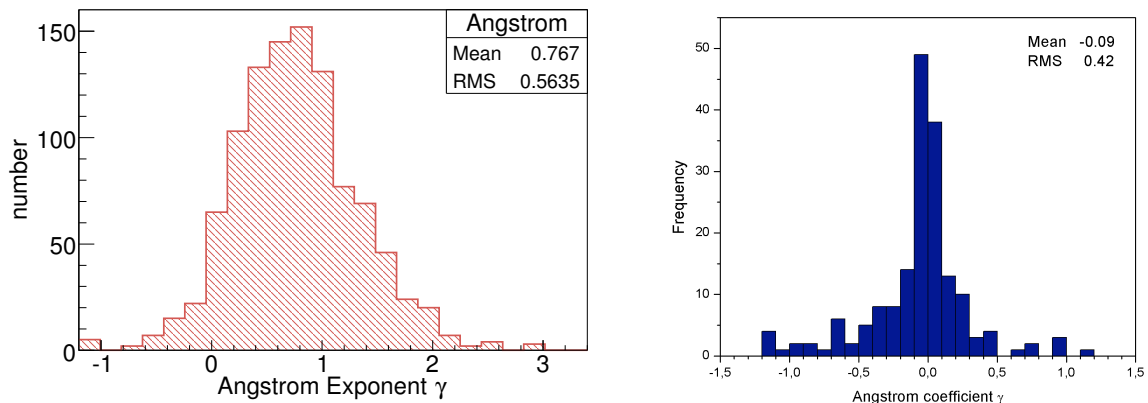


Figure 4.25: **Distributions of the Ångström exponent observed by the two monitors dedicated to this measurement at the Pierre Auger Observatory.** (a) Estimation of γ from the HAM for data recorded between July 2006 and February 2007. (b) Measured γ distribution for data collected by the FRAM from June 2006 until December 2008.

installed to estimate this key parameter: the Horizontal Attenuation Monitor (HAM) and the F/(Ph)otometric Robotic Atmospheric Monitor (FRAM).

The HAM consists of a high intensity discharge lamp located at Coihueco providing a large wavelength range source. To record the emitted light, a CCD camera is placed around 45 km away at Los Leones [29]. With this configuration the total horizontal atmospheric attenuation across the SD array can be obtained. Using a filter wheel, the camera records the aerosol attenuation between the two sites at five different wavelengths between 350 and 550 nm. By fitting the signal with respect to the wavelength, it is possible to estimate the Ångström exponent γ . From the data recorded between July 2006 and February 2007, the wavelength dependence displays a value $0.2 \leq \gamma \leq 1.2$ (see Figure 4.25(a)). The uncertainties are dominated by measurement fluctuations, and include a systematic effect due to subtraction of the estimated molecular attenuation between Los Leones and Coihueco.

The main task of the FRAM telescope is the continuous monitoring of the wavelength dependence of the aerosol attenuation [30]. The facility is located close to the Los Leones FD building. The method is the following: the telescope observes a set of chosen standard stars and, from these observations, it obtains extinction coefficients and their wavelength dependence. Five filters are used, for wavelengths between 360 and 547 nm. As preliminary results, the FRAM telescope estimates a value $-0.5 \leq \gamma \leq 0.3$ (see Figure 4.25(b)), lower than the results from the HAM instrument.

The small value of the exponent γ suggests that the Auger Observatory has a large component of coarse-mode aerosols, meaning aerosols larger than around $1 \mu\text{m}$.

4.4 Cloud detection at the Pierre Auger Observatory

Cloud coverage has an influence on the FD measurements: it biases the estimation of X_{\max} by producing bumps or dips in the longitudinal profiles and it decreases the observable flux of cosmic ray events. Thus, an event is reconstructed only if the cloud fraction is lower than 25%. Around 30% of the events are rejected due to cloudy conditions. During recent years, the Auger Collaboration has developed several methods to perform night time cloud monitoring.

Cloud coverage at the Pierre Auger Observatory is recorded by Raytheon 2000B infrared cloud cameras (IRCC) located on the roof of each FD building [31]. The cameras have a spectral range of 7 μm to 14 μm . During FD data acquisition, each IRCC records pictures of the whole FD field-of-view every 5 minutes: the raw image is converted into a binary image (white: cloudy / black: clear sky), then the fraction of cloud coverage for each pixel of the FD cameras is calculated producing the so-called FD pixel coverage mask. Different numerical filters are applied in succession to remove camera artefacts and to obtain a clear sky background as uniform as possible. In Figure 4.26, the raw IRCC images of the FD field of view are shown together with the final mask. The cloud information for each pixel is updated every 5 – 15 minutes, depending on the cloud coverage reconstruction. These cloud masks are stored in a database and are now used as quality cuts after the air shower reconstruction. Figure 4.27 gives an example of a cloud mask superposed on a telescope camera display, with the corresponding longitudinal profile showing dips and bumps typical for cloudy conditions.

A new method of identifying clouds above the Auger Observatory using infrared data from the imager instrument on the GOES-12/13 geostationary satellite is also used [32]. It obtains images of the South American continent every 30 minutes. Full-hemisphere images are produced in one visible band, and four Infrared bands centred at wavelengths 3.9, 6.5, 10.7 and 12.3 μm , respectively. A brightness temperature T_i is assigned to the i -th band. The whole array is described by 360 pixels: the infrared pixels projected on the ground have a spatial resolution of ~ 2.4 km horizontally and ~ 5.5 km vertically. The cloud identification algorithm uses the combination of $T_2 - T_4$ and T_3 to produce cloud probability maps (see Fig. 4.28). Data from the satellite indicate clear conditions (cloud probability lower than 20%) during $\sim 50\%$ of the FD data acquisition periods and cloudy (cloud probability higher than 80%) during $\sim 20\%$.

With the IRCC and the satellite data, cloud coverage can be followed throughout the night, but cloud height is not measured. At the Auger Observatory, this information is provided by the CLF / XLF and the lidars. The maximum height of clouds detected by these two techniques is between 12 km and 14 km, depending on the FD site. A cloud positioned on the vertical laser track scatters a higher amount of light, producing a peak in the recorded light profile. On the other hand, a cloud located between the laser and the FD site produces

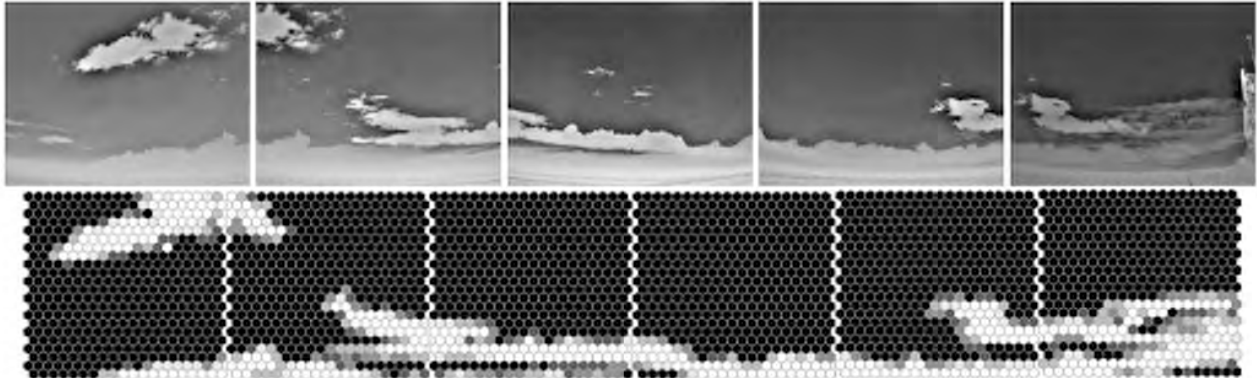


Figure 4.26: Cloud coverage for each pixel for a FD field-of-view. *Top panel:* Raw IRCC image. *Bottom panel:* FD pixel coverage mask, lighter values on the greyscale represent greater cloud coverage.

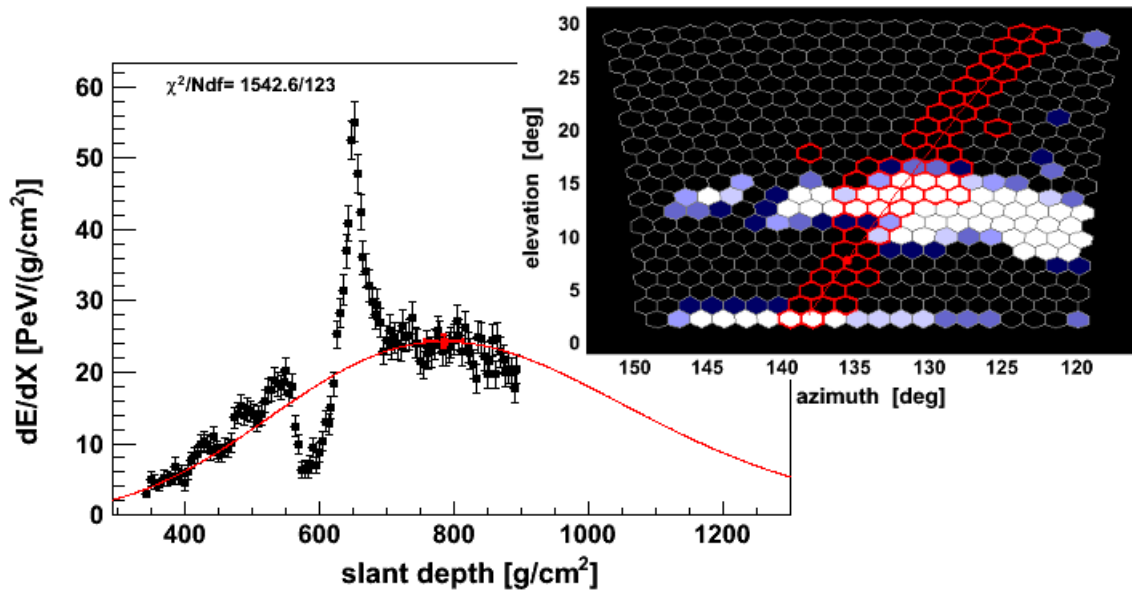


Figure 4.27: Display of an event recorded by an FD camera, with index of cloud coverage for each pixel (lighter pixels mean higher cloud coverage / pixels with no cloud are in black). Example of a measured extensive air shower where extra light has been scattered towards a fluorescence detector as a result of passing through a cloud. The corresponding cloud coverage mask is given as used in the event browser for the data files.

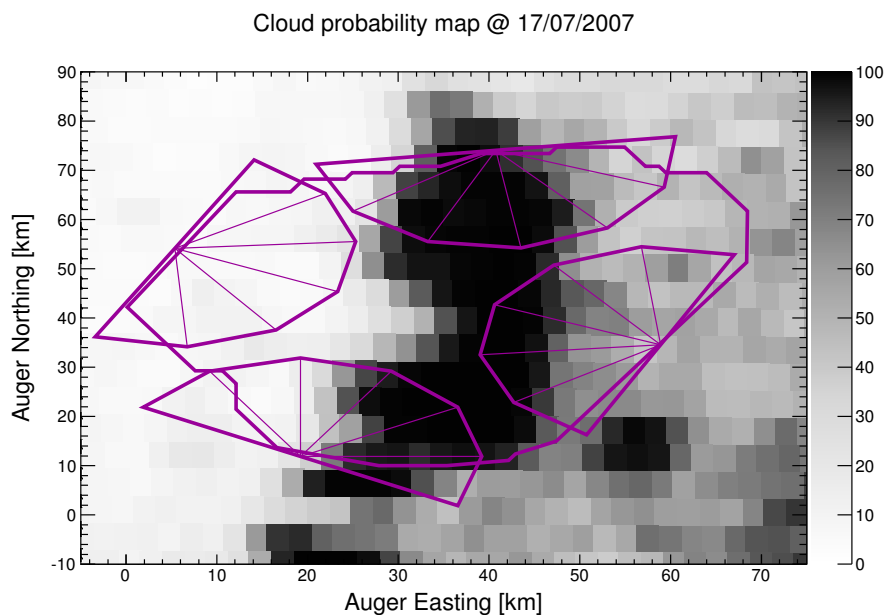


Figure 4.28: **Cloud probability map for 17/07/2007 at 01:09:24 UT from the GOES-12/13 satellite images.** The cloud probability for a region on a ground is given by the gray-scale on the right.

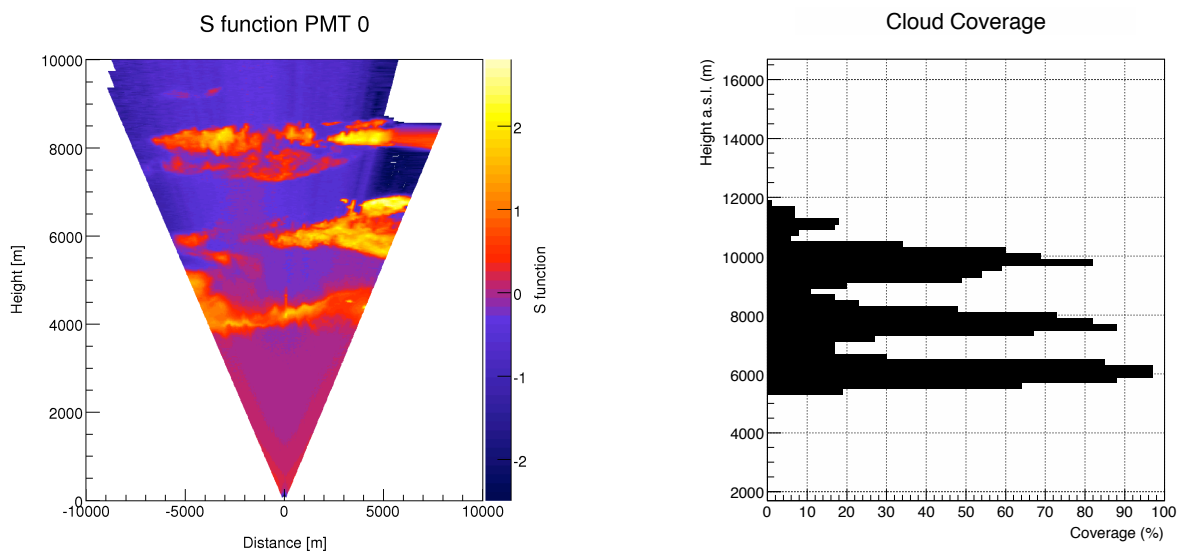


Figure 4.29: **Detection of several cloud layers at different heights by lidar (from [33]).** *Left panel:* Continuous scan in azimuth taken by the Coihueco lidar station. *Right panel:* From the cloud information, cloud coverage is estimated for each horizontal layer. Heights are relative to sea level.

4.5. Impact of the atmosphere on the reconstruction accuracy of air shower parameters¹³⁷

a local decrease in the laser light profile.

Finally, the lidars sweep the sky providing a 10 minute scan every hour. Clouds are detected as strong light scatter regions in the backscattered light profiles recorded by the lidars. The height of a cloud is deduced from the arrival time of the detected photons. The cloud-finding algorithm starts with the subtraction of the expected signal for a simulated purely molecular atmosphere from the real signal. Result is approximately constant in the zone outside the cloud, and has a non-zero slope inside the cloud. A second-derivative method to identify cloud candidates and obtain cloud thickness is applied. Figure 4.29 shows the intensity of the backscattered light as a function of height and horizontal distance from the lidar station, and its corresponding aerosol coverage reconstructed by the algorithm. After several months of lidar scans, the measurements have identified two cloud populations located at about 2.5 km and 8.0 km above sea level. These two peaks correspond to different kinds of clouds, the *alto* and the *strato* for the lowest one, and the *cirrus* for the highest one. The *cirrus* clouds, usually present at altitudes higher than 5.0 km, are in the cold region of the troposphere. At this height, water freezes: the clouds are composed of ice crystals. On the other side, the *alto* clouds created between 2.0 km and 5.0 km and the *strato* ones produced up to 2.0 km, composed mainly of water droplets, should represent this second peak.

4.5 Impact of the atmosphere on the reconstruction accuracy of air shower parameters

The atmospheric measurements described in Sections 4.2, 4.3 and 4.4 are fully integrated into the reconstruction procedure for the hybrid events recorded at the Pierre Auger Observatory. Whereas the molecular and aerosol data provide estimates for the systematic uncertainties in the cosmic ray measurements, cloud detection is only used as a quality cut. All the atmospheric information is used in the off-line reconstruction of an event.

In this section, we remind the reader of the results obtained in [9] with hybrid events recorded between December 2004 and December 2008. Strong quality cuts were applied to the data to remove events contaminated with clouds, as well as geometry cuts to eliminate events poorly viewed by the FD telescopes. Figure 4.30 lists the systematic uncertainties in the hybrid reconstruction due to atmospheric influences on light attenuation or production. It summarizes the impact of the atmosphere on the energy and X_{\max} measurements of the hybrid detector at the Pierre Auger Observatory. Except for quenching effects in the molecular category, the aerosols currently dominate the systematic uncertainties. The aerosol optical depth represents the largest source of error, with minor contributions from the Ångström parameter and the aerosol phase function. The use of hourly aerosol data offers a significant improvement over a static aerosol model, and when it is used decreases the systematic

Systematic uncertainties					
Source	log (E/eV)	$\Delta E/E$ (%)	RMS($\Delta E/E$) (%)	ΔX_{\max} (g cm ⁻²)	RMS(X_{\max}) (g cm ⁻²)
<i>Molecular light transmission and production</i>					
Horiz. uniformity	17.7–20.0	1	1	1	2
Quenching effects	17.7–20.0	+5.5	1.5–3.0	–2.0	7.2–8.4
p, T, u Variability	17.7–20.0	–0.5		+2.0	
<i>Aerosol light transmission</i>					
Optical depth	<18.0	+3.6, –3.0	1.6 ± 1.6	+3.3, –1.3	3.0 ± 3.0
	18.0–19.0	+5.1, –4.4	1.8 ± 1.8	+4.9, –2.8	3.7 ± 3.7
	19.0–20.0	+7.9, –7.0	2.5 ± 2.5	+7.3, –4.8	4.7 ± 4.7
λ -Dependence	17.7–20.0	0.5	2.0	0.5	2.0
Phase function	17.7–20.0	1.0	2.0	2.0	2.5
Horiz. uniformity	<18.0	0.3	3.6	0.1	5.7
	18.0–19.0	0.4	5.4	0.1	7.0
	19.0–20.0	0.2	7.4	0.4	7.6
<i>Scattering corrections</i>					
Mult. scattering	<18.0	0.4	0.6	1.0	0.8
	18.0–19.0	0.5	0.7	1.0	0.9
	19.0–20.0	1.0	0.8	1.2	1.1

Figure 4.30: **Systematic uncertainties in the hybrid reconstruction due to atmospheric influences on light attenuation or production (from [9]).**

uncertainties by a factor of two.

While molecular and aerosol scattering mainly attenuates shower light, it will also increase the recorded signal by scattering photons back into the field of view. This causes a systematic overestimation of the shower energy, especially at low altitudes where more scattering occurs. Several Monte Carlo studies have parameterized this multiply-scattered component of shower light as a function of the optical depth [34, 35]. Once multiple scattering is included in the reconstruction, the systematic uncertainties between various parameterizations of multiple scattering are $\Delta E/E < 1\%$ and $\Delta X_{\max} \simeq 1 \text{ g/cm}^2$.

The combined values from all atmospheric measurements are, as a function of energy:

- $\text{RMS}(\Delta E/E) \simeq (5 \pm 1)\%$ to $(9 \pm 1)\%$,
- $\text{RMS}(\Delta X_{\max}) \simeq (11 \pm 1) \text{ g/cm}^2$ to $(13 \pm 1) \text{ g/cm}^2$,

where the RMS values can be interpreted as the spread in measurements of energy and X_{\max} due to current limitations in the atmospheric monitoring program.

In this thesis, as will be explained later, we will focus on the aerosol component of the atmosphere, and especially on the effect of the aerosol size. The Auger Collaboration has assumed, up to now, a fixed aerosol phase function, with an asymmetry parameter $g = 0.6$. In the multiple-scattering corrections, this same aerosol phase function is used. One of the purposes of this thesis will be to show how a more realistic aerosol phase function can change the estimation of the energy and X_{\max} , and the corresponding systematic uncertainties (particularly for multiple scattering).

Bibliography

- [1] L Wiencke, for the Pierre Auger Collaboration, *Atmospheric "Super Test Beam" for the Pierre Auger Observatory*, Proc. 32nd ICRC, Beijing, China (2011).
- [2] B Keilhauer *et al.*, *Altitude dependence of fluorescence light emission by extensive air showers*, NIMA **597** (2008) 99–104.
- [3] B Keilhauer and M Will, *Data from the Global Data Assimilation System (GDAS) for the Pierre Auger Observatory*, **GAP-2011-015**.
- [4] J Burris *et al.*, *UV Raman Cross Sections in Nitrogen*, Appl. Spectrosc. **46** (1992) 1076–1076.
- [5] B Dawson, *New Rayleigh Scattering Implementation in the Offline*, **GAP-2006-007**.
- [6] A Bucholtz, *Rayleigh-scattering calculations for the terrestrial atmosphere*, Applied Optics **34** (1995) 2765–2773.
- [7] ER Peck and K Reeder, *Dispersion of air*, J. Opt. Soc. Am. **62** (1972) 958–962.
- [8] LC Henyey and JL Greenstein, *Diffuse radiation in the galaxy*, Astroph. J. **93** (1941) 70–83.
- [9] J Abraham *et al.* [Pierre Auger Collaboration], *A study of the effect of molecular and aerosol conditions in the atmosphere on air fluorescence measurements at the Pierre Auger Observatory*, Astropart. Phys. **33** 108–129.
- [10] RD Hudson, *Absorption cross sections of stratospheric molecules*, Can. J. Chem. **52** (1974) 1465–1478.
- [11] I Sokolik, *Atmospheric radiative transfer*, Fall 2005, http://irina.eas.gatech.edu/EAS8803_Fall12005/Lectures_fall12005.htm
- [12] J Orphal and K Chance, *Ultraviolet and visible absorption cross-sections for HITRAN*, Journal of Quantitative Spectroscopy & Radiative Transfer **82** (2003) 491–504.
- [13] J Brion *et al.*, *Absorption spectra measurements for the ozone molecule in the 350–830 nm region*, Journal of Atmospheric Chemistry **30** (1998) 291–299.
- [14] C Hermans *et al.*, *Fourier transform measurements of SO₂ absorption cross sections: temperature dependence in the 24000–29000 cm⁻¹ (345–420 nm) region*, Journal of Quantitative Spectroscopy & Radiative Transfer **110** (2009) 756–765.
- [15] JL Jimenez, *Lecture 7: Photochemistry of important atmospheric species*, Atmospheric Chemistry, CHEM-5151, Spring 2005.

- [16] CD Ahrens, *Essentials of Meteorology – An invitation to the Atmosphere*, 3rd Edition, Thomson Brooks/Cole.
- [17] *Ambient Concentrations of Nitrogen Dioxide*, US EPA, <http://cfpub.epa.gov> (2010).
- [18] *Sulfur dioxide*, US EPA, <http://www.epa.gov/airtrends/sulfur.html> (2009).
- [19] M Chiwa *et al.*, *Atmospheric concentrations of nitric acid, sulfur dioxide, particulate nitrate and particulate sulfate, and estimation of their dry deposition on the urban- and mountain-facing sides of Mt. Gokurakuji, Western Japan*, *Environ. Monit. Assess* **140** (2008) 349–360.
- [20] M Gottwald *et al.*, *Monitoring the Changing Earth’s Atmosphere*, published by DLR (2006).
- [21] D Epperlein *et al.*, *Investigation of Applying a Global Atmospheric Model to the Southern Site of the Pierre Auger Observatory*, **GAP-2010-074**.
- [22] B Fick *et al.*, *The Central Laser Facility at the Pierre Auger Observatory*, *JINST* **1** (2006) 11003–11019.
- [23] RU Abbasi *et al.* [HiRes Collaboration], *Techniques for measuring atmospheric aerosols at the high resolution Fly’s Eye experiment*, *Astropart. Phys.* **25** (2006) 74–83.
- [24] M Ambrosio *et al.*, *Evaluation of atmospheric aerosol concentration from CLF data analysis*, **GAP-2005-056**.
- [25] MD Roberts, *Atmospheric aerosol determination using vertical laser tracks from the central laser facility*, **GAP-2006-067**.
- [26] S BenZvi *et al.*, *The Rapid Atmospheric Monitoring System of the Pierre Auger Observatory*, **GAP-2010-073**.
- [27] DR Longtin *et al.*, *A wind dependent desert aerosol model: radiative properties*, Air Force Geophysics Laboratories (1988) **AFL-TR-88-0112**.
- [28] MI Micheletti *et al.*, *in press* (2011).
- [29] S BenZvi, for the Pierre Auger Collaboration, *Measurement of Aerosols at the Pierre Auger Observatory*, *Proc. 30th ICRC, Mérida, México* **4** (2007) 355–358.
- [30] P Trávníček, for the Pierre Auger Collaboration, *New method for atmospheric calibration at the Pierre Auger Observatory using FRAM, a robotic astronomical telescope*, *Proc. 30th ICRC, Mérida, México* **4** (2007) 347–350.
- [31] MG Winnick, *Cloud cameras at the Pierre Auger Observatory*, **GAP-2010-111**.

-
- [32] J Chirinos *et al.*, *Identifying clouds over the Southern Auger Observatory using satellite data*, **GAP-2010-094**.
- [33] R Mussa *et al.*, *Detecting clouds with elastic lidar telescopes*, **GAP-2007-038**.
- [34] MD Roberts, *The role of atmospheric multiple scattering in the transmission of fluorescence light from extensive air showers*, *J. Phys. G* **31** 1291–1301.
- [35] J Pekala *et al.*, *Atmospheric multiple scattering of fluorescence and Cherenkov light emitted by extensive air showers*, *NIMA* **605** (2009) 388–398.

Ramsauer approach for light scattering on non-absorbing spherical particles

Contents

5.1	Light scattering on spherical particles	145
5.1.1	Scattering by single particles: general considerations	145
5.1.2	Scattering by small particles: Rayleigh scattering	147
5.1.3	Scattering in the intermediate size range: Mie scattering	148
5.2	Application of the Ramsauer effect for light scattering	151
5.2.1	The Ramsauer scattering phase function	151
5.2.2	The simplified Ramsauer scattering phase function	155
5.2.3	Validity of the Ramsauer solutions	156
5.2.4	Effects of averaging over sizes	158
5.3	The Ramsauer total cross section and extinction efficiency	158
5.3.1	Ramsauer total cross section via the Optical theorem	161
5.3.2	Ramsauer total cross section via the differential cross section	165
5.4	Ramsauer approach to large aerosols as a possible source of the FD halo	166
5.4.1	Description of the FD halo phenomenon, and its discovery	166
5.4.2	The Aerosol Phase Function at the Pierre Auger Observatory	168
5.4.3	On possible underestimation of phase function at small angles	169
5.4.4	Explanation of the FD halo by a component with large aerosol size	172
5.5	Conclusion	175
	Bibliography	177

Introduction: We present in this chapter a new method to study light scattering on non-absorbing spherical particles. This method is based on the Ramsauer approach, a model known in atomic and nuclear physics. Its main advantage is its intuitive understanding of the underlying physics phenomena. This work led to a journal paper published at the end of

the first year of my PhD thesis¹. This model was later applied to the Auger context and the results were presented in an internal note².

¹Ramsauer approach to Mie scattering of light on spherical particles, *Phys. Scr.* **80** (2009) 035403.

²Ramsauer approach to large atmospheric aerosols as a possible source of the FD halo, **GAP-2009-173**.

The subject of light scattering by small particles is present in several scientific areas such as astronomy, meteorology and biology [1]. The first model by Lord Rayleigh in 1871 dealt with light scattering by particles whose dimensions are small compared to the wavelength. A significant improvement came with the Mie solution [2] which describes light scattering by spherical particles of any size. In an apparently different domain, the scattering of a low energy electrons by atoms studied by Ramsauer experimentally [3] showed surprising structures, and it was several years before the explanation found by Bohr by describing the electron as a plane wave [4–6]! The Ramsauer effect is certainly the first phenomenon showing the wave properties of matter. This framework has since then been used to describe very different types of collisions such as atom-atom [7] or even neutron-nucleus [8–12]. Our idea is that since light behaves like a wave, it should be also possible to apply Ramsauer’s ideas to light scattering by spherical particles.

In this chapter, we calculate, using the Ramsauer approach, the differential scattering cross section normalized to the total cross section, the so-called phase function. Section 5.1 is a brief reminder of some basic aspects concerning light scattering on (non-absorbing) spherical particles. Section 5.2 describes the Ramsauer effect and provides details on the way to obtain the Ramsauer phase function. We compare the Ramsauer predictions with the Mie calculations, emphasizing certain characteristics of light scattering. Then, in Section 5.3, we integrate the differential cross section to obtain the total cross section and the associated extinction efficiency parameter using the Ramsauer approach. Finally, Section 5.4 presents an application of the Ramsauer approach in the context of the Pierre Auger Observatory; an unexpected phenomenon was observed during an FD calibration campaign which can possibly be explained by large aerosols in the atmosphere.

5.1 Light scattering on spherical particles

It is straightforward to calculate the cross section for plane wave light scattering from a uniform dielectric sphere using classical electromagnetic theory. One possible application of the resulting formulae is the determination of particle sizes by measuring the distribution of angular scattering intensity. This section presents briefly the light scattering problem, applied to spherical particles.

5.1.1 Scattering by single particles: general considerations

When light interacts with particles, two different kinds of processes can occur. The energy received can be reradiated by the particle at the same wavelength. Usually, the reradiation takes place with different intensities in different directions. This process is called *scattering*. Alternatively, the radiant energy can be transformed into other forms of energy, such as heat:

absorption takes place. In Auger, with a fluorescence spectrum produced in the UV range, it can be assumed that scattering dominates absorption.

The light attenuation process can be analyzed by considering a single particle of arbitrary size and shape, irradiated by a plane electromagnetic wave. At a distance r , large compared to the particle size and the wavelength, the scattered energy appears as a spherical wave, centered on the particle and having a phase shift with respect to the incident beam.

The intensity of light scattered at an angle θ by a single spherical particle with a radius R , from a beam of unpolarized light of wavelength λ and intensity I_0 is given by

$$I(\theta) = \frac{I_0}{r^2} \times \sigma_{\text{sca}}(R, \lambda) \times P(\theta), \quad (5.1)$$

where I_0 is the initial intensity of the beam, $\sigma_{\text{sca}}(R, \lambda)$ the scattering cross section and $P(\theta)$ the scattering phase function³. The *scattering cross section* $\sigma_{\text{sca}}(R, \lambda)$ has the dimension of area but is not in general equal to the particle cross-sectional area. Indeed it is customary to define a *scattering efficiency*

$$Q_{\text{sca}} = \frac{\sigma_{\text{sca}}(R, \lambda)}{\pi R^2}, \quad (5.2)$$

where πR^2 is the geometric cross section in the case of a sphere of radius R .

The scattering efficiency represents the ratio of the energy scattered by the particle to the total energy in the incident beam intercepted by the geometric cross section of the particle. Similarly, absorption efficiency Q_{abs} is defined as the fraction of the incident beam absorbed per unit of cross-sectional area of particle. The total energy removed from the incident beam, the extinction energy, is the sum of the energy scattered and absorbed. The corresponding extinction efficiency is given by

$$Q_{\text{ext}} = Q_{\text{sca}} + Q_{\text{abs}} \iff \sigma_{\text{tot}} = \sigma_{\text{sca}} + \sigma_{\text{abs}}. \quad (5.3)$$

As already mentioned, the ratio of the particle size to the wavelength of the radiation of interest is of crucial importance for the particle's optical properties as well as for the choice of a suitable method for calculating those properties. We therefore define the dimensionless size parameter as

$$x = \frac{2\pi R}{\lambda} = k_{\text{out}} R, \quad (5.4)$$

where R is the radius of a spherical particle, λ the light wavelength and k_{out} the wave number outside the sphere. In the case of non-spherical particles, R might represent the radius of a sphere having the same volume.

³The integral of $P(\theta)$ over all solid angles has to be equal to unity.

5.1.2 Scattering by small particles: Rayleigh scattering

Historically, Rayleigh was the first to provide a quantitative description of light scattering phenomena. The success of this model came from its ability to explain why the sky appears blue. It assumes single scattering and incoherent summing of intensities in the far field. Rayleigh scattering occurs if the particle scattering the light is much smaller than the incident wavelength.

Light, being an electromagnetic wave, is characterized by electric and magnetic field vectors. In the Rayleigh conditions, the particles, in this case the molecules composing the medium, may be considered to be placed in a homogeneous electric field \vec{E}_0 of the incoming unpolarized light. The induced dipole moment can be written as

$$\vec{p} = \alpha \vec{E}_0, \quad (5.5)$$

α being the polarizability of the particle, has the dimension of a volume and is a scalar for an isotropic spherical particle. The scattered electric field for this dipole is given at large distances r as

$$\vec{E} = \frac{1}{c^2 r} \frac{\partial \vec{p}}{\partial t} \sin \beta, \quad (5.6)$$

where β is the angle between the induced dipole moment \vec{p} and the direction of observation. The dipole oscillates and radiates in all directions. The resulting intensity of the scattered light is [13]

$$I(\theta) = \frac{I_0}{r^2} \alpha^2 \left(\frac{2\pi}{\lambda} \right)^4 \frac{1 + \cos^2 \theta}{2}. \quad (5.7)$$

Combining Equations (5.1) and (5.7), the Rayleigh scattering cross section σ_{Ray} and the Rayleigh scattering phase function P_{Ray} are defined as

$$\sigma_{\text{Ray}}(\lambda) = \alpha^2 \frac{128\pi^5}{3\lambda^4}, \quad \text{and} \quad P_{\text{Ray}}(\theta) = \frac{3}{16\pi} (1 + \cos^2 \theta) \quad (5.8)$$

Because the intensity of the scattered light varies inversely with the fourth power of the wavelength, blue light (short wavelength) is scattered preferentially to red. This strong dependence leads to the blue color of the sky and contributes to the red colors observed at sunset.

In this study, we choose the case of a non-absorbing sphere ($Q_{\text{abs}} = 0$), i.e. particles with a refractive index n defined only with a real part: therefore, it will be equivalent to compute Q_{ext} or Q_{sca} . Integrating $I(\theta)/I_0$ over a sphere of radius r surrounding the particle gives the Rayleigh extinction efficiency

$$Q_{\text{ext}} = Q_{\text{sca}} = \frac{8}{3} x^4 \left(\frac{n^2 - 1}{n^2 + 2} \right)^2. \quad (5.9)$$

5.1.3 Scattering in the intermediate size range: Mie scattering

The theory describing the scattering of an electromagnetic plane wave by a homogeneous sphere of arbitrary size was originally presented by Gustav Mie [2]. Particles with a size comparable to the wavelength of visible light are relatively common in nature. Atmospheric visibility, for instance, is limited by particles whose size is of the same order as the wavelength of light in the optical range, from 0.1 to 1.0 μm in diameter. In this range, the Rayleigh theory is not applicable anymore because the field is not uniform over the entire particle volume. The laws describing the total scattered intensity as a function of the incident wavelength and the characteristics of the particle are much more complex than those for Rayleigh scattering.

Extinction efficiency: the total cross section

The $1/\lambda^4$ dependence of the total scattered intensity found by Rayleigh is no longer valid generally for the Mie solution. The extinction efficiency factor $Q_{\text{ext}} = \sigma_{\text{tot}}/(\pi R^2)$ depends on the radius R and on the relative refractive index of the particle n . The relative refractive index is defined as the ratio of the refractive index of the particle over the refractive index of the medium. In the following, where the medium is air, the relative refractive index corresponds to the refractive index of the particle n .

The Mie theory uses Maxwell's equations to obtain a wave propagation equation for the electromagnetic radiation in a three dimensional space, with appropriate boundary conditions at the surface of the spherical particle. The extinction efficiency factor obtained is

$$Q_{\text{ext}} = \frac{2}{x^2} \sum_{\ell=1}^{\infty} (2\ell + 1) \text{Re}(a_{\ell} + b_{\ell}). \quad (5.10)$$

The Mie scattering coefficients a_{ℓ} and b_{ℓ} are functions of the size parameter $x = 2\pi R/\lambda = k_{\text{out}}R$ and of the index of refraction n ,

$$a_{\ell} = \frac{x\psi_{\ell}(x)\psi'_{\ell}(y) - y\psi'_{\ell}(x)\psi_{\ell}(y)}{x\zeta_{\ell}(x)\zeta'_{\ell}(y) - y\zeta'_{\ell}(x)\zeta_{\ell}(y)}, \quad (5.11)$$

$$b_{\ell} = \frac{y\psi_{\ell}(x)\psi'_{\ell}(y) - x\psi'_{\ell}(x)\psi_{\ell}(y)}{y\zeta_{\ell}(x)\zeta'_{\ell}(y) - x\zeta'_{\ell}(x)\zeta_{\ell}(y)}, \quad (5.12)$$

where $y = nx$. $\psi_{\ell}(z)$ and $\zeta_{\ell}(z)$ are the Riccati-Bessel functions (the prime denotes differentiation with respect to the argument) related to the spherical Bessel functions $j_{\ell}(z)$ and $y_{\ell}(z)$ through the equations

$$\psi_{\ell}(z) = zj_{\ell}(z), \quad (5.13)$$

$$\zeta_{\ell}(z) = zj_{\ell}(z) - izy_{\ell}(z). \quad (5.14)$$

To compute Q_{ext} numerically using Equation (5.10), it is necessary to truncate the series, keeping enough terms to obtain a sufficiently accurate approximation. The criterion developed by Bohren in [14] was obtained through extensive computation. The number of required terms N has to be at least the closest integer to $x + 4x^{1/3} + 2$. For instance, for a raindrop of $50 \mu\text{m}$ radius and a visible wavelength of $0.6 \mu\text{m}$, the number of required terms is $N = 558$. Nowadays, computers have reached a point where computing time is no longer a major problem. The closed form Ramsauer approach, which we will develop later, would have been useful some years ago to provide computational ease. In the present context it furnishes useful insights into the different physical processes involved.

Figure 5.1 shows, for three values of the index of refraction, Q_{ext} as a function of the size parameter $x = 2\pi R/\lambda = k_{\text{out}}R$, where k_{out} is the wave number of the light outside the sphere. Each curve is characterized by a succession of maxima and minima with superimposed ripples. The amplitude of the large oscillations and of the ripples grows with n .

For particles much larger than the wavelength of the incoming light, i.e. with a size parameter $x \gg 1$, it might be expected from geometrical optics that the total cross section would be πR^2 , and thus Q_{ext} would approach 1. However, Figure 5.1 shows an interesting and somewhat puzzling trend, the scattering efficiency approaching 2. It is the so-called *extinction paradox*, and is discussed in detail by Van de Hulst [1]. The phenomenon is apparent only for observations made far from an object, so that light that is scattered even at a small angle can be considered removed from the beam. The total cross section results from the geometrical contribution (classical limit) of πR^2 and an equal contribution from the diffraction of the incident plane wave at the surface of the sphere. The diffraction contribution is strongly peaked forward. For nearby macroscopic objects, this diffracted light is not distinguishable from unscattered light at $\theta = 0^\circ$ and the paradox is not observed.

Angular scattering: the differential cross section

Mie scattering by single particles irradiated by laser sources is sufficiently strong to be detected with high signal-to-noise ratios for particles larger than about $0.1 \mu\text{m}$. The noise results from Rayleigh scattering by residual molecules and from the electronics used. The recorded signal depends on the scattering angle, as well as on the particle size and refractive index [15].

The angular dependence can be calculated from Mie theory. In this study, we use a code developed by Philip Laven⁴. For values of the size parameter x approaching unity, an asymmetry favouring forward scattering appears. For $x \gg 1$, forward scattering increases even more strongly, showing very rapid changes for small increases in the scattering angle θ . Some of this behaviour is shown in Figure 5.2 for water droplets of different sizes when illuminated by unpolarized light of $\lambda = 0.6 \mu\text{m}$. Very small droplets show typical Rayleigh behaviour with a symmetric curve and a weak minimum at 90° . When the size parameter x increases,

⁴<http://www.philiplaven.com/mieplot.htm>

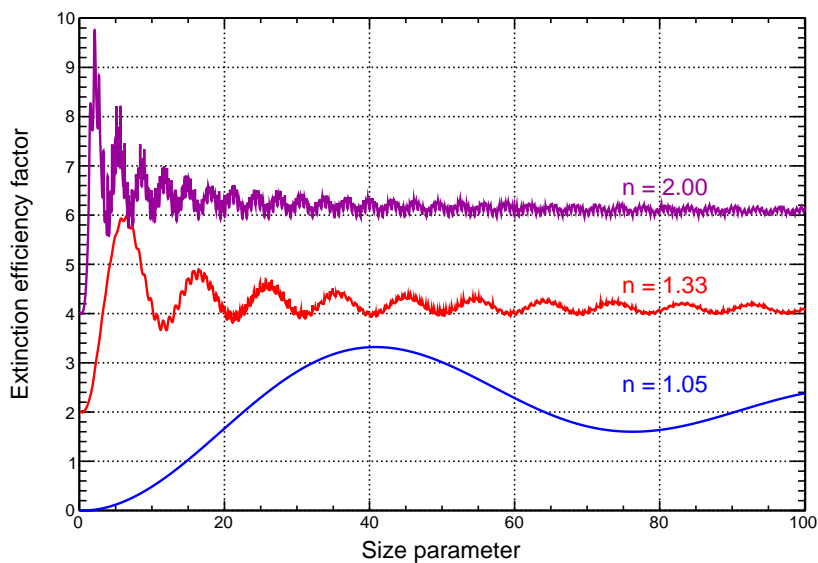


Figure 5.1: The extinction efficiency factor Q_{ext} versus the size parameter x , for non absorbing spherical particles with relative refractive indices $n = 1.05, 1.33,$ and 2.00 . x is given by the relation $x = 2\pi R/\lambda = k_{\text{out}}R$. The vertical scale applies only to the lowest curve, the others being successively shifted upward by 2.

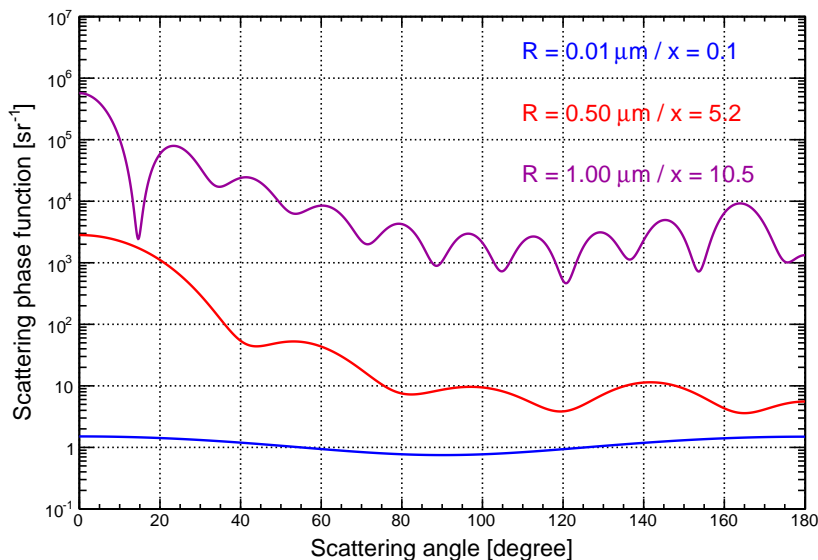


Figure 5.2: Angular scattering for water droplets illuminated by unpolarized light. The vertical scale applies only to the lowest curve, the others being successively multiplied by 100. The incident wavelength is fixed at $0.6 \mu\text{m}$.

additional minima and maxima appear and a strong asymmetry develops with the forward scattering several orders of magnitude stronger than the backscattering.

5.2 Application of the Ramsauer effect for light scattering

The Ramsauer effect was discovered in 1921 [3] while studying electron scattering on argon atoms. The total cross section versus the electron energy showed a surprising dip around 1 eV. In Figure 5.3 we see recent measurements of electron scattering over krypton and neutron scattering on lead nuclei.

5.2.1 The Ramsauer scattering phase function

The idea in modelling the phenomenon is to consider the incident particle as a plane wave with one part going through the target and another which does not (Figure 5.4). The two parts recombine behind the target and then interfere with each other, producing the oscillating behaviour. Depending upon the impact parameter b (Figure 5.5), light rays going through the drop accumulate a phase shift.

Let us first have a reminder about the Huygens-Fresnel principle. The propagation of light can be described with the help of virtual secondary sources. Each point of a chosen wavefront becomes a secondary source and the light amplitude at any chosen location is the integral of all these sources emitting spherical waves towards that observation point. The secondary sources are driven by the incident wave. Their amplitude is

$$-\frac{i}{\lambda} \frac{(1 + \cos \theta)}{2} A_{\text{incident}} dS$$

where λ is the wavelength, A_{incident} is the amplitude of the incoming light, θ is the angle between the direction of the incident light and the direction from the virtual source to the observation point, and dS is the elementary area of the secondary source stands.

We define the plane P, shown in Figure 5.5, as the location of our secondary sources. The shadow of the sphere on the plane P is the disk CD. If the plane Q is chosen as the origin of the phases, the incident light is a plane wave which, on the plane P, has the amplitude e^{i2kR} . The amplitude distributions of the secondary sources can be split into two parts: an undisturbed plane wave and a perturbation in the CD region only. The undisturbed initial plane wave, when integrated, is described by a Dirac delta function in the forward direction. Thus the differential cross section comes from the sources on CD. The observation points are considered to be very far away so, to get the amplitude at an angle θ , we just sum all directions parallel to θ .

Let ρ and ϕ be the polar coordinates in the plane P. The amplitudes from the virtual

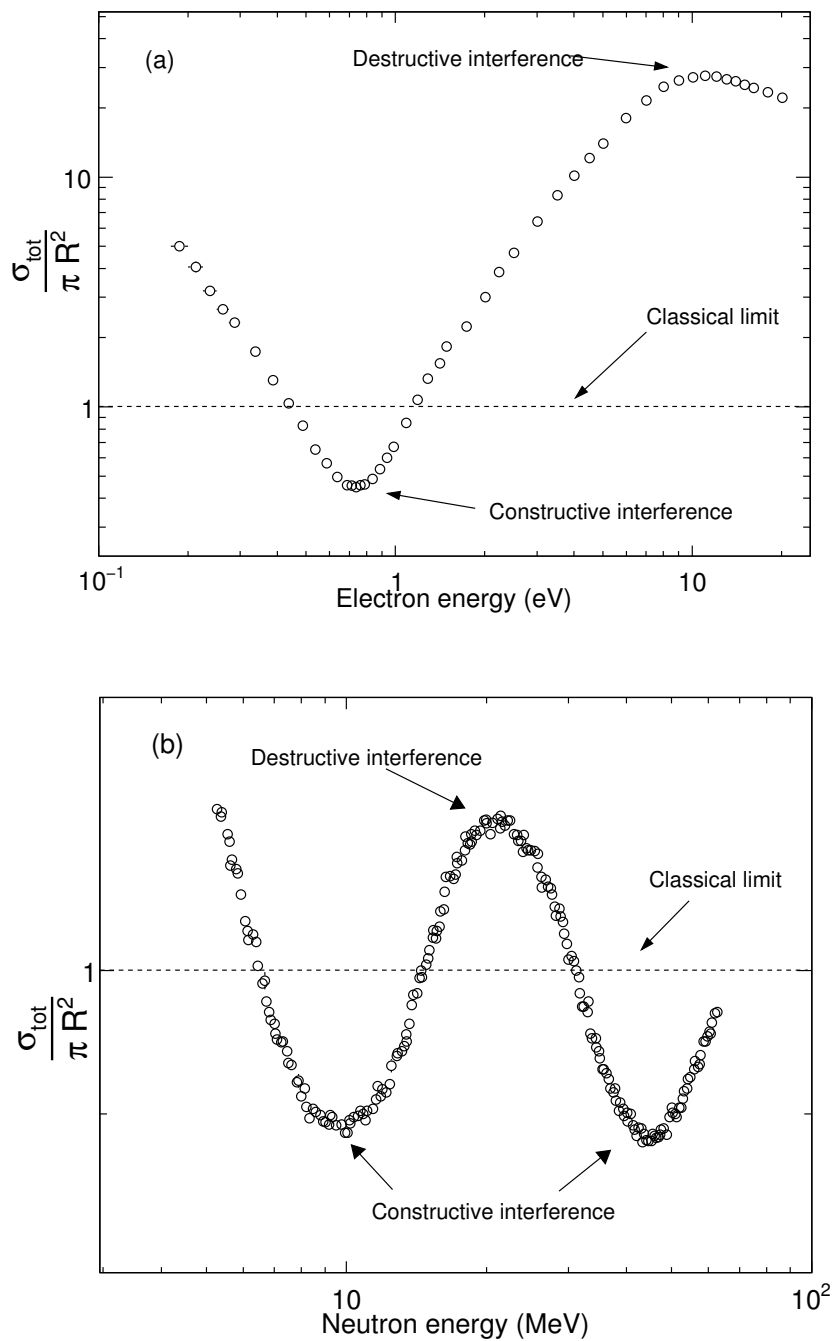


Figure 5.3: (a) Electron-krypton normalized total cross section versus energy [6]. (b) Normalized neutron-lead total scattering cross section versus energy [12].

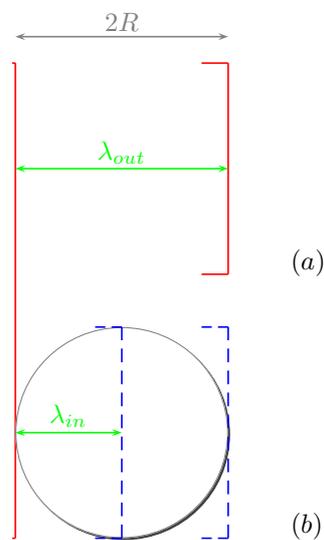


Figure 5.4: **Qualitative picture of the Ramsauer phenomenon.** The wavelength of the light is supposed to be reduced in the dielectric. This picture shows the case where the contraction of the wavelength between (a) outside and (b) inside the medium (dashed line) is such that they come out in phase. Thus the sphere looks invisible resulting in an almost zero cross section.

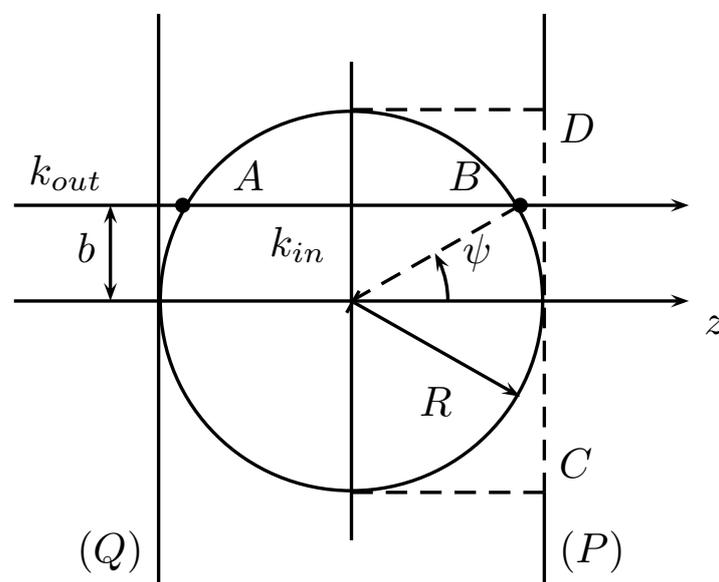


Figure 5.5: **Definition of the variables used in the text to calculate the phase function for light scattering by a spherical particle of radius R .** k_{in} and k_{out} are the wavenumbers for the light inside and outside, respectively, and b is the impact parameter.

sources in the disk CD are then

$$\begin{aligned} A_{\text{disk}}(\rho) &= -\frac{i}{\lambda} \left[-e^{i2kR} + e^{in2k\sqrt{R^2-\rho^2}} e^{ik(2R-2\sqrt{R^2-\rho^2})} \right] \frac{1+\cos\theta}{2} \\ &= i\frac{k}{2\pi} e^{i2kR} \left[1 - e^{i2k\sqrt{R^2-\rho^2}(n-1)} \right] \frac{1+\cos\theta}{2}. \end{aligned} \quad (5.15)$$

The resulting scattering amplitude $f_{\text{sphere}}(\theta)$ is obtained after moving the origin of the phases to the plane P. This is simply done through a multiplication by e^{-i2kR}

$$\begin{aligned} f_{\text{sphere}}(\theta) &= e^{-i2kR} \int_0^{2\pi} d\phi \int_0^R A_{\text{disk}}(\rho) \rho e^{ik\rho \cos\phi \sin\theta} d\rho \\ &= i\frac{k}{2\pi} \frac{1+\cos\theta}{2} \int_0^{2\pi} d\phi \int_0^R e^{ik\rho \cos\phi \sin\theta} \left[1 - e^{i2k\sqrt{R^2-\rho^2}(n-1)} \right] \rho d\rho, \end{aligned} \quad (5.16)$$

where the term $\rho \cos\phi \sin\theta$ represents the path length difference between a source in the disk and a source at the disk center for an observer placed at an infinite distance from the disk.

The integral over the angle ϕ is a Bessel function

$$J_0(u) = \frac{1}{2\pi} \int_0^{2\pi} e^{iu \cos\phi} d\phi. \quad (5.17)$$

Thus Equation (5.16) becomes

$$f_{\text{sphere}}(\theta) = ik \frac{1+\cos\theta}{2} \int_0^R \rho J_0(k\rho \sin\theta) \left[1 - e^{i2k\sqrt{R^2-\rho^2}(n-1)} \right] d\rho. \quad (5.18)$$

This integral has no analytical solution. The Ramsauer differential cross section is

$$\left[\frac{d\sigma}{d\theta} \right]_{\text{sphere}} = |f_{\text{sphere}}(\theta)|^2, \quad (5.19)$$

and we deduce directly the Ramsauer phase function

$$P_R(\theta) = \frac{1}{\sigma} \left[\frac{d\sigma}{d\theta} \right]_{\text{sphere}} = \frac{|f_{\text{sphere}}(\theta)|^2}{\int_0^{2\pi} d\Phi \int_0^\pi d\theta \sin\theta |f_{\text{sphere}}(\theta)|^2}. \quad (5.20)$$

This solution has to be computed numerically. Thus, this illustrates that predicting the behaviour of light scattering is not easy.

5.2.2 The simplified Ramsauer scattering phase function

We can get a formula in closed form if the sphere is replaced by a disk of radius R and of height $2R$ along z . Equation (5.18) simplifies into

$$\begin{aligned} f_{\text{disk}}(\theta) &= ik \frac{1 + \cos \theta}{2} \int_0^R \rho J_0(k\rho \sin \theta) \left[1 - e^{i2kR(n-1)} \right] d\rho \\ &= ik \frac{1 + \cos \theta}{2} \left[1 - e^{i2(n-1)kR} \right] \int_0^R \rho J_0(k\rho \sin \theta) d\rho \\ &= i \frac{1 + \cos \theta}{2} e^{i\frac{2(n-1)kR}{2}} (-2i) \sin \left[\frac{2(n-1)kR}{2} \right] \frac{R}{\sin \theta} J_1(kR \sin \theta), \end{aligned} \quad (5.21)$$

since the integral can be simplified using the fact that

$$\int_0^R u J_0(u) du = R J_1(R).$$

The differential cross section is

$$\left[\frac{d\sigma}{d\theta} \right]_{\text{disk}} = |f_{\text{disk}}(\theta)|^2 = R^2 \left[kR \frac{1 + \cos \theta}{2} \sin [(n-1)kR] \frac{2J_1(kR \sin \theta)}{kR \sin \theta} \right]^2. \quad (5.22)$$

In fact, in the Ramsauer approach, the total cross section for a disk is given by

$$\sigma_{\text{tot}}^{\text{disk}} = \int_0^{2\pi} d\Phi \int_0^\pi d\theta \sin \theta \left[\frac{d\sigma}{d\theta} \right]_{\text{disk}} = 4\pi R^2 \sin^2 [(n-1)kR]. \quad (5.23)$$

Thus, the differential cross section can be expressed as

$$\left[\frac{d\sigma}{d\theta} \right]_{\text{disk}} = \frac{1}{4\pi} \sigma_{\text{tot}}^{\text{disk}} \left[kR \frac{(1 + \cos \theta)}{2} \frac{2J_1(kR \sin \theta)}{kR \sin \theta} \right]^2. \quad (5.24)$$

As we will see in Section 5.2.3, it is possible to use a similar equation for the differential cross section with a sphere, i.e.

$$\left[\frac{d\sigma}{d\theta} \right]_{\text{sphere}} = \frac{1}{4\pi} \sigma_{\text{tot}}^{\text{sphere}} \left[kR \frac{(1 + \cos \theta)}{2} \frac{2J_1(kR \sin \theta)}{kR \sin \theta} \right]^2. \quad (5.25)$$

In this subsection, we have shown that in the simplified Ramsauer approach (SR), the total cross sections for a disk and for a sphere can be different but the scattering phase functions coincide and are given by the relation

$$P_{\text{SR}}(\theta) = \frac{1}{\sigma} \frac{d\sigma}{d\theta} = \frac{1}{4\pi} \left[kR \frac{(1 + \cos \theta)}{2} \frac{2J_1(kR \sin \theta)}{kR \sin \theta} \right]^2. \quad (5.26)$$

It seems interesting to note that this simplified phase function is independent of the relative refractive index. The validity of this independence will be verified in Section 5.2.3.

As can be seen in Equation (5.26), the Ramsauer approach is much more intuitive than Mie model. In Figure 5.6 we give the phase functions for two distributions with different mean radii. We note three properties of the Ramsauer phase function:

1. The amount of light scattered in the forward direction ($\theta = 0^\circ$) is proportional to the target area, i.e. square of the target radius: at constant wavelength, a larger sphere scatters more light in the forward direction, in agreement with the Mie prediction.

$$\frac{1}{\sigma} \frac{d\sigma}{d\theta}(\theta = 0^\circ) \propto R^2.$$

2. The full width at half maximum (FWHM) of the forward scattering peak is proportional to the inverse of kR .

$$\Delta\theta_{\text{FWHM}} = \frac{2}{kR}.$$

3. For greater angles, the phase function is proportional to the inverse of the scattering angle to the third power.

$$\frac{1}{\sigma} \frac{d\sigma}{d\theta} \propto \frac{1}{\theta^3}.$$

By detailed Mie calculations, these phase function properties deduced from the analytical Ramsauer solution can be verified. Figure 5.7 gives the phase function for pure forward scattering as a function of R and the full width at half maximum as a function of the size parameter. For three different refractive indices, the observed behaviour is confirmed by the Mie calculations. Whereas it is difficult to obtain clear physical interpretations with Mie theory, the solutions being in the form of infinite series, the simplified Ramsauer solution makes easier prediction of light scattering behaviour possible.

5.2.3 Validity of the Ramsauer solutions

From the Ramsauer approach, two scattering phase functions were obtained: one from an exact calculation, $P_R(\theta)$, and the second resulting from an approximation but given by a closed formula, $P_{\text{SR}}(\theta)$. The goal of this section is to evaluate the two solutions with respect to the Mie theory, taken here as the reference.

As noted above, the simplified solution does not depend on the refractive index of the target. It is thus important to see how the Mie calculations and the Ramsauer solution evolve with respect to the refractive index. Figure 5.8 shows the phase functions obtained from the Ramsauer solution (*top panel*) and Mie theory (*bottom panel*) for different refractive indices. For comparison, the one obtained from the simplified Ramsauer formula is also plotted with

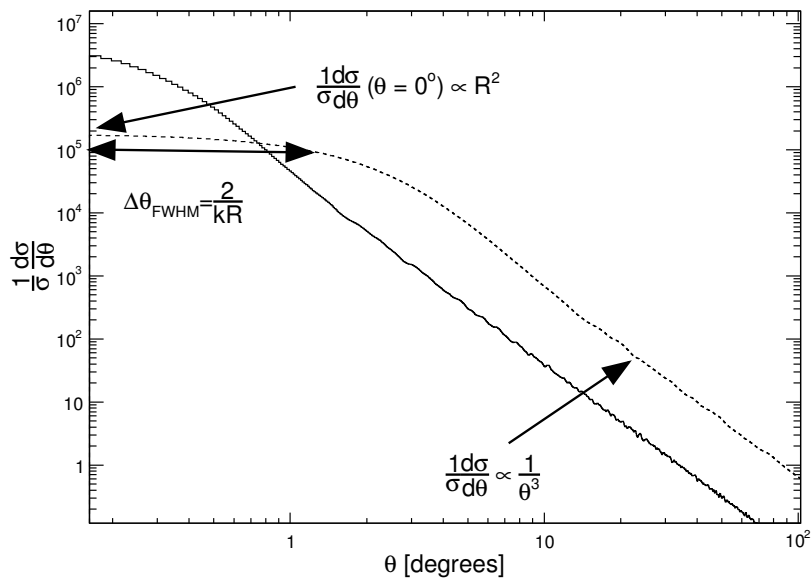


Figure 5.6: **Intuitive properties of the Ramsauer phase function.** The curves are obtained from Equation (5.26) for two distributions with different mean radii: $\bar{R} = 3 \mu\text{m}$ (dashed line) and $\bar{R} = 24 \mu\text{m}$ (continuous line). The wavelength is fixed at $0.6 \mu\text{m}$.

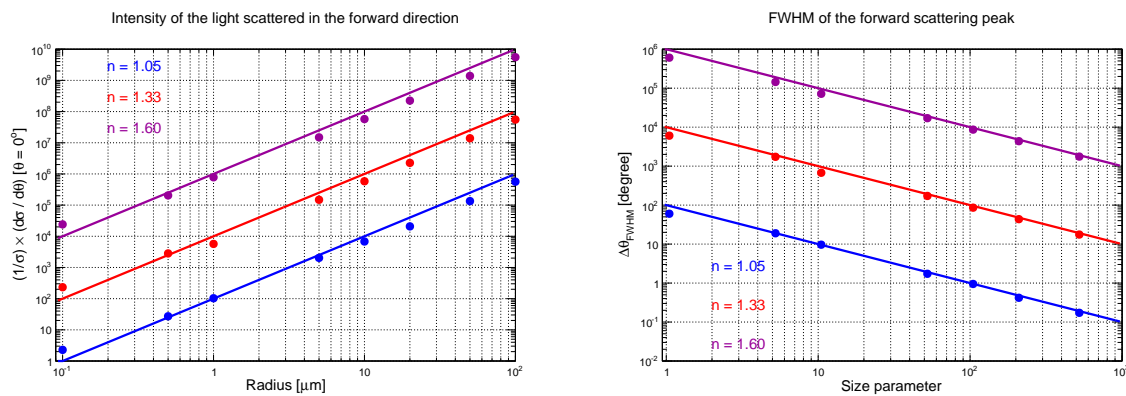


Figure 5.7: **Characteristic behaviours of physics quantities from the phase function.** The curves are obtained by Mie calculations (using [18]) for an incident wavelength of $0.6 \mu\text{m}$. Three different refractive indices are shown: $n = 1.05$ (blue), $n = 1.33$ (red) and $n = 1.60$ (magenta). The vertical scale applies only to the lowest curve, the others being successively multiplied by 100.

a thick black line. Although the phase function is almost independent of the refractive index for high n values, this is not the case when $|n - 1|$ approaches 0. Moreover, the Ramsauer solution is in better agreement with the Mie curves when the refractive index is low.

Consequently, when we want to study light scattering phenomena for spherical particles, we can develop models without knowing the refractive index of the particles. This is due to the fact that Fraunhofer diffraction is mostly responsible for small-angle scattering and it is nearly independent of the relative refractive index. Thus, forward scattering is sometimes favoured in the design of optical particle counters to eliminate the effect of refractive index on the measurement of particle size.

5.2.4 Effects of averaging over sizes

Most natural and artificial collections of spherical particles do not exhibit the large fluctuations as in Figure 5.8. Even a narrow dispersion in the distribution of the particle size washes out these features that strongly depend on size.

The size distribution can be described using a log-normal function defined as follows

$$n(R|\bar{R},\sigma) = \frac{dN(R)}{dR} = \frac{N}{\sqrt{2\pi} \log_{10} \sigma} \frac{1}{R} \exp\left(-\frac{\log_{10}^2(R/\bar{R})}{2 \log_{10}^2 \sigma}\right), \quad (5.27)$$

where R is the radius of a spherical particle, $\log_{10} \sigma$ is the geometric standard deviation, \bar{R} is the geometric mean radius, and N is the total number of particles. Figures 5.9–5.10 illustrate the dependence of the phase function on the radius distribution. According to the first figure, the light scattering in the forward direction has a narrower and higher peak when spheres are larger. This is what is expected from the simplified Ramsauer scattering phase function. Also, as shown in the second figure, a lower geometric standard deviation implies a wavier phase function. Consequently, in Nature, where particle radii are always dispersed, light scattering will be described using smoothed phase functions.

5.3 The Ramsauer total cross section and extinction efficiency

Since the results of the phase function predicted by the Ramsauer approach seem in agreement with the Mie calculations, this section will check if this is also the case for the total cross section. Two different methods will be presented to get the cross section by the Ramsauer approach: the first one based on the optical theorem (and independent of the results given in Section 5.2), and the second by integrating the differential cross section over (θ, ϕ) .

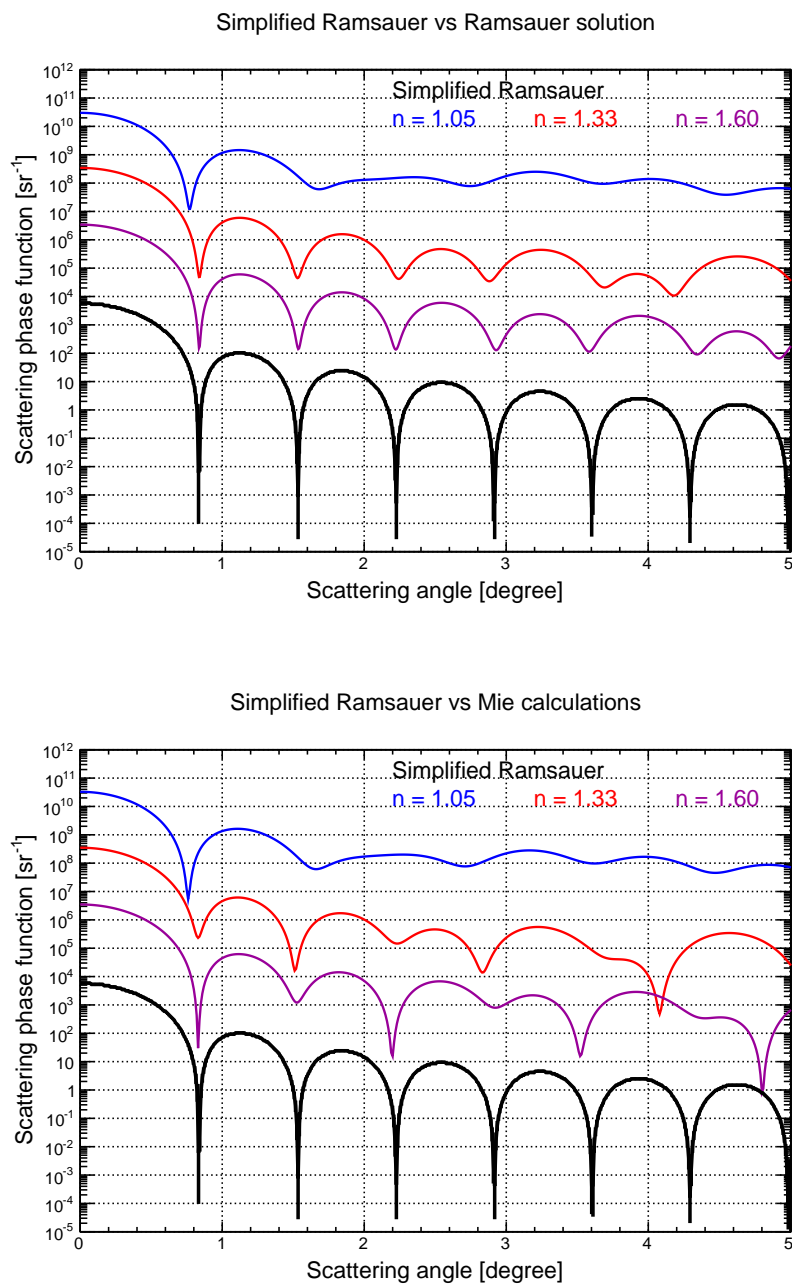


Figure 5.8: **The simplified Ramsauer solution, independent of the refractive index, compared to the Ramsauer solution and Mie calculations.** *Top panel:* SR vs Ramsauer. *Bottom panel:* SR vs Mie theory. Three different refractive indices are shown: $n = 1.05$ (blue line), $n = 1.33$ (red line) and $n = 1.60$ (magenta line). The simplified solution, independent of the refractive index, is in black. The vertical scale applies only to the lowest curve, the others being successively multiplied by 100. The incident wavelength is fixed at $0.6 \mu\text{m}$ and the sphere radius is equal to $10 \mu\text{m}$.

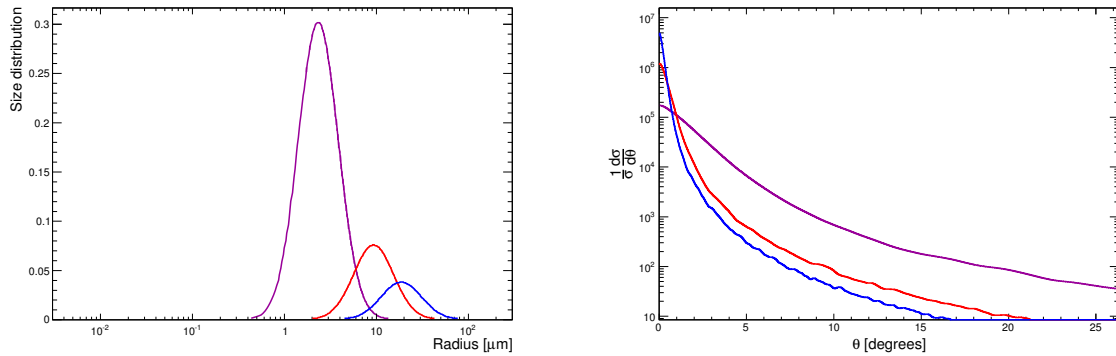


Figure 5.9: **Dependence of the scattering phase function on mean radius \bar{R}** ($n = 1.44$, $\lambda = 0.55 \mu\text{m}$). *Left panel:* Particle size distributions for three different mean radii at $\log_{10}\sigma = 1/2$: $3 \mu\text{m}$ (magenta), $12 \mu\text{m}$ (red) and $24 \mu\text{m}$ (blue). *Right panel:* Phase functions obtained by the Ramsauer approach for these three distributions.

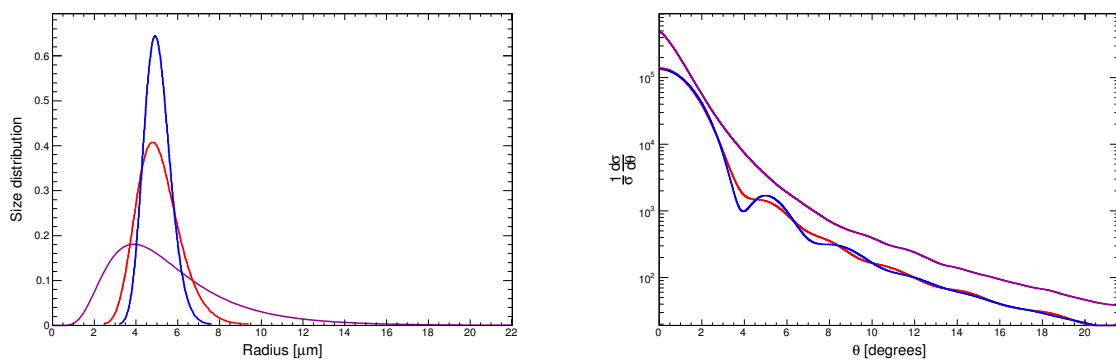


Figure 5.10: **Dependence of the scattering phase function on different standard deviations** ($n = 1.44$, $\lambda = 0.55 \mu\text{m}$). *Left panel:* Particle size distributions for three different values of $\log_{10}\sigma$ at $\bar{R} = 5 \mu\text{m}$: $1/2$ (magenta), $1/5$ (red) and $1/8$ (blue). *Right panel:* Phase functions obtained by the Ramsauer approach for these distributions.

5.3.1 Ramsauer total cross section via the Optical theorem

In scattering theory, the wave function far away from the scattering region must have up to the normalisation factor the form of a plane wave and an out-going spherical wave,

$$\Psi(\vec{r}) = e^{i\vec{k}\vec{r}} + f(\theta) \frac{e^{ikr}}{r}. \quad (5.28)$$

The optical theorem asserts that

$$\sigma_{\text{tot}} = \frac{4\pi}{k_{\text{out}}} \text{Im} f(\theta = 0), \quad (5.29)$$

where $f(\theta = 0)$ is the forward scattering amplitude. Under the approximation for the scattering of a scalar (spinless) wave on a spherical and symmetric potential, the scattering amplitude at a given polar angle θ can be written as a sum over partial wave amplitudes, each of different angular momentum ℓ ,

$$f(\theta) = \frac{1}{2ik_{\text{out}}} \sum_{\ell=0}^{\infty} (2\ell + 1) P_{\ell}(\cos \theta) \left[\eta_{\ell} e^{2i\delta_{\ell}} - 1 \right], \quad (5.30)$$

where η_{ℓ} is the inelasticity factor ($\eta_{\ell} = 1$ in our case of a non-absorbing sphere), δ_{ℓ} is the phase shift (δ_{ℓ} is real for pure elastic scattering), and $P_{\ell}(\cos \theta)$ is the Legendre polynomial.

From Figure 5.5, $\delta_{\ell} = (k_{\text{in}} - k_{\text{out}})R \cos \psi$. In the approximation of forward scattering, $P_{\ell}(\cos \theta) \rightarrow 1$. From Bohr momentum quantization applied to the impact parameter $b = R \sin \psi$ (see Figure 5.5), we have $b p = \ell \hbar$ and $p = \hbar k$ with $\ell = b k_{\text{out}}$. By substituting the discrete sum over ℓ by an integral over ℓ or over the impact parameter

$$\sum_{\ell} \rightarrow \int d\ell \rightarrow k_{\text{out}} \int db,$$

the forward scattering amplitude can be written in terms of the impact parameter

$$f(\theta = 0) = \frac{k_{\text{out}}}{i} \int_0^R \left(e^{i2(k_{\text{in}} - k_{\text{out}})R \cos \psi} - 1 \right) b db, \quad (5.31)$$

or in terms of the angle ψ

$$f(\theta = 0) = \frac{k_{\text{out}} R^2}{2i} \int_0^1 \left(1 - e^{i2(k_{\text{in}} - k_{\text{out}})R \cos \psi} \right) d \cos^2 \psi. \quad (5.32)$$

Then, the expression for the total cross section is obtained from Equation (5.31) and setting

$w = \cos \psi$, we get

$$\begin{aligned}\sigma_{\text{tot}} &= \text{Im} \left[i 4\pi R^2 \int_0^1 w \left(1 - e^{i(k_{\text{in}} - k_{\text{out}})2Rw} \right) dw \right] \\ &= \text{Im} \left[i 2\pi R^2 - i 4\pi R^2 \int_0^1 w e^{i(k_{\text{in}} - k_{\text{out}})2Rw} dw \right].\end{aligned}\quad (5.33)$$

Then, from integration by parts, we obtain

$$\begin{aligned}\sigma_{\text{tot}} &= \text{Im} \left[i 2\pi R^2 - i 4\pi R^2 \left(\left[\frac{w e^{i(k_{\text{in}} - k_{\text{out}})2Rw}}{i(k_{\text{in}} - k_{\text{out}})2R} \right]_0^1 - \int_0^1 \frac{e^{i(k_{\text{in}} - k_{\text{out}})2Rw}}{i(k_{\text{in}} - k_{\text{out}})2R} dw \right) \right] \\ &= \text{Im} \left[i 2\pi R^2 - i 4\pi R^2 \left(\frac{e^{i(k_{\text{in}} - k_{\text{out}})2R}}{i(k_{\text{in}} - k_{\text{out}})2R} + \frac{e^{i(k_{\text{in}} - k_{\text{out}})2R} - 1}{(2R)^2 (k_{\text{in}} - k_{\text{out}})^2} \right) \right] \\ &= 2\pi R^2 - 4\pi R^2 \left[\frac{\sin(2R(k_{\text{in}} - k_{\text{out}}))}{2R(k_{\text{in}} - k_{\text{out}})} - \frac{1}{2} \left[\frac{\sin(R(k_{\text{in}} - k_{\text{out}}))}{R(k_{\text{in}} - k_{\text{out}})} \right]^2 \right].\end{aligned}\quad (5.34)$$

If we introduce the parameter $\Delta_R = 2R(k_{\text{in}} - k_{\text{out}})$, the analytic expression for the cross section becomes

$$\sigma_{\text{tot}} = 2\pi R^2 \left[1 - 2 \frac{\sin \Delta_R}{\Delta_R} + \left(\frac{\sin \Delta_R/2}{\Delta_R/2} \right)^2 \right].\quad (5.35)$$

In this expression, the total cross section approaches $2\pi R^2$ at high energies. This is the so called "black disk" approximation. Nevertheless, from a purely geometrical viewpoint, between two spheres, a collision occurs if the distance between their centres is less than $r_1 + r_2$, where r_1 and r_2 are their radii. So the geometrical cross section is equal to $\pi(r_1 + r_2)^2$. In our case, the photon may be considered to be a particle with a diameter equal to its reduced wavelength $\bar{\lambda} = \lambda/2\pi$ [16, 17]. Consequently, Equation (5.35) becomes

$$\sigma_{\text{tot}} = 2\pi \left(R + \frac{\lambda}{4\pi} \right)^2 \left[1 - 2 \frac{\sin \Delta_R}{\Delta_R} + \left(\frac{\sin \Delta_R/2}{\Delta_R/2} \right)^2 \right].\quad (5.36)$$

Finally, an expression for Δ_R as a function of the index of refraction n is needed. According to the conservation of phase, it is $k_{\text{in}} = n k_{\text{out}}$. With this relation and the fact that $\lambda = 2\pi/k_{\text{out}}$

$$\begin{aligned}\sigma_{\text{tot}} &= 2\pi R^2 \left(1 + \frac{n-1}{\Delta_R} \right)^2 \left[1 - 2 \frac{\sin \Delta_R}{\Delta_R} + \left(\frac{\sin \Delta_R/2}{\Delta_R/2} \right)^2 \right] \\ Q_{\text{ext,R}} &= 2 \left(1 + \frac{n-1}{\Delta_R} \right)^2 \left[1 - 2 \frac{\sin \Delta_R}{\Delta_R} + \left(\frac{\sin \Delta_R/2}{\Delta_R/2} \right)^2 \right],\end{aligned}\quad (5.37)$$

where $\Delta_R = 2R(k_{\text{in}} - k_{\text{out}}) = 2R(n-1)k_{\text{out}} = 2x(n-1)$. This result is derived using the

approximation of scalar light, unlike the Mie solution. Therefore our formula applies only to scattering of unpolarized light.

Note that the first factor of Equation (5.37) explains the fact that the amplitude of the large oscillations grows with n . The extinction efficiency factors, when plotted against Δ_R , show a universal shape (see Figure 5.11). Our model and the Mie predictions are in good agreement for the three refractive indices used.

Explanation of the superimposed ripples

A small fraction of light, internally reflected (IR) twice, will also contribute to the forward flux. The amplitude of the internal reflection coefficient $r = (n - 1)/(n + 1)$ is small ($r = 1/7$ for visible light upon water drop in air). The phase shift will be roughly $\Delta_{\text{IR}} = 2 \times 2 R k_{\text{in}} = 4 R n k_{\text{out}} = 4 n x$. Thus the main Ramsauer extinction efficiency factor $Q_{\text{ext,R}}$ is modulated by the internal reflection factor

$$F_{\text{IR}} = 1 + r^2 \cos \Delta_{\text{IR}} = 1 + r^2 \cos(4 n x). \quad (5.38)$$

Finally, the global extinction efficiency factor is

$$Q_{\text{ext}} = Q_{\text{ext,R}} \times F_{\text{IR}}. \quad (5.39)$$

For a visible light ray ($\lambda = 0.6 \mu\text{m}$) incident on a drop of water ($n = 1.33$) in the air, the Mie and the Ramsauer predictions are compared in Figure 5.12. The Mie solution is a series with more than 600 terms that have to be computed for each value of the abscissa. On the contrary, from the Ramsauer approach we have purely analytical functions (Equations (5.37), (5.38), (5.39)) with clear physical concepts. The Ramsauer model reproduces quite well both the amplitude and the peak positions of the Mie prediction, except for the main peak position which is lower by almost 10%. At small parameter values, the two curves differ. The analytical formula (5.37), obtained using the light ray approximation, is not expected to be a good description of reality when the wavelength of the incident light is very much larger than the size of the droplet. This is the Rayleigh regime where the cross section behaves as $1/\lambda^4$. In terms of the variable x , this implies, as $x \ll 1$, an x^4 behaviour whereas our formula approaches a parabola. Even though the small ripples are also present, they are less pronounced in the Ramsauer curve. Another particularity of our model is that it justifies the ratio between the Ramsauer-pseudo period Δ_R and the internal reflection-pseudo period Δ_{IR} . Since one has already determined the phase difference for each case, it is straightforward to derive their ratio using the equations that require constructive interference for the axis $k_{\text{out}} R$,

$$\frac{\Delta_R}{\Delta_{\text{IR}}} = \frac{n - 1}{2 n}. \quad (5.40)$$

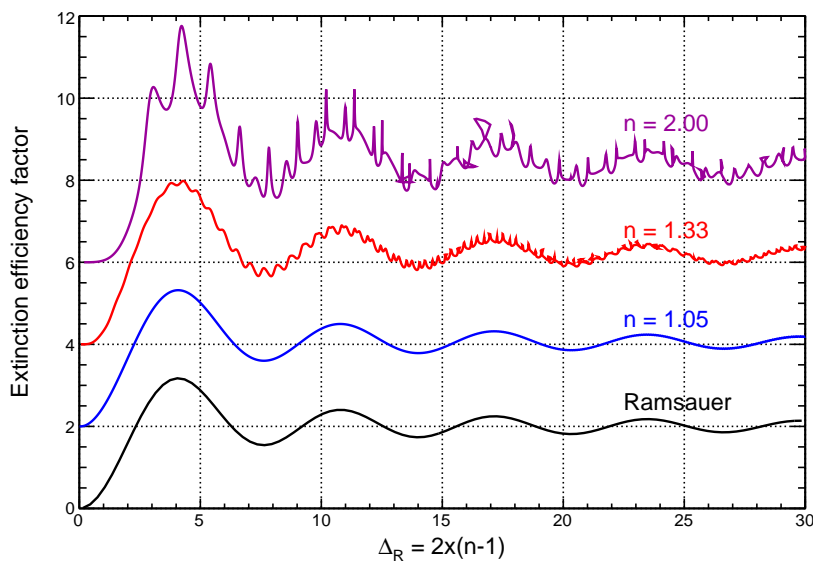


Figure 5.11: The extinction efficiency factor versus the phase shift Δ_R , for non absorbing spherical particles with relative refractive indices $n = 1.05, 1.33,$ and 2.00 . The Ramsauer solution for $n = 1.05$ is also given. The vertical scale applies only to the lowest curve, the others being successively shifted upward by 2.

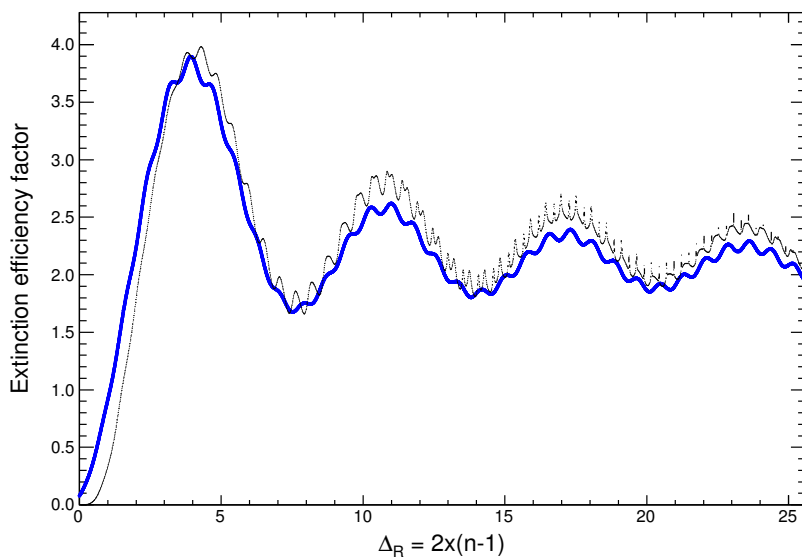


Figure 5.12: Comparison of the extinction efficiencies, the Mie prediction (thin line), and the prediction of the Ramsauer model including multiple internal reflections (thick line). x is given by the relation $x = 2\pi R/\lambda = k_{\text{out}}R$. The refractive index is fixed at 1.33 (water).

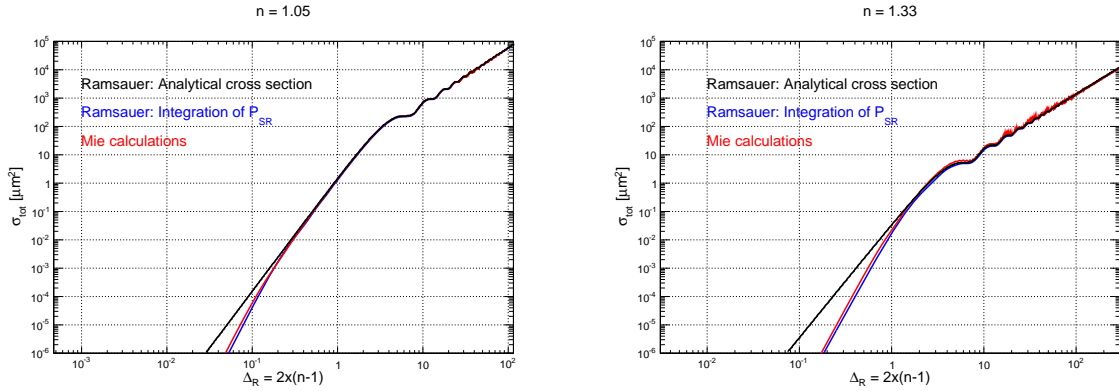


Figure 5.13: Total cross section as a function of the phase shift $\Delta_R = 2x(n - 1)$ for a refractive index fixed at (left) $n = 1.05$ and (right) $n = 1.33$. The simplified Ramsauer solution from Equation (5.41) is in blue, the Mie prediction in red (using [18]) and the formula from Equation (5.35) in black. The incident wavelength is fixed at $0.6 \mu\text{m}$.

In the case of a raindrop with $n = 1.33$, there is thus a factor 8 between the two pseudo periods. Therefore, we have a simple physical explanation for the origin of the oscillations at two frequencies, and we have derived the ratio of their periods.

5.3.2 Ramsauer total cross section via the differential cross section

The simplified Ramsauer formula is very convenient to use, in computing the phase function, as we have just seen, and also in calculating the total cross section. In this section, we compare the Mie prediction with the one obtained by integration of Equation (5.26). From the phase function, the total cross section is given by

$$\sigma_{\text{tot}} = \int_0^{2\pi} d\Phi \int_0^\pi d\theta \sin\theta P_{\text{SR}}(\theta). \quad (5.41)$$

Figure 5.13 compares, for two values of the index of refraction, the integrated Ramsauer phase function and the Mie theory result. The analytical solution from Equation (5.35) is also plotted. Each curve is characterized by a succession of maxima and of minima. While there is generally a good agreement between the three curves, only the integration of the simplified Ramsauer solution P_{SR} reproduces the Mie curve at small phase shift Δ_R , the so-called Rayleigh regime. The agreement improves when the refractive index decreases. In fact, at low phase shift, i.e. at small size parameter, the behaviour of Equation (5.35) is not proportional to λ^{-4} as expected by the Rayleigh theory, but only to λ^{-2} . Of the two methods, only the integration of the simplified Ramsauer solution is able to reproduce correctly the physics of Rayleigh regime.

5.4 Ramsauer approach to large aerosols as a possible source of the FD halo

At the Pierre Auger Observatory, each fluorescence telescope consists of a mirror with a camera at its focal centre, composed of 440 photomultipliers. Each pixel is a hexagon with a typical diameter of 1.5° . In front of this setup is a 2.2 meter diaphragm with a UV filter.

When the absolute pixel calibration and the shower geometry are known, the signal recorded by the camera can be converted to the number of UV photons detected. Since the fluorescence light produced is proportional to the energy deposited by the shower, the primary cosmic ray energy can be estimated if the fluorescence yield is known. Different longitudinal profile reconstructions have been developed by the Auger collaboration [19, 20]. These algorithms determine which pixels contribute to the total signal collected in each 100 ns time bin. One of these methods, referred to as the "zeta search" algorithm, has been implemented in an `Offline` module called `FdApertureLightFinder`. Once the geometry is reconstructed, the position of the light spot on the camera for each time bin is known. A circle of angular radius ζ is defined for each point on the track (see Figure 5.14). Then, for each time bin, the procedure defines the total track signal to be the sum of the signals for pixels having their centre within the circle of radius ζ . The choice of ζ is determined by the optimization of the signal to noise ratio (calculated over the whole track) in a range between 0.5° and 4.5° . Typically, a $\zeta = 1.2^\circ$ is usually chosen as a reference (including a "safety margin" of 0.2° [19]). For instance, Figure 5.15(a) shows the results of a ζ search in the case of a vertical CLF laser shot as seen from Los Leones. Here, a value of $\zeta = 1.2^\circ$ includes about 90% of the total signal along the track. Usually, the signal outside is called *halo* and is interpreted as the effect of multiple scattered light in the atmosphere. If this is the case, the halo should be subtracted from the total signal recorded in the energy estimation. On the other hand, if the halo is due to scattering inside of the FD building, the halo has to be included. Note that another reconstruction method used in the Auger collaboration takes into account the halo by fixing ζ at larger values, typically $\zeta = 1.4^\circ$ [20].

5.4.1 Description of the FD halo phenomenon, and its discovery

It was during a campaign for telescope calibration in 2008 that an unexpected observation was made in an FD camera [21]. To further investigate this phenomenon, a zeppelin-shaped balloon filled with helium was launched carrying a flasher lamp. It was brought into the field of view of the telescope at a distance of about one kilometre. The flasher was an isotropic UV light source ($\bar{\lambda} = 380$ nm) composed of an aluminium body on which light emitting diodes were mounted. The diameter of the flasher was 16 cm: its angular radius viewed from the telescope was around 0.01° . Thus, the flasher should have appeared as a point source for the

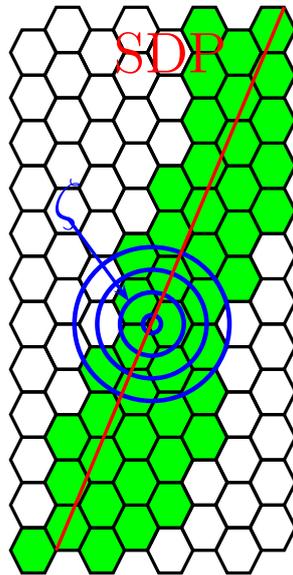


Figure 5.14: Example of a track recorded on an FD camera in a given time bin. The pixels with a significant signal are coloured in green. The geometrical reconstruction is represented by the Shower Detector Plane (SDP), shown in red. The ζ circles are shown in blue.

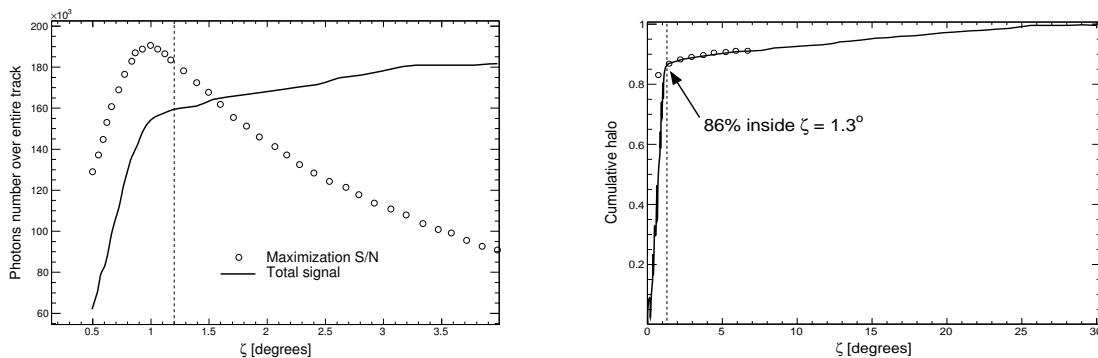


Figure 5.15: **(a) Results of a ζ search for a vertical CLF laser shot observed from Los Leones [19]).** The solid line shows the total signal along the track inside the angular distance ζ as a function of ζ . The circles represent the ratio S/N. The optimal value of ζ , given by the optimization of the ratio and including a "safety margin" of 0.2° , is 1.2° . This is indicated by the vertical dashed line. **(b) Accumulated halo distribution obtained after telescope calibration [21].** 86% of the total intensity is located within 1.3° of the spot centre. The circles correspond to an earlier measurement [22]. The two campaigns are in agreement for $\zeta > 1.5^\circ$.

telescope. The spherical aberration radius of the telescope optics is 0.25° and is lower than the pixel radius $r_p = 0.75^\circ$: a maximum of three illuminated pixels was expected.

However, the observational data clearly disagree with this prediction (see Figure 5.16). In fact, a significant complete halo was observed on the FD camera: around 14% of the light was outside the FD camera pixel, or focal-spot size (see Figure 5.15(b)). This can only be explained with a light distribution covering an area bigger than that produced by aberration since it can not reproduce the peak width in Figure 5.16. Detailed simulations of the telescope with the `Offline` module `TelescopeSimulatorLX` have shown that about 16% of the halo originates from telescope aberration effects, 7% can be attributed to Rayleigh scattering in photon propagation and the same quantity to Mie scattering. This leaves more than 70% of the halo unexplained.

Subsequently, studies were done to check if the halo could be induced by the UV filter [23]. Indeed, even when the flasher is out of the telescope's field of view, the filter is still illuminated. Hence, the UV light could be scattered in the filter. An experimental setup was developed to perform preliminary scattering measurements on an equivalent reference filter. The authors show that a possible source of the halo is the scattering of the UV light in the filter. Nevertheless, even if this idea explained the observations for high ζ , the experimental curve in [23] cannot reproduce the large peak between 0° and 2° as is illustrated in Figure 5.16. Several months later, this idea was rejected.

This discrepancy suggests that multiple scattering effects in the atmosphere should be considered in the longitudinal profile reconstruction. This halo, much higher than expected, distorts the shower energy estimation since the number of photons detected by the telescopes is overestimated in the reconstruction procedure. By developing a Monte Carlo simulation, we will make an attempt to explain the halo by multiple scattering on aerosols during photon propagation from the flasher to the telescope.

5.4.2 The Aerosol Phase Function at the Pierre Auger Observatory

Whereas the scattering properties of the molecular component are well known, the aerosol scattering properties have to be determined by specific measurements. The APF light sources, coupled with the FD, can measure the aerosol phase function. There are two monitors in this experiment, one at Coihueco and the other at Los Morados. The APF monitor emits hourly horizontal pulsed light beams at 350 nm and 390 nm across the field of view of the FD installation. In this way, the aerosol phase function can be reconstructed from the intensity of the light measured as a function of scattering angle (between 30° and 150°).

Figure 5.17 shows the measurements made at the Pierre Auger Observatory in 2006 by BenZvi *et al.* [24] with the APF system. The aerosol phase function obtained from the measurements is in agreement with the Henyey-Greenstein (HG) parameterization defined by

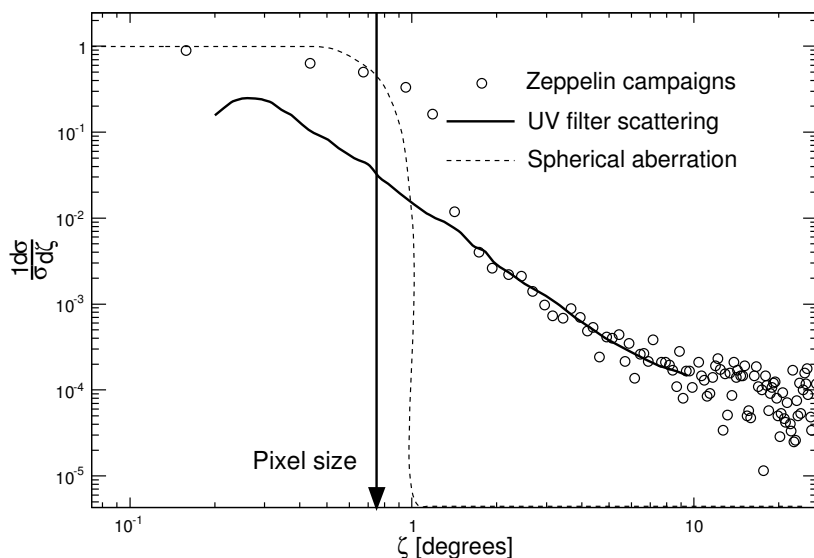


Figure 5.16: **Differential intensity distribution obtained from the zeppelin calibration campaigns [21].** The dashed line represents the spherical aberration effect due to the geometry of the optics. It does not reproduce the data. The preliminary scattering measurements made on the filter in [23] are given by the continuous line.

($g = 0.6$, $f = 0.4$). In Figure 5.17, It is also compared to the phase function from the Longtin desert model [25] which is based on Mie scattering. The Longtin desert model considers aerosols as a mixture of three components: carbonaceous particles (which have the smallest radii, typically lower than $10^{-2} \mu\text{m}$), water soluble particles and sand (with the highest radii, typically greater than $1 \mu\text{m}$). The main particularity of this model is its strong dependence on wind: a stronger wind means a higher sand component, i.e. an increase of the mean aerosol radius.

5.4.3 On possible underestimation of phase function at small angles

As noted in Section 5.4.2, the Auger measurements were made only between 30° and 180° because of the location of the APF monitor with respect to the telescope building. Moreover, according to the authors, data for angles greater than 150° are unavailable because of the increased light attenuation. Indeed, at large angles, the data points seem to be lower than can be expected from pure Rayleigh scattering values: the authors preferred to limit the range between 30° and 150° .

Therefore, there is a large uncertainty for the lowest and the highest scattering angles. At low angles, there is a large disagreement between the Longtin and the HG phase functions. As was shown in Section 5.2, aerosols with high radii contribute principally in this

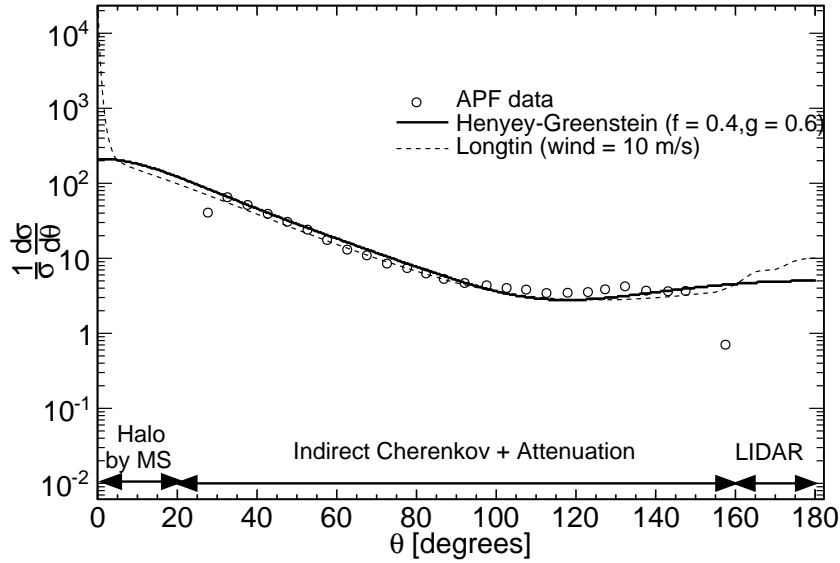


Figure 5.17: **Parameterization of the aerosol phase function in the Pierre Auger Observatory.** Data from BenZvi *et al.* [24] are represented by the circles. The continuous line is the Henyey-Greenstein (HG) function. The HG curve fits well the data obtained by the APF with ($g = 0.6$, $f = 0.4$). The dashed line is the Longtin parameterization (desert atmosphere simulated with a wind speed of 10 m/s) at a wavelength $\lambda = 0.55 \mu\text{m}$. The arrows represents the angle ranges affecting each physics phenomenon or technique.

range of scattering angles. Either the HG parameterization underestimates the contribution of large aerosols or the Longtin model overestimates their contribution. But, as we will see in Section 5.4.4, these large aerosols contribute the most to the halo.

In order to understand this effect, it seems interesting to consider the Ramsauer approach. The goal here is to estimate a mean aerosol radius for the two parameterizations. For the HG phase function one needs a single aerosol type, whereas for the Longtin phase function two species need to be defined. To simplify the modelling of the aerosol size distribution, an aerosol type is defined by the parameters $(\bar{R}, \log_{10}\sigma)$ of their log-normal distribution.

In Figures 5.18 and 5.19 the results from the Ramsauer approach for the HG and Longtin parameterizations are given. To provide for agreement in the low scattering angle range, a log-normal distribution ($\bar{R}_1 = 0.25 \mu\text{m}$, $\log_{10}\sigma_1 = 1/2$) is needed. However, in the Longtin case, it is necessary to have an additional aerosol population at large mean radius: ($\bar{R}_2 = 9 \mu\text{m}$, $\log_{10}\sigma_2 = 1/2$). The appropriate weights for these two distributions in this case are 0.85 for the first population and 0.15 for the second one.

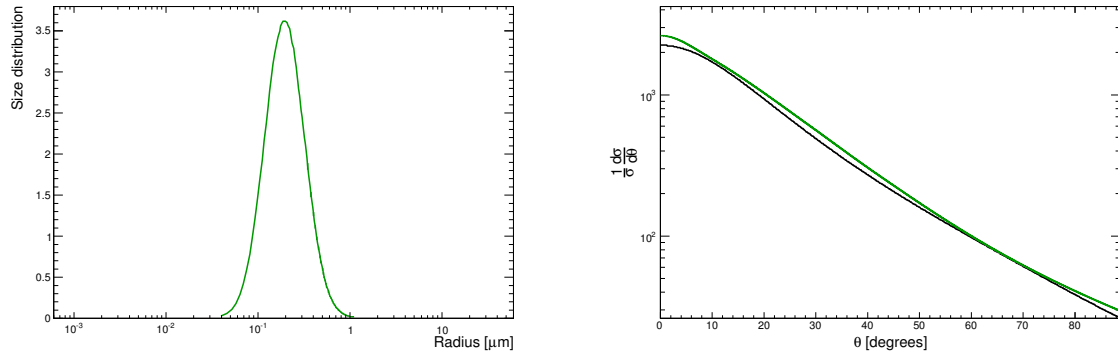


Figure 5.18: **Henyey-Greenstein phase function for one aerosol component.** *Left panel:* The aerosol size distribution obtained from the Ramsauer approach to reproduce the HG parameterization: ($\bar{R} = 0.25 \mu\text{m}$, $\log_{10} \sigma = 1/2$). *Right panel:* HG phase function (in black) compared with the Ramsauer phase function (in green) with an aerosol size distribution defined as in the left panel.

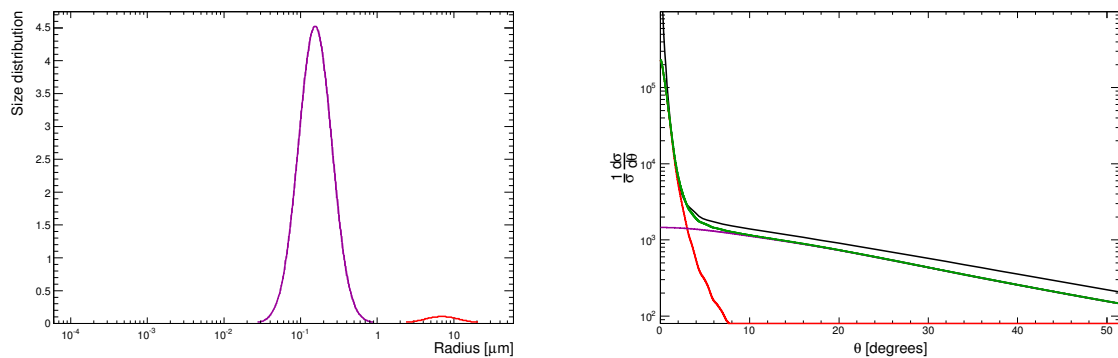


Figure 5.19: **Longtin phase function for two aerosol components.** *Left panel:* The aerosol size distributions obtained from the Ramsauer approach to reproduce the Longtin parameterization: ($\bar{R}_1 = 0.25 \mu\text{m}$, $\log_{10} \sigma_1 = 1/2$, fraction = 85%) in magenta and ($\bar{R}_2 = 9 \mu\text{m}$, $\log_{10} \sigma_2 = 1/2$, fraction = 15%) in red. *Right panel:* The Longtin phase function (in black) compared with the Ramsauer phase function (in green) with aerosol size distributions defined as in the left panel. The red and magenta curves represent the phase functions for the individual aerosol components.

5.4.4 Explanation of the FD halo by a component with large aerosol size

The effect of Mie scattering has, in previous studies, been considered to be similar to Rayleigh scattering. It turns out that this approximation is not accurate for large aerosol radii. The goal of this section will be to estimate the typical aerosol radius needed to reproduce the first peak.

As a first step, photon propagation in the atmosphere is simulated, from the zeppelin to the telescope. A Monte Carlo procedure was implemented to simulate aerosol scattering during photon propagation. An isotropic photon point source is assumed for the zeppelin. The lengths travelled before scattering by an aerosol are given by an exponential distribution. Typical values for the aerosol extinction length in the atmosphere are around 10 km (altitude dependence is neglected here). In fact, this parameter can be modified to reproduce a more or less high aerosol concentration. The photons undergo scattering according to the phase function derived in Equation (5.25). Use of the closed Ramsauer formula massively reduces the execution time of the simulation compared to what it would be with the full Mie calculations. To simplify the model, the photon is assumed to scatter only once during propagation. The optical axis (ST) is the line connecting the zeppelin to the telescope. The emission angle α' and the reception angle α have rotational symmetry around the (ST) axis. The scattering angle is equal to $\theta = \alpha + \alpha'$. It can be seen in Figure 5.20 that, for a given reception angle α , scattering occurring close to the zeppelin involves a large emission angle α'_1 and thus a large scattering angle $\theta_1 = \alpha + \alpha'_1$, whereas scattering near the telescope induces a smaller emission angle α'_2 and a smaller scattering angle $\theta_2 = \alpha + \alpha'_2$. Hence, according to the phase function, scattering far from the zeppelin and close to the telescope is more probable. This simulation procedure provides the reception angular distribution $(1/\sigma)(d\sigma/d\alpha)$ for a fixed aerosol radius.

The optical axis and the light spot axis generally do not coincide with the pixel axis, but are shifted by an angle ζ . The light spot centre is set at point O in Figure 5.21 whereas the pixel centre is set at O' . The pixel field of view is given by the disk centered at O' with angular radius r_p . Photons from the halo are detected when they have a reception angle α inside the disk (O', r_p). As ζ is the measured angle in the detector, one has to rewrite the distribution $(1/\sigma)(d\sigma/d\alpha)$ in terms of $(1/\sigma)(d\sigma/d\zeta)$. Thus, for a fixed ζ , the distribution of reception angle is integrated on the whole pixel defined by (r, ϕ) in the polar coordinate system

$$\frac{1}{\sigma} \frac{d\sigma}{d\zeta} = \int_0^{2\pi} d\phi \int_0^{r_p} r dr \frac{1}{\sigma} \frac{d\sigma}{d\alpha}(r, \phi), \quad (5.42)$$

where the integration is evaluated numerically by a Monte Carlo procedure, sampling pixels uniformly in $0 \leq r \leq r_p$ and $\phi \in [0, 2\pi]$.

From the data reconstruction procedure, the uncertainty in the barycentre estimation for the light spot is around 0.7° . To include this uncertainty in the simulation, the light spot

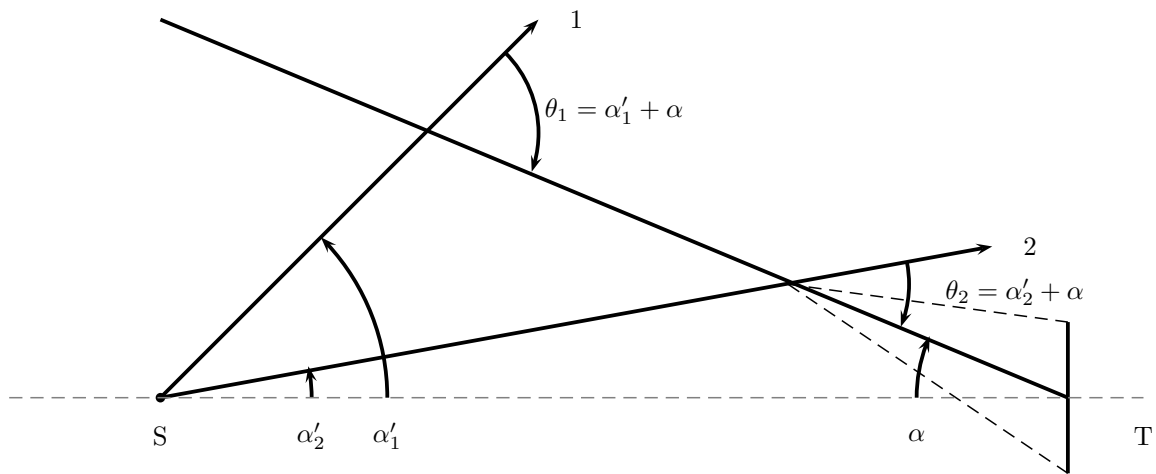


Figure 5.20: Two different photon paths for photon propagation from the zeppelin to the telescope. The length between the source (S) and the telescope (T) is fixed at 1 km.

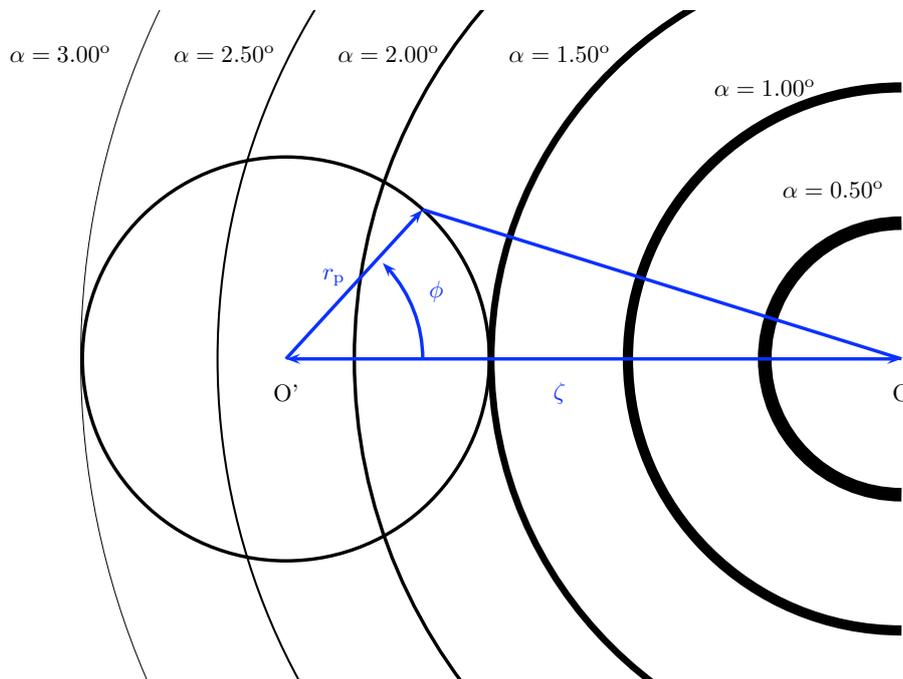


Figure 5.21: Light spot and pixel field of view used in the integration procedure. The thickness of the line representing the spot for different values of α is proportional to the number of photons.

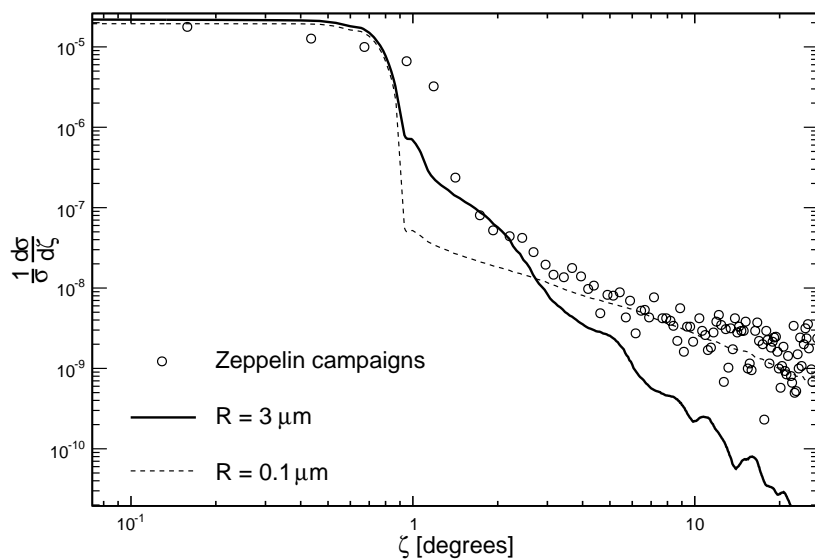


Figure 5.22: **Differential intensity distribution obtained from the Ramsauer approach.** The aerosol extinction length is fixed at 10 km for the two populations and the wavelength at $0.38 \mu\text{m}$. The circles represent the data from [21]. The continuous line illustrates the case where $R = 3 \mu\text{m}$ and the dashed line where $R = 0.1 \mu\text{m}$.

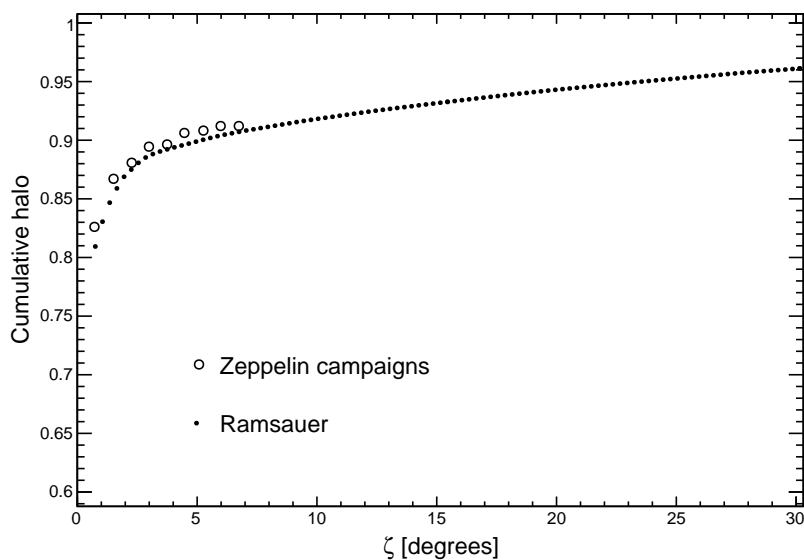


Figure 5.23: **Accumulated halo distribution obtained from the Ramsauer approach.** The dots represent the aerosol distributions obtained in Figure 5.22. The circles represent the data from [21].

position is displaced randomly on a disk of that radius. The angular distance α is given by

$$\alpha = \sqrt{(\zeta + r_{\text{Rand}} \cos \beta - r_p \cos \phi)^2 + (r_{\text{Rand}} \sin \beta - r_p \sin \phi)^2}$$

where r_{Rand} is distributed uniformly between 0° and 0.7° , and β is the randomly generated polar angle.

Figure 5.22 shows the differential intensity distribution obtained from the Monte Carlo procedure (the direct light is included). The halo data from the zeppelin campaigns are well reproduced up to $\zeta = 2^\circ$ for an aerosol radius equal to $3 \mu\text{m}$. The behaviour seen above 2° could be due to an additional aerosol population of radius $R = 0.1 \mu\text{m}$.

Another way to present this result is to plot the cumulative halo which represents the integrated signal between the pixel centre and an angular distance ζ . From the zeppelin campaigns and normalizing to the data set for $\zeta = 30^\circ$, 86% of the total intensity lies within 1.3° of the spot centre (see Figure 5.15(b)). Figure 5.23 compares the data from [21] with the accumulated halo distribution characterized by the two populations obtained in Figure 5.22. Contrary to the zeppelin analysis, the cumulative halo from the Ramsauer approach is normalized to the data for $\zeta = 85^\circ$.

5.5 Conclusion

We have shown that within the experimental errors the Ramsauer method predicts an extinction efficiency factor and a scattering phase function compatible with those given by the Mie solution. The large oscillatory behaviour for the extinction efficiency factor is understood as the consequence of the interference between the fraction of light going through and the fraction passing close to the drop. The small ripples which are observed can be explained by reflected light interfering with the other two components.

Two Ramsauer solutions have been given for the scattering phase function. The form of the first one, $P_R(\theta)$, without approximations, does not lead itself to obvious physical interpretation. The second, the simplified Ramsauer solution $P_{\text{SR}}(\theta)$, is an analytical formula from which characteristic behaviour can be predicted. However it cannot reproduce the Rayleigh regime for small size parameters.

As an application of the Ramsauer approach, a first attempt to explain the FD halo phenomenon has been presented. To model this halo, we have developed a Monte Carlo procedure based on the Ramsauer approach. We have shown that aerosols are a possible explanation for the halo measured in the FD camera. Two aerosol populations were introduced: large aerosols, typically with radii around $3 \mu\text{m}$, for the first part of the halo, and a second aerosol population with radii around $0.1 \mu\text{m}$ for the rest. We will show in Chapter 8 that considering larger aerosols and multiple scattering on aerosols (i.e. number of scatterings greater than

one), we get a much better adequation with the experimental FD halo data.

Bibliography

- [1] HC Van De Hulst, *Light scattering by small particles*, Dover publications (1981).
- [2] G Mie, *Beiträge zur Optik Trüber-Medien, speziell Kolloidaler Metallösungen*, Ann. Physik **25** (1908) 377–452.
- [3] CW Ramsauer, Ann. Physik **64** (1921) 513.
- [4] WF Jr Egelhoff, *Semiclassical explanation of the generalized Ramsauer-Townsend minima in electron-atom scattering*, Phys. Rev. Lett. **71** (1993) 2883–2886.
- [5] Golden DE and Bandel HW, *Low-Energy e^- -Ar Total scattering cross sections: the Ramsauer-Townsend effect*, Phys. Rev. **149** (1966) 58–59.
- [6] GP Karwasz, *Positrons – an alternative probe to electron scattering*, European Physical Journal D **35** (2005) 267–278.
- [7] RS Grace *et al.*, *Ramsauer-Townsend effect in the total cross section of $^4\text{He} + ^4\text{He}$ and $^3\text{He} + ^3\text{He}$* , Phys. Rev. A **14** (1976) 1006–1008.
- [8] RW Bauer *et al.*, *Application of simple Ramsauer model to neutron total cross sections*, (1997) Preprint: Lawrence Livermore National Laboratory.
- [9] S Fernbach, R Serber and TB Taylor, *The scattering of high energy neutrons by nuclei*, Phys. Rev. **75** (1949) 1352–1355.
- [10] RS Gowda, SSV Suryanarayana and S Ganesan, *The Ramsauer model for the total cross sections of neutron nucleus scattering*, (2005) arXiv:nucl-th/0506004.
- [11] JM Peterson, *Neutron giant resonances – nuclear Ramsauer effect*, Phys. Rev. **125** (1962) 955–963.
- [12] WP Abfalterer *et al.*, *Measurement of neutron total cross sections up to 560 MeV*, Phys. Rev. C **63** (2001) 044608–044626.
- [13] B Keilhauer, *Investigation of Atmospheric Effects on the Development of Extensive Air Showers and their Detection with the Pierre Auger Observatory*, PhD thesis, Universität Karlsruhe (2003).
- [14] CF Bohren and DR Huffman, *Absorption and scattering of light by small particles*, Wiley-Interscience, New York (1983) p 477.
- [15] I Weiner *et al.*, *Particle size determination: an undergraduate lab in Mie scattering*, Am. J. Phys. **69** (2001) 129–136.

-
- [16] SSV Surya Narayan *et al.*, *Empirical estimates of the neutron-nucleus scattering cross sections*, arXiv:nucl-0409005 (2004).
- [17] RW Bauer *et al.*, *Application of simple Ramsauer model to neutron total cross sections*, International Conference on Nuclear Data for Science and Technology, Trieste, Italy (1997).
- [18] <http://www.philiplaven.com/mieplot.htm>
- [19] BR Dawson, M Debes and P Sommers, *Shower profile reconstruction with Engineering array FD data*, **GAP-2001-016**.
- [20] D Allard *et al.*, *A new method for the longitudinal profile reconstruction of the Auger fluorescence detector events*, **GAP-2006-026**.
- [21] J Parrisius, *Test of the calibration of the Auger fluorescence telescopes with an isotropic UV light source*, **GAP-2009-045**.
- [22] M Unger *et al.*, *Lateral shower light distributions in the Cherenkov-Fluorescence-Matrix profile reconstruction*, **GAP-2008-052**.
- [23] A Creusot and D Veberič, *(Possible) source of FD halo*, **GAP-2009-070**.
- [24] S BenZvi *et al.*, *Measurement of the Aerosol Phase Function at the Pierre Auger Observatory*, *Astropart. Phys.* **28** (2007) 312–320.
- [25] DR Longtin *et al.*, *A wind dependent desert aerosol model: radiative properties*, Air Force Geophysics Laboratories (1988) **AFL-TR-88-0112**.

Where do aerosols come from ? – Study done with HYSPLIT

Contents

6.1 HYSPLIT, an air modelling program	180
6.1.1 Trajectory computational method	181
6.1.2 Meteorological data all along the trajectory	182
6.2 Aerosol origin and their trajectory up to the Auger location	182
6.3 Seasonal profiles of the different meteorological quantities	190
6.4 Cross-checks between Aerosol optical depth data and HYSPLIT	194
6.5 HYSPLIT, a tool to better understand Rayleigh nights ?	196
6.6 Conclusion	199
Bibliography	200

Introduction: This chapter presents a complete study of the air mass trajectories passing through the Pierre Auger Observatory. Such a study has been done thanks to HYSPLIT, an air modelling program. Large fluctuations of the trajectories have been identified, showing that the aerosols (present in the air masses) do not come from the same region throughout the year. The study also focusses on seasonal behaviour for different meteorological variables. Finally, a cross-check with the aerosol optical depth data concludes that nights with low aerosol concentrations have as main origin the Pacific Ocean.

This work led to an internal note¹, and the next step is its publication in an atmospherical journal as an Auger full-author list paper. In this case, it would be the first Auger publication in atmospheric science.

¹K Louedec and M Urban, *Where do aerosols come from ? – Study done with HYSPLIT* GAP-2011-058

One of the defining characteristics of aerosols in the atmosphere is that they are highly mobile. Therefore atmospheric properties for a particular location are a function not only of local emissions but also of emissions and meteorological conditions in the surrounding. In our case, the Pierre Auger Observatory (35° S, 69° W) could be also affected by air masses potentially carrying aerosols from, for instance, Chile or the Pacific Ocean. Thus, any study having as a goal to explain aerosol properties over the SD array needs to include work on the air mass origins.

For a region outside of the SD array to influence local measurements, the following three conditions must occur simultaneously:

1. the region is a source of aerosols,
2. the air mass coming from the region has to transport the aerosols in a sufficiently short time so that the aerosol content is still present on arrival,
3. the air mass arriving at the SD array must be at an altitude that would affect the part of the atmosphere probed by the detector.

Meteorological data affect also the aerosol transport to the observatory location. It is known for instance that rainfall cleans the atmosphere. This means that when rainfall occurs, it can be assumed that aerosols, due to the aggregation with the raindrops, fall to the ground.

In Section 6.1, a brief presentation of the HYSPLIT air modelling program is given. Then, Section 6.2 will focus on the air mass trajectories and origin of the aerosols passing above the Auger location. Seasonal profiles of the main physical quantities will be extracted all along their path in Section 6.3. After having studied the air mass trajectories crossing the Auger Observatory, cross-checks with aerosol optical depth measurements done by the Central Laser Facility (CLF) will be presented in Section 6.4. Finally, a first attempt to explain the *Rayleigh nights* will be undertaken in Section 6.5. Up to now, the collaboration has not been able to explain why some nights have extremely low aerosol levels in the atmosphere above the array. In previous studies, only the data collected by the weather stations were used. Thus, only very local effects have been tested. The main purpose here will be to enlarge the study to the surrounding regions.

6.1 HYSPLIT, an air modelling program

Different air models have been developed to study air mass relationships between two regions. Among them, the *HYbrid Single-Particle Lagrangian Integrated Trajectory* model, or HYSPLIT [1, 2], is a commonly used air modelling program that can calculate air mass displacements from one region to another. Thus, it is possible to demonstrate whether one region

affects the aerosol transport. The HYSPLIT model developed by the Air Resources Laboratory, NOAA², is a complete system designed to support a wide range of simulations related to regional or long-range transport and dispersion of airborne particles. HYSPLIT computes simple trajectories to complex dispersion and deposition simulations using either puff or particle approaches with a Lagrangian framework.

In this work, HYSPLIT will be used only to get backward trajectories: by moving backward in time, the resulting backward trajectory indicates air mass arriving at a receptor for a particular time, thus identifies the regions affecting it. All along the air mass paths, meteorological data will be recorded every hour.

6.1.1 Trajectory computational method

If we assume that a particle passively follows the wind, then its trajectory is just the integration of the particle position vector in space and time. The final position is computed from the average velocity at the initial position (P) and the first-guess position (P')

$$P(t + dt) = P(t) + \frac{1}{2} (v [P(t)] + v [P'(t + dt)]) dt$$

$$P'(t + dt) = P(t) + v [P(t)] dt.$$

The integration time step is variable:

$$v_{\max} \times dt \leq 0.75,$$

where the value 0.75 is given in *meteorological grid spacing* (value fixed by HYSPLIT).

A key point when air mass trajectories are computed is to estimate the trajectory error. Usually, one expects the total error to be anywhere between 15 to 30% of the travel distance. The total error can be divided into three error components:

- **the physical error** due to the inadequacy of the data representation of the atmosphere in space and time. It is related to how well the numerical fields estimate the true flow field. There is no way of knowing this error without independent verification data.
- **the computational error** due to numerical uncertainties. This error is composed of *the integration error*, being estimated by computing a backward trajectory from the last forward trajectory endpoint, and *the data resolution error*, i.e. trying to represent a continuous function, the atmospheric flow field, with gridded data points of limited resolution in space and time.
- **the measurement error** in creating the model is meteorological data fields.

²NOAA, National Oceanic and Atmospheric Administration, U.S.A.

6.1.2 Meteorological data all along the trajectory

HYSPLIT is able to provide details on some of the meteorological parameters along the trajectory. Currently, it is possible to extract information on terrain height, pressure, ambient and potential temperature, rainfall, relative humidity and solar radiation. However, to produce a trajectory, HYSPLIT requires at least the wind vector, ambient temperature, surface pressure and height data. These data can come from different meteorological models. Among them, the most famous are the North American Meso (NAM), the NAM Data Assimilation System (NDAS) and the Global Data Assimilation System (GDAS). Only the GDAS model provides meteorological data for the whole Earth: its data are available in three-hour steps with a 1×1 degree of horizontal resolution. The validity of the GDAS model has already been checked by the Auger Collaboration: its agreement with ground-based weather station and meteorological radio-sonde launches has been verified [3]. The GDAS grid point assumed for the Auger location is (35° S, 69° W), i.e. just a little bit outside the array to the north-east. All these atmospheric data are especially formatted by NOAA using compressed binary files to minimize execution time and storage space. HYSPLIT downloads these data directly from the NOAA ARL ftp server [4].

6.2 Aerosol origin and their trajectory up to the Auger location

Three entire calendar years, from 2007 to 2009, were modelled so that seasonal variations could be observed and included in the analysis. A backward trajectory is computed over 48 hours every hour, throughout the year (i.e. 24 computed trajectories per day). Also, the evolution profiles of the different meteorological quantities are estimated and recorded. The key input parameters for the runs are given in Table 6.1. Figure 6.1 displays an example of a 48-hr backward trajectory from an altitude 500 m above the Malargüe location, estimated with HYSPLIT. A 2-day time scale is a good compromise with respect to aerosol lifetime, air mass dispersion and computing time.

Parameter	Setting
Meteorological dataset	GDAS
Trajectory direction	Backward
Trajectory duration	48 hours
Start point	Auger Observatory (35° S, 69° W)
Start height	500 m Above Ground Level (AGL)
Vertical motion	Model vertical velocity

Table 6.1: **Input parameters used for all HYSPLIT runs.**

Each run provides an aerial plot of a trajectory arriving at the Pierre Auger Observatory,

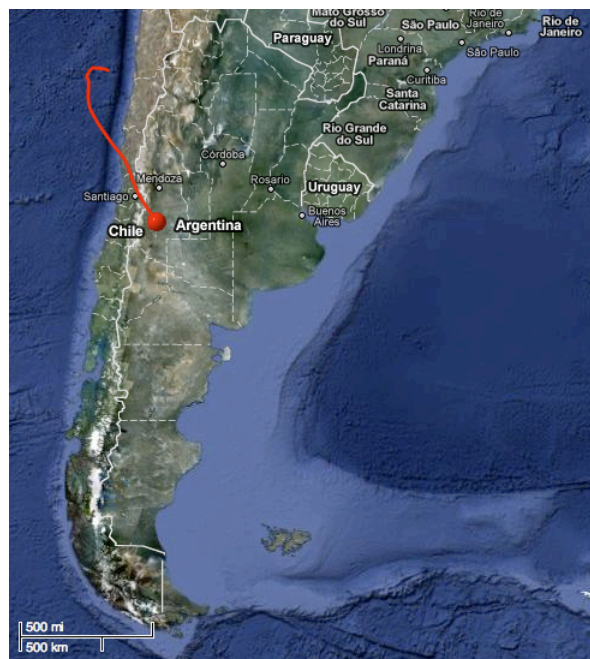


Figure 6.1: Example of a back trajectory from the Malargüe location, from HYSPLIT. The initial height is fixed at 500 m above ground level.

and the evolution of the relevant meteorological quantities all along the trajectory. Most of the aerial plots shows air masses having significant changes of direction during the previous 48 hours, even sometimes looping back on themselves. Therefore, two different methods were used to characterize air mass origin and mean trajectory.

The first kind of plot is a two-dimensional histogram having as axes longitude and latitude. From this display, it is possible to extract regional influence on Auger air quality. Also, direction changes are not missed. Therefore, all regions that an air mass path traversed during its entire 48-hr travel period to the Pierre Auger Observatory are recorded by this representation. It provides a complete picture of the regional influence on Auger atmospheric quality. Figures 6.2, 6.4 and 6.6 display the distribution of the backward trajectories for each month during the years 2007, 2008 and 2009. It is clear that air masses do not come from similar regions all along the year. Also, the fluctuations are more or less strong. June and/or July and/or August are really uncommon months where the air mass trajectories have large fluctuations. These observations will be recalled later in Section 6.4 and Section 6.5 when we will try to understand better the aerosol-free nights, the so-called *Rayleigh nights*.

Plot having as goal the direction of the air mass paths can also be shown: it consists to divide each air mass trajectory into two 24-hr sub-trajectories. A direction for the most recent sub-trajectory is then chosen among these height directions: North/N, North-East/NE,

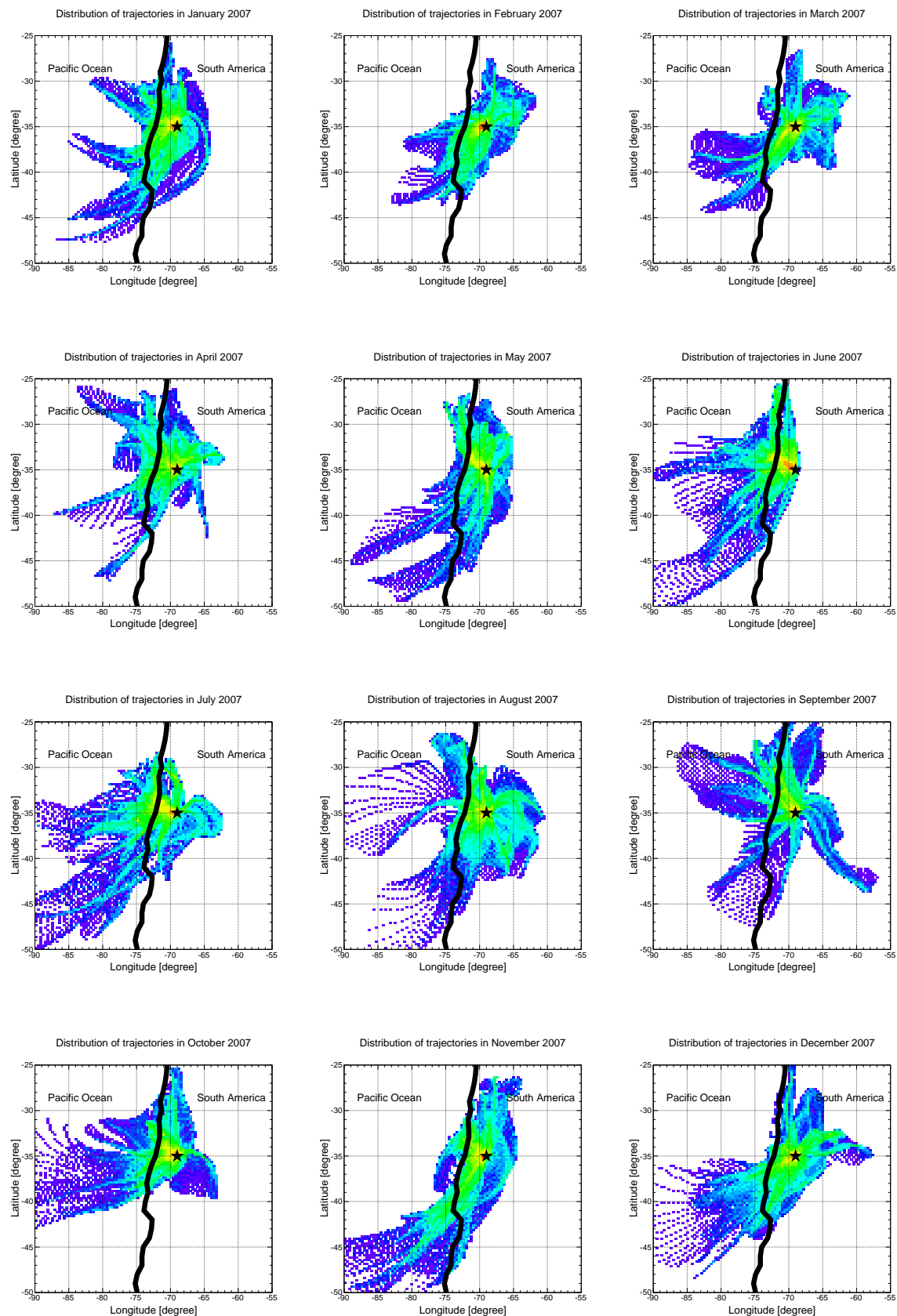


Figure 6.2: **Distribution of monthly 48-hr backward trajectories from the Malargüe location.** Paths estimated with HYSPLIT for the year 2007, with input parameters given in Table 6.1. The black star represents the Auger location. The black line represents the coast. The color indicates the frequency of a region, from blue to red.

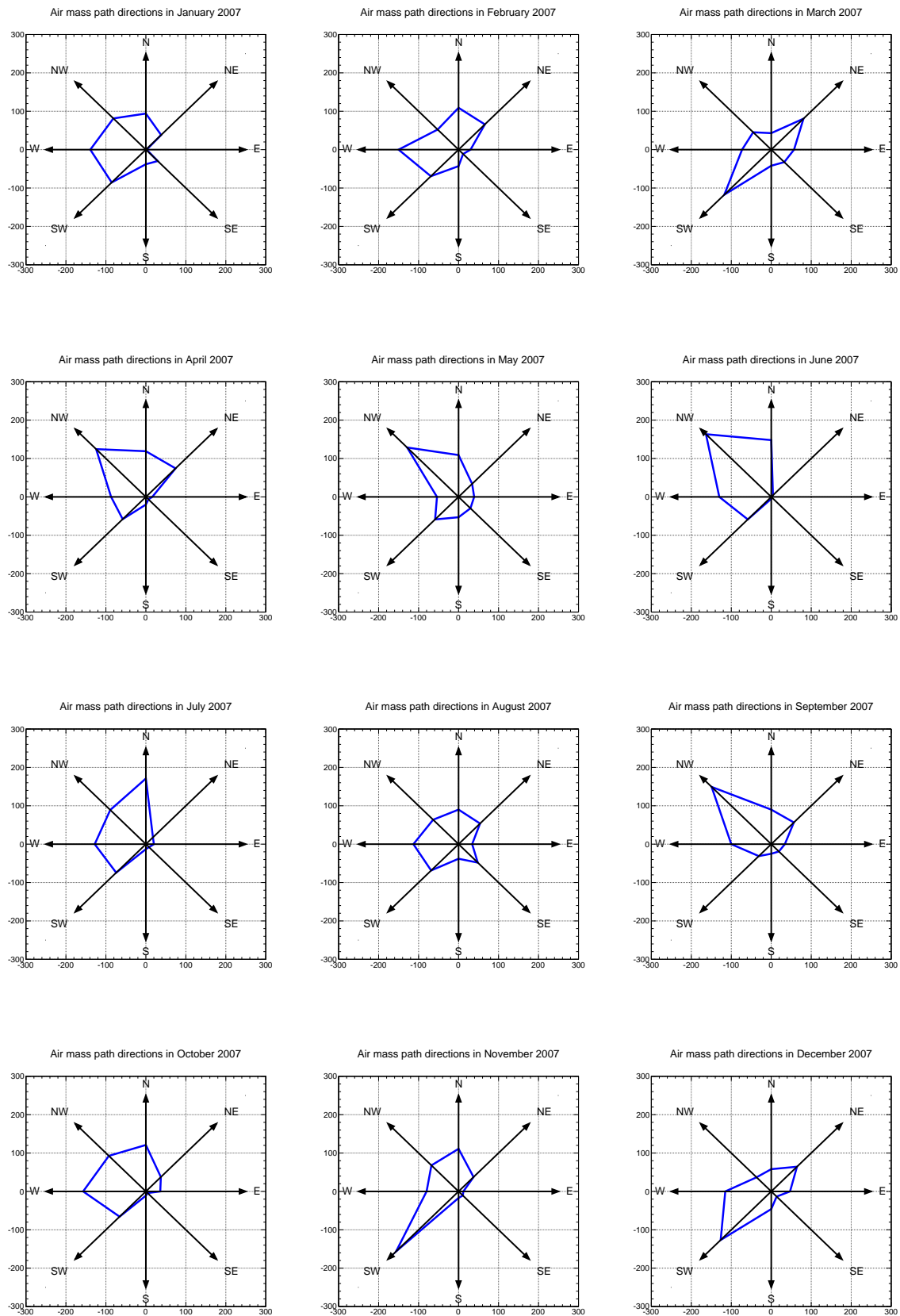


Figure 6.3: Direction of air masses influencing the Auger atmosphere for each month. Direction of trajectories estimated with HYSPLIT for the year 2007, with input parameters given in Table 6.1.

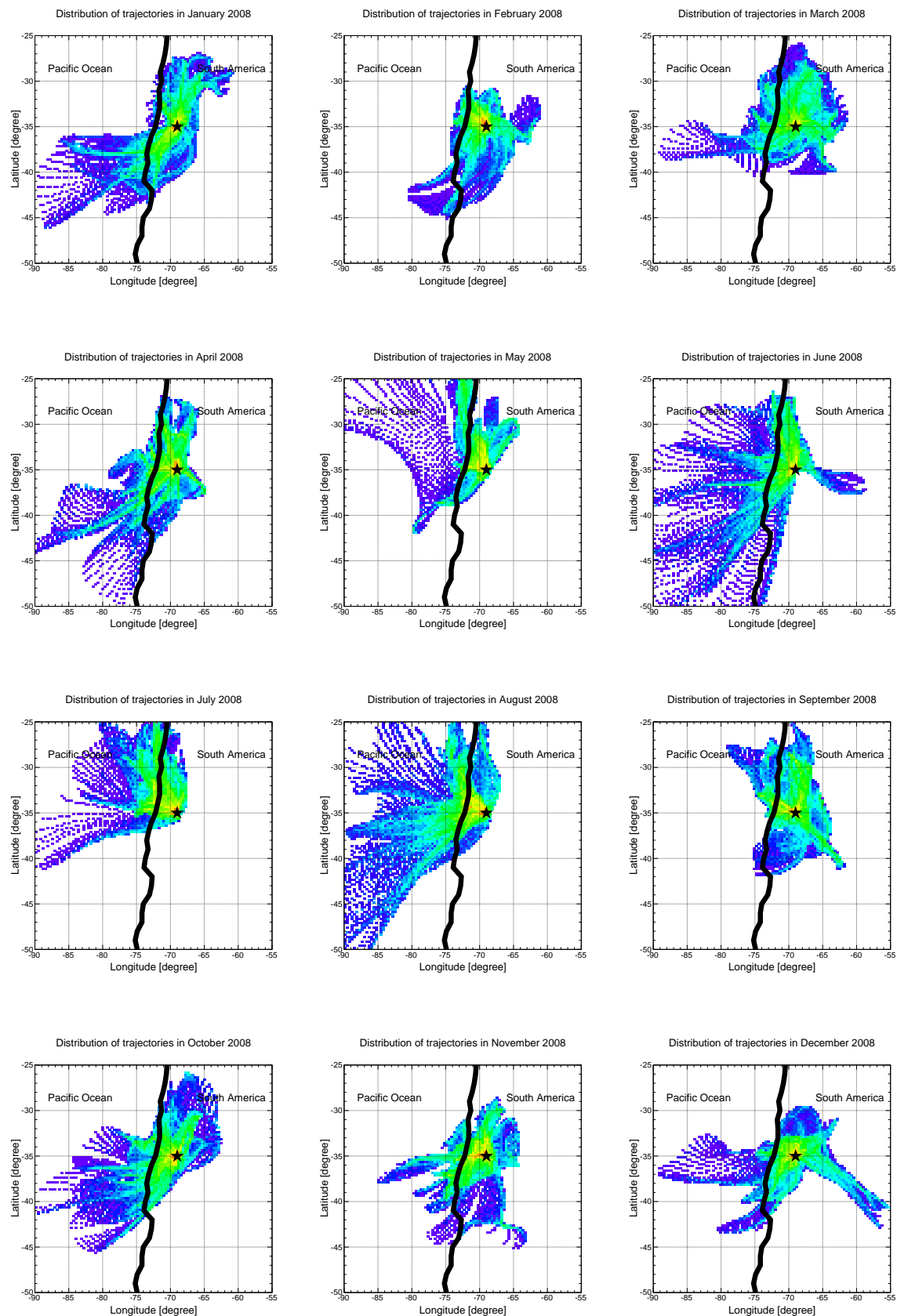


Figure 6.4: **Distribution of monthly 48-hr backward trajectories from the Malargüe location.** Paths estimated with HYSPLIT for the year 2008, with input parameters given in Table 6.1. The black star represents the Auger location. The black line represents the coast. The color indicates the frequency of a region, from blue to red.

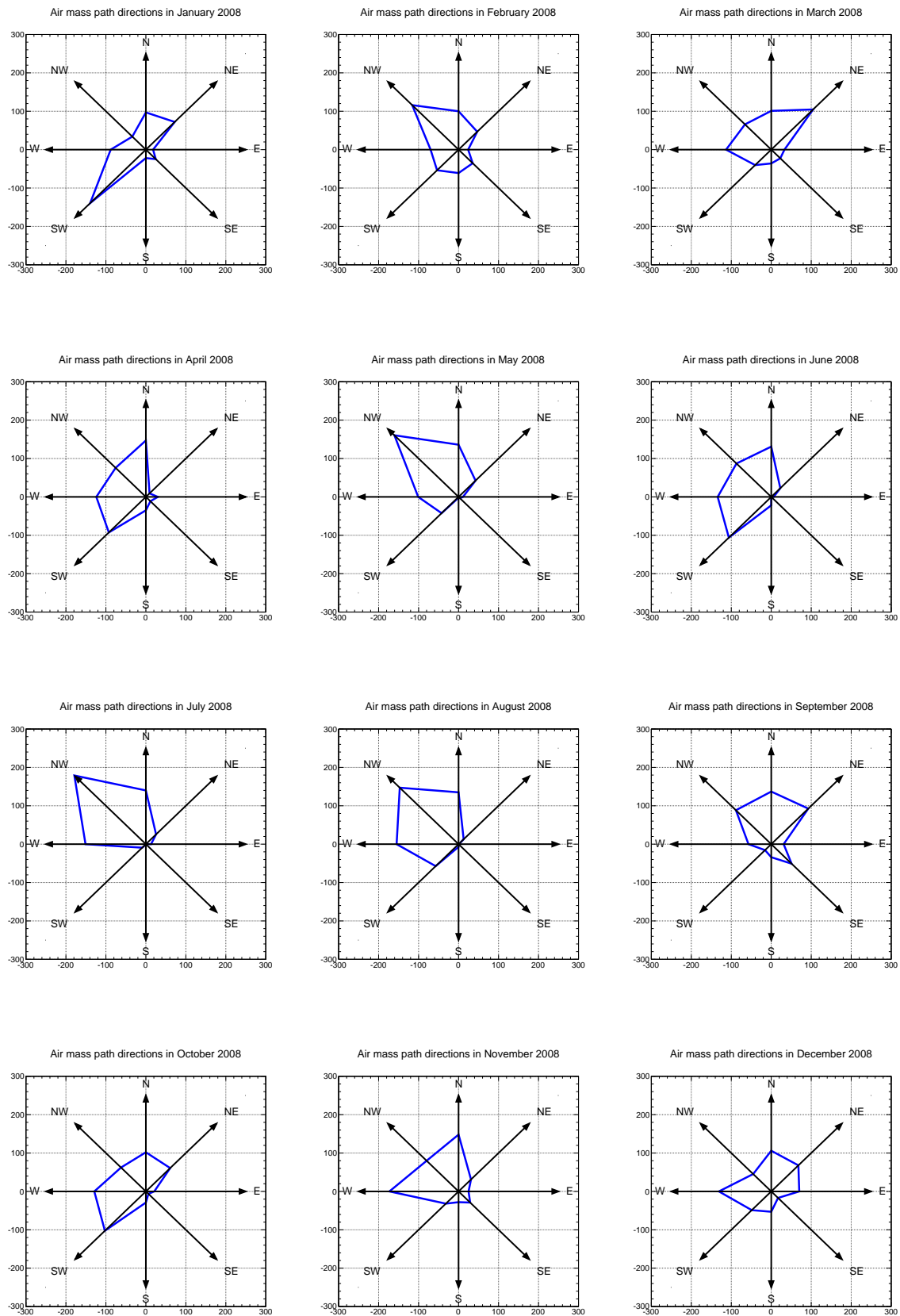


Figure 6.5: Direction of air masses influencing the Auger atmosphere for each month. Direction of trajectories estimated with HYSPLIT for the year 2008, with input parameters given in Table 6.1.

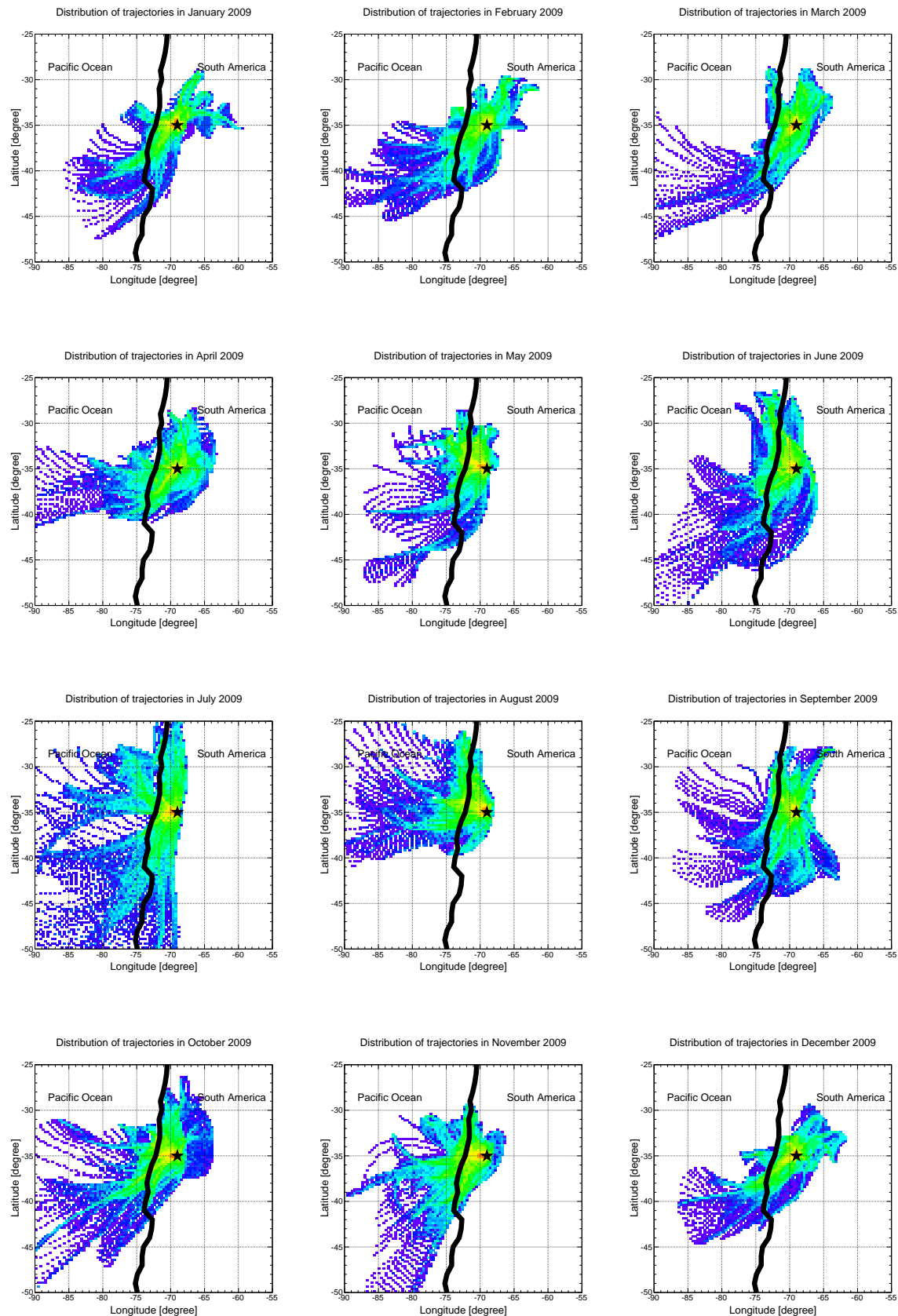


Figure 6.6: **Distribution of monthly 48-hr backward trajectories from the Malargüe location.** Paths estimated with HYSPLIT for the year 2009, with input parameters given in Table 6.1. The black star represents the Auger location. The black line represents the coast. The color indicates the frequency of a region, from blue to red.

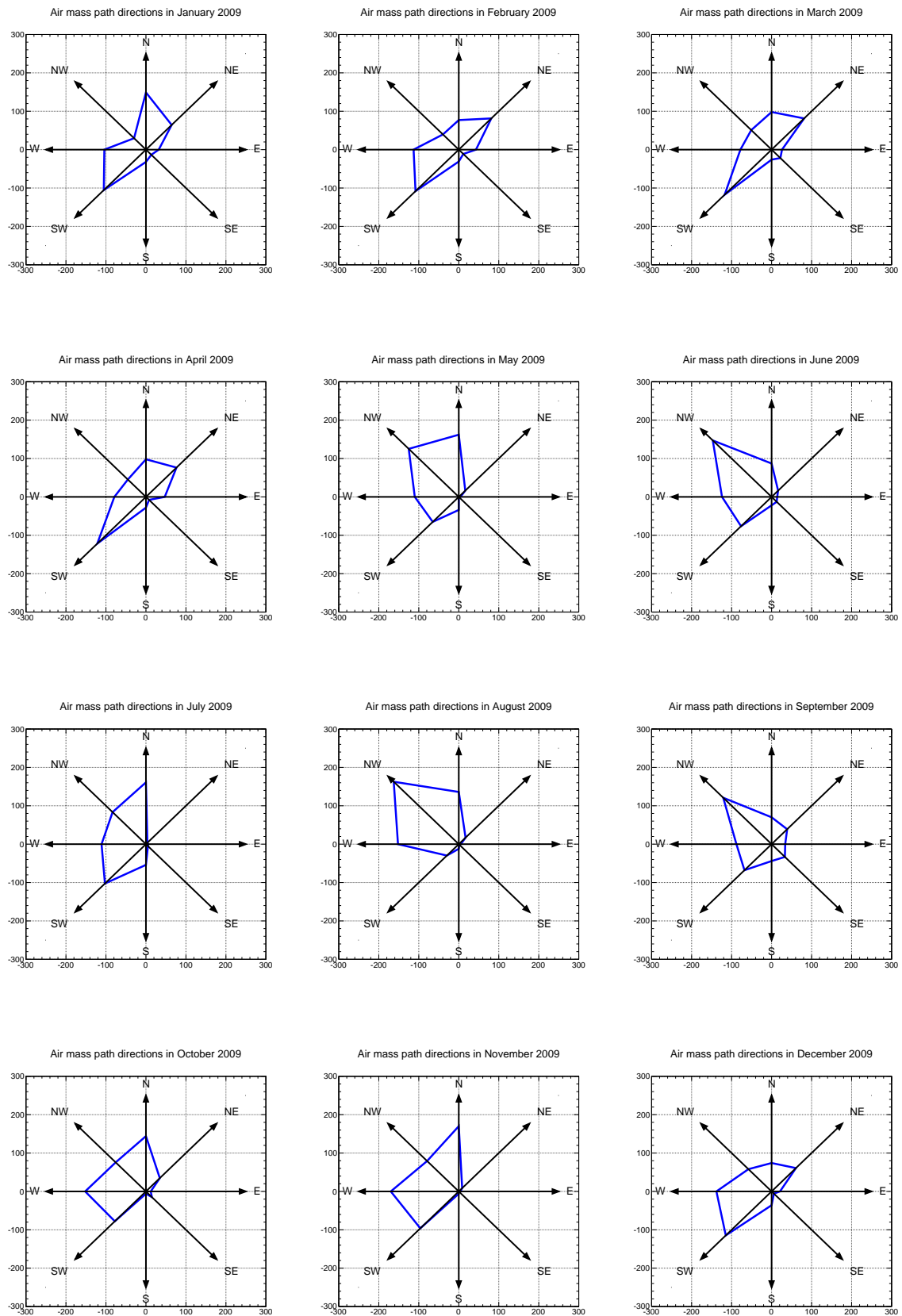


Figure 6.7: Direction of air masses influencing the Auger atmosphere for each month. Direction of trajectories estimated with HYSPLIT for the year 2009, with input parameters given in Table 6.1.

East/E, South-East/SE, South/S, South-West/SW, West/W, North-West/NW (origin of the frame being fixed at Auger location). This sub-path, being necessarily closer to the SD array, offers also a slightly better level of accuracy since modelling errors accumulate with increasing simulation time. The different directions recorded are then plotted in a histogram to compare their frequencies. Figures 6.3, 6.5 and 6.7 show these polar histograms for each month of the years 2007, 2008 and 2009. Most of the months have air masses with a North-West origin. Also, it can be seen immediately that it is unusual to have air masses coming from the East and travelling through the Malargüe location.

6.3 Seasonal profiles of the different meteorological quantities

Having determined the air-mass origins during the course of the year, it is now important to understand what happens during their travel. To answer this question, we have examined the meteorological data all along the path. HYSPLIT provides different physical quantities: among them, are pressure, mixed layer depth, temperature, rainfall and relative humidity which can be extracted hourly all along the trajectories.

Figures 6.8–6.10 display the different meteorological quantities all along the air-mass path for the years 2007, 2008 and 2009, respectively. The atmospheric mixed layer is defined as a layer of approximately constant potential temperature, or a layer in which the temperature gradient falls at a rate of around $10^{\circ}\text{C}/\text{km}$. Wind velocities are not constant throughout the mixed layer. First of all, the evolution profiles between each year are more or less the same, stressing the same typical behaviours. The height above ground level, for instance, has a typical behaviour during winter: the altitudes probed are in average higher than during the other seasons (especially than during summer). Knowing that aerosols are usually in the low part of the atmosphere (the mixed layer depth confirms this statement), these high altitudes could explain the lower concentrations of aerosol during winter. Also, it could involve differences in the aerosol size distribution or chemical composition of aerosols. The two maxima are observed in winter and summer seasons.

Around the Malargüe location, the atmospheric mixed layer depth is much higher during summer than winter. Even if the solar radiation is higher in summer, it is not enough to explain the difference between the values for the two seasons. The atmospheric mixed layer results from convective air motions, usually seen during the middle of the day when air at the surface is warmed up. It is then mixed by Rayleigh-Taylor instability. The mixed layer mediates the exchanges of heat or water between the Earth's surface and the overlying atmosphere. Thus, these exchanges happen at higher altitudes in summer than in winter.

The last main meteorological quantities influencing the aerosols are the relative humidity and rainfall. It is known that when it rains, raindrops catch the aerosols while falling and bring them to the ground level. The main effect is a cleaning of the atmosphere. From HYS-

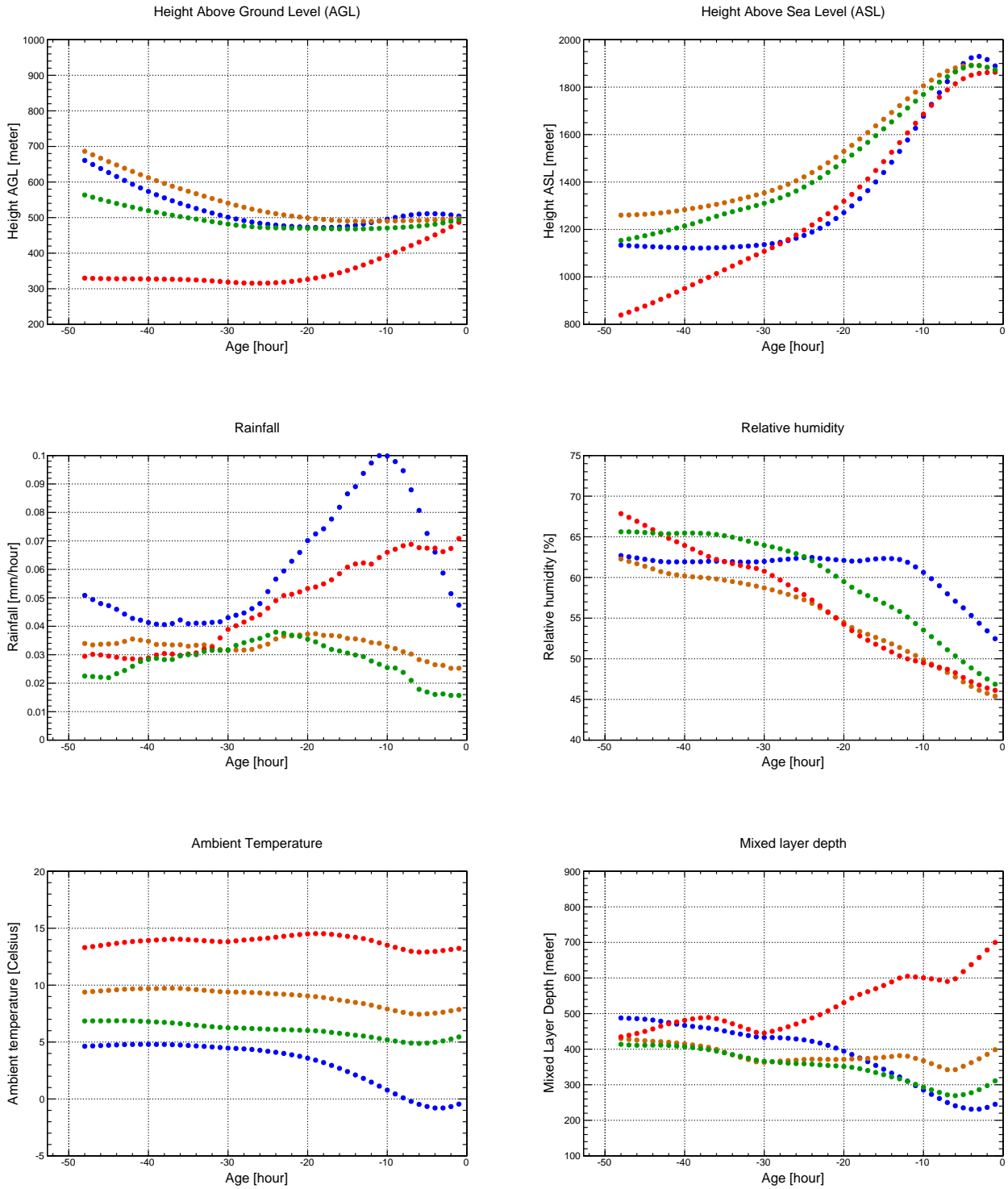


Figure 6.8: Seasonal profiles for different physical quantities along the backward trajectory. Quantities estimated with HYSPLIT for the year 2007, for each season: winter (*blue*), spring (*green*), summer (*red*), fall (*brown*). Input parameters given in Table 6.1.

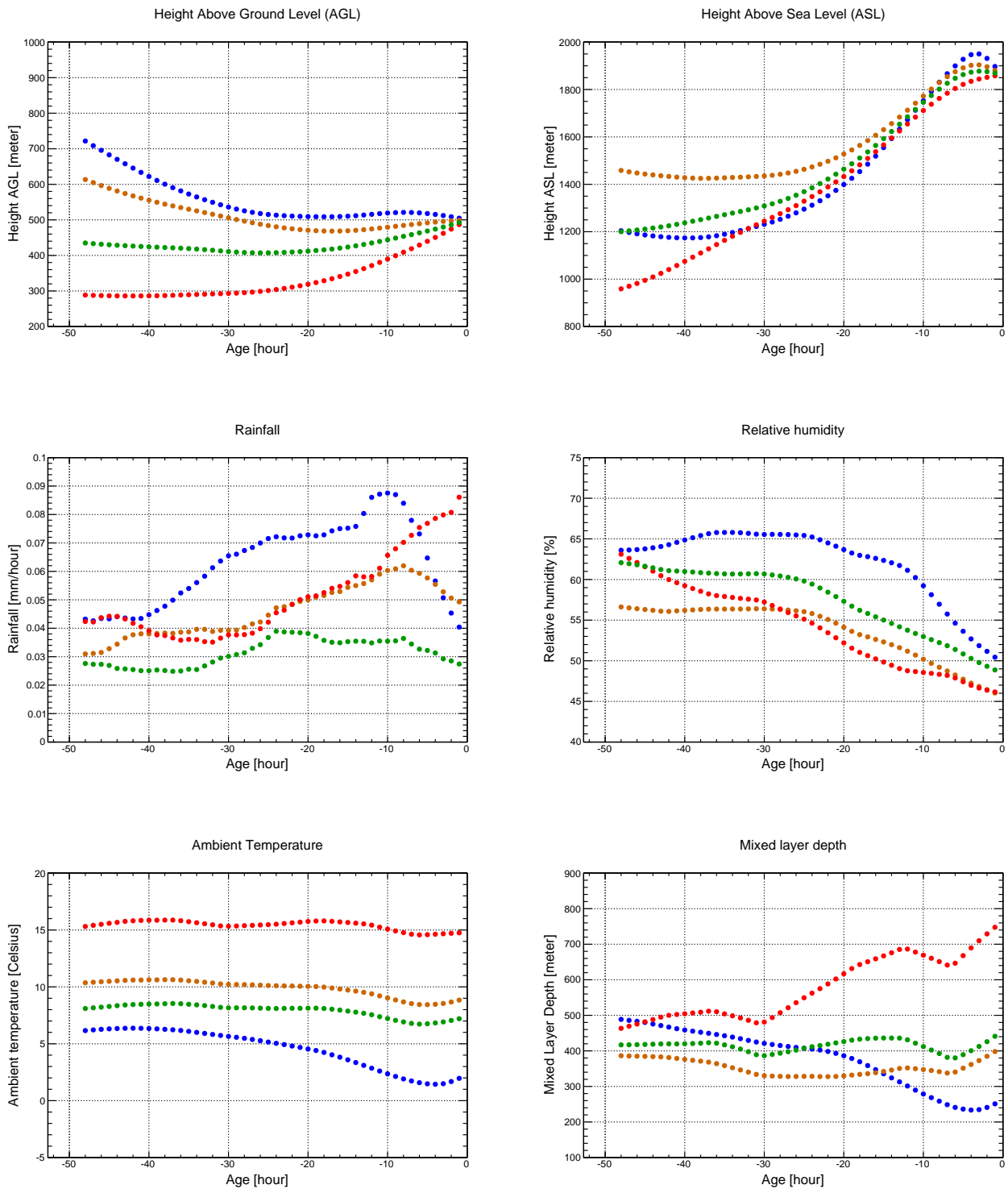


Figure 6.9: **Seasonal profiles for different physical quantities along the backward trajectory.** Quantities estimated with HYSPLIT for the year 2008, for each season: winter (*blue*), spring (*green*), summer (*red*), fall (*brown*). Input parameters given in Table 6.1.

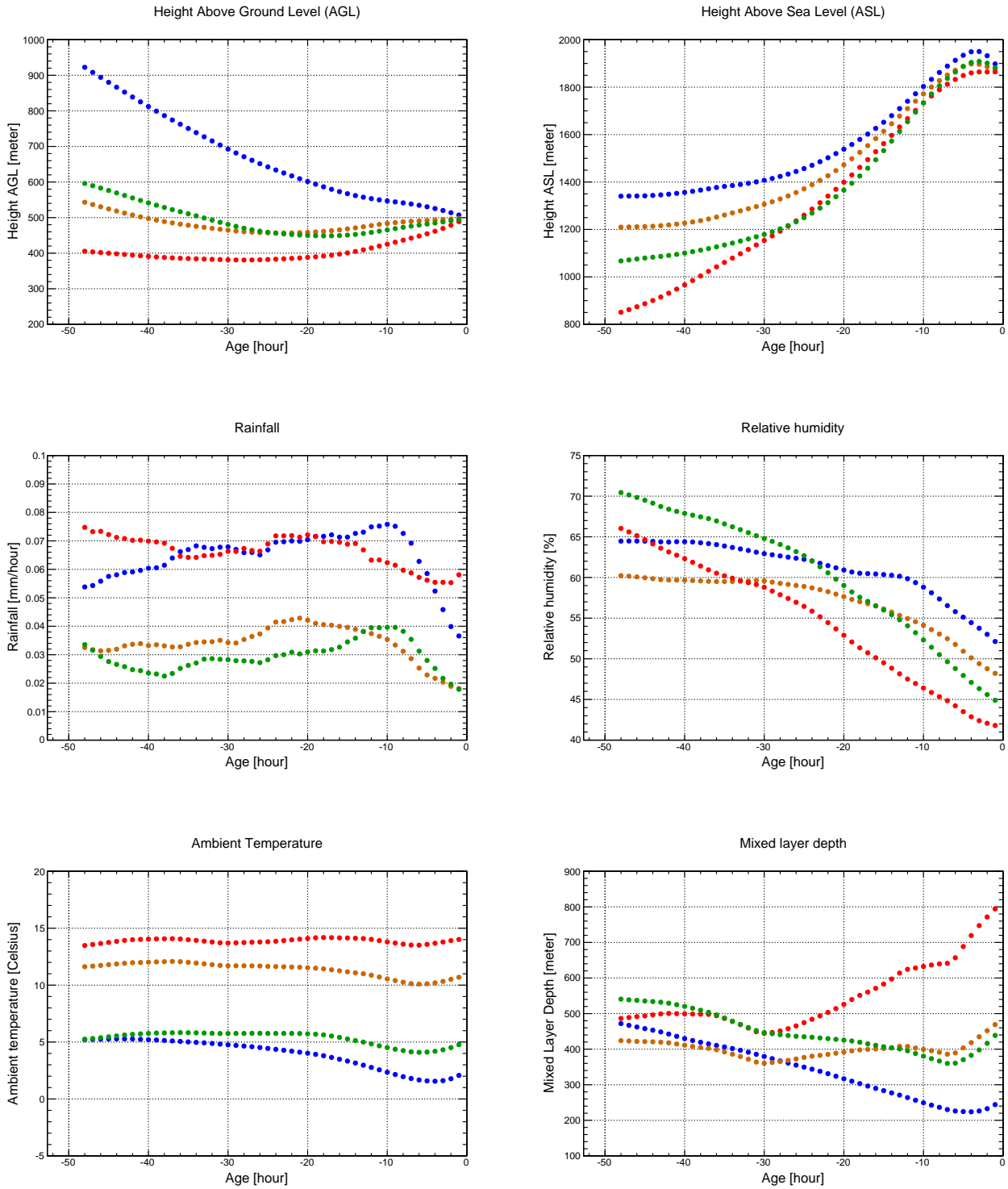


Figure 6.10: Seasonal profiles for different physical quantities along the backward trajectory. Quantities estimated with HYSPLIT for the year 2009, for each season: winter (*blue*), spring (*green*), summer (*red*), fall (*brown*). Input parameters given in Table 6.1.

PLIT, it can be seen that rainfall is more frequent during summer and winter: this could be a reason to have clear nights more frequently during these two periods.

6.4 Cross-checks between Aerosol optical depth data and HYSPLIT

At the Pierre Auger Observatory, several facilities have been installed to monitor the aerosol component in the atmosphere [5]. The aerosol monitoring is performed using two central lasers (CLF/XLF), four elastic scattering lidar stations, two aerosol phase function monitors (APF) and two optical telescopes (HAM/FRAM). The most important aerosol measurement made at Auger is the aerosol optical depth $\tau_a(h, \lambda_0)$ obtained by the Central Laser Facility at the wavelength $\lambda_0 = 355$ nm, for altitudes h above ground level up to about 10 km. It provides hourly altitude profiles at each FD site during FD data acquisition. Figure 6.11(a) depicts the distribution of the aerosol optical depth at 3.5 km above ground level, recorded at Los Leones, Los Morados and Coihueco [6]. Measurements from Loma Amarilla are not yet available due to its large distance from the CLF site. The mean value for $\tau_a(3.5$ km) is around 0.04. The nights with $\tau_a(3.5$ km) larger than 0.1, meaning a transmission factor lower than 90%, are rejected for air shower reconstruction.

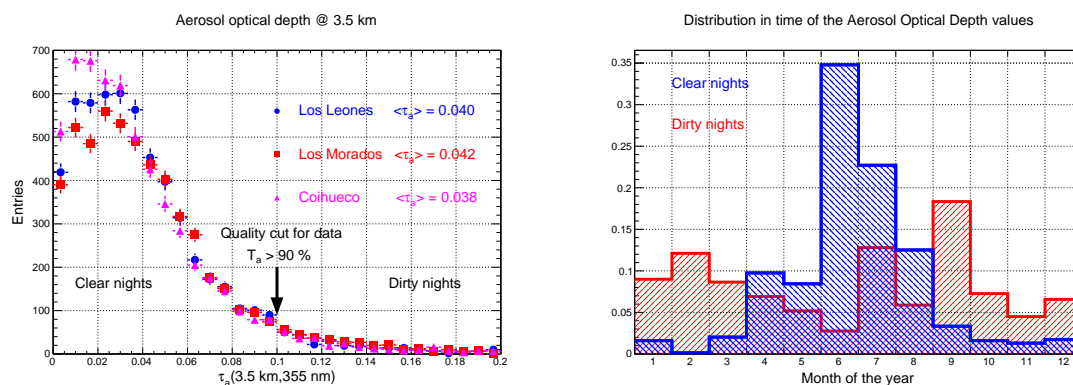


Figure 6.11: **Aerosol optical depth measurements from the CLF.** (a) Aerosol optical depth at 3.5 km above the fluorescence telescopes at Los Leones, Los Morados and Coihueco. Data set between January 2004 and December 2010. (b) Monthly frequency all along the year of “clear nights” ($0.00 \leq \tau_a \leq 0.01$) and “dirty nights” ($\tau_a \geq 0.10$) at Los Morados.

To perform this comparison we have divided our sample into three populations:

- **the clear nights** with the lowest aerosol concentrations: $\tau_a \leq 0.01$ (309 trajectories),
- **the dirty nights** with the highest aerosol concentrations: $\tau_a \geq 0.10$ (154 trajectories),
- **the other nights** being in the third category (2214 trajectories).

Figure 6.11(b) shows the relative frequency month by month for "clear nights" and "dirty nights". Clear nights are more common during the Austral winter than the rest of the year. In Section 6.2, we noted the large fluctuations for the air mass trajectories during winter (June / July / August). In addition, on the average, the height above ground for air masses is greater during this period. Let us assign each backward trajectory to one of the categories (following the aerosol depth measured by the CLF at the same time) and plot the distribution of the trajectories, and the atmospheric variables along their paths.

Figure 6.12 shows the distributions of the backward paths for "clear nights" and "dirty nights". The two plots are quite different: the air masses come mainly from the Pacific Ocean during the clear nights and travel principally through continental areas during the previous 48 hours for dirty nights. This observation can be explained as follows: the aerosols measured by Auger originate mainly from the soil. This is the conclusion of the chemical aerosol analysis done on the Auger site [7]. Thus 48-hr backward trajectories travelling mainly over the ocean can be characterized as air masses with a low concentration of soil aerosols. For those "oceanic" trajectories, only during the last hours before arrival at the site that aerosol contamination occurs, whereas for the overland trajectories it is possible during the full period. So it seems that the backward trajectories are the key point to explain the differences in aerosol concentration at the Auger Observatory.

Now that a difference in the backward trajectories has been identified, it seems interesting to plot the evolution of atmospheric quantities for the two categories for the previous 48 hours. Figure 6.13 gives the mean evolution profiles for height of the air masses, rainfall, relative humidity, temperature or mixed layer depth. Again, typical profiles are identified for clear and dirty nights. The clear nights involve travel mainly over the ocean, i.e. at above sea level height lower than for those travelling through the continental areas. Due to this decrease in the terrain height, air masses are thus at much higher AGL altitude for the clear nights. Contrary to that, during the dirty nights, the air masses are at low AGL height, where aerosols are mainly present. Another interesting point is the mixed layer depth and the relative humidity that have typical behaviours during the clear nights. Unlike the dirty nights or the rest of the nights, day/night cycle is not identified. This observation is probably due to the terrain change (oceanic/continental) over the aerosol path. On the other hand, from its evolution profile, rainfall does not seem to be a discriminating factor.

It is clear that a difference in the backward trajectories between the clear and the dirty nights has been identified thanks to HYSPLIT. Now, the next section will focus on the aerosol-free nights (a sub-sample among the clear nights) to check their consistency with this conclusion. Also, cross-checks with local atmospheric measurements will be made.

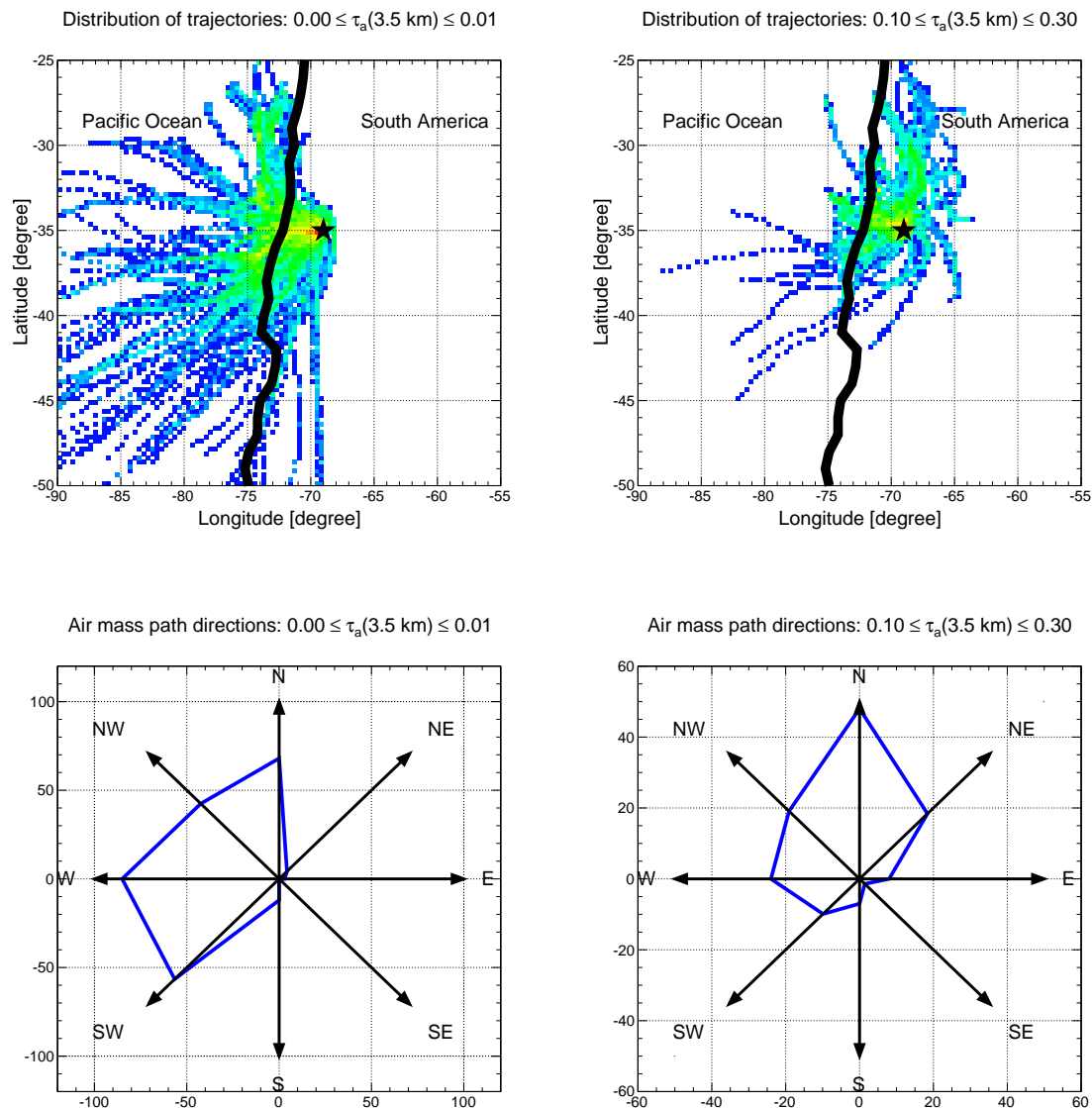


Figure 6.12: **Distribution of backward trajectories and direction of air masses for "clear nights" and "dirty nights"**. Paths estimated with HYSPLIT for the years 2007/2008/2009 and aerosol optical depth data coming from the CLF measurements. *Top panel:* Distribution of 48-hr backward trajectories from the Malargüe location. *Bottom panel:* Direction of air masses influencing the Auger atmosphere.

6.5 HYSPLIT, a tool to better understand Rayleigh nights ?

Over the past few years of FD operation, a few nights appear to have atmospheres without aerosol contamination: they are called aerosol-free nights, or *Rayleigh nights*. Such nights require two main conditions:

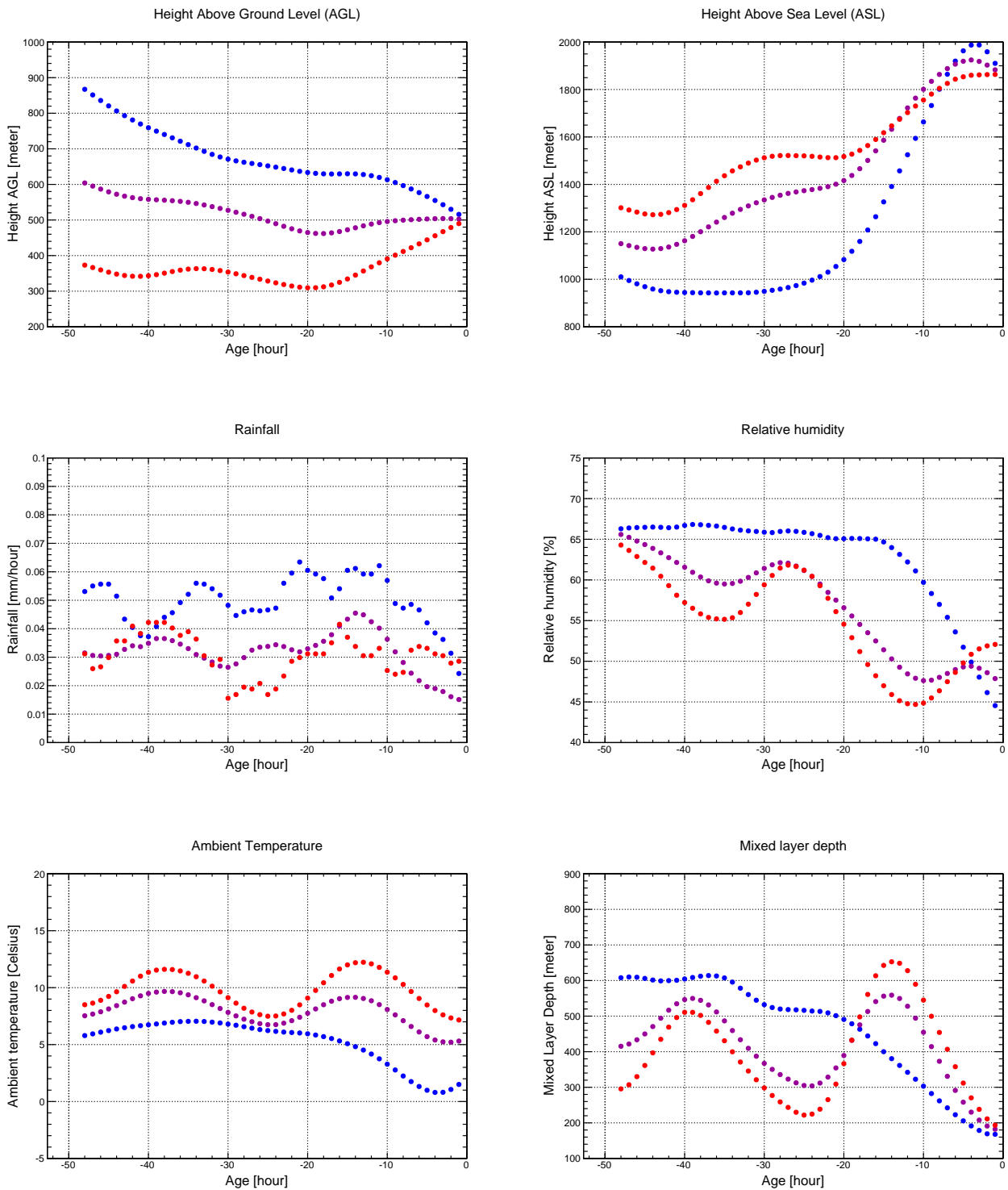


Figure 6.13: Evolution profiles for different atmospheric quantities over the backward trajectory, for clear nights, dirty nights and the rest of the nights. Quantities estimated with HYSPLIT for the years 2007/2008/2009, for each night category: clear (*blue*), dirty (*red*), and the others (*magenta*). Input parameters given in Table 6.1.

1. having a very low vertical aerosol optical depth (estimated by the CLF or XLF),
2. having a total phase function which is very close to the Rayleigh phase function. This means that the aerosol scattering contribution is negligible as estimated by the APF monitors.

These reference nights may not be the same for a given year and may not be the same for all FD eyes. Table 6.2 lists the Rayleigh nights for each CLF epoch and FD eye [8].

<i>Date range</i>	Los Leones	Los Morados	Coihueco
<i>01/2004–08/2004</i>	21/04/2004	No Op.	12/06/2004
<i>10/2004–11/2004</i>	16/10/2004	No Op.	16/10/2004
<i>12/2004–03/2005</i>	12/12/2004	17/05/2005	12/12/2004
<i>04/2005–03/2006</i>	04/06/2005	11/06/2005	04/06/2005
<i>04/2006–08/2006</i>	18/07/2006	18/07/2006	22/04/2006
<i>09/2006–12/2006</i>	22/08/2006	22/08/2006	22/08/2006
<i>01/2007–12/2007</i>	17/06/2007	17/06/2007	17/07/2007
<i>01/2008–12/2008</i>	05/07/2008	30/08/2008	08/06/2008
<i>01/2009–01/2010</i>	26/05/2009	26/05/2009	26/05/2009
<i>02/2010–09/2010</i>	20/04/2010	15/04/2010	15/04/2010

Table 6.2: **Rayleigh nights for all epochs and all FD eyes.** "No Op." means Not Operational.

Strong correlation between atmospheric data and aerosol concentration measurements should be seen. For instance, intuitively, one would expect that wind, above a certain threshold, would increase aerosol concentration in the lower atmosphere. However, up to now, no link between local atmospheric data measured by the Auger Collaboration and these aerosol-free nights has been identified. We feel that these local studies are not sufficient for understanding aerosols. Thus we have attempted to use HYSPLIT as a tool to get a global vision of the atmospheric parameters and the aerosol backward trajectories.

Appendix 8.5 displays, for each Rayleigh night, atmospheric data from HYSPLIT (*large-scale*) and from the CLF ground-based weather station (*local-scale*) collected at the Pierre Auger Observatory. Only Rayleigh nights identified by at least two FD eyes are studied here. Unfortunately, no trends emerge clearly from the HYSPLIT data. The low statistics, only eight Rayleigh nights, is probably a limiting factor. Also, the wind speed is a very local measurement and it is not justified to assume horizontal uniformity for this quantity. Thus, taking the wind speed recorded at CLF and applying it to the whole Auger array is not correct.

6.6 Conclusion

The HYSPLIT tool provides a better understanding of air mass behaviour affecting the Pierre Auger Observatory: air masses do not have the same origin all along the year. This origin difference affects the aerosol concentration. In addition, the winter season presents very large fluctuations in the distribution of the 48-hr backward trajectories.

The air mass trajectories seem to be the key point to explain the differences in aerosol concentrations observed at the Auger location. It has been shown that clear nights have air masses coming much more directly from the Pacific Ocean. A way to check this fact could be to develop a large aerosol sampling program over the SD array. Then, a study of the chemical composition of the aerosols could confirm this origin if a salt excess were to be observed during the clear nights.

Seasonal trends have been identified for air masses and for meteorological data: the mixed layer depth is smaller and the air masses travel at greater height above ground level during winter (due to the difference of the terrain height between seasons). Also, rainfall is more frequent during winter and summer. These observations necessarily have consequences on the aerosol component at Malargüe. However, no strong conclusion could be drawn on a night-by-night basis to explain why a Rayleigh night happens.

Bibliography

- [1] RR Draxler and GD Hess, *Description of the HYSPLIT 4 modelling system*, NOAA Tech Memo **ERL ARL-224** (2007).
- [2] RR Draxler and GD Hess, *An overview of the HYSPLIT 4 modeling system of trajectories, dispersion, and deposition*, *Aust. Met. Mag.* **47** (1998) 295–308.
- [3] B Keilhauer and M Will, *Data from the Global Data Assimilation System (GDAS) for the Pierre Auger Observatory*, **GAP-2011-015**.
- [4] <http://ready.arl.noaa.gov/gdas1.php>
- [5] J Abraham *et al.* [Pierre Auger Collaboration], *A study of the effect of molecular and aerosol conditions in the atmosphere on air fluorescence measurements at the Pierre Auger Observatory*, *Astropart. Phys.* **33** (2010) 108–129.
- [6] K Louedec, for the Pierre Auger Collaboration, *Atmospheric Monitoring at the Pierre Auger Observatory – Status and Update*, Proc. 32nd ICRC, Beijing, China (2011).
- [7] MI Micheletti *et al.* *in press* (2011).
- [8] D Schuster *et al.*, *Comments on Aerosol Databases*, **GAP-2010-125**.

Extracting Aerosol properties using the Central Laser Facility

Contents

7.1 Laser shot characteristics for each of the FD sites	203
7.2 Extracting of the Aerosol Phase Function	205
7.2.1 Signal from the laser shots recorded by the FD eyes	206
7.2.2 Geometrical reconstruction	212
7.2.3 Parameter estimation with an example: ($\theta_{FD} = 3^\circ$, $\phi_{FD} = 6^\circ$) at Los Leones	213
7.2.4 Description of the APF reconstruction procedure	215
7.3 Test of the reconstruction validity with <u>Offline</u> simulations	216
7.3.1 Reconstruction of the phase functions by a basic fit	216
7.3.2 Estimation of the aerosol parameters using a 4-parameter fit	218
7.4 First results	218
7.5 Conclusion	221
Bibliography	223

Introduction: The aerosol phase function is an important parameter, necessary to correctly model the indirect Cherenkov photon flux and the multiple scattering contribution. This chapter presents a new method for estimating the aerosol phase function using very inclined CLF laser shots, its main advantage being that it can be used for each FD data-taking period.

The distribution of the asymmetry parameter estimated from this method was presented in the proceedings¹ published for the International Cosmic Ray Conference (ICRC) which took place at Beijing (China) in August 2011. The result obtained for the mean value of the asymmetry parameter is in agreement with the previous one obtained using the APF monitor operated at Coihueco, and a new population of large aerosols was identified.

¹K Louedec, for the Pierre Auger Collaboration *Atmospheric monitoring at the Pierre Auger Observatory – Status and Update Proc. 32nd ICRC, Beijing, China (2011)*.

The Pierre Auger Observatory uses the atmosphere as a giant calorimeter. Since it operates as a hybrid detector, the energy for SD events is calibrated using the hybrid events, which are being recorded only during moonless nights. For the calibration to be meaningful, the properties of the atmosphere must be well-known. As has already been shown in Chapter 4, an extensive program to monitor the atmosphere has been deployed.

Two forms of atmospheric light scattering (explained in Chapter 5) need to be considered: molecular scattering (or *Rayleigh scattering*) mainly due to nitrogen and oxygen molecules, and aerosol scattering (or *Mie scattering*) due to particles much larger than the Ångström scale and coming from different sources. The aerosol phase function has, up to now, been monitored by two Aerosol Phase Function (APF) facilities consisting of two UV light sources operating at the Coihueco and Los Morados FD sites. A near-horizontal light beam is sent across the FD field of view 5 or 10 times per hour. The APF is reconstructed from the intensity of light observed by the telescopes, for scattering angles between 30° and 150° . Following a study developed in [1], an average aerosol phase function was extracted and implemented in the Offline for Cherenkov photon scattering (useful to estimate the indirect Cherenkov photon contribution). In this work, the multiple scattering component was assumed negligible.

However, the two Multiple Scattering (MS) parameterizations used in the Offline assume a standard APF, without taking into account the atmospheric conditions. But it has been shown that the multiple scattering contribution to the total light, even at low integration angles, increases considerably when the aerosol size increases, especially at the lowest elevation angles, the aerosol layer being mainly located just above ground level². From the Ramsauer approach, we have learned that, unfortunately, to monitor the largest aerosols, data for small scattering angles are needed. Indeed, at a fixed wavelength, the FWHM of the forward peak in the APF is proportional to the inverse of the aerosol radius. Thus, if we want to estimate the level of large aerosols at the Pierre Auger Observatory, the part of the APF at low scattering angles has to be measured.

In this chapter we will describe this new method to monitor, throughout the night, the two main aerosol parameters, the aerosol phase function $P_a(\zeta)$, depending on the aerosol size (ζ being the scattering angle), and the aerosol attenuation length Λ_a , depending also on the aerosol concentration. The Central Laser Facility (CLF) is used and advantage is taken of its ability to fire laser shots at very large zenith angles. Whereas the light sources at Coihueco and Los Morados stay fixed during the whole night, the CLF furnishes the possibility to probe the whole atmosphere and almost the whole range of scattering angles.

This chapter is structured as follows. Section 7.1 presents the optimized laser shot properties used to probe the lowest scattering angles. Section 7.2 explains the method used to extract the APF and the aerosol attenuation length. Its validity is checked using CLF laser shots simulated in the Offline software. Finally, Section 7.4 presents first results from laser

²A complete study of this effect on the energy and X_{\max} reconstructions is given in Chapter 8.

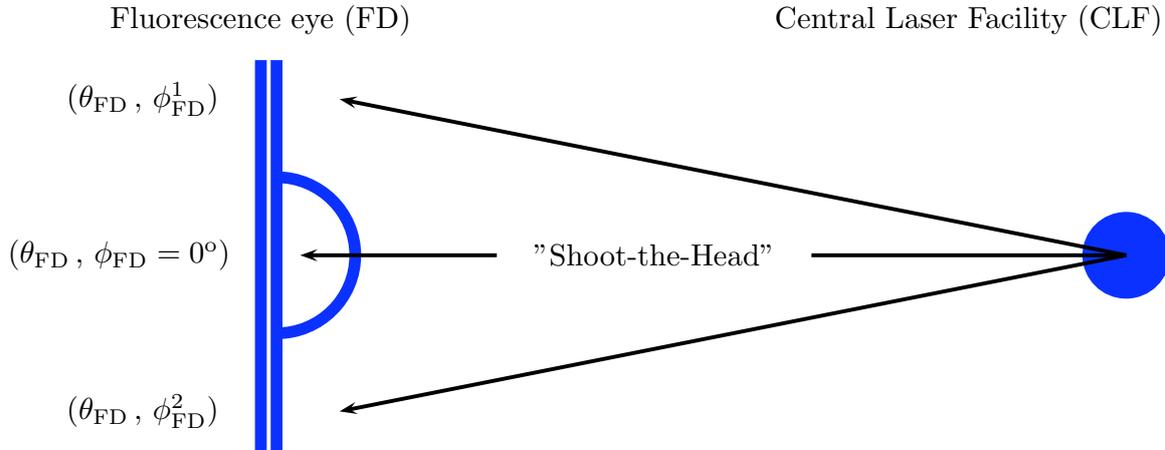


Figure 7.1: **Geometrical arrangement, viewed from above, of the central laser CLF and an FD site.** The zenith angle is defined with respect to the horizontal, and the azimuthal angle has its origin defined by the so-called "shoot-the-head" laser shot, in which the laser track on the FD camera is seen as a vertical line.

data taken in 2009 at Los Leones.

7.1 Laser shot characteristics for each of the FD sites

The Central Laser Facility is located at site towards the centre of the Auger array. The laser produces a beam at a wavelength of 355 nm. It is pulsed with a width of 7 ns and a maximum energy per pulse of 6.5 mJ. Depending on the location of the FD sites with respect to the CLF, the parameters $\{\text{zenith angle } \theta_{CLF}, \text{ azimuthal angle } \phi_{CLF}, \text{ energy } E_{CLF}\}$ for the laser shots which have to be fired change from one FD installation to another. Indeed, since the main goal is to access scattering angles ζ as low as possible for the aerosol phase function $P_a(\zeta)$, the parameters vary. In Figure 7.1 is defined the coordinate system used in this chapter. The zenith angle θ_{FD} is defined as equal to 0° when the laser shot is horizontal, and equal to 90° when it is vertical. The azimuthal angle ϕ_{FD} uses as reference the CLF azimuthal angle allowing to "shoot-the-head" of the FD eye. Thus, this azimuthal angle is different for each FD eye. Table 7.1 gives the location-dependent parameters for each FD site.

Different distances to the CLF and different minimum elevation angles at the FD telescopes imply different angles for the CLF to get the same scattering angles ζ . Figures 7.2–7.4 display the location where $\phi_{FD} = 0^\circ$ and the different ranges of azimuthal angles being possible to probe. Only at first sight, it can be concluded already that Los Morados would be the best one to reach the highest scattering angles since its camera has the largest $\Delta\phi_{FD}$ on its right side. The tables accompanying the FD camera displays in each figure provide the scat-

Parameters	Los Leones (LL)	Los Morados (LM)	Coihueco (CO)
UTM Easting [zone 19H]	459208.3	498901.8	445346.0
UTM Northing [zone 19H]	6071871.5	6094569.6	6114141.8
Distance to CLF [meter]	25 987	29 566	30 271
Altitude ASL/wrt CLF [meter]	1 416.2/ + 4.2	1 415.5/ + 3.5	1 691.9/ + 279.9
Minimum elevation angle	2.26°	1.85°	4.26°
Azim. angle $\phi_{\text{FD}} = 0^\circ$ at CLF	(156.67 \pm 0.2)°	(267.13 \pm 0.2)°	(52.55 \pm 0.2)°
Azim. angle $\phi_{\text{FD}} = 0^\circ$ at <u>Offline</u>	66.77°	177.46°	322.42°
Azim. angle $\phi_{\text{FD}} = 0^\circ$ at ADST	246.77°	357.46°	142.42°

Table 7.1: **Location parameters for each of the FD eyes.** The Offline values are useful for the files produced by this software. The ADST values correspond to the frame in the Observer files.

tering angle ranges accessible and their corresponding duration in time, for each pair (θ_{FD} , ϕ_{FD}). When selecting the laser shot parameters, a compromise is necessary between obtaining a low scattering angle and having sufficient time spread for the collected light profile. Indeed, if the time spread is too short the FD eye may not trigger.

For each eye, three different laser shot configurations have been chosen. First of all, the laser shot ($\theta_{\text{FD}} = 3^\circ$, $\phi_{\text{FD}} = \pm 6^\circ$) will be studied: it permits to extract the APF over a large range of scattering angles. From this shot, it is possible to obtain the minimum of the APF. Another reason for this choice is that this shot is already fired every night at Malargüe for every FD site. Then, for each eye, two other laser shots are selected to provide access to the lowest scattering angles, domain unexplored until now by the Auger Collaboration. They are coloured in red and green in the tables. At Coihueco, due to a large difference in height with respect to the CLF and a large minimum elevation angle, it seems that it would be difficult to reach the very low scattering angles.

These nine laser shots were simulated in the Offline using the modules **LaserGeneratorNA** and **LaserLightSimulatorNA** developed in [2]. Rayleigh scattering and Mie Scattering were parameterized by the modules **ParametricXMLRayleighModel** and **ParametricXMLMieModel**. We fixed the aerosol attenuation length at 20 km, and the vertical aerosol scale at 2.9 km. The APF is parameterized by a Henyey-Greenstein function [3], with $g = 0.6$ and $f = 0.4$ (the meaning of these parameters will be explained later, in Section 7.2). Figures 7.5–7.7 give for each laser shot its FD camera display and the light profile expected. The discontinuities in the light profiles come from the overlap in the fields of view of pixels located at the transition between two telescopes: the real signal is approximately one half of that in the zone of the discontinuity.

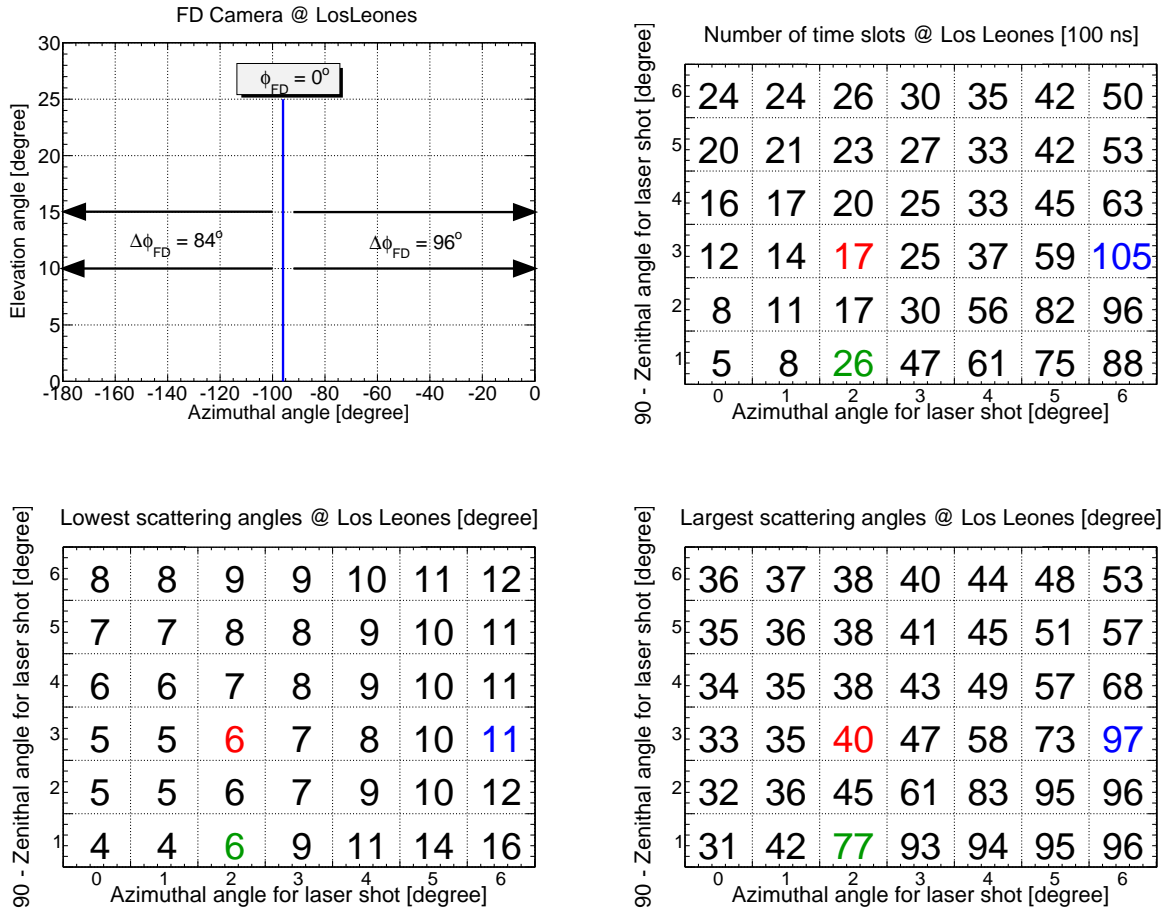


Figure 7.2: **Table for laser shots at Los Leones.** On the left top panel, a display of the FD camera at Los Leones is shown: the $\phi_{FD} = 0^\circ$ value indicates the $\Delta\phi_{FD}$ range on the right and on the left sides. Also, for the whole set of laser shots having $\theta_{CLF} \in [1^\circ, 6^\circ]$ and $\phi_{FD} \in [1^\circ, +6^\circ]$, the lowest scattering angle, the largest scattering angle and the number of time slots expected are given in the three tables.

7.2 Extracting of the Aerosol Phase Function

The Central Laser Facility can be used to measure the APF throughout the night during FD data taking. The CLF, using its steering head, produces pulsed light beams in the directions selected in the previous section. The APF can then be reconstructed from the intensity of the light observed by the FD cameras as a function of the scattering angle ζ . Different scattering angles can be accessed, corresponding to different positions of the recorded signals in the cameras.

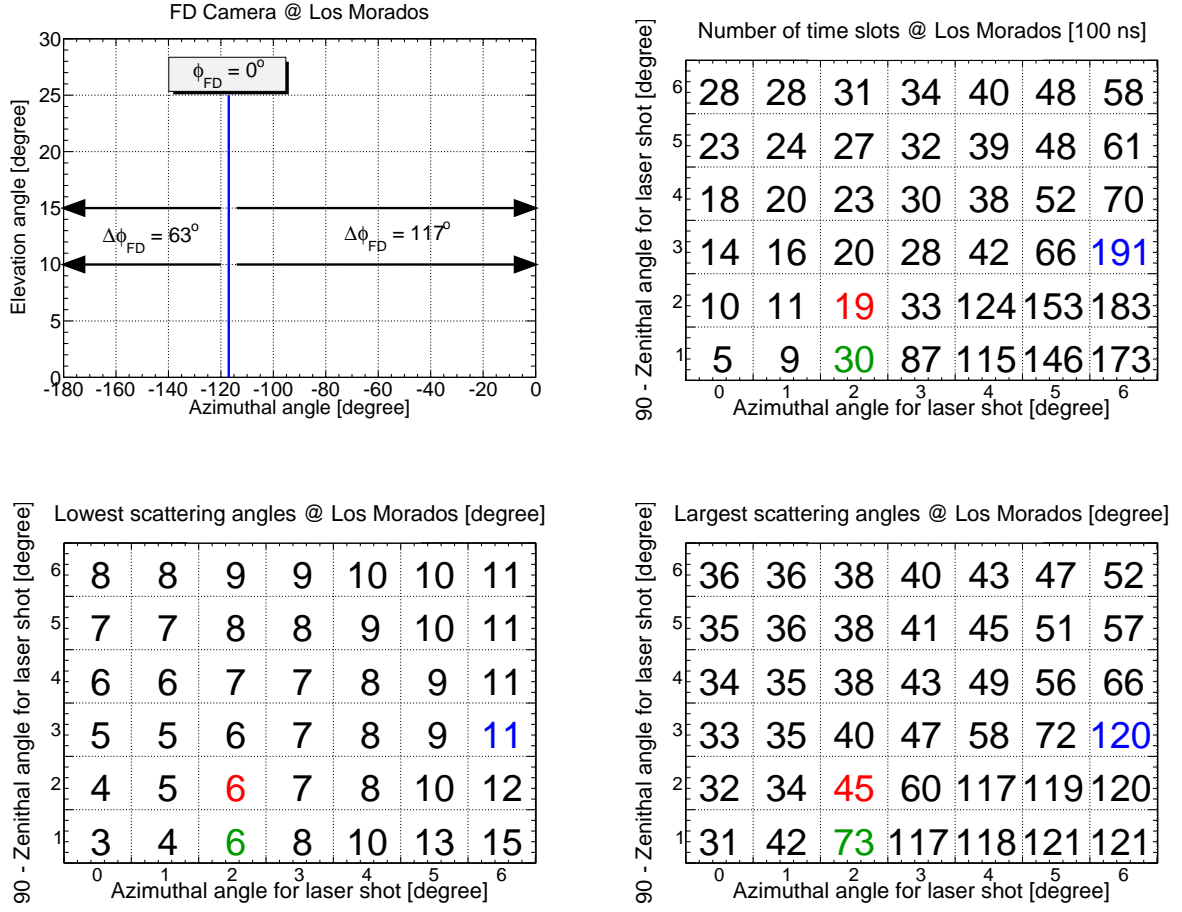


Figure 7.3: **Table for laser shots at Los Morados.** On the left top panel, a display of the FD camera at Los Leones is shown: the $\phi_{\text{FD}} = 0^\circ$ value indicates the $\Delta\phi_{\text{FD}}$ range on the right and on the left sides. Also, for the whole set of laser shots having $\theta_{\text{CLF}} \in [1^\circ, 6^\circ]$ and $\phi_{\text{FD}} \in [1^\circ, +6^\circ]$, the lowest scattering angle, the largest scattering angle and the number of time slots expected are given in the three tables.

7.2.1 Signal from the laser shots recorded by the FD eyes

The signal from the CLF shot observed by the i th pixel of the fluorescence detector can be expressed as

$$S_i = I_0 \times \langle T_m \rangle_{\Delta z_i} \times \langle T_a \rangle_{\Delta z_i} \times \left[\frac{1}{\langle \Lambda_m \rangle_{\Delta z_i}} P_m(\zeta) + \frac{1}{\langle \Lambda_a \rangle_{\Delta z_i}} P_a(\zeta) \right] \times \Delta z_i \times \langle \Delta \Omega_i \rangle_{\Delta z_i}, \quad (7.1)$$

where I_0 is the original light beam intensity, ζ the scattering angle corresponding to the i th pixel, Δz_i the laser track length observed by the pixel and $\Delta \Omega_i$ the solid angle. The physical quantities inside the brackets $\langle X \rangle_{\Delta z_i}$ mean that their value is not constant within the pixel. Thus, we have to use the mean value, obtained by averaging over the length of track seen.

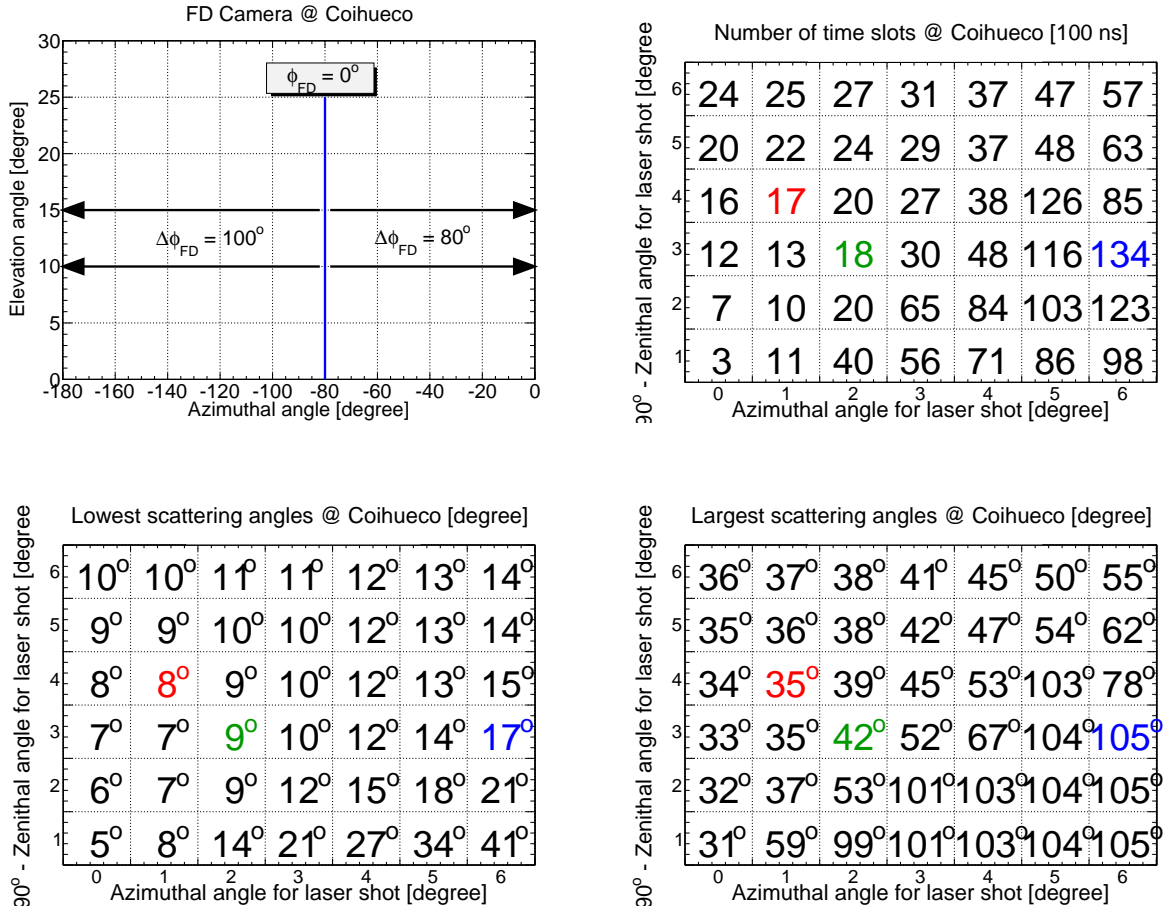


Figure 7.4: **Table for laser shots at Coihueco.** On the left top panel, a display of the FD camera at Los Leones is shown: the $\phi_{FD} = 0^\circ$ value indicates the $\Delta\phi_{FD}$ range on the right and on the left sides. Also, for the whole set of laser shots having $\theta_{CLF} \in [1^\circ, 6^\circ]$ and $\phi_{FD} \in [1^\circ, +6^\circ]$, the lowest scattering angle, the largest scattering angle and the number of time slots expected are given in the three tables.

Λ_m and Λ_a are the molecular attenuation length and the aerosol attenuation length, respectively. Their values change as a function of the altitude. Since the CLF shot cannot be considered horizontal here, this altitude variation must be involved (especially for the aerosol layer). The most common parameterization uses an exponential (the so-called *U.S. Standard Atm. Model*), described as follows

$$\begin{cases} \Lambda_m(h) = \Lambda_m^0 \exp(h/h_m^0) & \text{where } \Lambda_m^0 \simeq 8.0 \text{ km at Malargüe level,} \\ \Lambda_a(h) = \Lambda_a^0 \exp(h/h_a^0) & \text{where } \Lambda_a^0 \simeq 1.4 - 2.9 \text{ km at Malargüe,} \end{cases} \quad (7.2)$$

where h is defined as the altitude above ground level.

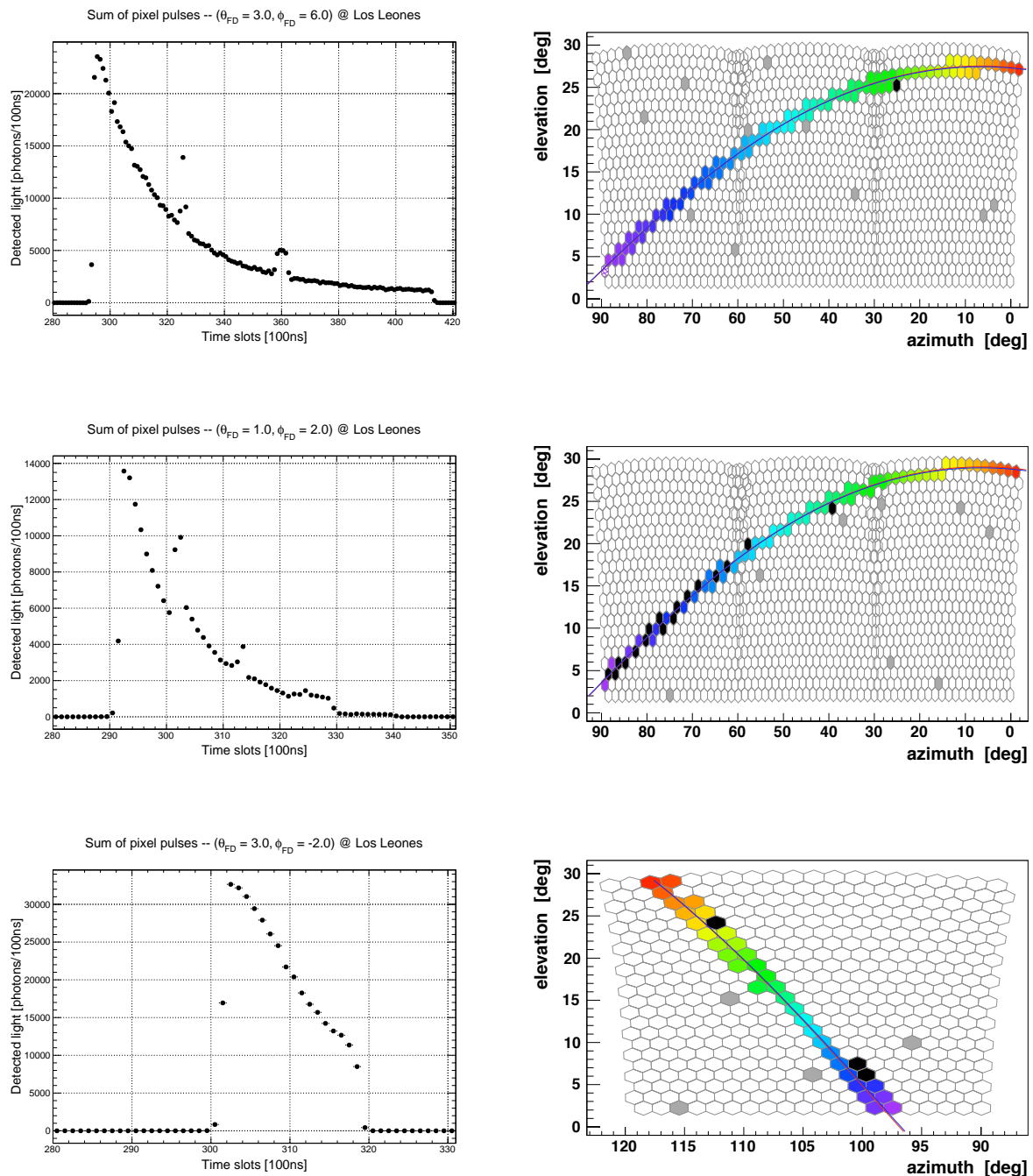


Figure 7.5: **Laser shot selection at Los Leones.** *Left panel:* Light time profiles, averaged over 15 shots, expected from *Offline* simulations for the three different laser shots selected from Figure 7.4. *Right panel:* Simulated FD camera displays for the same three shots. The colour code gives timing information, blue corresponding to the earliest and red to the latest times.

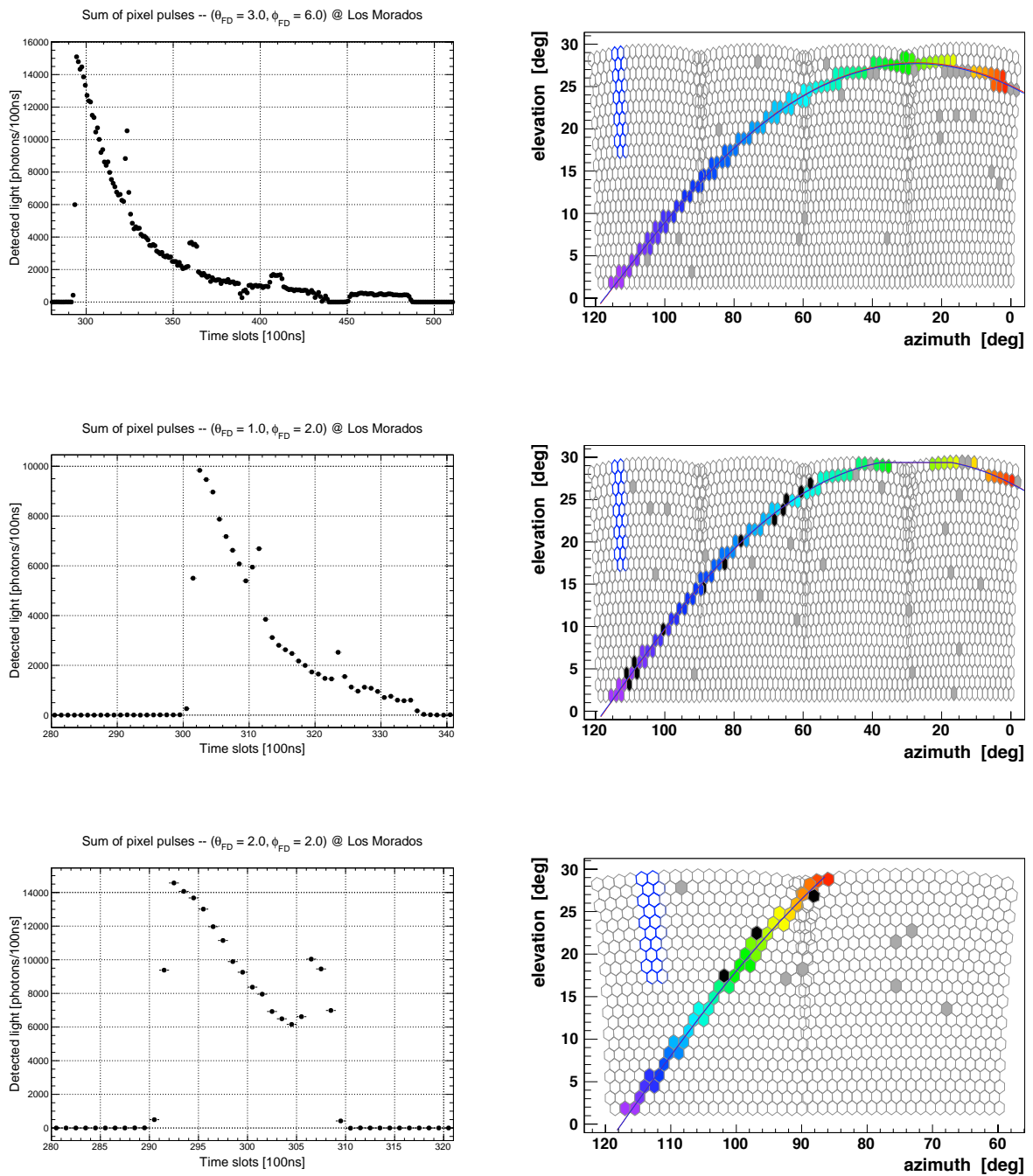


Figure 7.6: **Laser shot selection at Los Morados.** *Left panel:* Light time profiles, averaged over 15 shots, expected from Offline simulations for the three different laser shots selected from Figure 7.4. *Right panel:* Simulated FD camera displays for the same three shots. The colour code gives timing information, blue corresponding to the earliest and red to the latest times. The hexagons in blue correspond to missing pixels in the camera.

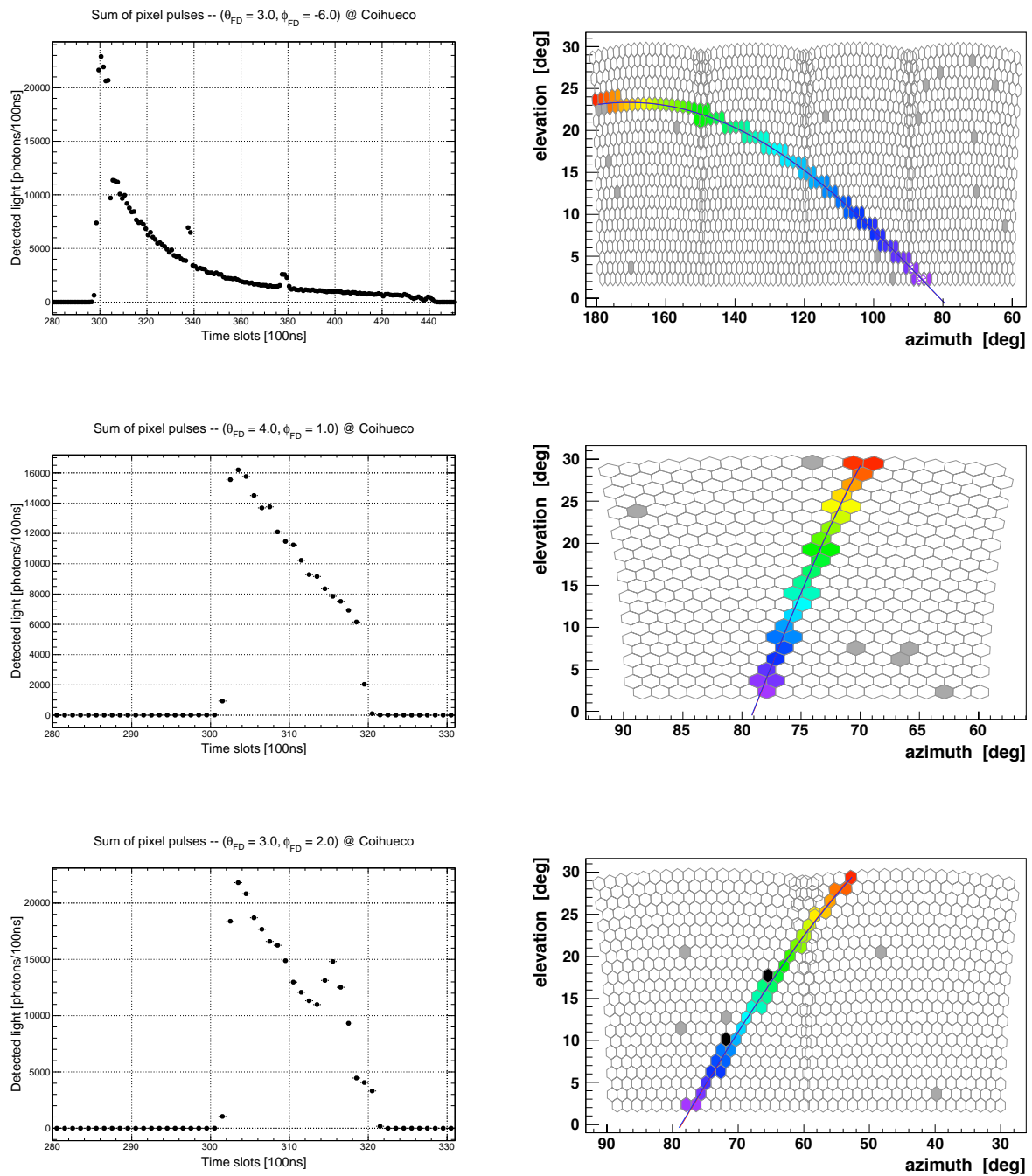


Figure 7.7: **Laser shot selection at Coihueco.** *Left panel:* Light time profiles, averaged over 15 shots, expected from *Offline* simulations for the three different laser shots selected from Figure 7.4. *Right panel:* Simulated FD camera displays for the same three shots. The colour code gives timing information, blue corresponding to the earliest and red to the latest times.

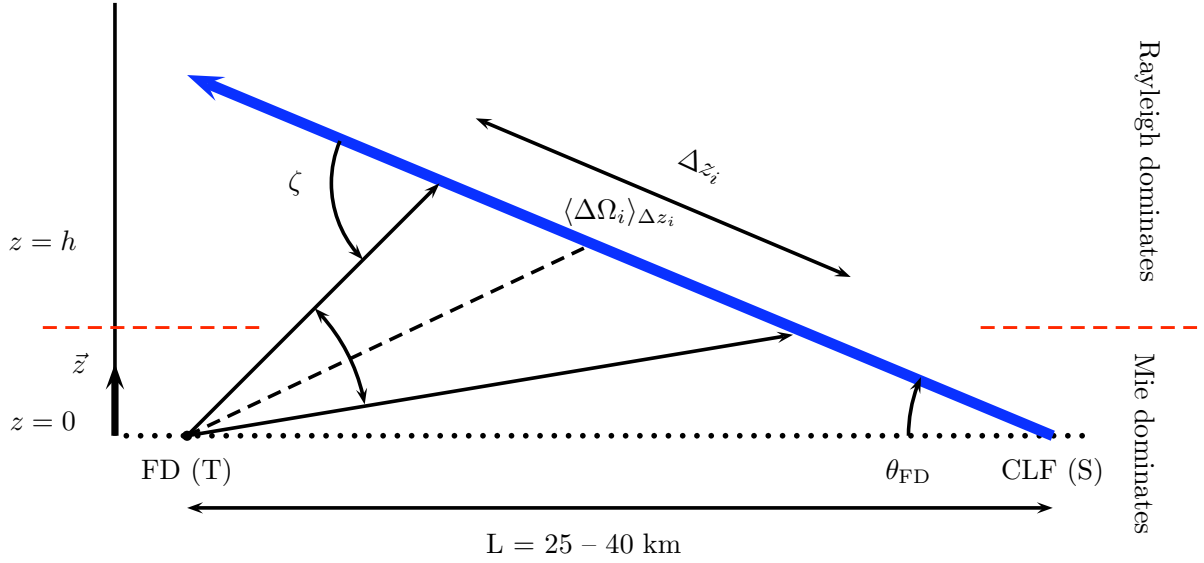


Figure 7.8: **Sketch of the experimental setup using the CLF seen by one FD eye.** L represents the distance between the source point S , or CLF, and the detector point T , or FD telescope. Mie scattering dominates in the low altitude layer below the red line, whereas Rayleigh scattering dominates above it.

T_m and T_a are the molecular attenuation factor and the aerosol attenuation factor, respectively. Since the distances travelled are too different from one pixel to another, the attenuation factors cannot be removed from Equation (7.1). At an altitude h above ground level, the attenuation is given by

$$T_X(h) = \exp \left[\frac{1}{\sin \theta_{\text{FD}}} \frac{h_X^0}{\Lambda_X^0} \left(e^{-h/h_X^0} - 1 \right) \right] \times \exp \left[\frac{1}{\cos(\vec{T}\vec{M}, \vec{z})} \frac{h_X^0}{\Lambda_X^0} \left(e^{-h/h_X^0} - 1 \right) \right], \quad (7.3)$$

where X is either the Rayleigh case or the Mie case, and \vec{z} the unitary vector for the vertical axis (see Figure 7.8). The first exponential describes the attenuation from S to the scattering location, and the second one the attenuation from the scattering location to T .

$P_m(\zeta)$ and $P_a(\zeta)$ are the scattering phase functions for molecular scattering and aerosol scattering, respectively. They are defined such that their integral over all solid angles is equal to one. From Rayleigh scattering theory, the well-known analytical phase function is given by

$$P_m(\zeta|\gamma) = \frac{1}{\sigma_m} \frac{d\sigma_m}{d\Omega} = \frac{3}{16\pi(1+2\gamma)} \left[(1+3\gamma) + (1-\gamma) \cos^2 \zeta \right], \quad (7.4)$$

where γ includes the effect of molecular anisotropy in Rayleigh scattering. In the Auger Collaboration, its value is fixed at 0.03 [4].

For aerosol scattering, the modified Henyey-Greenstein parameterization is used. It is defined as

$$P_a(\zeta|g, f) = \frac{1}{\sigma_a} \frac{d\sigma_a}{d\Omega} = \frac{1-g^2}{4\pi} \left[\frac{1}{(1+g^2-2g\cos\zeta)^{3/2}} + f \frac{3\cos^2\zeta-1}{2(1+g^2)^{3/2}} \right], \quad (7.5)$$

where g is the asymmetry parameter and f describes the strength of the backscattering component.

7.2.2 Geometrical reconstruction

The goal of this geometrical reconstruction is to assign to each pixel its scattering angle and the correction factors which will be needed to reconstruct the APF from the signal collected by the FD eye. In this inclined shot study, no approximation about the attenuation can be made. Also, it is necessary to describe the laser beam geometry very accurately at the beginning of its path since the track length viewed by the telescope changes very quickly. The method used here is a Monte Carlo simulation: the program covers the entire path of the laser beam using a fixed step ℓ_{step} . It can be interpreted as a numerical integration over the laser shot length shown in blue in Figure 7.8, where ℓ_{step} corresponds to the infinitesimal length $d\ell$.

At each step, the program registers which pixels are able to collect signal from that particular point on the beam. We include a spread function of 0.25° to describe the aberration effects, coming from the optics, this has been studied previously by the Auger Collaboration. It has to be noted that the pixels are assumed circular here. For each pixel that triggers, these different operations are done: its track length is incremented by the ℓ_{step} value, and the scattering angle, the solid angle, the total travelled length, the altitude, the Rayleigh attenuation factor and the Rayleigh attenuation length are added to its own array defined for each of these parameters. When the pixel is not triggered anymore, its track length Δz_i is directly obtained and the other geometrical quantities are only the mean of the values stored in the corresponding array. This method requires a sufficiently small step to provide a minimum of N values in each array for calculating mean values.

A criterion on their FADC trace is applied to skip the pixels just slightly triggered by the laser shot. It permits to avoid the pixels with low signal with large shot-to-shot fluctuations in the data (and thus it is difficult to obtain right correction factors). They will be plotted as gray pixels later in the chapter.

Simulation of the collected signal in each pixel

Using the Monte Carlo simulation, it is now very easy to estimate the charge for each pixel or the light profile as a function of time.

The signal recorded by the i th pixel at the step j is given by

$$S_{ij} = W_i^j \times T_m^j \times T_a^j \times \left[\frac{L_{\text{step}}}{\Lambda_m^j} P_m(\zeta^j) + \frac{L_{\text{step}}}{\Lambda_a^j} P_a(\zeta^j) \right] \times \Delta\Omega^j, \quad (7.6)$$

where only W_i^j depends on the pixel under consideration. W_i^j is the weight of the signal recorded by the i th pixel at the j th step. It represents the area common to two circles: one representing the pixel and the other representing the aberration effect. This weight is defined as

$$W_i^j = \begin{cases} 0 & \text{if } d_i^j \geq r_{\text{pix}} + r_{\text{ab}}, \\ \pi r_{\text{pix}}^2 & \text{if } d_i^j \leq (2/3) r_{\text{pix}}, \\ A(r_{\text{pix}}, r_{\text{ab}}, d_i^j) & \text{otherwise} \end{cases} \quad (7.7)$$

with

$$A(r_{\text{pix}}, r_{\text{ab}}, d_i^j) = r_{\text{ab}}^2 \cos^{-1} \left(\frac{d_i^{j2} + r_{\text{ab}}^2 - r_{\text{pix}}^2}{2 d_i^j r_{\text{ab}}} \right) + r_{\text{pix}}^2 \cos^{-1} \left(\frac{d_i^{j2} + r_{\text{pix}}^2 - r_{\text{ab}}^2}{2 d_i^j r_{\text{pix}}} \right) - \frac{1}{2} \sqrt{(-d_i^j + r_{\text{ab}} + r_{\text{pix}})(d_i^j + r_{\text{ab}} - r_{\text{pix}})(d_i^j - r_{\text{ab}} + r_{\text{pix}})(d_i^j + r_{\text{ab}} + r_{\text{pix}})},$$

where r_{pix} is the pixel radius equal to 0.75° at the Pierre Auger Observatory, r_{ab} represents the spread function due to aberration effects (0.25°) and d_i^j is the distance between the i th pixel centre and the impact location on the camera at the step j (in other words, the impact parameter).

Consequently, the total charge expected for the i th pixel is just the sum

$$S_i = \sum_j S_{ij}, \quad (7.8)$$

7.2.3 Parameter estimation with an example: ($\theta_{\text{FD}} = 3^\circ$, $\phi_{\text{FD}} = 6^\circ$) at Los Leones

Let us see how the reconstruction geometry algorithm works with an example. The three FD sites have in common the laser shot ($\theta_{\text{FD}} = 3^\circ$, $\phi_{\text{FD}} = 6^\circ$). Here Los Leones will be used.

Figure 7.9 gives the camera display simulated by our program. The laser shot axis is reconstructed and drawn in red. All the triggered pixels are filled. The gray pixels are then rejected since, as explained in Section 7.2.2, they have large fluctuations from shot to shot due to their very short FADC trace in time. Only the pixels coloured in green are used in the APF reconstruction: thus, the program provides these pixels with all their parameters needed for the reconstruction. The three parameters needed are given in Figure 7.9: the solid angle, the track length and the Rayleigh attenuation factor. They are plotted as a function of

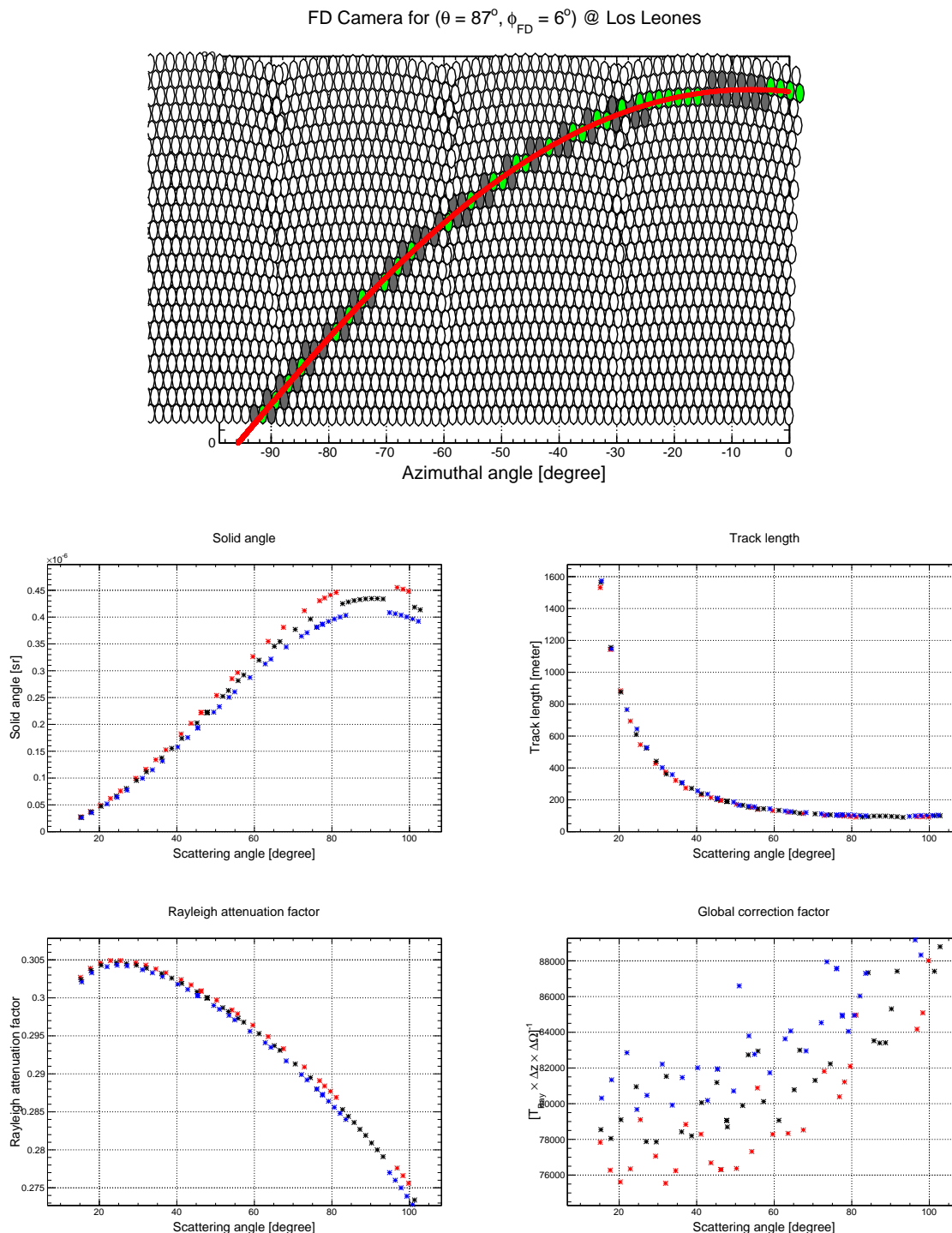


Figure 7.9: **Parameter estimation for the laser shot ($\theta_{\text{FD}} = 3^\circ, \phi_{\text{FD}} = 6^\circ$) at Los Leones during a Rayleigh night.** *Top panel:* the laser track on the FD camera simulated by our Monte-Carlo code is displayed. The gray pixels are rejected: only the green ones are used in the geometrical parameter estimation. The red curve is the image of the laser beam. *Bottom panel:* the track length Δz_i , the solid angle $\langle \Delta \Omega_i \rangle_{\Delta z_i}$ and the Rayleigh attenuation factor $\langle T_m \rangle_{\Delta z_i}$ are plotted as a function of the scattering angle (or implicitly, for each green pixel). Also, their global correction factor is plotted. The black dots correspond to the true ϕ_{FD} , the red to $\phi_{\text{FD}} - 1^\circ$ and the blue to $\phi_{\text{FD}} + 1^\circ$. The method is not sensitive to an uncertainty on the azimuthal angle.

the scattering angle ζ , each green pixel corresponding to a unique scattering angle. Whereas the Rayleigh attenuation does not change greatly with the scattering angle, the track length increases steeply at the lowest scattering angles. The solid angle behaviour shows that the lowest distance FD-CLF is reached for a scattering angle around 90° .

7.2.4 Description of the APF reconstruction procedure

In Equation (7.1), $P_m(\zeta)$ is exactly known from Equation (7.4) and $\{\langle T_m \rangle_{\Delta z_i}, \langle \Lambda_m \rangle_{\Delta z_i}, \langle \Delta \Omega_i \rangle_{\Delta z_i}, \Delta z_i\}$ are calculated using our program.

The factor I_0 depends on the laser performances and on the detector, it cannot be estimated by the program. It is obtained as follows: when a Rayleigh night occurs (meaning that the signal collected by the cameras can be easily fitted using only the Rayleigh scattering contribution), Equation (7.1) becomes

$$S_{i|\text{Ray}} = I_0 \times \langle T_m \rangle_{\Delta z_i} \times \left[\frac{1}{\langle \Lambda_m \rangle_{\Delta z_i}} P_m(\zeta) \right] \times \Delta z_i \times \langle \Delta \Omega_i \rangle_{\Delta z_i}. \quad (7.9)$$

Thus, all the parameters, except I_0 , are known and a value can be obtained for I_0 . For each green pixel, we compute the ratio of $S_{i|\text{Ray}}$ to all the other parameters: we get a distribution of values I_0^i . The estimated I_0 is then the mean of this distribution. The spread of the distribution must not be too large for the I_0 value to be considered valid.

This I_0 estimation is to be made independently for each laser shot configuration: this means that an I_0 value will be attributed to each set of laser shot parameters $\{\text{zenith angle } \theta_{\text{FD}}, \text{ azimuthal angle } \phi_{\text{FD}}, \text{ energy } E_{\text{CLF}}\}$. For instance, for the laser shot ($\theta_{\text{FD}} = 3^\circ$, $\phi_{\text{FD}} = 6^\circ$) at Los Leones, Figure 7.10 plots, on the right, the I_0 distribution for 200 laser pulses during a Rayleigh night. On the left is plotted the $\langle I_0^i \rangle$ for each reconstructed pixel, and their shot-to-shot fluctuations. Some pixels, mainly at low scattering angles, have a $\langle I_0^i \rangle$ far from the I_0 value: these pixels will not be taken into account in the APF reconstruction.

At this point, all the parameters needed to extract the APF are calculated. It becomes possible to calculate the parameters linked to the aerosols in the atmosphere. As previously said, these parameters are strongly time dependent and, thus, they have to be calculated frequently throughout the night. The APF reconstruction procedure involves the following steps:

1. From the data file, the light collected by the green pixels is extracted. We assign to each pixel a signal value S_i .
2. For each i th pixel, we divide its signal by the correction factors $\{\langle T_m \rangle_{\Delta z_i}, \langle \Delta \Omega_i \rangle_{\Delta z_i}, \Delta z_i\}$

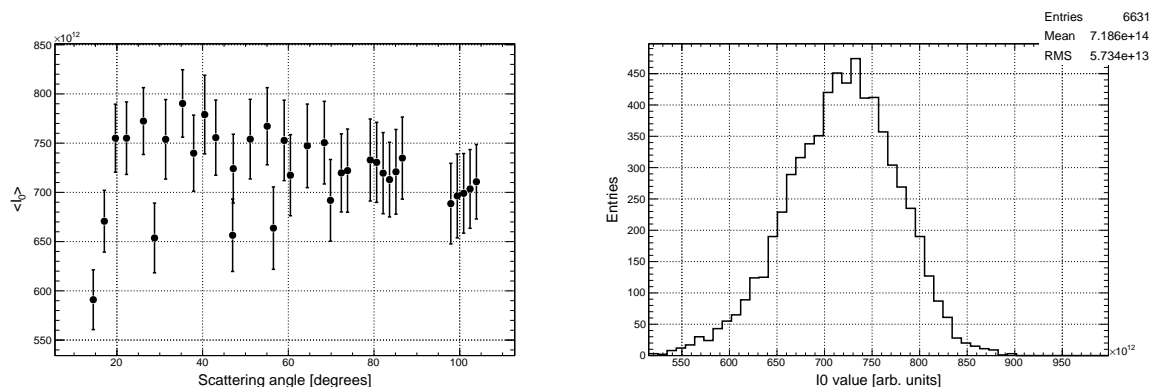


Figure 7.10: Distribution of I_0^i values for each pixel for the laser shot ($\theta_{\text{FD}} = 3^\circ$, $\phi_{\text{FD}} = 6^\circ$) at Los Leones during a Rayleigh night. The histogram contains 200 laser shots.

and also by the source factor I_0 as follows

$$S'_i = \frac{S_i}{I_0 \times \langle T_m \rangle_{\Delta z_i} \times \Delta z_i \times \langle \Delta \Omega_i \rangle_{\Delta z_i}} = \langle T_a \rangle_{\Delta z_i} \times \left[\frac{1}{\langle \Lambda_m \rangle_{\Delta z_i}} P_m(\zeta) + \frac{1}{\langle \Lambda_a \rangle_{\Delta z_i}} P_a(\zeta) \right].$$

We get a new signal value S'_i depending only on the aerosol parameters, that is $\{g, f, \Lambda_a^0, h_a^0\}$, the Rayleigh scattering contribution being known from Equations (7.2)–(7.4).

3. Finally, the binned laser shot signal acquired by the FD eyes is subjected to a 4-parameter fit. The method employed is to simulate expected profiles for each $\{g, f, \Lambda_a^0, h_a^0\}$ configuration. Then, a χ^2 test is run to determine which set of parameters best fits the profile.

7.3 Test of the reconstruction validity with Offline simulations

Once the reconstruction process was implemented, its validity was checked using simulations. This will be illustrated for the laser shot ($\theta_{\text{FD}} = 3^\circ$, $\phi_{\text{FD}} = 6^\circ$) at Los Leones as in the previous section.

7.3.1 Reconstruction of the phase functions by a basic fit

As a first step, we can check that the phase functions are correctly reconstructed in the Offline simulations. Two different cases are studied: a Rayleigh night to extract only the Rayleigh Phase Function (RPF) and a basic night to extract this time the Total Phase Function (TPF), the APF then being obtained by subtracting the Rayleigh contribution. Figures 7.11–7.12 show the light profiles predicted by our Monte Carlo simulation and the phase functions reconstructed from the Offline simulations. The error bars are the shot-to-shot fluctuations

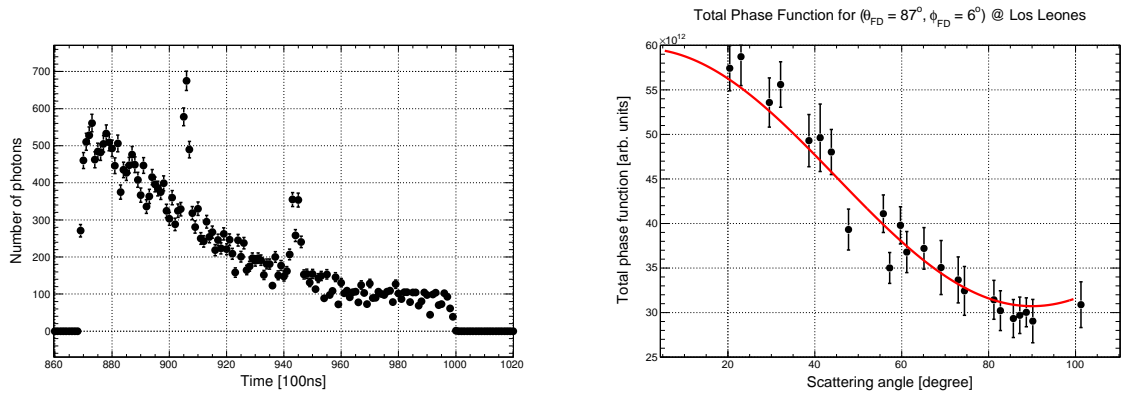


Figure 7.11: **Reconstructed phase function for the laser shot ($\theta_{\text{FD}} = 3^\circ$, $\phi_{\text{FD}} = 6^\circ$) at Los Leones during a Rayleigh night.** *Left panel:* Light intensity as a function of time from our MC simulation for this shot in the Rayleigh case. *Right panel:* Rayleigh phase function reconstructed from an Offline simulation for a Rayleigh night. The study was done with 15 simulated shots. The red curve represents the true Rayleigh phase function used by the Offline simulation.

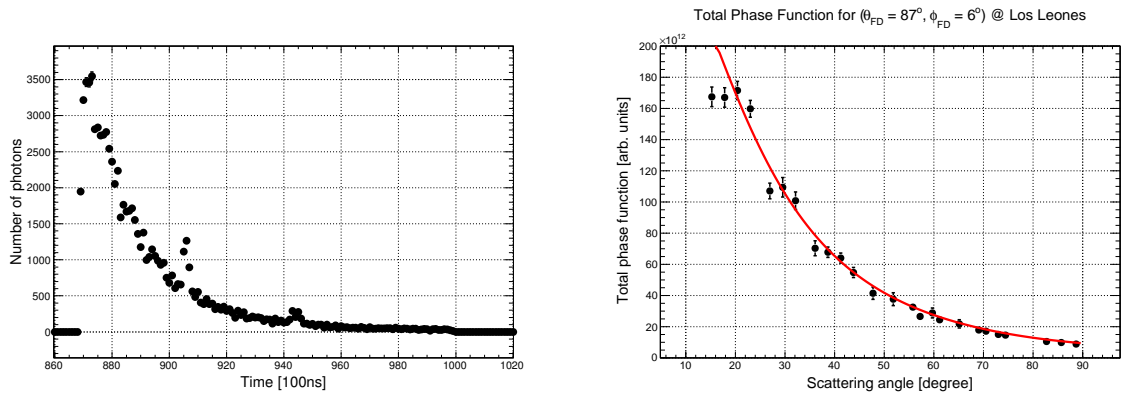


Figure 7.12: **Reconstructed phase function for the laser shot ($\theta_{\text{FD}} = 3^\circ$, $\phi_{\text{FD}} = 6^\circ$) at Los Leones during a normal night.** *Left panel:* Light intensity as a function of time from our MC simulation for this shot in the Rayleigh case. *Right panel:* Total phase function reconstructed from an Offline simulation for an aerosol component defined as follows: $\Lambda_a^0 = 20$ km, $h_a^0 = 2.9$ km, $g = 0.6$ and $f = 0.4$. The study was done with 15 simulated shots. The red curve represents the true total phase function used by the Offline simulation.

(over 15 shots) and the red curves are the true phase functions provided as input to the simulations. The reconstructed Rayleigh phase function fluctuates much more than a scattering phase function for a basic night because of the lower signal. One reason to explain the disagreement at some scattering angles, i.e. at some pixels, between the theoretical curve and the reconstructed points is that the laser track does not cross all the pixels in their centre. Thus, the signal collected in a particular pixel depends on the laser track position within the pixel. It is this dependence on the laser track which is the origin the disagreement with the true total phase function.

7.3.2 Estimation of the aerosol parameters using a 4-parameter fit

The APF reconstruction procedure was described in Section 7.2.4. This method will be applied to the Offline simulations to see how well the aerosol parameters are reconstructed. Since the shots studied in this work cannot access the angles corresponding to the backward peak, the f value is fixed at 0.4 as suggested in [1]. In each case we have simulated 15 shots while varying g from 0.1 to 0.9 and Λ_a^0 from 10 km to 80 km.

Figure 7.13 shows the aerosol parameter estimation results for the case of an aerosol attenuation length at ground level Λ_a^0 of 10 km, for asymmetry parameters going from 0.1 to 0.9. The black disk corresponds to the parameter values used as input in the Offline simulation. The colour code represents the χ^2 of the procedure, where blue corresponds to the best fit. We observe a small bias in the estimation of the asymmetry parameter, except at the highest g values ($g \geq 0.9$). This bias is also present for other values of aerosol attenuation length.

Figure 7.14 shows the mean light profiles recorded by the FD telescopes for each of the aerosol conditions shown in Figure 7.13. It is important to stress the fact that these light profiles are not modified by the reconstruction program, but just obtained from the signal recorded by the telescope. We note that, except for the highest g values, a small decrease is observed at the lowest scattering angle, i.e. in the forward scattering peak. This feature in the simulation program produces a bias on the reconstruction of the asymmetry parameter.

7.4 First results

We have applied the method described in Section 7.2 to data recorded during the year 2009 at the Los Leones site. The study was done for the laser shots ($\theta_{FD} = 3^\circ$, $\phi_{FD} = 6^\circ$) since they were the only ones fired during this period. Figure 7.15 shows the distribution of the asymmetry parameter g . The average g value is 0.57 with a standard deviation of 0.16 for the data period analyzed.

Figure 7.15 also shows the distribution obtained by the APF monitor operated at Coihueco between June 2006 and July 2008. It is interesting to see that the average asymmetry param-

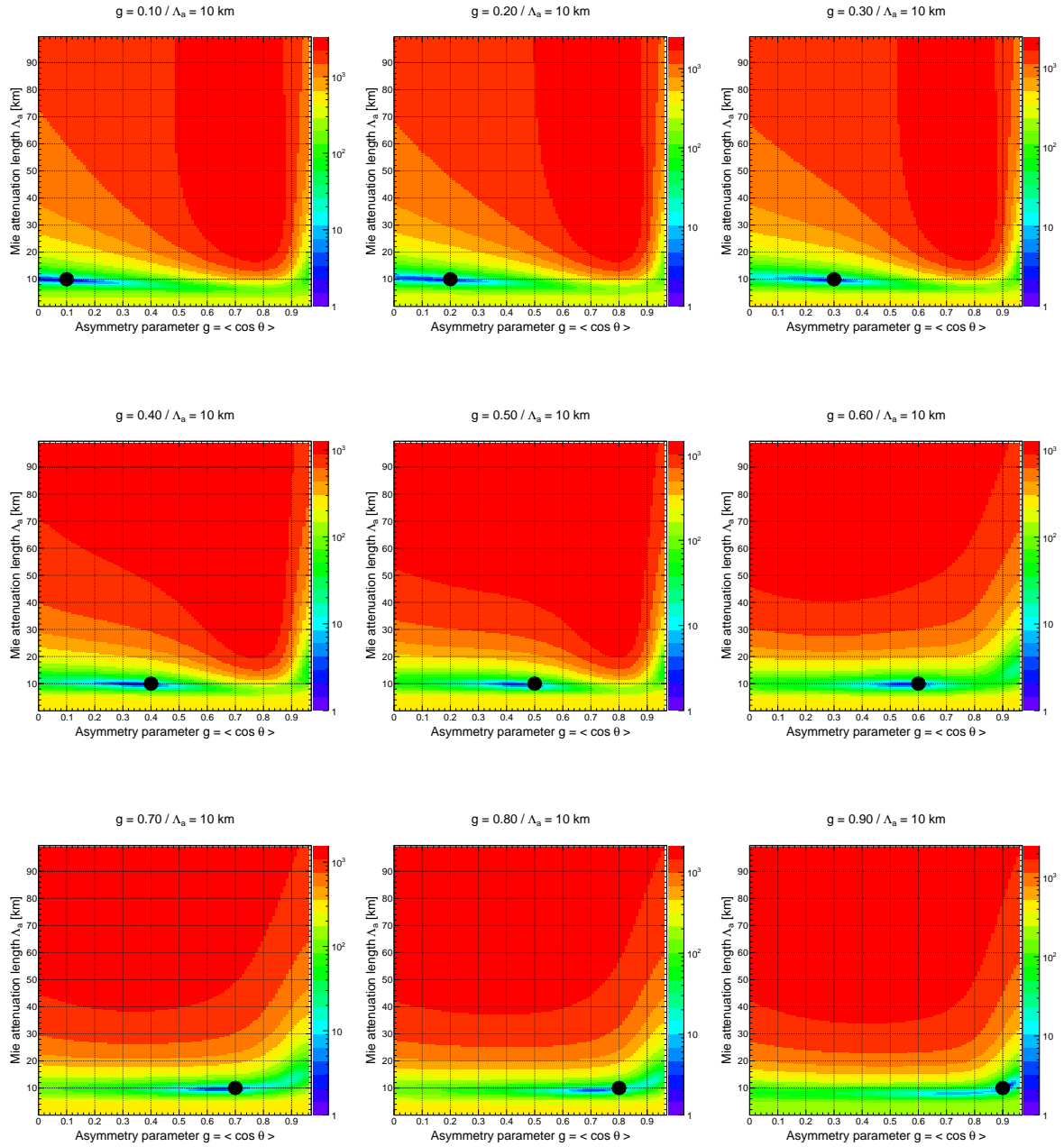


Figure 7.13: Estimation of the aerosol parameters for the laser shot ($\theta_{FD} = 3^\circ$, $\phi_{FD} = 6^\circ$) at Los Leones for different asymmetry parameters. The aerosol attenuation length at ground level is fixed at 10 km. The black disk corresponds to the input value for the aerosol parameters. The colour represents the χ^2 value, blue corresponding to the best agreement with the reconstructed light profile.

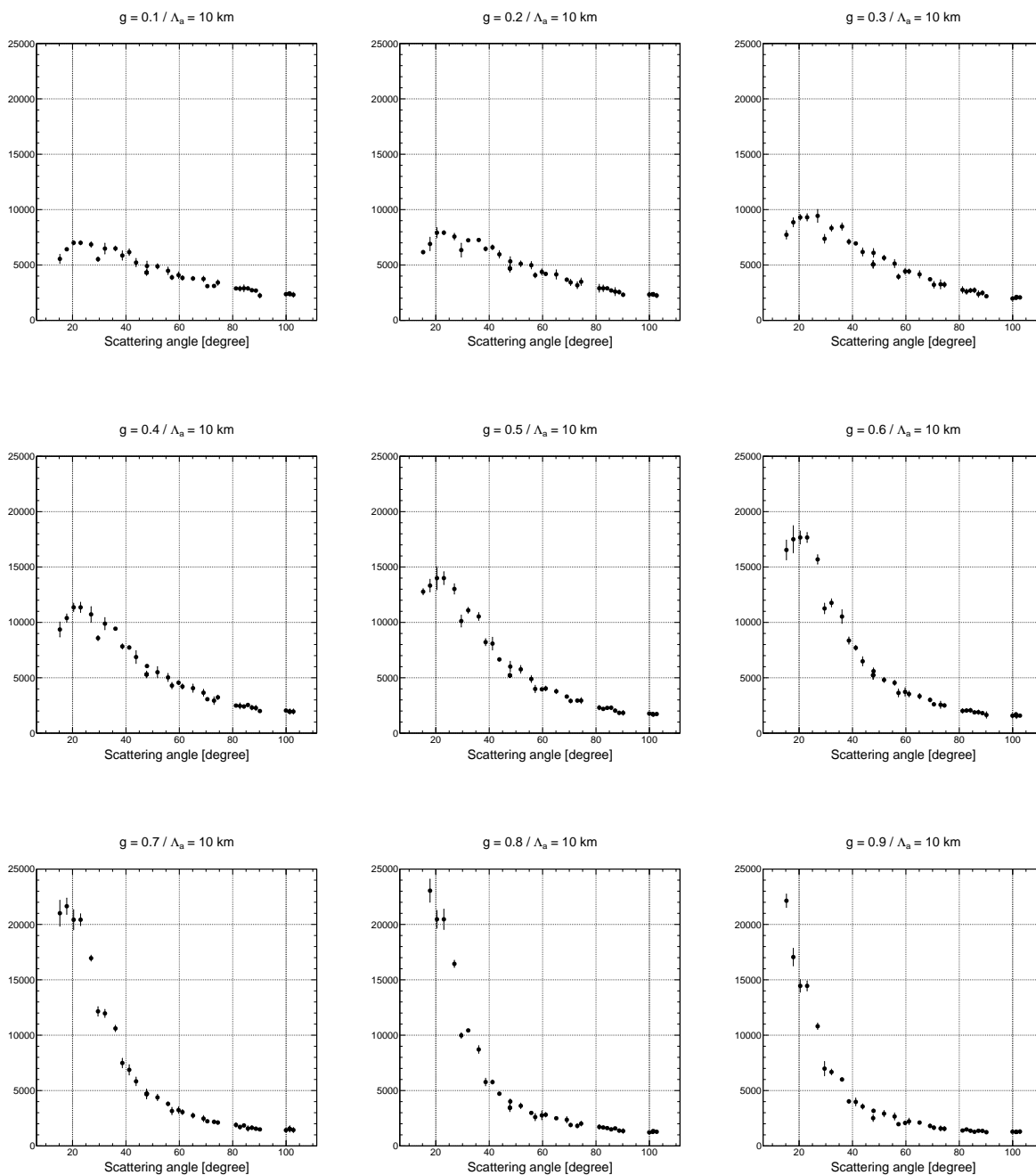


Figure 7.14: Light profiles recorded by the fluorescence telescopes for the laser shot ($\theta_{FD} = 3^\circ$, $\phi_{FD} = 6^\circ$) at Los Leones, for different asymmetry parameters. The aerosol attenuation length at ground level is fixed at 10 km. The error bars correspond to the statistical fluctuations observed for 15 laser shots.

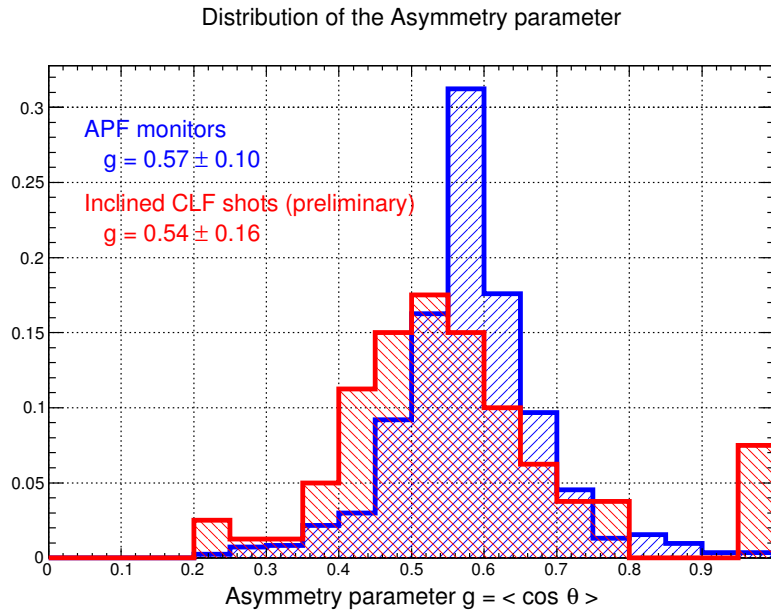


Figure 7.15: **Asymmetry parameter distribution measured by the APF monitor and the very inclined CLF laser shots.** The APF monitor data were measured at Coihueco between June 2006 and July 2008 [5]. The values from the new method were obtained with laser shots ($\theta_{\text{FD}} = 3^\circ$, $\phi_{\text{FD}} = 6^\circ$) at Los Leones recorded in 2009.

eter obtained from the very inclined CLF laser shots at Los Leones is compatible with the g measurement made previously using the APF monitors. However, a population with large asymmetry parameters, $g \geq 0.95$, is identified in measurements coming from the very inclined CLF laser shots, not visible from the APF data. Due to the limitation on the lowest scattering angle, the APF monitors cannot detect this aerosol population. Indeed, a g value of 0.95 corresponds to an aerosol with a radius of around $2 \mu\text{m}$. According to the Ramsauer results, aerosols of this size produce a forward peak with a FWHM of about 3° , much lower than the lowest scattering angle value probed by the APF monitors.

7.5 Conclusion

A new method to estimate the aerosol phase function has been developed. Using very inclined CLF laser shots, it provides access to the lowest scattering angles ever probed by the Auger Collaboration. The procedure involves use of the Henyey-Greenstein parameterization and the asymmetry parameter g is reconstructed.

A selection of laser shot parameters for each of the FD sites has been proposed. These laser shot sets provide very low scattering angles, and thus improve our knowledge on the large aerosols present in the atmosphere. Since April 2011, these laser shots are fired every

night during FD data taking. The analysis of these data will become possible once sufficient statistics have been acquired, including notably reference (“molecular”) nights.

A new population of large aerosols has been identified with the new method applied to inclined shots at Los Leones recorded in 2009. It is the first time that such large aerosols can be probed by a facility at the Pierre Auger Observatory. If the presence of this population is confirmed in the near future, this could be an important fact to be taken into account in calculating the uncertainty on the energy and X_{\max} in the shower reconstruction procedure. This will be discussed in the next chapter.

Bibliography

- [1] S BenZvi *et al.*, *Measurement of the aerosol phase function at the Pierre Auger Observatory*, *Astropart. Phys.* **28** (2007) 312–320.
- [2] L Valore, *Atmospheric aerosol determination using vertical laser tracks in the Pierre Auger Experiment*, PhD thesis, Università Degli Studi Di Napoli "Federico II" (2007) **GAP-2008-020**.
- [3] LC Henyey and JL Greenstein, *Diffuse radiation in the galaxy*, *Astroph. J.* **93** (1941) 70.
- [4] B Dawson, *New Rayleigh Scattering Implementation in the Offline* , **GAP-2006-007**.
- [5] J Abraham *et al.* [Pierre Auger Collaboration], *A study of the effect of molecular and aerosol conditions in the atmosphere on air fluorescence measurements at the Pierre Auger Observatory*, *Astropart. Phys.* **33** (2010) 108–129.

Aerosol size effect on multiple scattering and shower reconstruction

Contents

8.1	Aerosol size distribution and its implications for aerosol physics	228
8.1.1	Aerosol attenuation length	229
8.1.2	Aerosol phase function	230
8.2	The FD-to-SD energy ratio as a possible proof of an aerosol effect	231
8.3	Atmospheric multiple scattering of light emitted by a point source	234
8.3.1	Multiple scattering and the elevation angle	238
8.3.2	Application to the FD halo measurements	240
8.4	Effect of multiple scattering on energy and X_{\max} reconstruction	244
8.5	Conclusion	247
	Bibliography	248

Introduction: The estimation of air shower energy depends on the multiple scattering of fluorescence photons in the atmosphere, from their emission to their detection. In this note, we explain how the aerosol size distribution affects the photon scattering during its propagation. Thanks to the Ramsauer approach, already presented in a previous note [1], the relationship between aerosol phase function and aerosol size can be understood. Using a Monte Carlo simulation for the multiple scattering, the dependence on the aerosol conditions of the multiple scattering contribution to the recorded signal is fully parameterized. To understand the FD halo at low integration angles, we suggest a contribution of large aerosols, typically with diameters around 5 μm . Finally, the effect of the aerosol size on the energy and on the X_{\max} reconstructions is presented: a systematic overestimation of these two quantities is observed when the aerosol size is underestimated.

This work led to an internal note¹.

¹K Louedec and M Urban, *Aerosol size effect on the multiple scattering and shower reconstruction*, GAP-2011-073.

The Pierre Auger Observatory calibrates the surface detector energy measurements using the FD energy, the latter being assumed less dependent on the hadronic models at ultra-high energy. Since the fluorescence detector uses the atmosphere as a giant calorimeter, it is important to understand and monitor its properties. When the charged particles emitted by an air shower traverse through the atmosphere, they produce a large number of fluorescence and Cherenkov photons. The fact that the fluorescence light is proportional to the energy deposited by the shower is used to estimate the primary cosmic ray energy. Nevertheless, the FD reconstruction has to correct for the attenuation of the light and subtract the Cherenkov light scattered into the FD's field of view. Also, the multiply scattered (MS) light has to be taken into consideration in the procedure. The latter causes a systematic overestimate of the recorded signal and consequently of the estimated shower energy. Therefore, the scattering properties of the atmosphere have to be well understood. In order to better define this problem, Figure 8.1 shows different effects that have to be taken into account in the FD photon counting procedure. From the emission point to the telescope, all the photons emitted in the direction of the telescope N_{true} are not detected because of the scattering in the atmosphere: this attenuation phenomenon is quantified by $N_{\text{scattering out FOV}}$. N_{outFOV} are photons emitted in a "wrong" direction. However some of these photons can be scattered back to the right direction for detection by the telescope: they are represented by $N_{\text{scattering in FOV}}$ and they have to be subtracted. The main problem in correcting for these effects is that multiple scattering is very difficult to estimate in the atmosphere.

Several studies have already been made to parameterize multiple scattering for atmospheric showers. The two main contributions come from Roberts [2] and Pekala [3]. Both are now implemented in the **FdProfileReconstruction** Offline module. They predict the multiple scattering fraction, i.e. the ratio of multiply scattered light to the total light arriving at the telescope within the resolution time (100 ns) of its FADC electronics and within a circle of angular radius equal to ζ . While the Roberts parameterization focuses only on the scattered fluorescence light, the Pekala parameterization also takes into account the scattered Cherenkov light. Stasielak had shown that these two methods give similar results for the energy and X_{max} estimations [4]. Pekala's energy correction due to MS is smaller, whereas the X_{max} reconstruction gives larger values.

The multiple scattering in the atmosphere can be divided into two categories. The first is the Rayleigh regime describing the photon scattering on air molecules. The second, the Mie regime, tries to explain the scattering on larger particles (assumed spherical), the aerosols. The ratio between the incident wavelength and the target size determines the physical phenomenon governing the scattering. For each of these two regimes, we have an attenuation length Λ and a phase function $P(\theta)$, i.e. the differential scattering cross section normalized to the total cross section (where θ is the scattering angle). Obviously, these parameters are strongly affected by the atmospheric properties. Whereas the molecular properties are now

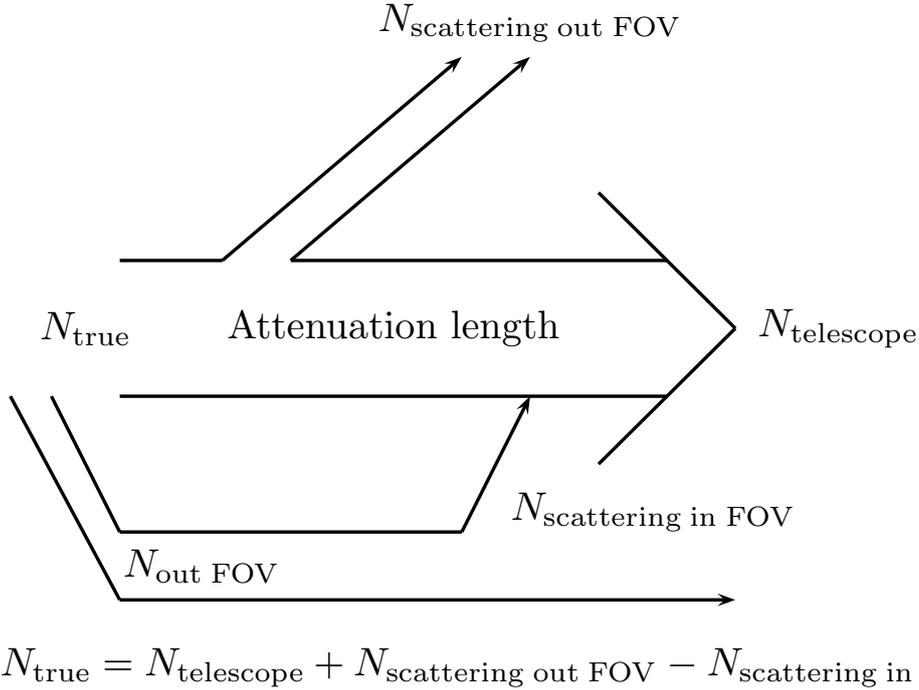


Figure 8.1: **Multiple scattering effects on the number of photons arriving at the telescope.** N_{true} is the number of generated photons in the Field Of View (FOV) of the telescope. $N_{\text{scattering out FOV}}$ is the number of photons scattered out of the FOV (one or more scatterings). $N_{\text{scattering in FOV}}$ is the number of photons undergoing multiple scattering, then coming back in the detector's FOV. The standard calculation evaluates $N_{\text{scattering out FOV}}$, but neglects $N_{\text{scattering in FOV}}$, leading to an overestimation of N_{true} or an underestimation of $N_{\text{telescope}}$ in the simulations.

well monitored and understood in the Pierre Auger collaboration [5], this is still not the case for the aerosol component. Indeed, we only have the aerosol phase function (APF) for scattering angles greater than 25° and smaller than 160° [6]. Also, only an average phase function is used in the Offline.

Thus, although we do not monitor the complete aerosol phase function yet, the MS parameterizations did assumptions on its value at the beginning of their development. In this note, we will examine the consequences of this absence of information at small scattering angles (where APF data do not exist at Auger). In Section 8.1, we use the Ramsauer approach to explain how the aerosol size distribution affects the aerosol phase function and the aerosol attenuation length. In Section 8.2, the Golden Hybrid events are used to estimate the FD-to-SD energy ratio and its possible dependence on the aerosols. Then, simulations of multiple scattering of light emitted from a point source are described and analyzed in Section 8.3. We show how the aerosol phase function affects the multiple scattering and how it affects the signal collection in the FD telescopes. An application of the results to the FD halo measure-

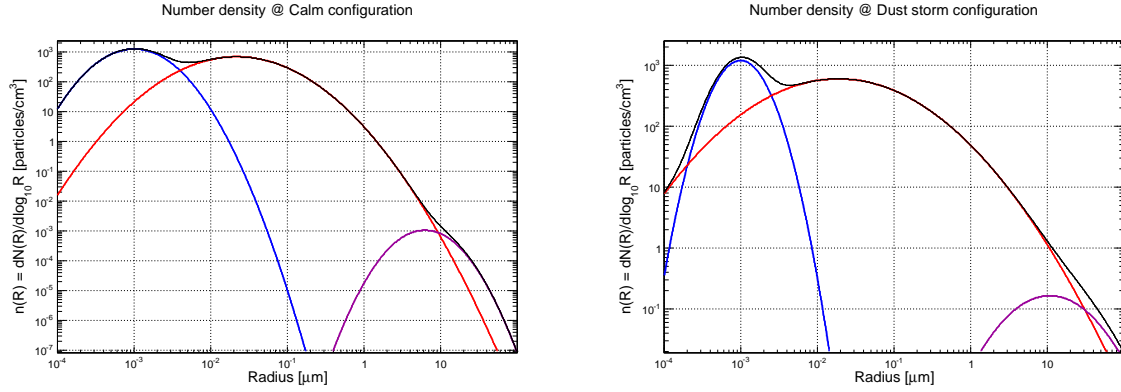


Figure 8.2: **Number density distribution for the desert aerosol model.** *Left panel:* Calm configuration. *Right panel:* Dust storm configuration. The *blue* line represents the nucleation mode, the *red* one the accumulation mode and the *magenta* one the coarse mode.

ments is also presented. Finally, in Section 8.4, a first estimation of the aerosol size effect on the shower reconstruction is given for the Golden Hybrid events recorded in 2010.

8.1 Aerosol size distribution and its implications for aerosol physics

The aerosol size distribution is usually modelled by a sum of three log-normal distributions

$$n(R) = \frac{dN(R)}{d \log_{10} R} = \sum_{i=1}^3 \frac{N_i}{\sqrt{2\pi} \log_{10} \sigma_i} \exp \left[-\frac{\log_{10}^2(R/\bar{R}_i)}{2 \log_{10}^2 \sigma_i} \right], \quad (8.1)$$

where R is the radius of an aerosol (it is assumed that the aerosols have a spherical shape), σ_i is the geometric standard deviation, \bar{R}_i is the mean radius, and N_i is the total number of particles for the distribution i . Three size ranges are usually used to describe aerosols in the atmosphere: the Aitken or nucleation mode ($0.01 \mu\text{m} \leq R \leq 0.1 \mu\text{m}$), the large or accumulation mode ($0.1 \mu\text{m} \leq R \leq 1.0 \mu\text{m}$) and the giant or coarse mode ($R \geq 1.0 \mu\text{m}$).

In the rest of this section, we will use the desert aerosol model. Originally developed by Patterson and Gillette, it claims that the aerosol size distribution can be described by two configurations, the calm desert configuration and the desert dust storm configuration [7]. We report in Table 8.1 the log-normal parameters and in Figure 8.2 the size distributions, for the desert model. The main difference between the two situations is the increase in the concentration for the coarse mode when a dust storm occurs (see Table 8.1). The particles are assumed to be injected by high winds during the storm.

Now, according to the Ramsauer approach (of course, we would obtain the same conclu-

Aerosol configuration	i	N_i [cm^{-3}]	$\log_{10} \sigma_i$	R_i [μm]
Calm Desert	1	997	0.328	0.0010
	2	842.4	0.505	0.0218
	3	7.10×10^{-4}	0.277	6.24
Desert Dust Storm	1	726	0.247	0.0010
	2	1140	0.770	0.0188
	3	1.78×10^{-1}	0.438	10.8

Table 8.1: Desert model parameters for the log-normal distributions

sions from the Mie theory), the aerosol size distribution affects the aerosol attenuation length Λ_a and the aerosol phase function $P_a(\theta)$. Contrary to the Mie model, it provides some intuitive results and permits one to use only analytical formulae in the scattering studies on spherical particles [1, 8]. Thus, we give here the total cross section σ_{tot} and the phase function obtained from the Ramsauer approach

$$\sigma_{\text{tot}}(R) = 2\pi R^2 \left[1 - 2 \frac{\sin [2(n-1)kR]}{2(n-1)kR} + \left(\frac{\sin [(n-1)kR]}{(n-1)kR} \right)^2 \right], \quad (8.2)$$

and

$$P_a(\theta) = \frac{1}{\sigma} \frac{d\sigma}{d\theta} = \frac{1}{4\pi} \left[kR \frac{1 + \cos \theta}{2} \frac{2J_1(kR \sin \theta)}{kR \sin \theta} \right]^2, \quad (8.3)$$

where n is the refractive index of the sphere and $k = 2\pi/\lambda$ the wavenumber (λ is the incident wavelength).

8.1.1 Aerosol attenuation length

At the Pierre Auger Observatory, the aerosol attenuation length is measured by the CLF and the Lidar systems. We obtain it directly from the aerosol extinction $\alpha(h)$ defined as follows

$$\alpha(h) = \frac{1}{\Lambda_a} \exp \left(-\frac{h}{H_a} \right), \quad (8.4)$$

where h is the altitude above ground level, H_a the vertical scale of the aerosol layer (typically, $H_a = 1.2$ km) and Λ_a the aerosol attenuation length at ground.

Also, the attenuation length can be defined as a function of the aerosol density and the total cross section

$$\Lambda_a(R) = \frac{1}{n(R) \times \sigma_{\text{tot}}(R)}. \quad (8.5)$$

In Figure 8.3, the attenuation length is plotted as a function of the radius for the two configurations of the desert model at a wavelength $\lambda = 355$ nm. The dashed area represents

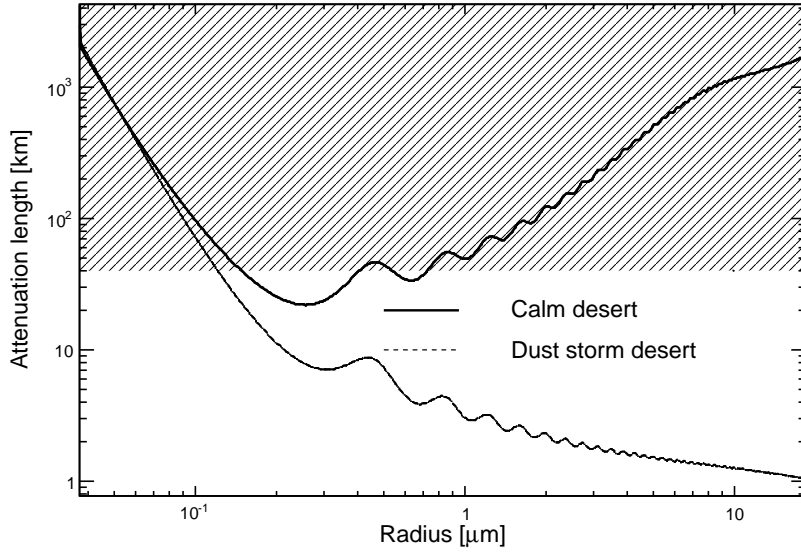


Figure 8.3: **Evolution of the aerosol attenuation length with respect to the radius for the desert aerosol model.** The Rayleigh attenuation length Λ_m is fixed at 22 km at ground level (for the Malargüe altitude). The dashed area represents the cases where the aerosol component decreases by at least one third the total attenuation length, i.e. $(1/3) \times \Lambda_{\text{tot}} \leq \Lambda_a$, where $(1/\Lambda_{\text{tot}}) = (1/\Lambda_a) + (1/\Lambda_m)$.

the cases where the aerosol component decreases by at least one third the total attenuation length (Rayleigh and aerosol). Thus, it is seen immediately for which ranges we have to take into account not only the Rayleigh attenuation, but also the aerosol attenuation. Whereas in a calm desert only the aerosols with a radius $r \in [0.15, 0.70] \mu\text{m}$ have to be considered for photon propagation studies, all the radii greater than $0.1 \mu\text{m}$ have to be considered in a sand storm configuration.

8.1.2 Aerosol phase function

According to Equation (8.3) obtained by the Ramsauer approach, the intensity of the light scattered in the forward direction is proportional to the square of the target radius, i.e. $P_a(\theta = 0^\circ) \propto R^2$, and the FWHM of the forward scattering peak is proportional to the inverse of kR , i.e. $\Delta\theta_{\text{FWHM}} = 2/kR$.

In the following, the aerosol phase function will be described by the Henyey-Greenstein (HG) function [9]. This is a parameterization usually used in experiments such as Auger to reproduce scattering on scattering centers large with respect to the incident wavelength. In the case where the backscattering can not be neglected, the HG function becomes a "Double

HG" and is given by

$$P_a(\theta|g, f) = \frac{1 - g^2}{4\pi} \left[\frac{1}{(1 + g^2 - 2g \cos \theta)^{3/2}} + f \frac{3 \cos^2 \theta - 1}{2(1 + g^2)^{3/2}} \right], \quad (8.6)$$

where $g = g_{\text{HG}} = \langle \cos \theta \rangle$ is the so-called asymmetry parameter and f represents the strength of the backward scattering peak.

Figure 8.4 shows the relationship between g_{HG} values and mean aerosol sizes (i.e. diameter in the case where aerosols are assumed spherical). If the incident wavelength is fixed at 355 nm, the relation $\Delta\theta_{\text{FWHM}} = 2/kR$ becomes

$$R[\mu\text{m}] \simeq \frac{6}{\Delta\theta_{\text{FWHM}}[^\circ]}.$$

It is interesting to note that aerosol sampling techniques already developed for the Auger array use a lower limit for the aerosol size fixed at 0.22 μm , i.e. a lower limit on the asymmetry parameter around 0.2. The default APF used in the Auger Offline reconstruction is equal to 0.6, consequently assuming that aerosols at the Auger site have sizes around 0.5 μm .

In Figure 8.5 we plot the Henyey-Greenstein functions for three different asymmetry parameters, i.e. for three different mean aerosol sizes. The largest aerosols affect the forward peak the most. However, as has been said in the introduction, up to now, the aerosol phase function at Auger has only been measured between 25° and 160° [6]. Thus, the largest aerosols, typically larger than 0.5 μm (i.e. $g_{\text{HG}} \geq 0.6$), cannot be detected by the APF monitors in Auger.

The purpose of the next sections is to see if such large aerosols are present or not in the Auger atmosphere, and to determine their effect on the MS contribution to the total light recorded by the FD telescopes.

8.2 The FD-to-SD energy ratio as a possible proof of an aerosol effect

The shower energy measured with the FD detector is compared with the signal in the tanks at 1000 meters, S_{1000} , in order to calibrate the SD energy. To take into account the S_{1000} dependence on the zenith angle and on geometrical effects, attenuation curve is parameterized as

$$CIC(\theta) = 1 + a (\cos^2 \theta - \cos^2 38^\circ) + b (\cos^2 \theta - \cos^2 38^\circ)^2,$$

where $a = 0.87$ and $b = -1.49$ for the Golden Hybrid events v7r2 [10]. Then, an energy estimator independent of the zenith angle, S_{38° , is defined as representing the S_{1000} value that

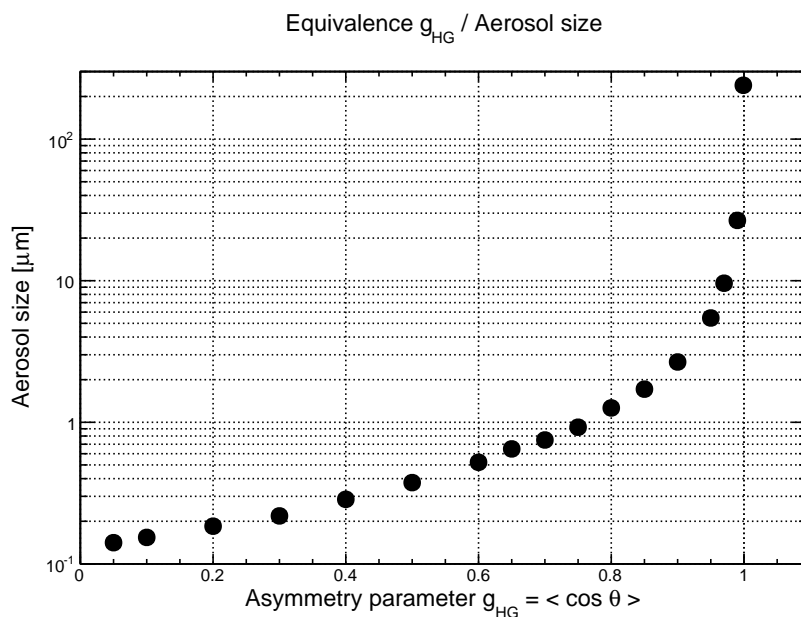


Figure 8.4: **Relationship between the asymmetry parameter of the Henyey-Greenstein function and the mean aerosol size.** The mean aerosol size corresponds to the diameter in the case of spherical aerosols.

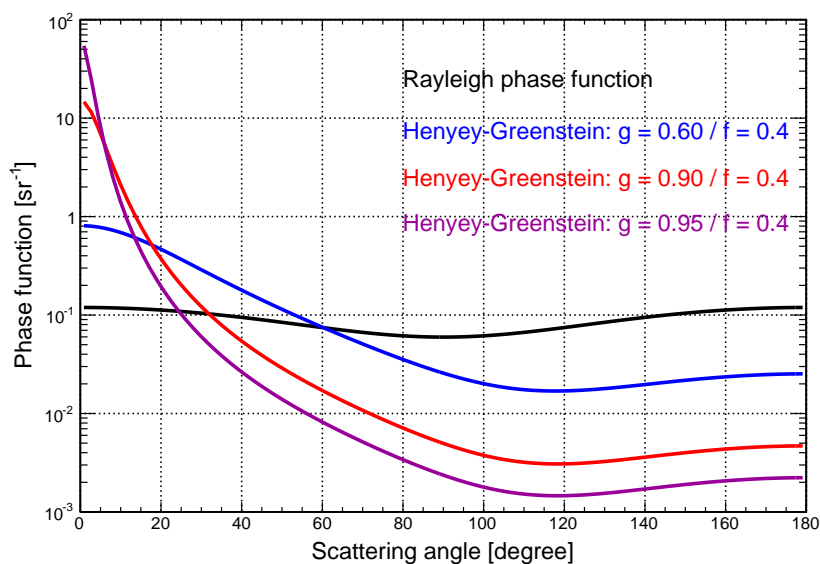


Figure 8.5: **Henyey-Greenstein functions representing the aerosol phase function for three different asymmetry parameters: $g_{HG} = 0.60, 0.90, 0.95$.** The Rayleigh phase function, representing scattering properties for the molecular component of the atmosphere, is also plotted.

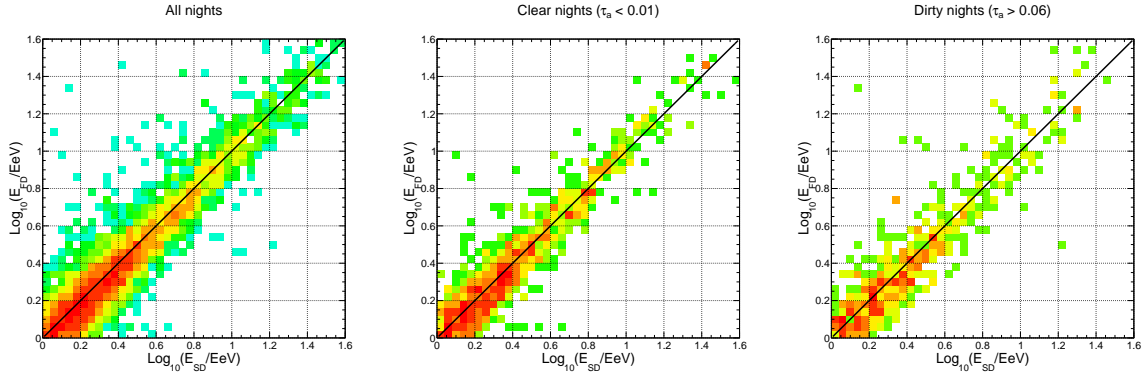


Figure 8.6: Equivalence SD energy/FD energy for the whole Golden Hybrid data set, for clear nights and for dirty nights. The aerosol optical depth is measured at an altitude of 3.5 km above the FD site.

the shower would have if it had come with a zenith angle of 38°

$$S_{38^\circ} = \frac{S_{1000}}{CIC(\theta)}.$$

This angle is chosen since it is the median zenith angle, so the impact of this correction factor is minimized. Using the information provided by the FD measurements, it is possible to obtain the energy corresponding to each S_{38° (except for assumptions on energy going to muons, the so-called "missing energy" since it cannot be seen by the FD telescopes). Then, a calibration curve is estimated and the SD energy is defined as

$$E_{SD}[\text{eV}] = A S_{38^\circ}^B,$$

where $A = (1.68 \pm 0.05) \times 10^{17}$ eV and $B = 1.035 \pm 0.009$ [10].

The energy calibration of the surface detector (SD) is done using the Golden Hybrid events recorded necessarily at night. Of course, the aerosol scattering affects only the light collected by the FD telescopes. Thus, only the FD energy is modified by the aerosols. To study this effect, we divide the event sample into two populations:

- **the clear nights** with the lowest aerosol optical depths ($\tau_a(3.5 \text{ km}) < 0.01$),
- **the dirty nights** with the highest aerosol optical depths ($\tau_a(3.5 \text{ km}) > 0.06$).

If the multiple scattering due to aerosols is confirmed, the average ratio of FD energy to calibrated SD energy, $\langle E_{FD}/E_{SD} \rangle$, should be higher during the dirty nights than during the clear nights. In fact, when the energy increases, the shower is further from the FD telescope and deeper: it means that photons travel much farther in the region where aerosols are concentrated the most. Thus, the multiple scattering contribution should increase when the

shower energy increases.

The data set used contains the Golden Hybrid events (reconstruction version ADST v7r2²), and recorded by the Pierre Auger Observatory through the end of the year 2010. The quality cuts applied are the usual ones, as used in the X_{\max} studies [11], except for the aerosol optical depth which has no cut here.

Figure 8.6 plots SD energy versus FD energy, for all of the Golden Hybrid events, for clear nights ($\tau_a < 0.01$) and for dirty nights ($\tau_a > 0.06$). Figure 8.7 gives the average ratio of the FD energy to the calibrated SD energy, written as $\langle E_{\text{FD}}/E_{\text{SD}} \rangle$, and shows how it varies with SD energy. As previously, the curves are given for clear nights and dirty nights. As expected, the $\langle E_{\text{FD}}/E_{\text{SD}} \rangle$ values are higher (in all the energy bins) during the dirty nights than they are during the nights with low aerosol concentrations. The FD-to-SD energy ratio goes from 5% at $10^{18.3}$ eV to 20% at $10^{19.5}$ eV in the case of the dirty nights. This overestimation of the FD energy could be explained as an additional contribution to the collected signal coming from the aerosols by multiple scattering. The energy shift appears to increase with the SD energy, and this can be explained easily by multiple scattering. To quantify the discrepancy between the two samples, Table 8.2 estimates the standard deviations for an aerosol optical depth cut to the dirty nights fixed at 0.06.

Since the aerosol optical depth is proportional to $n(R) \sigma_{\text{tot}}(R)$, i.e. $n(R) R^2$, it is interesting to notice that we cannot know if the clear nights (i.e. the density $n(R)$ is low) have particularly large aerosols.

8.3 Atmospheric multiple scattering of light emitted by a point source

The contribution of the scattering effect has to be well estimated for precise shower reconstruction. Multiple scattering (MS) increases the amount of light arriving at the detector from the source. The purpose of this section is to describe the multiple scattering phenomenon as it can be expected to happen with the Auger detector. The Monte Carlo simulation used is the "Hybrid fadc" program [12], modified by Jan Pekala to study multiple scattering in detail [3]. He introduced further modifications in order to study an isotropic point light source, instead of a longitudinal shower profile. The emission time and the number of emitted photons can be modified. The ray tracing is done for a fixed wavelength, by default $\lambda = 379$ nm. As in the original simulation program, the atmospheric conditions can be changed. Thus, with this version of the program, it was possible to investigate the effects of aerosols on multiple scattering.

Previously, a significant study concerning the aerosol effects has already been done in [3]

²<http://augerobserver.fzk.de/doku.php?id=datatree:root>

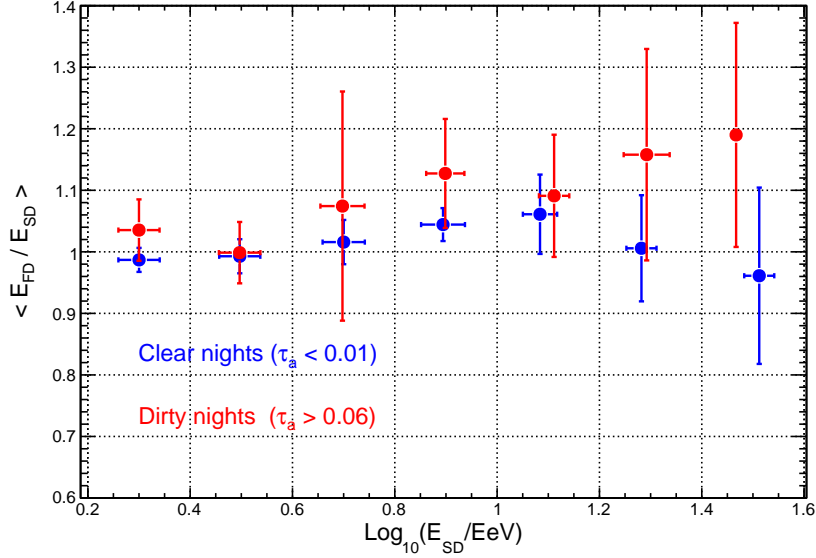


Figure 8.7: **FD-to-SD energy ratio, for clear nights and dirty nights.** Evolution of the average value $\langle E_{FD}/E_{SD} \rangle$ with respect to the SD energy. The error bars correspond to the error on the mean.

$\log_{10}(E_{SD}^{\min}/\text{eV})$	18.0	18.2	18.4	18.6	18.8	19.0	19.2	19.4
$\log_{10}(E_{SD}^{\max}/\text{eV})$	18.2	18.4	18.6	18.8	19.0	19.2	19.4	19.6
Number of events								
<i>Clear nights</i> ($\tau_a < 0.01$)	299	343	195	129	83	39	15	12
<i>Dirty nights</i> ($\tau_a > 0.06$)	146	179	125	53	43	27	18	3
Mean $\langle E_{FD}/E_{SD} \rangle$								
<i>Clear nights</i> ($\tau_a < 0.01$)	1.12	0.99	0.99	1.02	1.04	1.06	1.00	0.96
<i>Dirty nights</i> ($\tau_a > 0.06$)	1.19	1.03	1.00	1.07	1.13	1.09	1.16	1.19
Fluctuations $\text{RMS}(E_{FD}/E_{SD})$								
<i>Clear nights</i> ($\tau_a < 0.01$)	0.67	0.36	0.39	0.41	0.24	0.40	0.33	0.50
<i>Dirty nights</i> ($\tau_a > 0.06$)	1.62	0.67	0.56	1.35	0.58	0.52	0.73	0.32
Separation between the two samples								
<i>Dirty nights</i> ($\tau_a > 0.06$)	-0.54	-0.90	-0.10	-0.31	-0.89	-0.25	-0.79	-0.98
	→ Mean = -0.60							

Table 8.2: $\langle E_{FD}/E_{SD} \rangle$ **distributions for each energy bin.** The separation between two samples A and B is defined as $(\langle X_A \rangle - \langle X_B \rangle) / \sqrt{(\sigma_A^2/N_A) + (\sigma_B^2/N_B)}$.

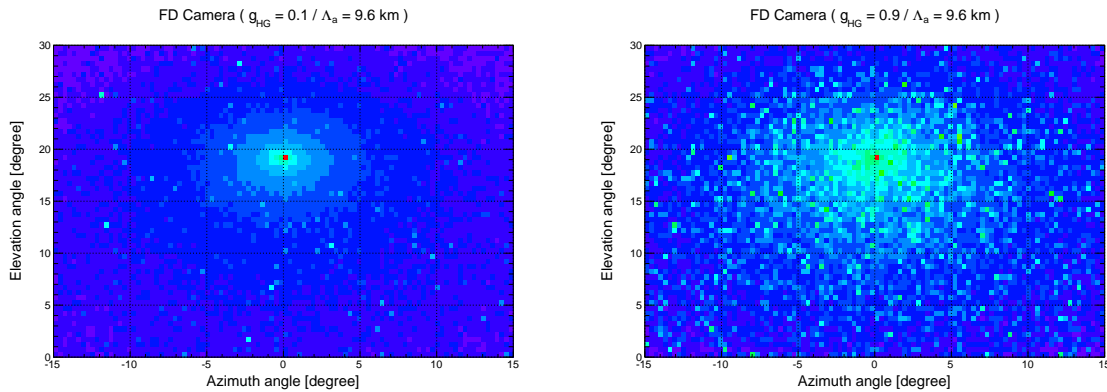


Figure 8.8: FD camera displays for two different asymmetry parameters g_{HG} in the aerosol phase function. *Left panel*: Mean aerosol size around $0.2 \mu\text{m}$ ($g_{\text{HG}} = 0.1$). *Right panel*: Mean aerosol size around $2.0 \mu\text{m}$ ($g_{\text{HG}} = 0.9$). The light source is located 15 km away from the FD telescope, and at an elevation angle of 19.2° .

by modifying the aerosol vertical scale H_a and the aerosol attenuation length Λ_a . Currently, this is one of the two parameterizations which can be used for shower reconstruction in the Offline (the so-called **ePekala**). But, the dependence of the MS on the aerosol phase function P_a has not been studied. Figure 8.8 shows FD camera displays for observing an isotropic point source, located 15 km away from the FD telescope and at an elevation angle³ of 19.2° , for the two configurations of the desert model: dominated by very small aerosols on the left (corresponding to the aerosol size range for the calm configuration in Figure 8.3), and by large aerosols on the right (corresponding to the dust storm configuration). As has been explained in Section 8.1, two aerosol sizes mean two different aerosol phase functions. Thus, these two displays show a clear effect of the APF on the multiple scattering signal.

As they propagate to the FD telescope, the photons can be scattered several times before reaching the camera. Figure 8.9 gives the distribution of the number of scatterings, and the distance travelled from the last scattering location to the detector, for the same source location as previously. The upper limit for the number of scatterings is fixed at 5 (indirectly, this also limits the time delay) in the simulation.

Now, let us look at the distribution of the light over the FD camera. As we know, the FD profile reconstruction follows several steps. Once the geometry is reconstructed, the position of the light spot on the camera is known every 100 ns. A circle of radius ζ is constructed with the spot as centre for each point of the track on the camera. Then, for each time bin, the procedure defines the total track signal as the sum of the signals for pixels having their centre within the circle of radius ζ . In our case, the light spot is the signal coming from the direct

³These two values represent the typical location of the shower maximum for an energy around $10^{18.6}$ eV.

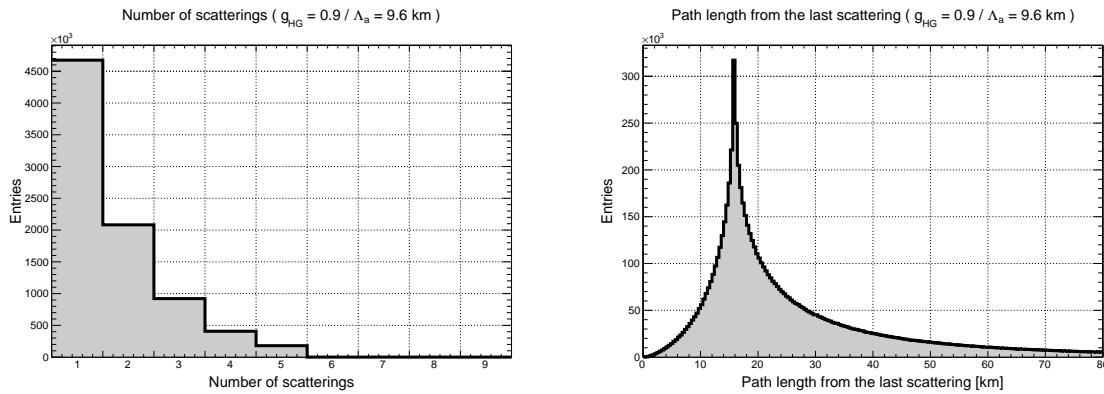


Figure 8.9: **Properties of the scattered photons reaching the FD camera.** The light source is located 15 km away from the FD telescope, and at an elevation angle of 19.2°. *Left panel:* Distribution of the number of scatterings for photons detected by the camera. *Right panel:* Distribution of the distances travelled by photons from their last scattering location to the detector.

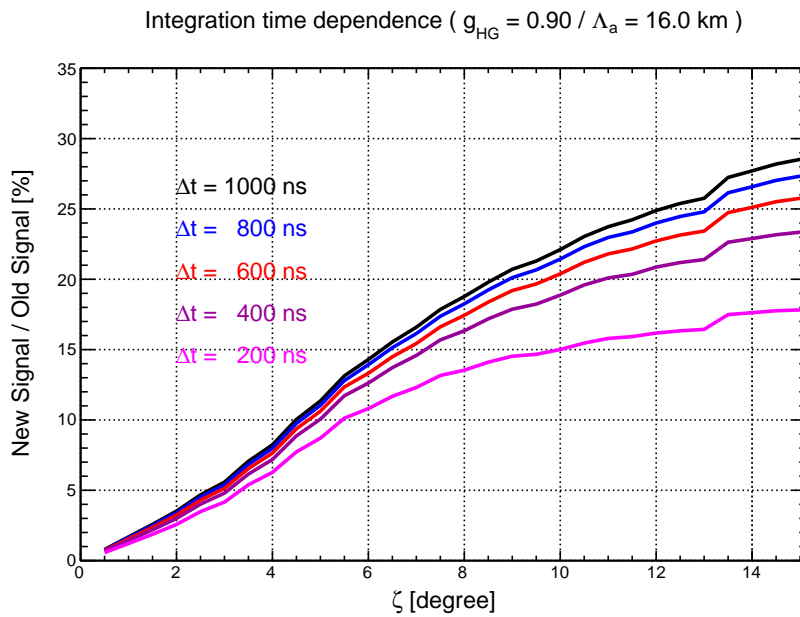


Figure 8.10: **Evolution of the multiple scattering contribution with the integration angle, for different integration times.** The light source is located 15 km away from the FD telescope, and at an elevation angle of 19.2°. The aerosol component is defined with an asymmetry parameter $g_{HG} = 0.90$ and a horizontal aerosol attenuation length $\Lambda_a = 16$ km.

light and it stays fixed. The multiple scattering contribution, named M , is defined as follows

$$M = \frac{\text{Scattered Light}}{\text{Direct Light}} = \frac{\text{New Signal}}{\text{Old Signal}} \quad (8.7)$$

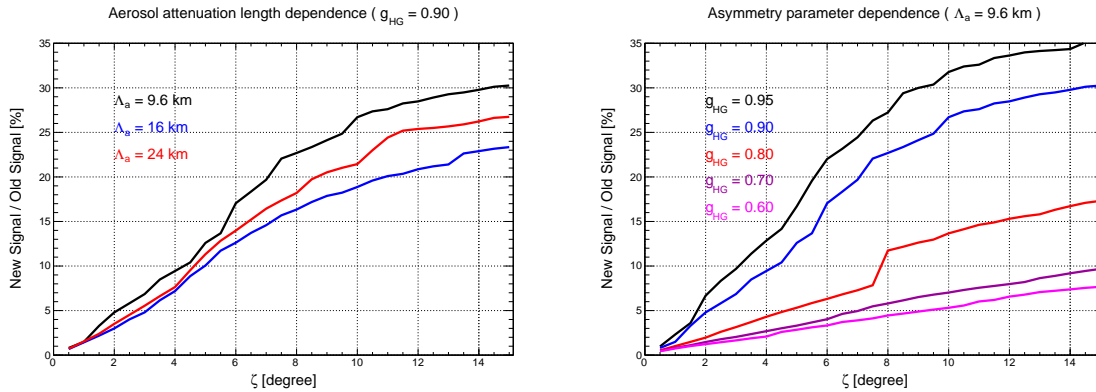


Figure 8.11: Evolution of the multiple scattering contribution with the integration angle, for different aerosol conditions. *Left panel:* Dependence of the M factor on the aerosol concentration. *Right panel:* Dependence of the M factor on the aerosol size. The light source is located 15 km away from the FD telescope, and at an elevation angle of 19.2° .

Figure 8.10 shows the evolution of the factor M with the integration angle ζ , for different integration times Δt . The times are defined with respect to the arrival time of the direct light. As expected, the photons with low delay times contribute mainly to the low ζ values, and photons with several scatterings contribute to the multiple scattered light at large ζ values. This means that when studying the MS contribution to the shower energy estimation, if the light is collected within ζ angles around 1.5° , the dependence on the integration time is not significant. In the following, a $\Delta t = 400$ ns is used. However, in studies of the FD halo for instance, where large ζ angles are used, it seems necessary to take into account the effect of the integration time.

Figure 8.11 shows the dependence of the MS contribution on the aerosol conditions, for different integration angles ζ . It is relevant to observe that the asymmetry parameter, contrary to the aerosol attenuation length, significantly affects the M factor, even at very low ζ values. Thus, more than the aerosol concentration, it is their size distribution which affects the MS contribution in the estimation of the shower energy.

8.3.1 Multiple scattering and the elevation angle

Aerosols are mainly present in the lower layers of the atmosphere, i.e. in the first kilometers above ground. Since the aerosols have an effect on the MS signal recorded by the camera, their impact should be higher at low elevation angles. The purpose of this sub-section is to examine the behaviour of the MS signal with the elevation angle of the light source, and its dependence on the aerosol conditions (and especially with respect to the aerosol phase function).

Pekala shows in [3] that, for a fixed value of horizontal aerosol attenuation length, the M

factor is parameterized as a function of the ζ angle, the elevation angle θ and the horizontal distance to the light source L

$$M(\theta|\zeta, L, \Lambda_{\text{tot}}) = A(\Lambda_{\text{tot}}) \zeta \frac{L}{\cos \theta} \exp\left(-\frac{L \tan \theta}{B(\Lambda_{\text{tot}})}\right), \quad (8.8)$$

where A and B are two fit parameters defined as

$$A(\Lambda_{\text{tot}}[\text{km}]) = 1.774 \exp(-\Lambda_{\text{tot}}/4.365) + 0.1387 \quad \text{and} \quad B(\Lambda_{\text{tot}}[\text{km}]) = 0.1976 \Lambda_{\text{tot}} + 1.402$$

The linear dependence of the M factor on the integration angle ζ can be seen in Figure 8.12 for different ζ values (the lowest elevation angle recorded by the FD camera at Auger is around $\theta = 3^\circ$). For other values of the horizontal aerosol attenuation length, similar fits are shown in Figure 8.13, while applying the dependence on aerosol attenuation length for the fit parameters A and B .

For all these fits, the fit parameters have to be defined as function of the asymmetry parameter g_{HG} too. Hence, for different aerosol attenuation lengths and different locations of the light source, the dependence on the g_{HG} parameter has been added. Figure 8.14 shows the evolution of the two fit parameters A and B as a function of the asymmetry parameter, for different aerosol concentrations and distances from the light sources. With this set of parameters, all the aerosol and geometrical conditions are studied. It is interesting to observe that the fit parameter B is more or less independent of the asymmetry parameter: this means that the aerosol size does not affect the exponential decrease of the MS contribution with elevation angle. In the following, we will assume its independence with respect to the aerosol size.

In the case of the A parameter, the g_{HG} dependence has to be included. Since the distance of the light source L does not significantly affect the ratio $K_{\text{PS}}(g_{\text{HG}}) = A_{g_{\text{HG}}}/A_{0.6}$, the fit parameter A can be parameterized as follows

$$A(\Lambda_{\text{tot}}, g_{\text{HG}}) = K_{\text{PS}}(g_{\text{HG}}) A(\Lambda_{\text{tot}}), \quad (8.9)$$

where $A_{0.6}$ represents the value of the A parameter for the aerosol phase function used in the original Pekala parameterization, i.e. an asymmetry parameter fixed at $g_{\text{HG}} = 0.6$. Finally, the MS parameterization, taking into account the dependence of the aerosol size, is given by

$$M(\theta|\zeta, L, \Lambda_{\text{tot}}, g_{\text{HG}}) = K_{\text{PS}}(g_{\text{HG}}) A(\Lambda_{\text{tot}}) \zeta \frac{L}{\cos \theta} \exp\left(-\frac{L \tan \theta}{B(\Lambda_{\text{tot}})}\right), \quad (8.10)$$

where $K_{\text{PS}}(g_{\text{HG}})$ is defined as

$$K_{\text{PS}}(g_{\text{HG}}) \simeq 30 g_{\text{HG}}^2 - 36 g_{\text{HG}} + 12.$$

8.3.2 Application to the FD halo measurements

This unexpected phenomenon was identified for the first time during a campaign for telescope calibration in August 2008. A zeppelin-shaped balloon filled with helium carried a flasher lamp, i.e. an isotropic UV light source. Located at a distance of about 1 km from the FD telescope, this light source should have appeared as a point source for the FD camera. Instead of recording a maximum of three triggered pixels on the camera, a whole halo was observed: around 15% of the light was outside the central pixel [13]. Subsequently, several additional campaigns were undertaken, at different FD telescopes and different distances to the telescopes. Thanks to these measurements, several effects were excluded as possible source of the halo: electronic and optical cross-talks, dust on filters and mirrors, diffuse transmission through filters and reflections on the camera backside.

Finally, in a study conducted jointly by the Olomouc group and the KIT group, reflections on the PMT glass were proposed to explain the halo distribution at large angles [14]. This implies that the value of the PMT reflectivity previously assumed in the `Offline` was too small. Instead of about 8%, a value of about 20% at 375 nm seems more likely. Figure 8.15 gives a simulation done in the `Offline` while increasing the PMT reflectivity to 20% in the module `TelescopeSimulatorLX`: by doing this, all the halo recorded at integration angles ζ larger than 15° can be fully reproduced. The light distribution on the camera simulated under those conditions is for the largest ζ angles, very similar to the distribution measured with the flasher. The flat tail of the differential halo distribution can be explained by photons that are reflected on the PMT surface and afterwards in the mirror before they hit the camera in a broad beam. Considering this correction, only the part at low ζ angles remains to be understood. This part still represents 6% of the total light.

During the year 2009, before the idea of reflections on the PMT glass, we proposed aerosols as a possible source of this FD halo [1]. The argument was the following: aerosol conditions, i.e. concentration and size distribution, affect the multiple scattering contribution to the signal recorded by the telescopes. Even for low distances between the light source and the detector, aerosols, if they are large enough, could explain the halo phenomenon.

Hence, it seems interesting to estimate the aerosol effect on the multiple scattering contribution for the measurements done in August 2008 during the zeppelin campaign. Following the positions of the light source during data acquisition, most of the measurements were done at elevation angles lower than 10° with respect to the ground, i.e. where the aerosols are the most numerous (as shown in Section 8.3). In this halo study, we fix the light location at 1 km from the telescope and at an elevation angle of 7.2° . Since the pulse length of the light source was fixed at $8 \mu\text{s}$ in the measurements, the integration time was increased with respect to previous values. This difference will increase the contribution of scattered photons with larger time delays, i.e. reaching the FD camera with larger ζ angles. Figure 8.16 displays

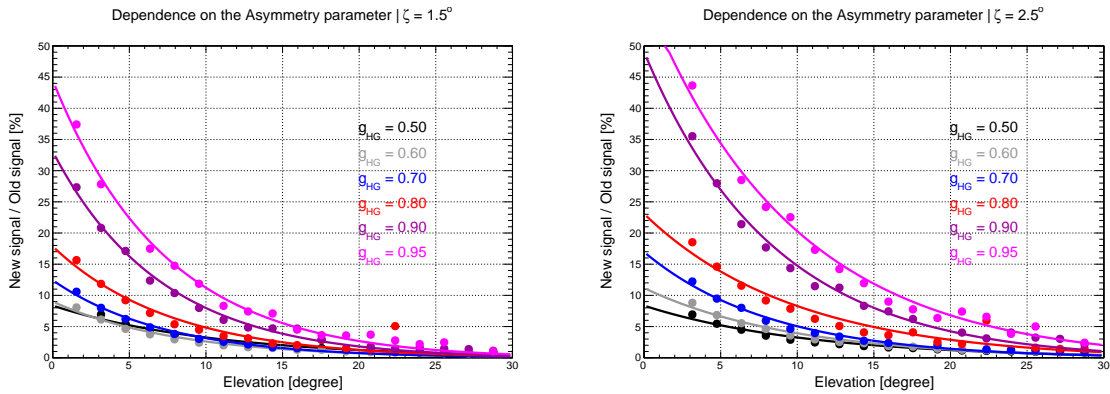


Figure 8.12: Contribution of the MS signal to the direct light versus the elevation angle of the light source for different values of the light collecting angle ζ . The lines represent fits of Equation (8.8) for different asymmetry parameters g_{HG} . The horizontal length to the light source is 15 km and the aerosol attenuation length is fixed at 12 km.

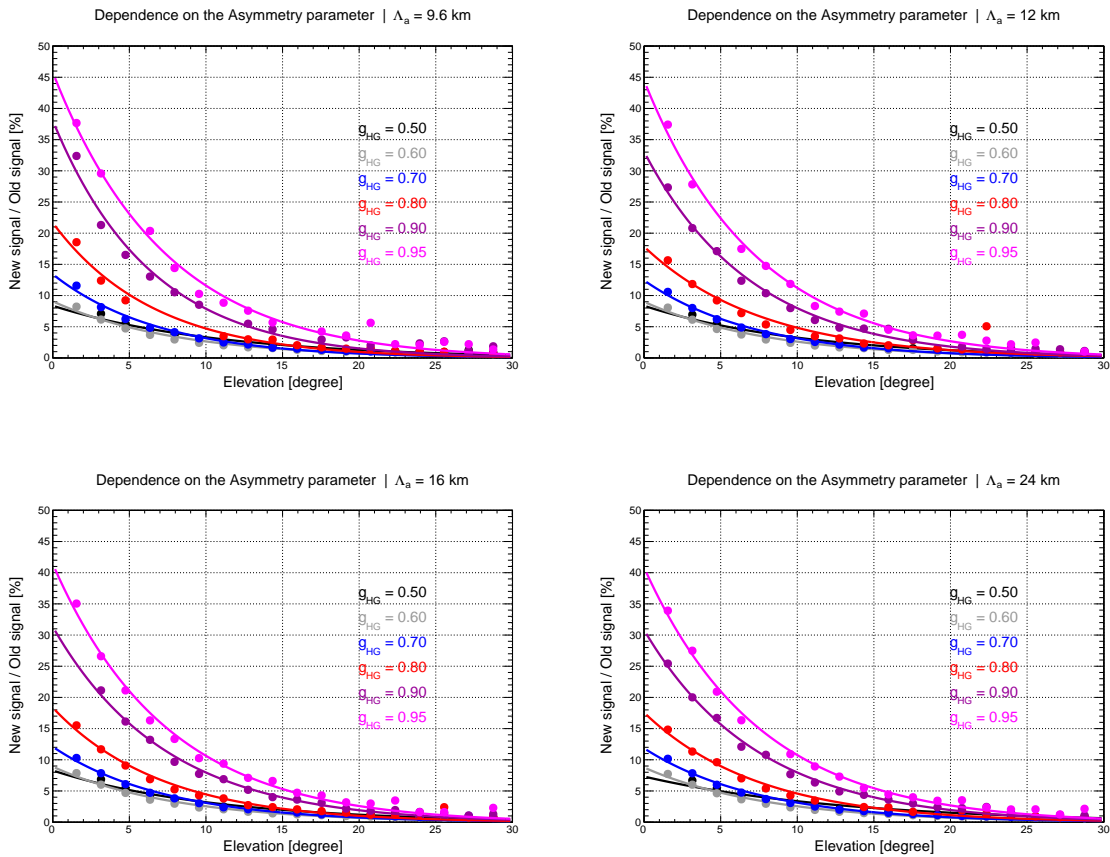


Figure 8.13: Contribution of the MS signal to the direct light versus the elevation angle of the light source for different values of aerosol attenuation length: $\Lambda_a = 9.6$ km, 12 km, 16 km, 24 km. The contributions are integrated within the angle $\zeta = 1.5^\circ$. The lines represent fits of Equation (8.8) for different asymmetry parameters g_{HG} . The horizontal length to the light source is 15 km.

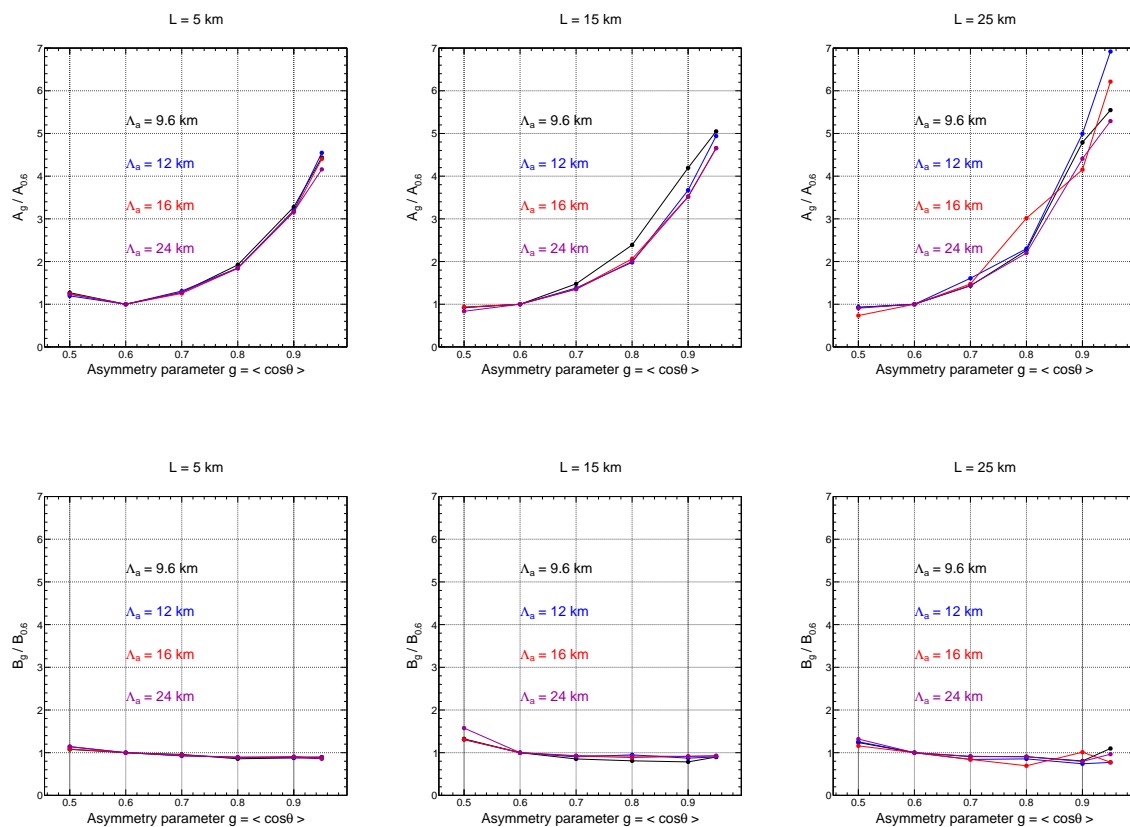


Figure 8.14: **Fit parameters.** Evolution of the values of the two fit parameters A and B with the asymmetry parameter, for different aerosol conditions and different source locations.

the signal recorded by the telescope for such a source location.

Figure 8.17 gives the evolution of the multiple scattering contribution with respect to the integration angle ζ , for different aerosol attenuation lengths and aerosol phase functions. As it has already been explained in [1], conditions with large aerosols (a few microns in diameter) could explain the 6% of the total signal remaining to be understood. A transposition in terms of cumulative halo can be done to estimate the aerosol population needed to reproduce the data from the zeppelin campaign. As was explained in Section 8.1, aerosols are divided into different aerosol populations (or modes). Figure 8.15 gives the aerosol mode needed to correspond to the FD halo recorded in the cameras: a large aerosol mode (or coarse mode), with a mean diameter equal to $5 \mu\text{m}$ ($g_{\text{HG}} = 0.95$). Concerning the aerosol concentration, its effect is very weak for aerosol attenuation lengths varying from 9.6 km to 24 km. Thus, thanks to the FD halo, it is possible to have a first estimation of the size of the largest aerosols at the Auger location.

It is interesting to note that aerosols of a few microns are typical of droplet sizes in fog or during hazy conditions. Maybe the largest aerosols do not come from the soil, but come

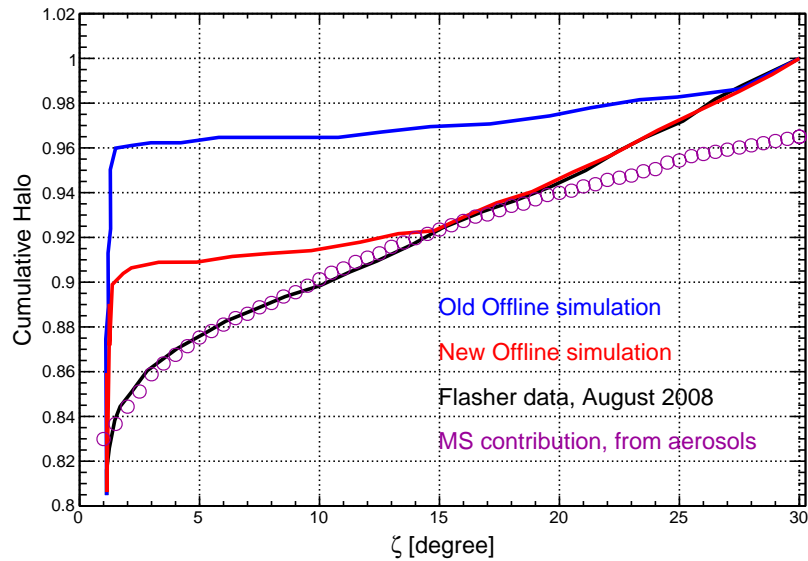


Figure 8.15: **Accumulated halo distribution (from [15]).** Halo measurements made in August 2008 are compared to the old Offline simulation and the new one while increasing the PMT reflectivity to 20%. The modifications were made in the **TelescopeSimulatorLX** module. The MS contribution due to the aerosols is the result of this study. It corresponds to an aerosol attenuation length equal to 24 km, and an asymmetry parameter g_{HG} fixed at 0.95.

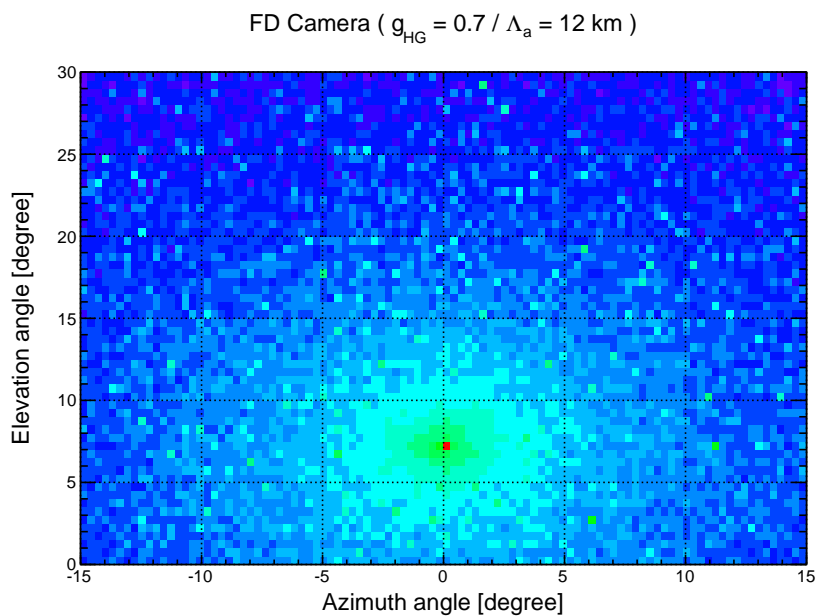


Figure 8.16: **FD camera display for a zeppelin located one kilometer from the detector, at a 7.2° elevation angle.** The aerosol attenuation length is fixed at 12 km and the asymmetry parameter g_{HG} at 0.7.

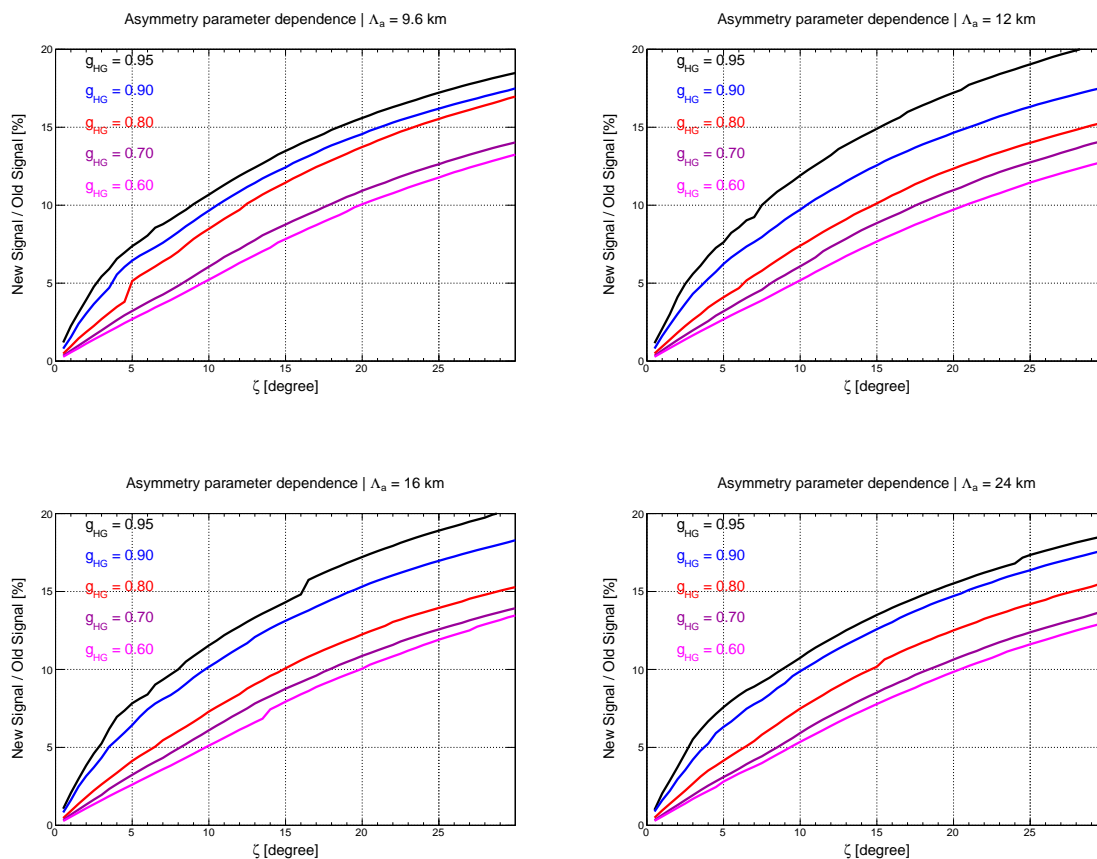


Figure 8.17: Evolution of the MS contribution with the integration angle, for different aerosol conditions (concentration and size). The light source is located 1 km from the telescope, and at an elevation angle of 7.2° .

from high altitudes and humidity. Having obtained such a result, we really believe that an aerosol measurement should be done at the same time as the next FD halo campaign. It could consist of aerosol sampling close to the FD telescope, combined with lidar measurements to get the profiles of the aerosol optical depth. Thanks to these two measurements, it should be possible to extract information about the aerosol component close to the detector.

8.4 Effect of multiple scattering on energy and X_{\max} reconstruction

In the case of air shower reconstruction, the multiple scattering contribution does not come exclusively from one point source. Indeed, the air shower can be described as multiple point sources extending in space and time. Thus, for a given pixel, the MS contribution represents also the MS signal coming from the neighbouring pixels. When using only the first neighbour pixels, as explained in Figure 8.18(a), the MS contribution in the case of a "thin" air shower

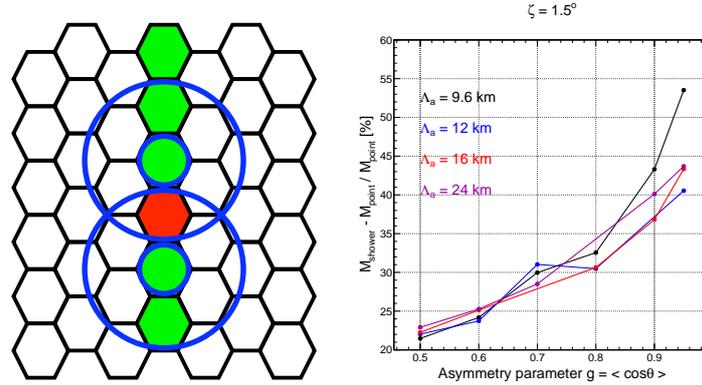


Figure 8.18: **Comparison between MS contributions in the cases of a point source or an extended air shower.** (a) *Left panel:* Total track recorded on a FD camera. Coloured pixels correspond to triggered pixels. The two crowns represent the halo from the two first neighbour pixels of the central one (in red). (b) *Right panel:* Difference of the MS signals between a point source and an extended light source, for different aerosol conditions. The light source is located 15 km from the FD telescope, and at an elevation angle of 19.2° . The integration angle ζ is equal to 1.5° and the integration time Δt is 400 ns.

becomes

$$M(\zeta \leq 1.5^\circ) \rightarrow M(\zeta \leq 1.5^\circ) + 2 \frac{1}{6} M(0.75^\circ \leq \zeta \leq 2.25^\circ),$$

where the factor $1/6$ represents the overlap factor between the central pixel (in red) and the first crown of the neighbour pixel (in blue), and "2" taking into account the two first neighbours.

Figure 8.18(b) gives the difference between the cases of a point source (as described in Section 8.3) and a shower, for different aerosol conditions. The light source is fixed at 15 km from the telescope, and at an elevation angle of 19.2° . The additional contribution is not negligible, even at low g_{HG} values. It can reach one half of the original MS contribution in the case of very large aerosols.

Now, let us focus on the Pekala's parameterization implemented in the Offline. As has already been said, it assumes an asymmetry parameter g_{HG} fixed at around 0.6. We will study here the most probable source location ($L = 15$ km, $\alpha = 19.2^\circ$). The idea of this toy parameterization fully dependent on the aerosol conditions is to estimate the multiplicative factor $K_{\text{SH}}(g_{\text{HG}}) = M_{g_{\text{HG}}}/M_{0.6}$. This parameter is defined as independent of the aerosol attenuation length as shown in Figure 8.19. The figure gives the $K_{\text{SH}}(g_{\text{HG}})$ curves for different aerosol concentrations and different integration angles ζ . The K_{SH} factor increases with the asymmetry parameter. Thus, during nights where large aerosols are more numerous, the MS contribution to the collected light, even for $\zeta = 1.5^\circ$, can be up to three times higher than for the original Pekala parameterization.

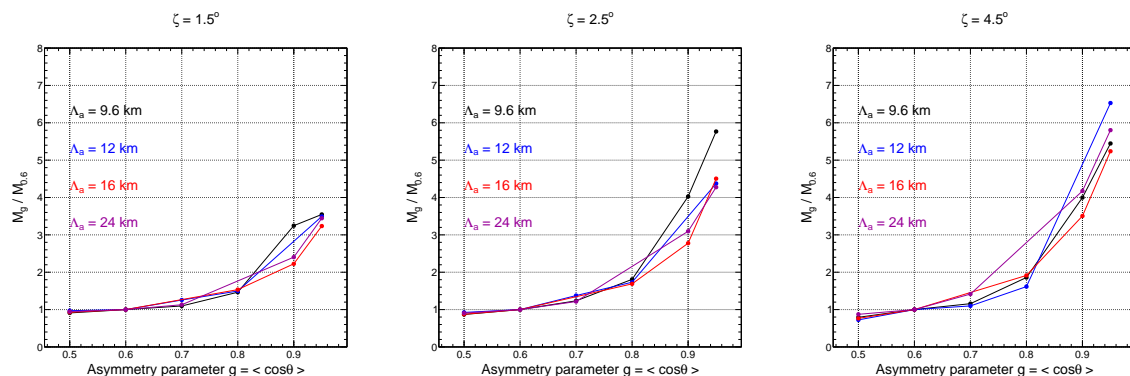


Figure 8.19: Evolution of K_{SH} with the asymmetry parameter, for different aerosol conditions and different integration angles $\zeta = 1.5^\circ, 2.5^\circ$ and 4.5° . The light source is located 15 km from the FD telescope, and at an elevation angle of 19.2° .

Once this toy parameterization has been defined, it is possible to get a first estimate of the effect of the aerosol size on the shower reconstruction. In this part, we use the Golden Hybrid events for the year 2010. We reconstruct these data with the `Offline` v2r6p5, for three different MS parameterizations. This modification is done in the file `CherenkovFluorescenceMatrix.cc` from the module `FdProfileReconstructorKG`. Three different parameterizations corresponding to three different asymmetry parameters are used in the event reconstruction: $g_{HG} = 0.60, 0.90$ and 0.95 . We then examine the changes in the energy estimation and the X_{max} reconstruction when aerosols are larger than originally assumed. Figure 8.20 plots the difference in the reconstructed energy and X_{max} for $g_{HG} = 0.90$ or 0.95 , with respect to the case where $g_{HG} = 0.60$ (value by default in the `Offline`). In the two cases, an overestimation of the energy and of the X_{max} is observed. For the largest aerosols, the energy difference $\Delta E/E$ reaches +4% and the X_{max} shifts +5 g/cm². Knowing that the total systematic uncertainty on X_{max} is around 12 g/cm² [11], the effect of the aerosols via MS is not negligible and should be monitored in more detail.

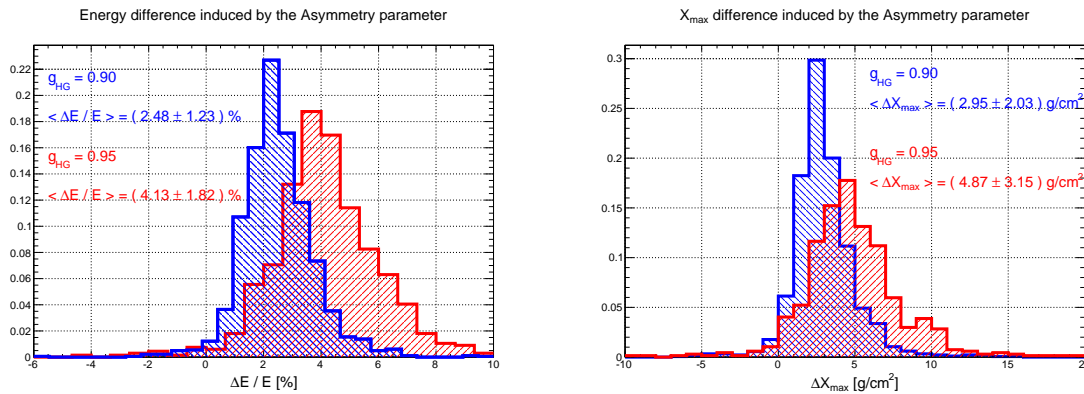


Figure 8.20: **Energy and X_{max} differences induced by the uncertainty in the asymmetry parameter.** The data set corresponds to the Golden Hybrid events recorded in 2010, and reconstructed with the Offline v2r6p5. The differences are defined with respect to the default g_{HG} value, equal to 0.6.

8.5 Conclusion

Throughout this note we have reported that the aerosol size, much more than the aerosol concentration, has an effect on the contribution of the MS to the total light. This work was done by changing the shape of the aerosol phase function. Thanks to the Ramsauer approach, the link between the phase function and the aerosol size has been explained.

After having taken a look at the Golden Hybrid events and identified a possible proof of an aerosol effect in the energy estimation, a toy parameterization fully dependent on the aerosol conditions, i.e. concentration and size, was defined. This work was done thanks to Pekala's simulation code, which has already been used to produce the MS parameterization used in the Offline. Simulations were also done to reproduce the experimental setup of the zeppelin campaign: we found that large aerosols, typically with diameters around $5 \mu m$, could explain the first part of the FD halo. It confirms the results already established in [1].

Finally, a first estimation of the effect of the aerosol size on the energy and X_{max} reconstructions was done: a clear systematic overestimation of these two quantities is noted in the case where one underestimates the size of aerosols present over the Auger array. The energy difference $\Delta E / E$ reaches +4% and the X_{max} shifts +5 g/cm^2 for the dust storm configuration in the desert model.

Bibliography

- [1] K Louedec *et al.*, *Ramsauer approach to large atmospheric aerosols as a possible source of the FD halo*, **GAP-2009-173**.
- [2] MD Roberts, *The role of atmospheric multiple scattering in the transmission of fluorescence light from extensive air showers*, *J. Phys. G* **31** 1291–1301.
- [3] J Pekala *et al.*, *Atmospheric multiple scattering of fluorescence and Cherenkov light emitted by extensive air showers*, *NIMA* **605** (2009) 388–398.
- [4] J Stasielak, *Comparison of the Pekala and Roberts corrections for the multiple scattering in the Offline hybrid reconstruction*, **GAP-2009-177**.
- [5] J Abraham *et al.* [Pierre Auger Collaboration], *A study of the effect of molecular and aerosol conditions in the atmosphere on air fluorescence measurements at the Pierre Auger Observatory*, *Astropart. Phys.* **33** 108–129.
- [6] S BenZvi *et al.*, *Measurement of the Aerosol Phase Function at the Pierre Auger Observatory*, *Astropart. Phys.* **28** (2007) 312–320.
- [7] DR Longtin *et al.*, *A wind dependent desert aerosol model: radiative properties*, Air Force Geophysics Laboratories (1988) **AFL-TR-88-0112**.
- [8] K Louedec, S Dagoret-Campagne and M Urban, *Ramsauer approach to Mie scattering of light on spherical particles*, *Phys. Scr.* **80** (2009) 035403–035408.
- [9] LC Henyey and JL Greenstein, *Diffuse radiation in the galaxy*, *Astroph. J.* **93** (1941) 70–83.
- [10] R Pesce, for the Pierre Auger Collaboration *Energy calibration of data recorded with the surface detectors of the Pierre Auger Observatory* Proc. 32nd ICRC, Beijing, China (2011).
- [11] EJ Ahn *et al.*, *Measurement of the Depth of Shower Maximum of Cosmic Rays above 10^{18} eV*, **GAP-2009-078**.
- [12] B Dawson *et al.*, *Simulations of a giant hybrid air shower detector*, *Astropart. Phys.* **5** (1996) 239–247.
- [13] J Bäuml, *Test of the calibration of the Auger fluorescence telescopes with an isotropic UV light source*, **GAP-2009-045**.
- [14] R Šmida *et al.*, *Measurements of PMT reflectivity*, Hybrid Reconstruction session, *Analysis Lecce Meeting* (2010).
- [15] J Bäuml *et al.*, *Comparison of telescope simulations with flasher data*, Hybrid Reconstruction session, *Analysis Lecce Meeting* (2010).

Conclusion

The Pierre Auger Observatory is making good progress in understanding the nature and origin of the highest energy cosmic rays, taking advantage of its huge collecting area. Using the hybrid detection technique provides large statistics, good mass and energy resolution, and solid control of systematic uncertainties. A number of important scientific results have thus far been obtained:

- a suppression of the energy spectrum has been observed in the region above $10^{19.6}$ eV. This observation is consistent with the predictions of the GZK cutoff, even though it could be explained by photo-disintegration interaction in the case where a heavy mass composition is confirmed. It could also correspond to a cosmic acceleration endpoint at the astrophysical source,
- the measurements of $\langle X_{\max} \rangle$ and $\text{RMS}(X_{\max})$ show a trend to heavier composition with energy, or, more speculatively, a possible change in interaction physics at extreme energies. Mass composition indicators from SD data confirm this observation.
- there is evidence for a correlation between the arrival directions of the highest energy events and nearby extragalactic matter, even though the correlation is weaker than expected from the earliest data,
- competitive bounds have been placed on the flux of cosmogenic neutrinos and of extremely high energy photons, ruling out some exotic models of the "top-down" scenario.

Motivated by the fact that a significant fraction of the highest energy events originate from the neighbourhood of Centaurus A and that a shower pointing to a source is more likely to have a proton primary, we checked for correlation between the muonic component and the arrival direction by using two muon counting methods developed by the Auger-LAL group. No difference for the muon fraction has been identified between the Cen A region and the rest of the sky.

Currently the Auger Observatory is collecting around $7000 \text{ km}^2 \text{ sr}$ of exposure each year, and is expected to run for almost two more decades. In addition, the Auger Collaboration has embarked on a program of enhancements to the Observatory baseline design. New detectors with HEAT and AMIGA will extend the energy detection threshold down to 10^{17} eV.

The power of the Auger hybrid technique has been amply demonstrated, and yet the statistical reach remains limited in hybrid mode because of the reduced FD duty cycle. Thus alternative techniques are under development to introduce radio and microwave detection coincident with the SD events. These efforts include the AERA (Auger Engineering Radio Array), AMBER (Air shower Microwave Bremsstrahlung Experimental Radiometer), MIDAS (Microwave Detection of Air Showers), FDWave and EASIER (Extensive Air Shower Identification using Electron Radiometer) projects. Although they are still in development, their first results are promising.

Another goal for the Auger Collaboration is to understand differences between its results and those of other experiments for the X_{\max} measurements and the energy spectrum. This understanding involves reducing the systematic uncertainty of the energy scale for the fluorescence detector. The error is still dominated by that of the absolute fluorescence yield (14%). It can be expected that, with new measurements from the AIRFLY Collaboration, this uncertainty will be reduced to about 5% in the near future. Thus, the next step is to reduce those corresponding to the reconstruction (10%) and to atmospheric effects (8%).

It is in this context that this PhD thesis was done. Through this manuscript, different analyses have been undertaken to improve our knowledge of the aerosols and their effect on light propagation. Light attenuation due to aerosols in the atmosphere is described by the Mie scattering theory. Since the Mie solutions are not particularly intuitive, we developed a new approach based on the Ramsauer model. This is the first time that this model, used in nuclear and atomic physics, has been applied to light scattering. This result has been published in a peer-reviewed scientific journal. We have calculated the total cross section and the scattering phase function for non-absorbing spherical particles. Then, these analytical solutions have been applied to the FD halo phenomenon which represents still 6% in the systematic uncertainties of the energy scale. As preliminary result, it was concluded that two aerosol populations with mean radii of 3 μm and 0.1 μm could explain the FD halo recorded by the fluorescence telescopes during calibration campaigns.

A study on the aerosol origin has been done. Using HYSPLIT, a modelling program computing air mass displacements, we have identified a seasonal cycle for the origin of the aerosols travelling through the Pierre Auger Observatory. Also, it has been shown that nights with low aerosol concentrations have air masses coming much more directly from the Pacific Ocean. It is the first time that the evolution with time of the aerosol concentrations measured at Auger is explained and understood. A paper on this result in an atmospheric science journal is currently being prepared by the Auger Collaboration. To extend this study, a large program of aerosol sampling over the SD array is planned at the Pierre Auger Observatory. Measurements of aerosol concentration, aerosol composition and aerosol size will be made.

Finally, an extensive study on aerosol size has been presented in this manuscript. Indeed, this is the first time that the effect of the aerosol size on light propagation has been estimated.

To explain intuitively the phenomenon, solutions derived from the Ramsauer approach were used. Then, a complete study of the multiple scattering parameterizations was conducted. Using a simulation code developed by members of the Auger Collaboration, the dependence on the aerosol size has been added to the parameterizations. A first estimation of the systematic uncertainties due to the aerosol size has been obtained for the energy and X_{\max} calculations in air shower reconstruction. In fact, a systematic overestimation of these two quantities is observed if one underestimates the aerosol size. The energy difference $\Delta E/E$ reaches +4% and the X_{\max} shifts +5 g/cm² for a typical case of large aerosols. These values are energy dependent: when the energy increases, the shower becomes deeper, i.e. fluorescence photons travel in a lower part of the atmosphere where the aerosol concentration is higher and the aerosol size larger.

Therefore, to reduce this systematic uncertainty taken into account in the reconstruction (via the FD halo) as well as in the atmospheric effects (via the multiple scattering and the light attenuation), a method has been developed to measure the aerosol size above the Auger array. It consists of using very inclined laser shots fired by the Central Laser Facility. New configurations of laser shots to probe aerosol sizes as large as possible have been proposed and they are now fired nightly. Large aerosol sizes ever estimated at the Pierre Auger Observatory can now be probed. First preliminary results using laser-shot data collected in the past have identified a population of large aerosols. The mean of the asymmetry parameter distribution is in agreement with a previous study done using the APF monitors.

Finally, it seems interesting to highlight the present excitement occurring in cosmic ray physics for atmospheric science. As proof, we can cite two important events that have happened this year. Last April, a workshop was organised at Cambridge (UK) concerning the interdisciplinary science at the Pierre Auger Observatory. The goal during these two days was to explore the possibilities of the Pierre Auger Observatory as a southern hemisphere centre for atmospheric research in the near future. The second event concerns the CLOUD experiment at CERN reporting its first results in a paper published in the journal *Nature*. The CLOUD experiment was designed to study the effect of cosmic rays on the formation of atmospheric aerosols under controlled laboratory conditions. The CLOUD results show that ionisation from cosmic rays significantly enhances aerosol formation. This measurement will contribute to a better assessment of the effects of clouds in climate models.

Appendix

Rayleigh night study with HYSPLIT and weather stations

This appendix gives, for each Rayleigh night identified by the Pierre Auger Collaboration, atmospheric data from HYSPLIT (*large-scale*) and from the ground-based weather station located at the CLF (*local-scale*). No correlation or logical link is identified between these two data sources, probably due to the too low statistics (only eight Rayleigh nights).

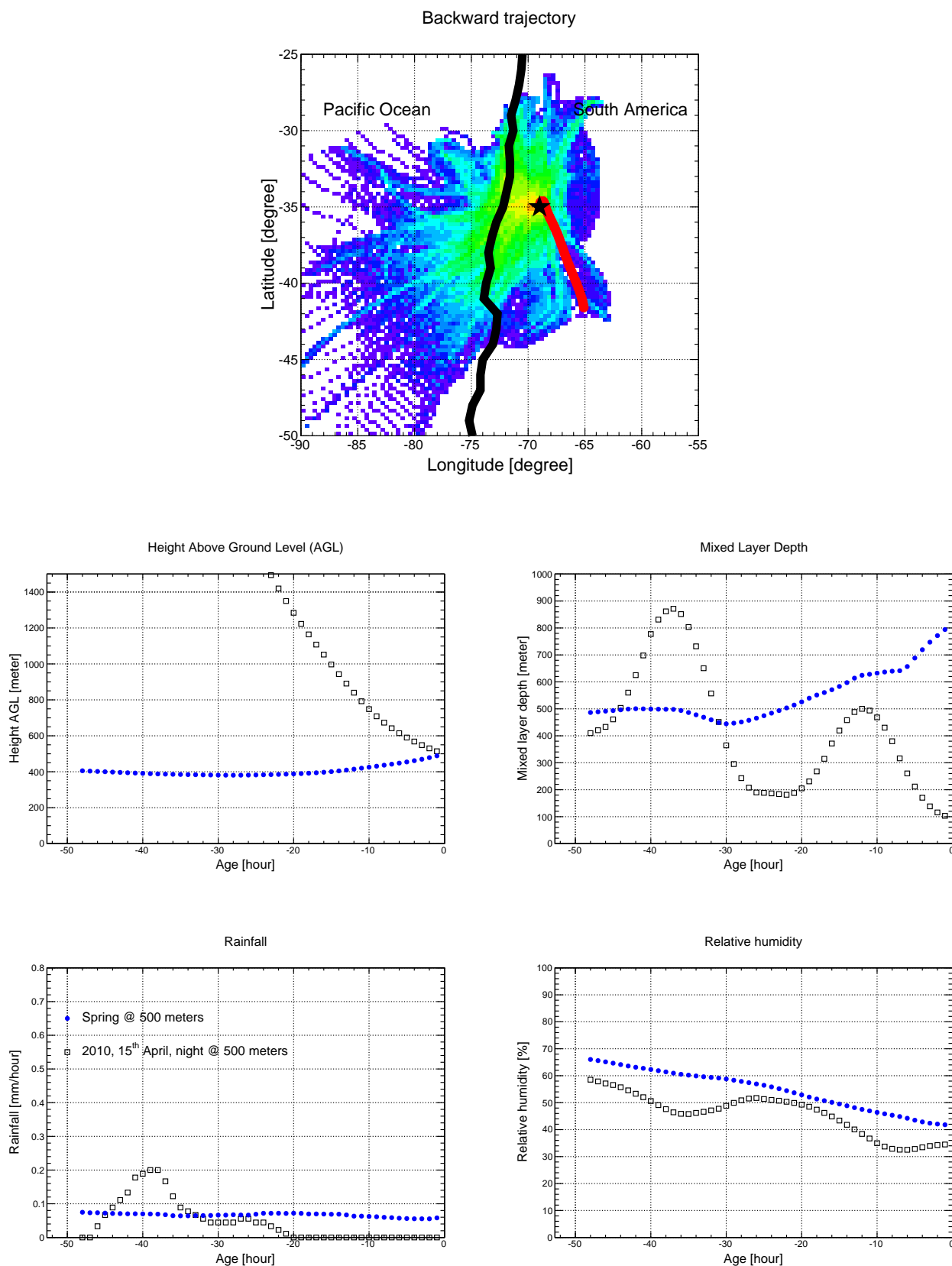


Figure 21: Rayleigh night on 15/04/2010 described with the HYSPLIT data. *Upper panel:* the mean backward trajectory for the night is given in red and the distribution of the trajectories for the whole corresponding season is overlaid. *Lower panel:* the mean evolution profile for the night is given in black and the mean profile of the corresponding season is overlaid in blue.

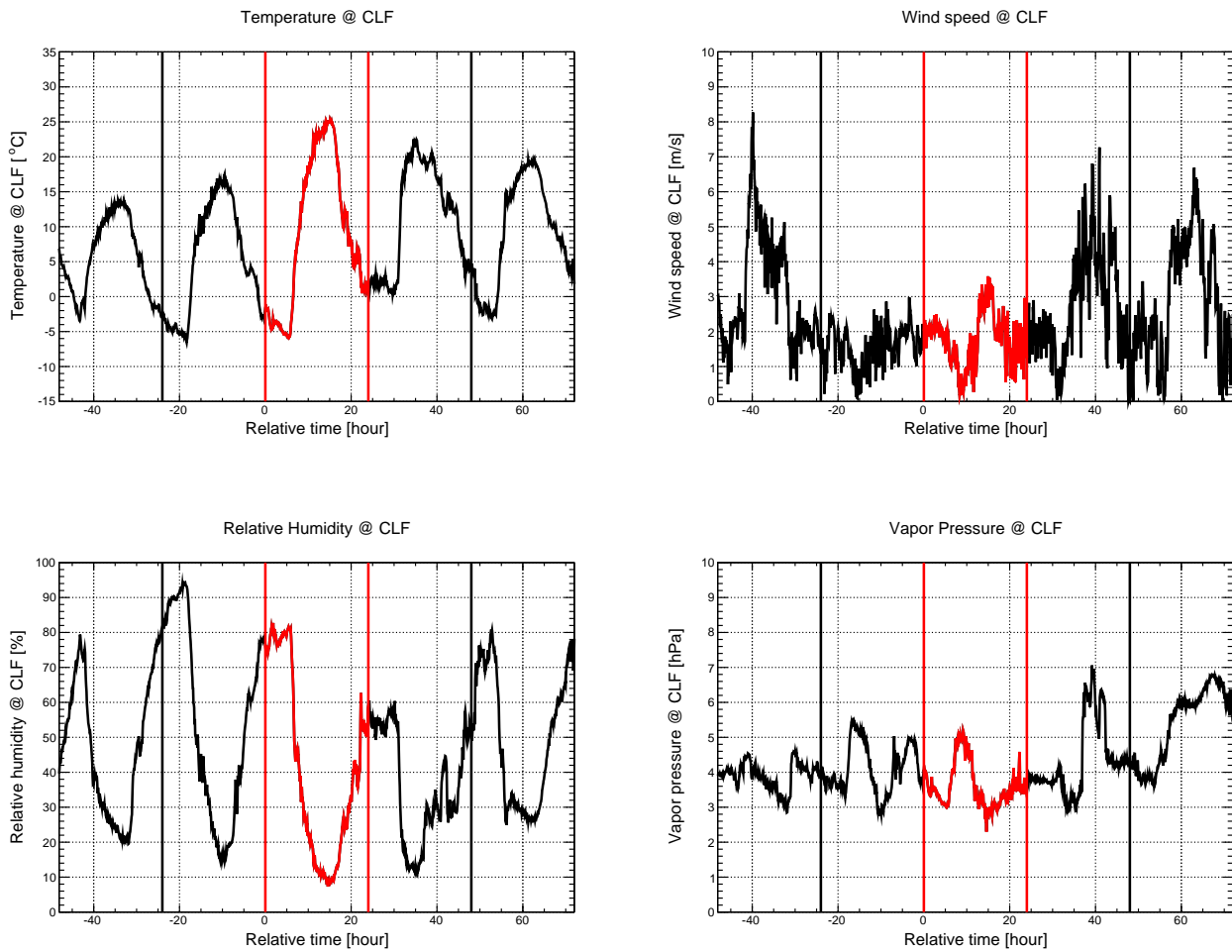


Figure 22: Rayleigh night on 15/04/2010 described with the ground-based weather station at CLF. Evolution of temperature, wind speed, relative humidity and vapor pressure are plotted over 5 days: two days before and after the corresponding Rayleigh night. The day where the Rayleigh night occurs is displayed in red color.

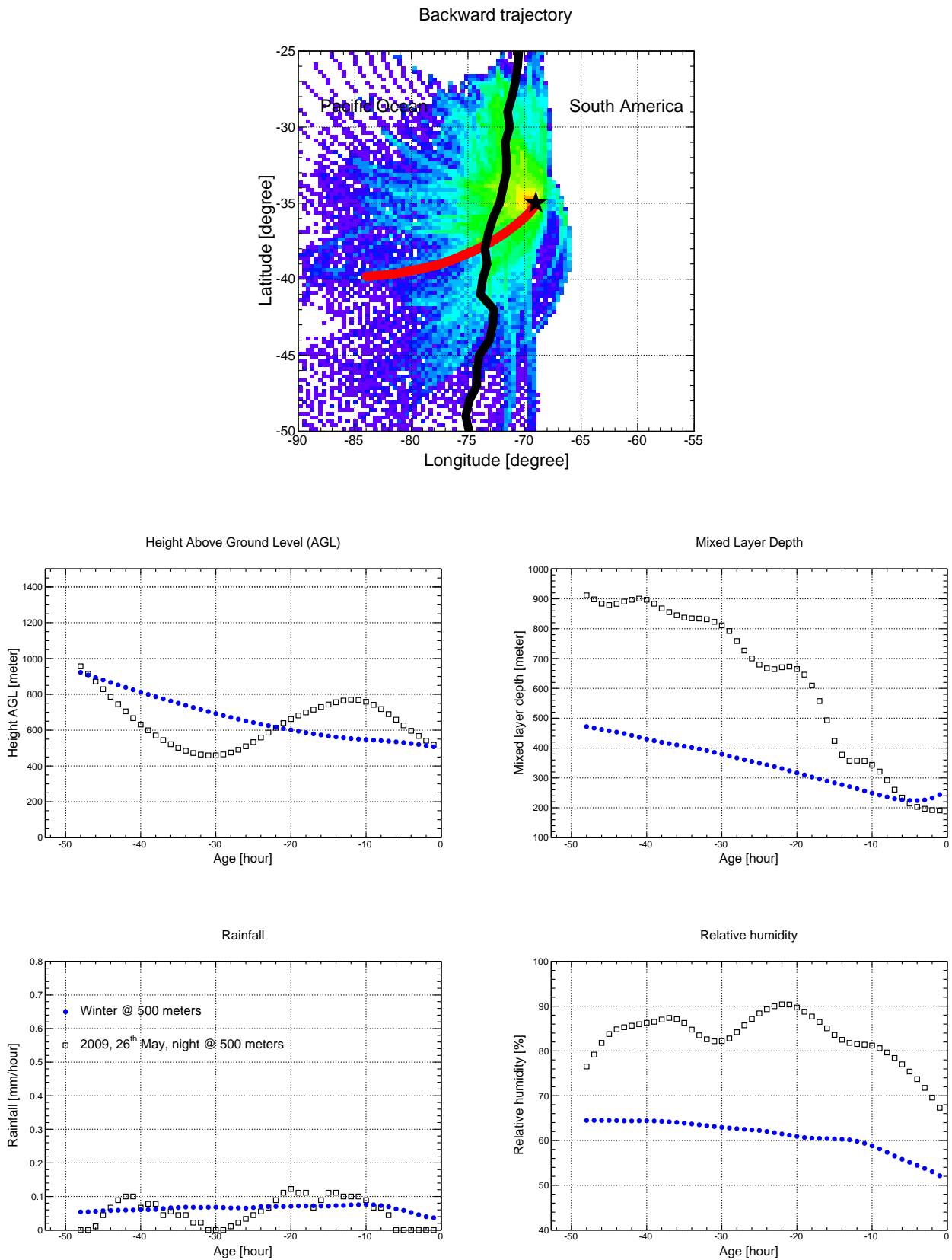


Figure 23: Rayleigh night on 26/05/2009 described with the HYSPLIT data. *Upper panel:* the mean backward trajectory for the night is given in red and the distribution of the trajectories for the whole corresponding season is overlaid. *Lower panel:* the mean evolution profile for the night is given in black and the mean profile of the corresponding season is overlaid in blue.

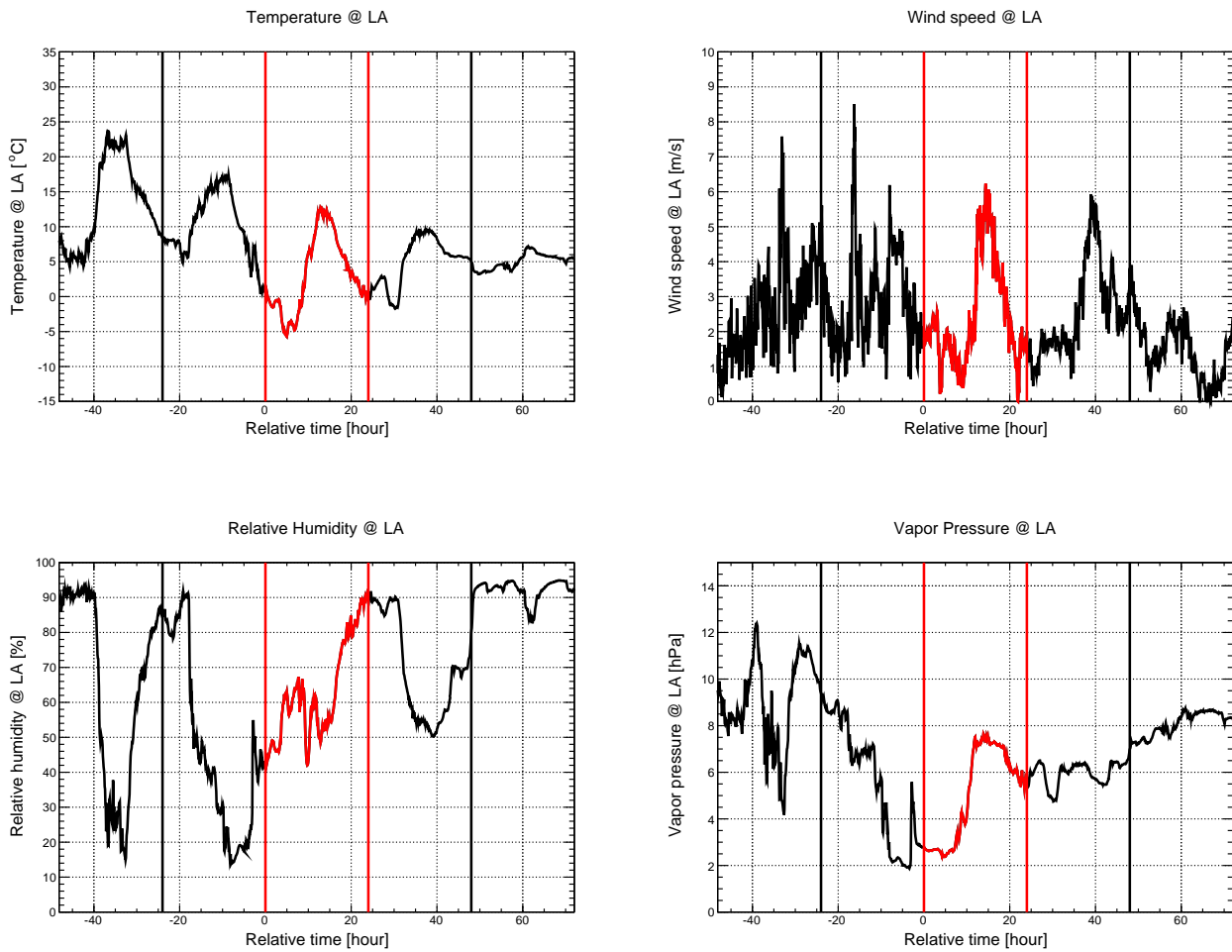


Figure 24: Rayleigh night on 26/05/2009 described with the ground-based weather station at CLF. Evolution of temperature, wind speed, relative humidity and vapor pressure are plotted over 5 days: two days before and after the corresponding Rayleigh night. The day where the Rayleigh night occurs is displayed in red color.

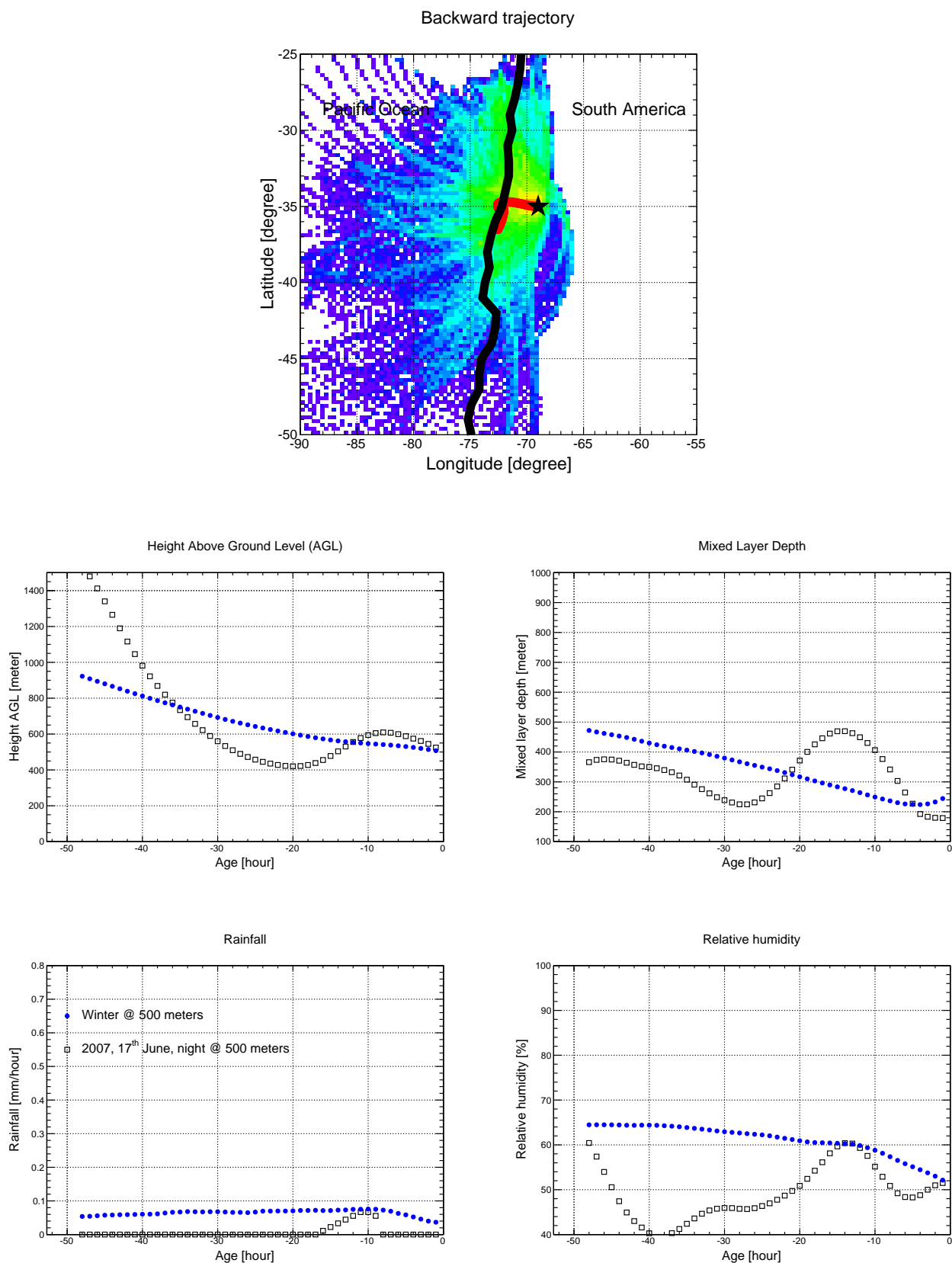


Figure 25: Rayleigh night on 17/06/2007 described with the HYSPLIT data. Upper panel: the mean backward trajectory for the night is given in red and the distribution of the trajectories for the whole corresponding season is overlaid. Lower panel: the mean evolution profile for the night is given in black and the mean profile of the corresponding season is overlaid in blue.

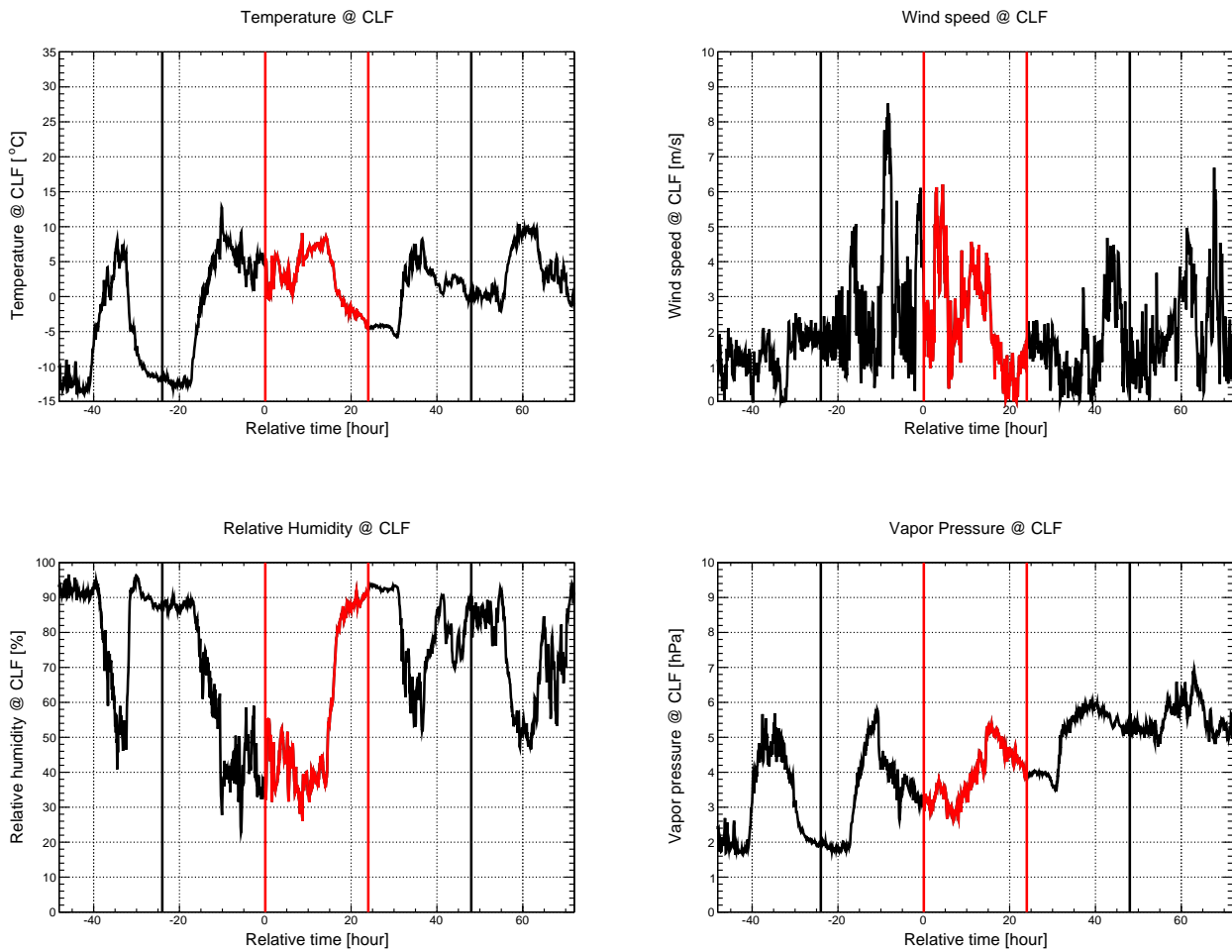


Figure 26: Rayleigh night on 17/06/2007 described with the ground-based weather station at CLF. Evolution of temperature, wind speed, relative humidity and vapor pressure are plotted over 5 days: two days before and after the corresponding Rayleigh night. The day where the Rayleigh night occurs is displayed in red color.

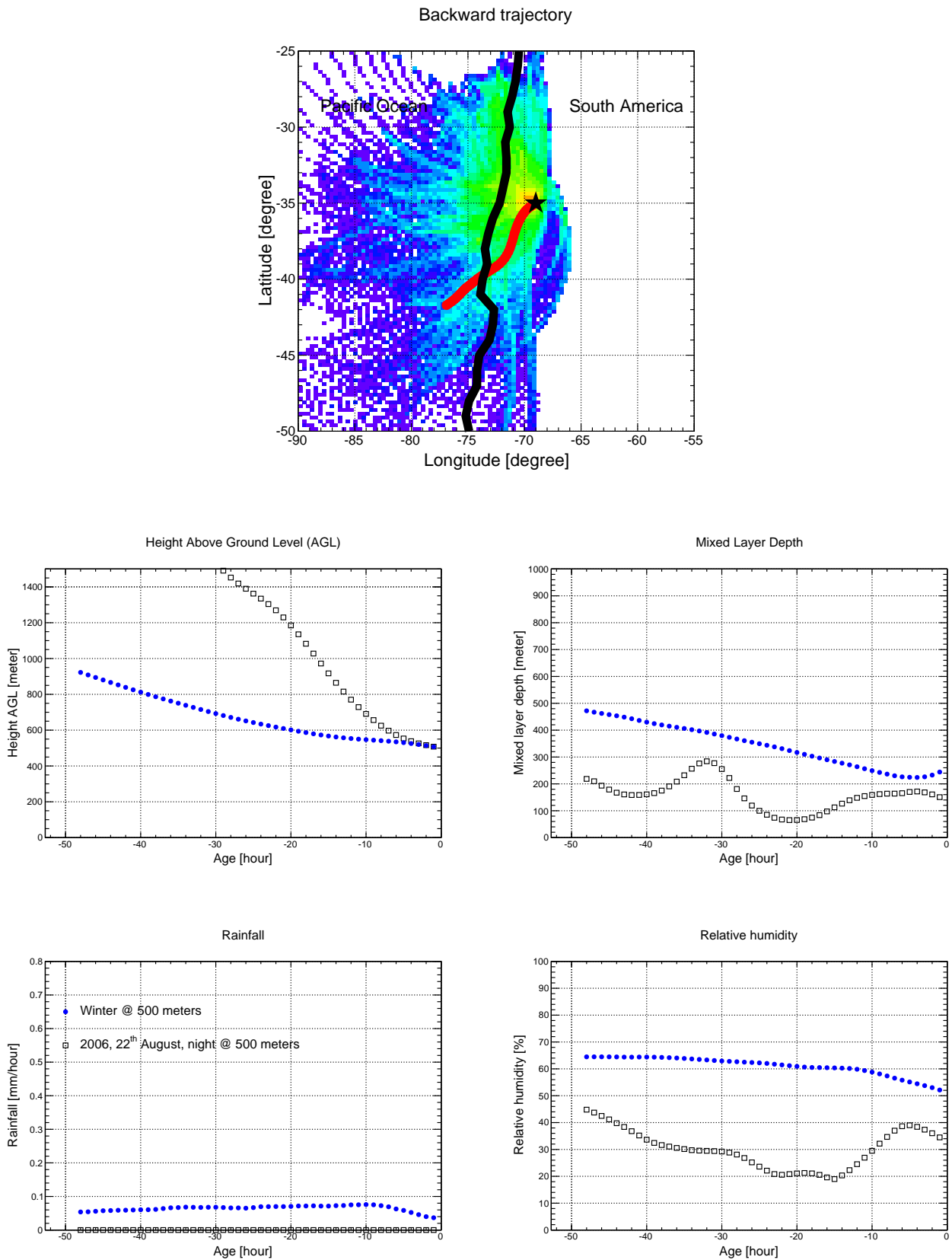


Figure 27: Rayleigh night on 22/08/2006 described with the HYSPLIT data. *Upper panel:* the mean backward trajectory for the night is given in red and the distribution of the trajectories for the whole corresponding season is overlaid. *Lower panel:* the mean evolution profile for the night is given in black and the mean profile of the corresponding season is overlaid in blue.

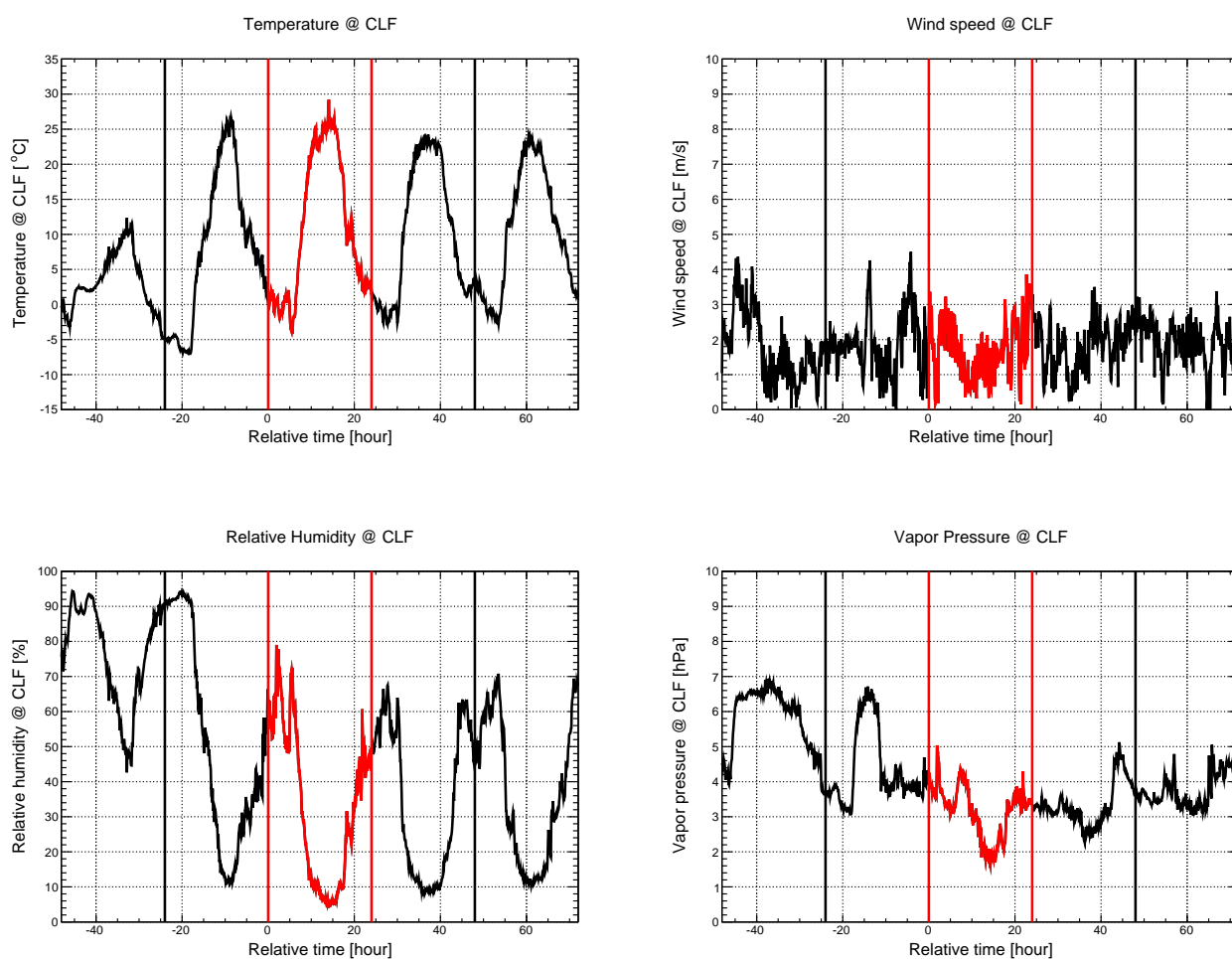
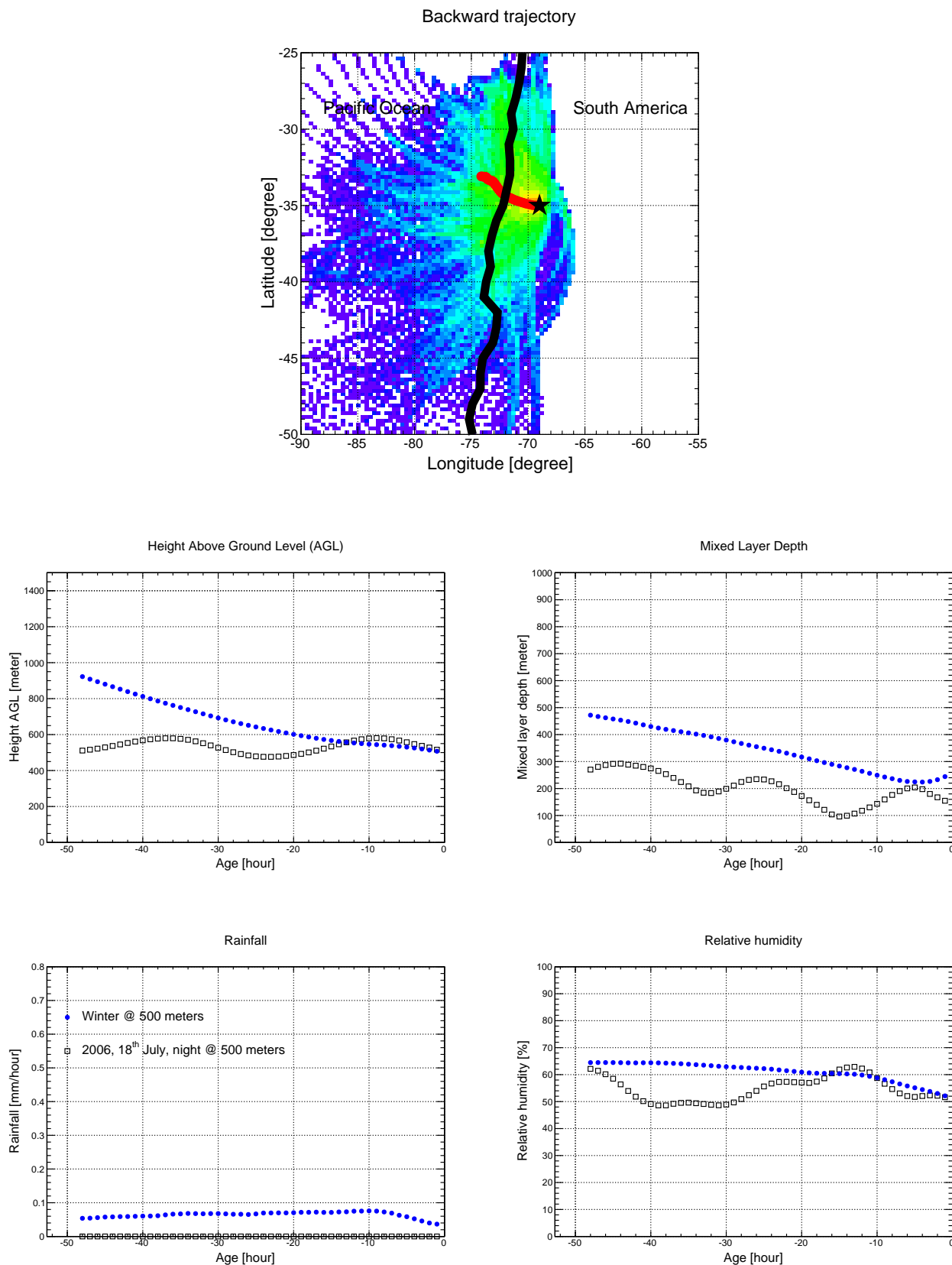


Figure 28: Rayleigh night on 22/08/2006 described with the ground-based weather station at CLF. Evolution of temperature, wind speed, relative humidity and vapor pressure are plotted over 5 days: two days before and after the corresponding Rayleigh night. The day where the Rayleigh night occurs is displayed in red color.



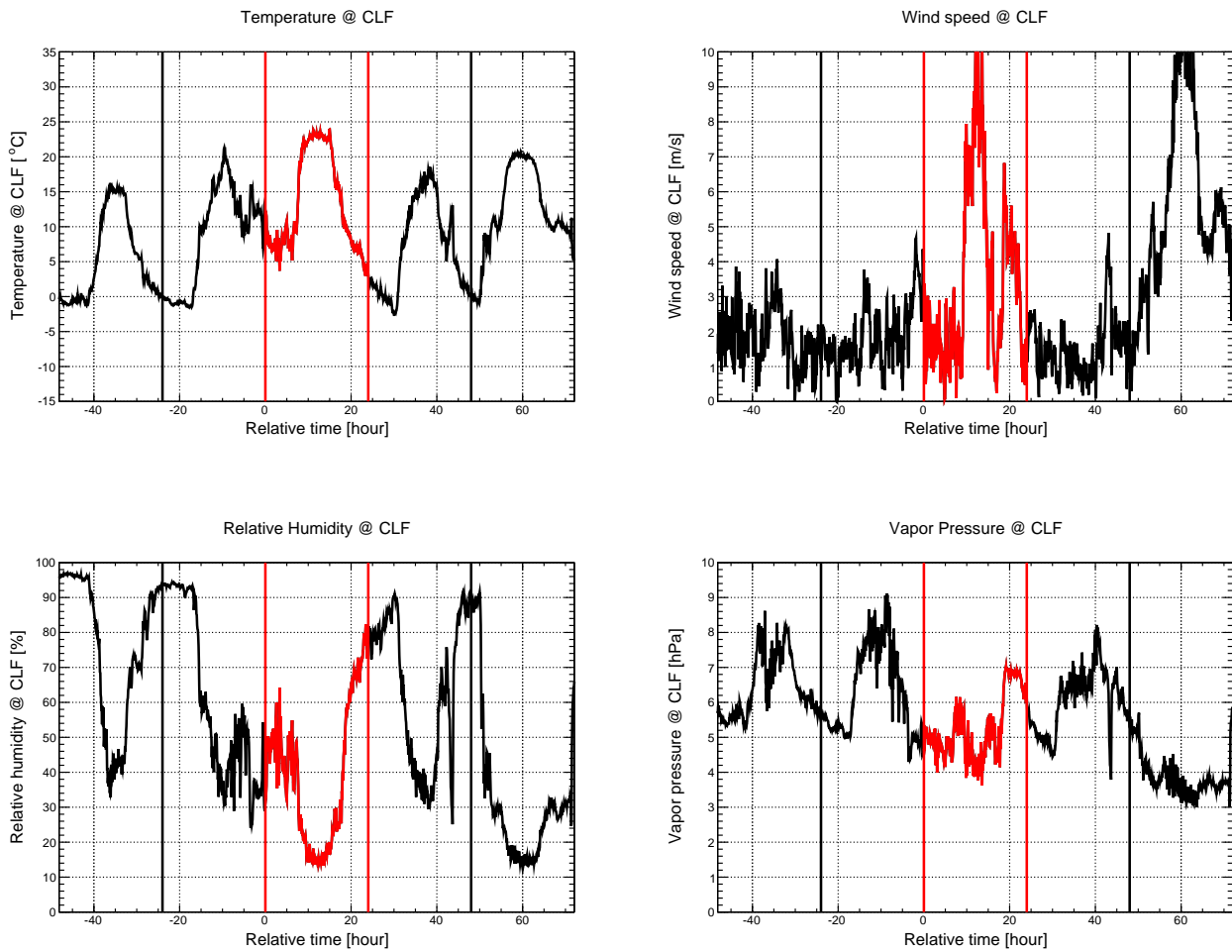
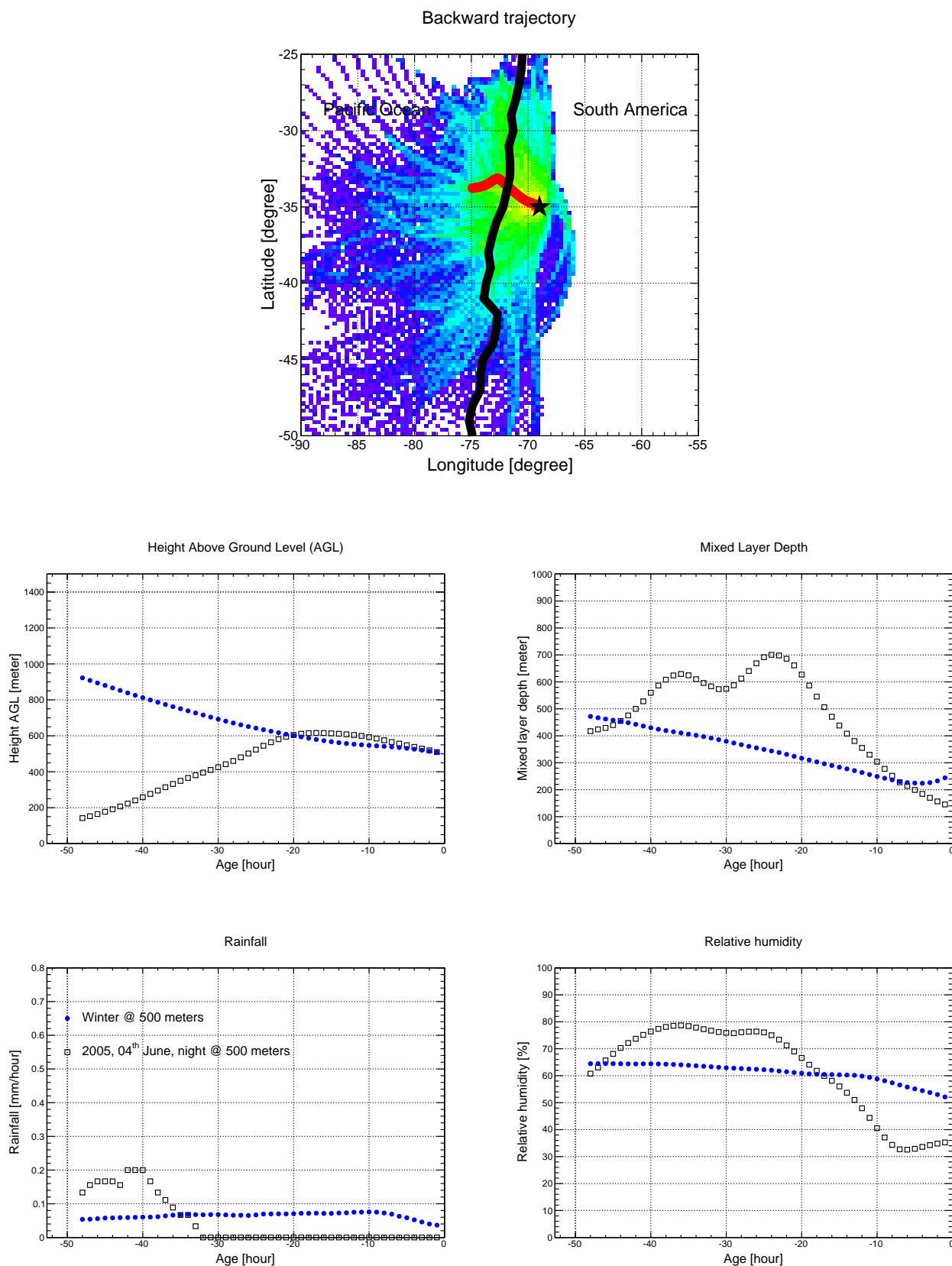


Figure 30: Rayleigh night on 18/07/2006 described with the ground-based weather station at CLF. Evolution of temperature, wind speed, relative humidity and vapor pressure are plotted over 5 days: two days before and after the corresponding Rayleigh night. The day where the Rayleigh night occurs is displayed in red color.



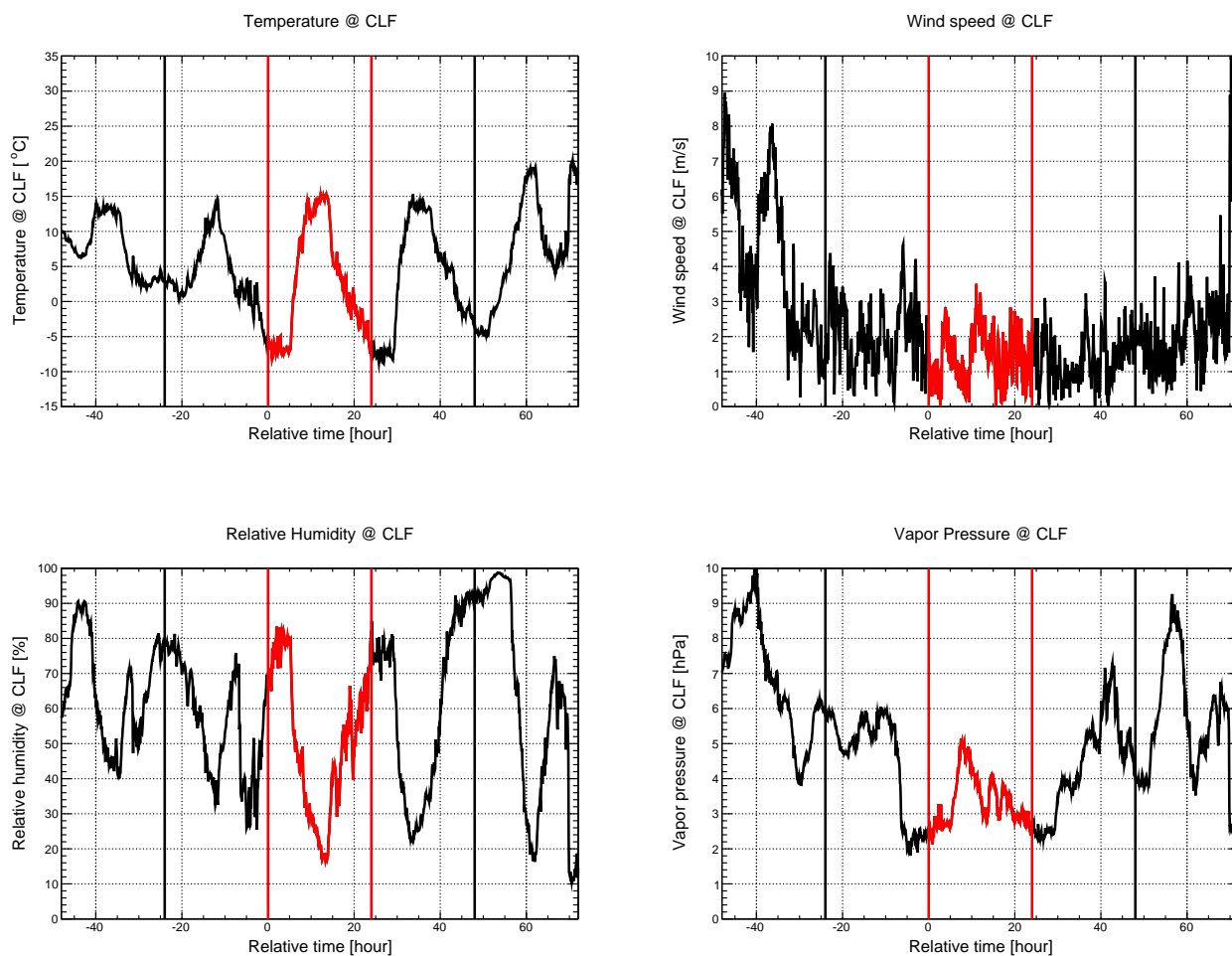


Figure 32: Rayleigh night on 04/06/2005 described with the ground-based weather station at CLF. Evolution of temperature, wind speed, relative humidity and vapor pressure are plotted over 5 days: two days before and after the corresponding Rayleigh night. The day where the Rayleigh night occurs is displayed in red color.

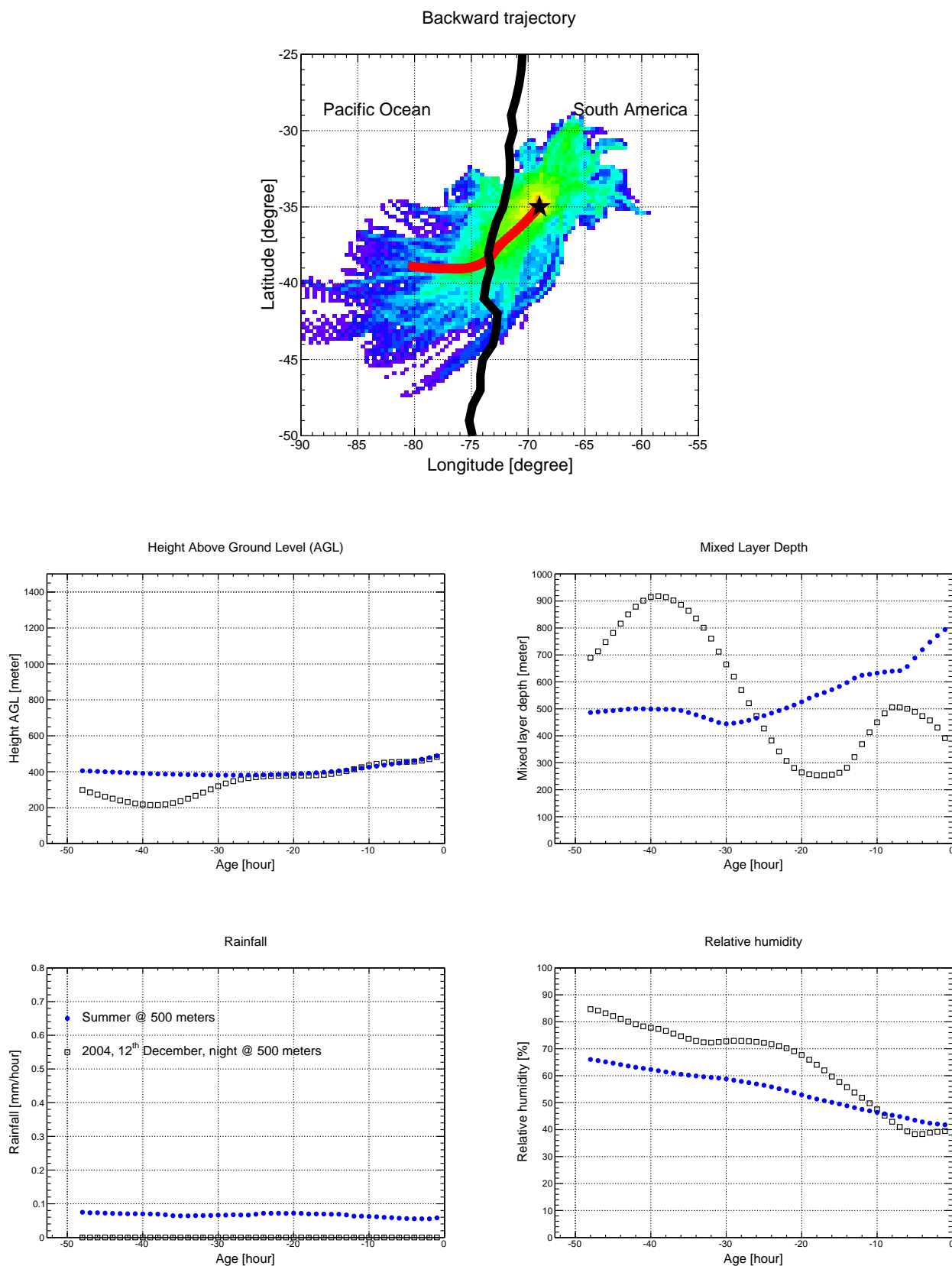


Figure 33: Rayleigh night on 12/12/2004 described with the HYSPLIT data. *Upper panel:* the mean backward trajectory for the night is given in red and the distribution of the trajectories for the whole corresponding season is overlaid. *Lower panel:* the mean evolution profile for the night is given in black and the mean profile of the corresponding season is overlaid in blue.

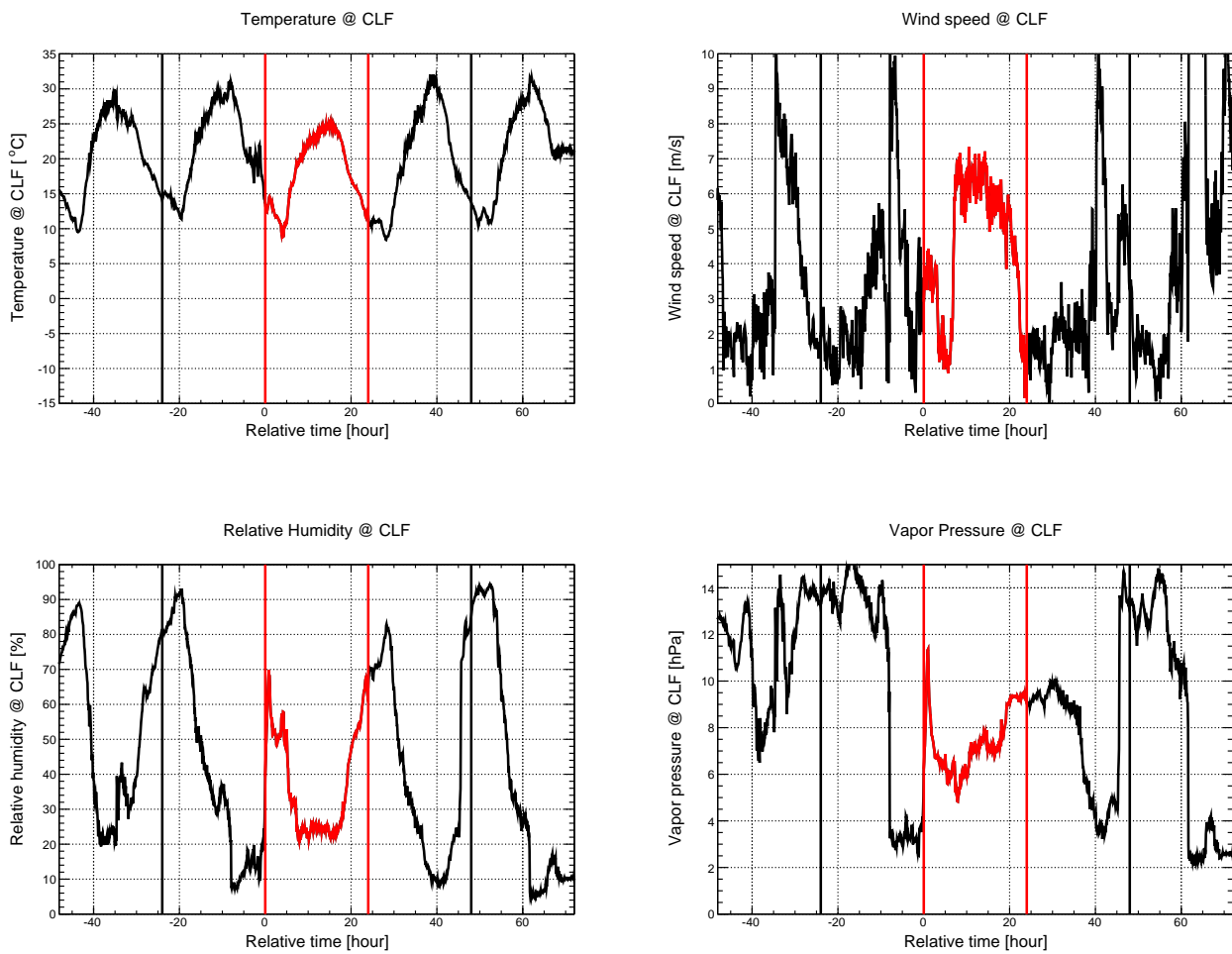


Figure 34: Rayleigh night on 12/12/2004 described with the ground-based weather station at CLF. Evolution of temperature, wind speed, relative humidity and vapor pressure are plotted over 5 days: two days before and after the corresponding Rayleigh night. The day where the Rayleigh night occurs is displayed in red color.

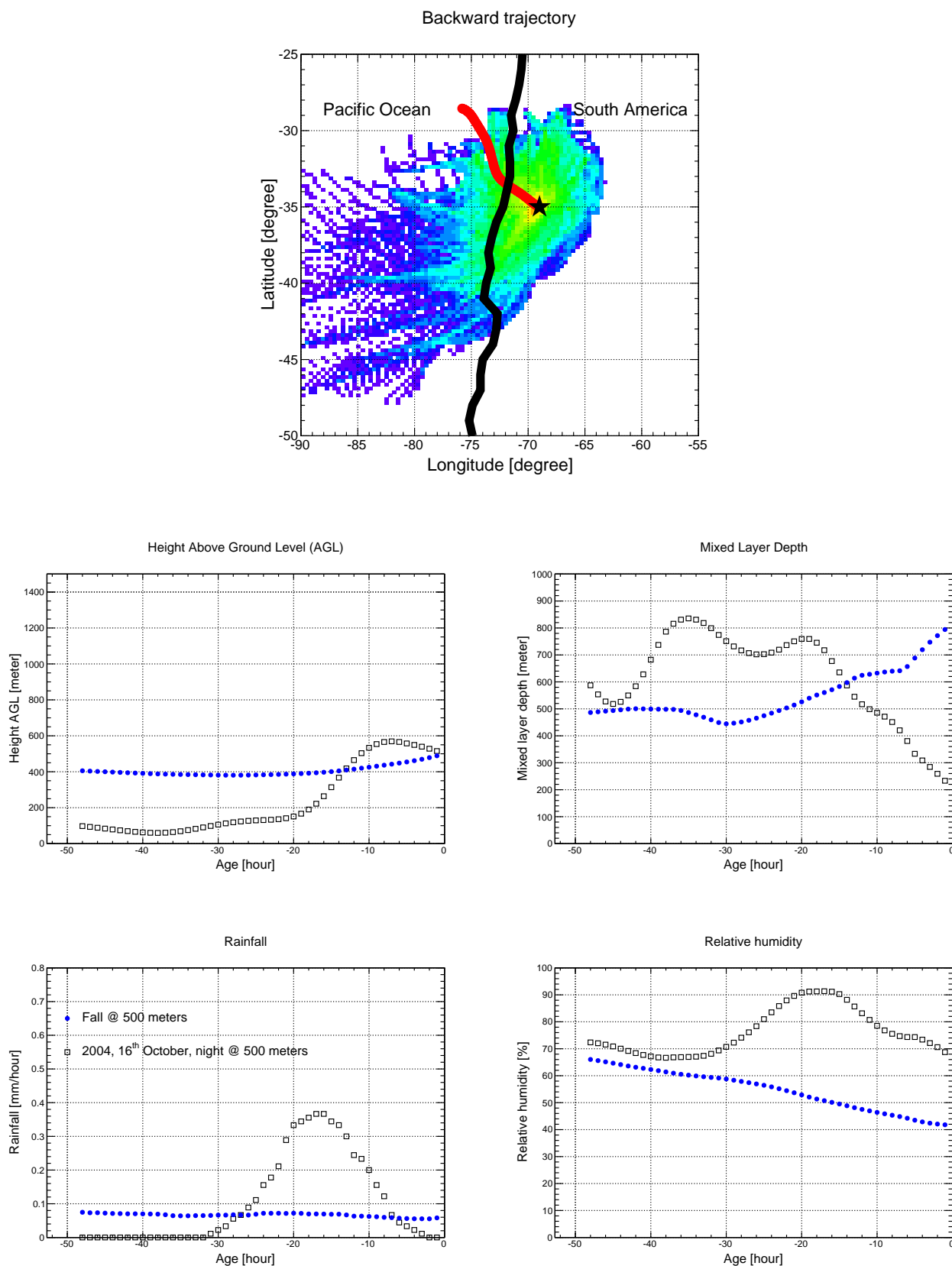


Figure 35: Rayleigh night on 16/10/2004 described with the HYSPLIT data. *Upper panel:* the mean backward trajectory for the night is given in red and the distribution of the trajectories for the whole corresponding season is overlaid. *Lower panel:* the mean evolution profile for the night is given in black and the mean profile of the corresponding season is overlaid in blue.

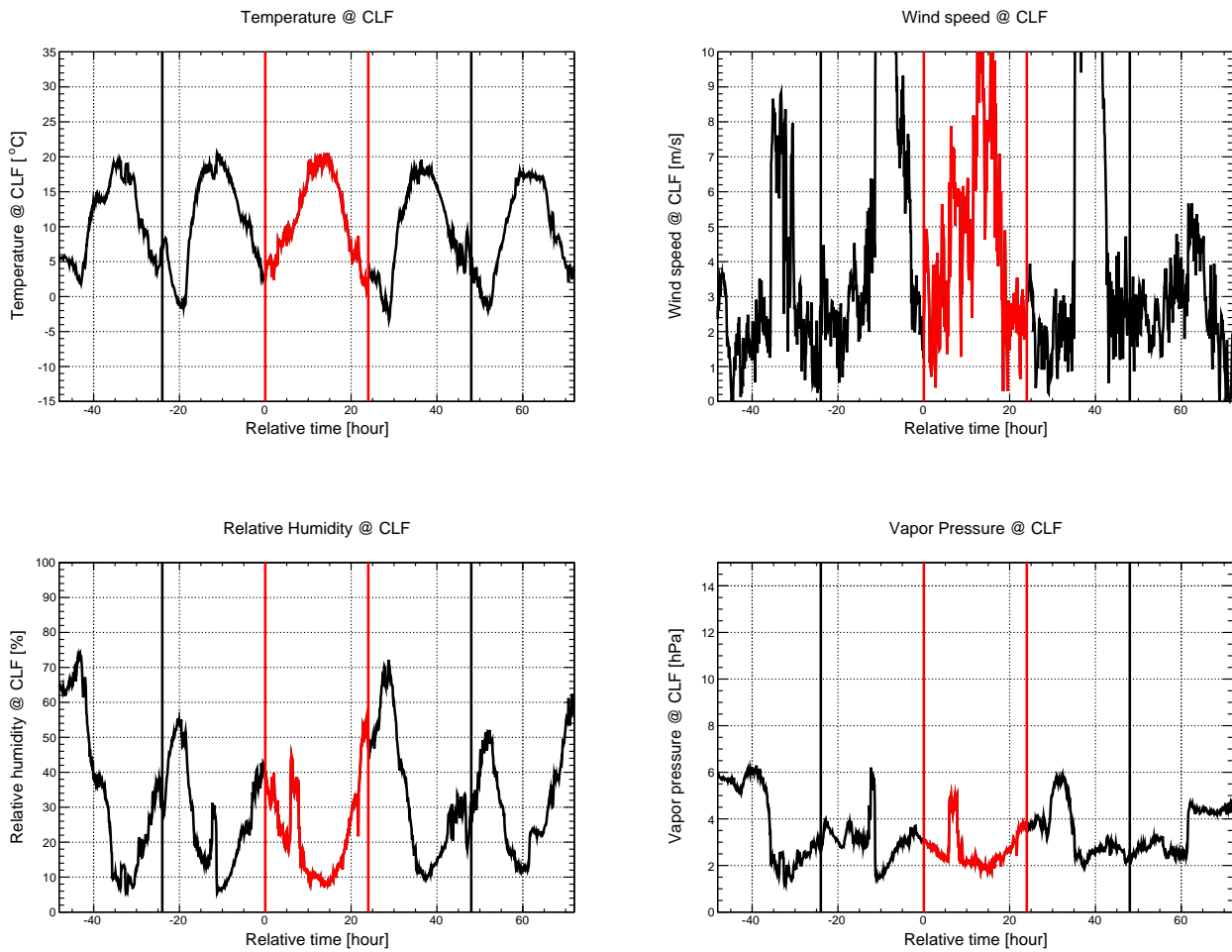


Figure 36: Rayleigh night on 16/10/2004 described with the ground-based weather station at CLF. Evolution of temperature, wind speed, relative humidity and vapor pressure are plotted over 5 days: two days before and after the corresponding Rayleigh night. The day where the Rayleigh night occurs is displayed in red color.

Atmospheric aerosols at the Pierre Auger Observatory: characterization and effect on the energy estimation for ultra-high energy cosmic rays

Abstract: The Pierre Auger Observatory, located in the Province of Mendoza in Argentina, is making good progress in understanding the nature and origin of the ultra-high energy cosmic rays. Using a hybrid detection technique, based on surface detectors and fluorescence telescopes, it provides large statistics, good mass and energy resolution, and solid control of systematic uncertainties.

One of the main challenges for the fluorescence detection technique is the understanding of the atmosphere, used as a giant calorimeter. To minimize as much as possible the systematic uncertainties in fluorescence measurements, the Auger Collaboration has developed an extensive atmospheric monitoring program. The purpose of this work is to improve our knowledge of the atmospheric aerosols, and their effect on fluorescence light propagation.

Using a modelling program computing air mass displacements, it has been shown that nights with low aerosol concentrations have air masses coming much more directly from the Pacific Ocean. For the first time, the effect of the aerosol size on the light propagation has been estimated. Indeed, according to the Ramsauer approach, large aerosols have the largest effect on the light scattering. Thus, the dependence on the aerosol size has been added to the light scattering parameterizations used by the Auger Collaboration. A systematic overestimation of the energy and of the maximum air shower development X_{\max} is observed.

Finally, a method based on the very inclined laser shots fired by the Auger central laser has been developed to estimate the aerosol size. Large aerosol sizes ever estimated at the Pierre Auger Observatory can now be probed. First preliminary results using laser-shot data collected in the past have identified a population of large aerosols.

Keywords: Pierre Auger Observatory – cosmic rays – atmosphere – aerosols – Ramsauer – Mie scattering – multiple scattering – HYSPLIT

Les aérosols atmosphériques à l'Observatoire Pierre Auger : caractérisation et effet sur l'estimation de l'énergie des rayons cosmiques d'ultra-haute énergie

Résumé: L'Observatoire Pierre Auger, situé dans la province de Mendoza en Argentine, réalise actuellement de grandes avancées dans la connaissance de la nature et de l'origine des rayons cosmiques d'ultra-haute énergie. Utilisant une technique de détection hybride, basée sur des détecteurs de surface et des télescopes de fluorescence, il fournit une large statistique, une bonne résolution en énergie, et un contrôle solide des incertitudes systématiques.

L'un des principaux défis pour la technique de détection par fluorescence est la compréhension de l'atmosphère, utilisée comme un calorimètre géant. Afin de réduire autant que possible les incertitudes systématiques sur les mesures par fluorescence, la Collaboration Auger a développé un important programme de suivi de l'atmosphère. Le but de ce travail est d'améliorer notre compréhension sur les aérosols atmosphériques, ainsi que leur effet sur la propagation de la lumière de fluorescence.

En utilisant un modèle de rétrotrajectographie des masses d'air, il a été montré que les nuits pauvres en aérosols ont des masses d'air provenant plus directement de l'Océan Pacifique. Pour la première fois, l'effet de la taille des aérosols sur la propagation de la lumière a été estimé. En effet, selon l'approche Ramsauer, les gros aérosols ont le plus grand effet sur la diffusion de la lumière. Ainsi, la dépendance en taille a été ajoutée aux paramétrisations décrivant la diffusion de la lumière et utilisée par la Collaboration Auger. Une surestimation systématique de l'énergie et du maximum de développement de la gerbe X_{\max} est observé.

Enfin, une méthode basée sur les tirs laser très incliné produit par le laser central d'Auger a été développée pour estimer la taille des aérosols. Des tailles d'aérosols jusque là jamais détectées à l'Observatoire Pierre Auger peuvent à présent être contraintes. De premiers résultats montrent une population d'aérosols de grande taille en utilisant des tirs laser effectués dans le passé.

Mots clés: Observatoire Pierre Auger – rayons cosmiques – atmosphère – aérosols – Ramsauer – diffusion de Mie – diffusion multiple – HYSPLIT
